# Unmanned aerial vehicles (UAVs) for multi-temporal crop surface modelling

–

## A new method for plant height and biomass estimation based on RGB-imaging

I n a u g u r a l - D i s s e r t a t i o n

zur

Erlangung des Doktorgrades

der Mathematisch-Naturwissenschaftlichen Fakultät

der Universität zu Köln

vorgelegt von

**Juliane Viktoria Bendig**

aus Neuss

Köln, 2015

Berichterstatter:    Prof. Dr. Georg Bareth

Prof. Dr. Karl Schneider

Tag der mündlichen Prüfung: 12.01.2015

# Abstract

Data collection with unmanned aerial vehicles (UAVs) fills a gap on the observational scale in remote sensing by delivering high spatial and temporal resolution data that is required in crop growth monitoring. The latter is part of precision agriculture that facilitates detection and quantification of within-field variability to support agricultural management decisions such as effective fertilizer application. Biophysical parameters such as plant height and biomass are monitored to describe crop growth and serve as an indicator for the final crop yield. Multi-temporal crop surface models (CSMs) provide spatial information on plant height and plant growth.

This study aims to examine whether (1) UAV-based CSMs are suitable for plant height modelling, (2) the derived plant height can be used for biomass estimation, and (3) the combination of plant height and vegetation indices has an added value for biomass estimation.

To achieve these objectives, UAV-flight campaigns were carried out with a red-green-blue (RGB) camera over controlled field experiments on three study sites, two for summer barley in Western Germany and one for rice in Northeast China. High-resolution, multi-temporal CSMs were derived from the images by using computer vision software following the structure from motion (SfM) approach. The results show that plant height and plant growth can be accurately modelled with UAV-based CSMs from RGB imaging. To maximise the CSMs' quality, accurate flight planning and well-considered data collection is necessary. Furthermore, biomass is successfully estimated from the derived plant height, with the restriction that results are based on a single-year dataset and thus require further validation. Nevertheless, plant height shows robust estimates in comparison with various vegetation indices. As for biomass estimation in early growth stages additional potential is found in exploiting visible band vegetation indices from UAV-based red-green-blue (RGB) imaging. However, the results are limited due to the use of uncalibrated images. Combining visible band vegetation indices and plant height does not significantly improve the performance of the biomass models.

This study demonstrates that UAV-based RGB imaging delivers valuable data for productive crop monitoring. The demonstrated results for plant height and biomass estimation open new possibilities in precision agriculture by capturing in-field variability.

## Zusammenfassung

Die Datenerfassung mit Unmanned Aerial Vehicles (UAVs) füllt eine Lücke auf der Beobachtungs-skala in der Fernerkundung durch die Bereitstellung von Daten mit hoher räumlicher und zeitlicher Auflösung, die für die Überwachung von Pflanzenwachstum erforderlich sind. Letzteres ist Teil der Präzisionslandwirtschaft, welche die Erfassung und Quantifizierung von Variabilität innerhalb von Getreidebeständen ermöglicht und so Entscheidungen des landwirtschaftlichen Managements unterstützt wie zum Beispiel bei effizienter Düngung. Die Überwachung biophysikalischer Para-meter wie Pflanzenhöhe und Biomasse dient der Erfassung des Pflanzenwachstums und liefert Indikatoren für den Ertrag. Multitemporale Oberflächenmodelle von Getreidebeständen (crop surface models - CSMs) liefern räumliche Informationen über die Pflanzenhöhe und das Pflanzen-wachstum.

Ziel dieser Studie ist es zu prüfen, ob (1) UAV-basierte CSMs sich zur Modellierung der Pflanzen-höhe eignen, (2) die abgeleitete Pflanzenhöhe für Biomasseschätzungen verwendet werden kann, und (3) die Kombination von Pflanzenhöhe und Vegetationsindizes einen Mehrwert für Biomasse-schätzung hat.

Um diese Ziele zu erreichen, wurden UAV-Flugkampagnen mit einer Rot-Grün-Blau (RGB)-Kamera in kontrollierten Feldversuchen in drei Untersuchungsgebieten durchgeführt, zwei für Sommer-gerste in Westdeutschland und eine für Reis im Nordosten Chinas. Aus den Bildern wurden hoch aufgelöste, multitemporale CSMs mit Hilfe von Computer-Vision-Software nach dem Structure from Motion (SFM) Ansatz abgeleitet. Die Ergebnisse zeigen, dass es genaue Modellierungen der Pflanzenhöhe und des Pflanzenwachstums mit UAV-basierten CSMs aus RGB Aufnahmen möglich sind. Um die Qualität der CSMs zu maximieren, sind eine genaue Flugplanung und wohlüberlegte Datenerfassung notwendig. Weiterhin lässt sich Biomasse erfolgreich mit der abgeleiteten Pflan-zenhöhe schätzen, mit der Einschränkung, dass die Ergebnisse aus einem einjährigen Datensatz erzeugt wurden und folglich eine weitere Verifizierung erfordern. Dennoch, zeigen die Schätzun-gen mittels Pflanzenhöhe robuste Ergebnisse im Vergleich mit verschiedenen Vegetationsindizes. Für die Biomasseschätzung in frühen Wachstumsstadien, zeigt sich zusätzliches Potential für die Biomasseschätzung mittels Vegetationsindizes im Bereich des sichtbaren Lichts, die aus UAV-ba-sierten Rot-Grün-Blau (RGB) Aufnahmen abgeleitet wurden. Eine Beschränkung der Ergebnisse ergibt sich aus der Verwendung von unkalibrierten Bildern. Die Kombination von Vegetationsindi-zes im Bereich des sichtbaren Lichts und der Pflanzenhöhe führte nicht zu einer signifikanten Ver-besserung in der Vorhersagequalität der Biomasse-Modelle.

Diese Studie zeigt, dass RGB-Aufnahmen auf der Basis von UAVs wertvolle Daten für die produktive Überwachung von Pflanzenwachstum liefern. Die gezeigten Ergebnisse für die Pflanzenhöhe und Biomasseschätzung eröffnen neue Möglichkeiten in der Präzisionslandwirtschaft durch die Erfassung von Variabilität innerhalb von Getreidebeständen.

## Acknowledgements

This dissertation and my entire time at the University of Cologne was a journey for me, a journey on which I met people who determined my itinerary. I would like to thank my supervisor Prof. Dr. Georg Bareth who introduced me to the world of remote sensing, who provided me the best educational opportunities in various places around the world and who often infected me with his enthusiasm. I would like to thank Dr. Andreas Bolten, Max Willkomm, Helge Aasen and all my other colleagues for support on the "dull, dirty and [thankfully rarely, J.B.] dangerous [UAV, J.B.] missions" (VAN BLYENBURGH, **1999**). Furthermore, I thank Dr. Andreas Bolten for teaching me so much technical know-how during building our small UAV fleet and for his editorial support. I thank Dr. Martin Gnyp for his highly constructive food for thought during the preparation of this dissertation. I thank my mother for her patient proof reading and the rest of my family and friends for their valuable moral support.

For the study site in Rheinbach I acknowledge the funding of the CROP.SENSe.net project in the context of Ziel 2-Programms NRW 2007-2013 "Regionale Wettbewerbsfähigkeit und Beschäftigung (EFRE)" by the Ministry for Innovation, Science and Research (MIWF) of the state North Rhine Westphalia (NRW) and European Union Funds for regional development (EFRE) (005-1103-0018).

For the study site in Jiansanjiang I acknowledge the The International Center for Agro-Informatics and Sustainable Development (ICASD).

Cologne was an excellent base camp for this journey. Let's see how it continues…

# Table of Contents

# 1 Introduction

## 1.1 Preface

In recent times the world's agricultural production system faces a number of challenges (**Oliver et al., 2013**). Today's agriculture and natural resources are pressured by population growth, increasing consumption of calorie- and meat-intensive diets and increasing use of cropland for non-food use like biofuel (**Foley et al., 2011; Food and Agriculture Organization of the United Nations, 2013; Mueller et al., 2012**). Population growth is accompanied by a decrease in available land. Furthermore, climate change will alter the reliability of critical components in crop production that causing production variability (**Atzberger, 2013; Srinivasan and Srinivasan, 2006**). Crop production can be quantified by agronomic parameters such as crop yield, leaf area index (LAI) or chlorophyll content (**Hatfield et al., 2008**). Parameters describing the crop status can be linked to climate modelling, for example when changing weather patterns cause production variability between two growing seasons. Within fields, variability is a result of soil quality, drainage conditions, physiography, aspect, salinity and nutrient management (**Oliver et al., 2013**). Additionally, variability may be of spatial or temporal nature. Spatial variability occurs across certain areas, whereas temporal variability occurs at different measurement times (**Whelan and Taylor, 2013**). Particularly, soil variability is closely linked to crop growth and hence crop production (**Adamchuk et al., 2010**). On the field and sub-field scale both natural variability as well as historic and recent management factors influence crop production. Humans have an impact on crop production variability through management decisions. Precision agriculture is a way of addressing production variability and optimising management decisions.

Precision agriculture accounts for production variability and uncertainties, optimises resource use and protects the environment (**Gebbers and Adamchuk, 2010; Mulla, 2013**). By definition, a complete precision agriculture system consists of four aspects: (1) field variability sensing and information extraction, (2) decision making, (3) precision field control, and (4) operation and result assessment (**Yao et al., 2011**). Precision agriculture adapts management practises within an agricultural field, according to variability in site conditions (**Seelan et al., 2003**). Consequently, there is a need for methods for characterizing such variability. Within-field crop monitoring is needed to describe site conditions with a high spatial and temporal resolution (**Campbell and Wynne, 2011**). In precision agriculture detailed in-field information is retrieved from using Global Position-

ing Systems (GPS), Geographical Information Systems (GIS) and Remote Sensing (RS) for agricultural decision making (**Seelan et al.**, **2003**). This information is required within a short time window for agricultural management (**Hunt Jr. et al.**, **2013**). RS provides such timely information for assessing within-field variability to adapt agricultural management purposes (**Atzberger**, **2013**). Once knowing the site conditions, fertilisers, herbicides and pesticides are only applied where and when they are needed (**Bongiovanni and Lowenberg-Deboer**, **2004**; **Nellis et al.**, **2009**). Ultimately, profitability increases and environmental contamination minimizes (**Whelan and Taylor**, **2013**). As a result, RS techniques are commonly used for crop monitoring (**Atzberger**, **2013**; **Clevers and Jongschaap**, **2001**).

Advances in computing, position-locating technologies and sensor development increased possibilities for using RS as an important data source of spatial and temporal information to adjust site-specific crop management (**Pinter et al.**, **2003**; **Shanahan et al.**, **2001**). RS refers to obtaining information from an object or phenomenon without getting into physical contact with it (**Lillesand et al.**, **2008**). In an agricultural context, RS includes non-destructive methods for crop monitoring opposed to destructive sampling and laboratory-based measurements (**Campbell and Wynne**, **2011**). Typically, RS records the surface reflectance in the visible or near-infrared parts of the electromagnetic spectrum (**Yao et al.**, **2011**). Reflectance is linked to crop biophysical parameters such as biomass or leaf area index (LAI) that indicate the final crop yield (**Cohen et al.**, **2003**). RS data is acquired fast and in high spatial and temporal detail compared to time, cost and labour-intensive destructive sampling (**Atzberger**, **2013**). Costs for RS data vary depending on the sensor and carrier platform (**Lillesand et al.**, **2008**). RS methods are classified according to the sensor type as either passive or active and according to the carrier platform. Passive RS employs instruments that sense emitted energy like optical or thermal sensors opposed to active RS with sensors emitting their own energy like radar or LIDAR sensors (**Campbell and Wynne**, **2011**). Sensors are carried by space-borne, manned or unmanned airborne or ground-based platforms (proximate sensing) (**Mulla**, **2013**). The platform determines the distance to the sensed object, resulting in a local, regional or global study scale. Common platforms for local scale studies include small aircraft and unmanned airborne platforms. The latter are referred to as unmanned aerial vehicles (UAVs), unmanned aerial systems (UAS) or remotely piloted aerial systems (RPAS) (**Colomina and Molina**, **2014**). UAV platforms are increasingly used in RS applications as demonstrated by **Colomina and Molina** (**2014**), **Hardin and Jensen** (**2011a**) and **Laliberte et al.** (**2011**), who give examples of different platforms and applications.

## 1.2    Research Problem and Aims

Agricultural production is influenced by the following variabilities: yield variability, field variability, soil variability, crop variability, anomalous factor variability and management variability (**Oliver et al.**, **2013**; **Zhang et al.**, **2002**). Those variabilities result in differences in crop growth within agricultural fields that can be quantified by monitoring crop canopy variables throughout the growing season. Important variables in this context include leaf area index (LAI), biomass, and nitrogen status (**Hansen and Schjoerring**, **2003**; **Serrano et al.**, **2000**). Biomass and nutrient use efficiency are considered as the main influencing factors on final crop yield (**Raun and Johnson**, **1999**). Moreover, biomass has a strong relationship with nitrogen (**Jensen et al.**, **1990**; **van Keulen et al.**, **1989**). Since nitrogen is an essential nutrient in crop production, it is often over-applied with negative impacts on yield and environment (**Hatfield et al.**, **2008**). Knowledge on crop status and condition can be used to effectively improve nitrogen application by eliminating nutrient overuse (**Atzberger**, **2013**; **Nellis et al.**, **2009**). In this context, the nitrogen nutrition index (NNI) is a powerful tool for assessing crop nitrogen status (**Mistele and Schmidhalter**, **2008**). The NNI is defined as the ratio of measured and critical nitrogen content. Biomass and nitrogen concentration are input values for the N dilution curve from which the critical nitrogen content is determined (**Lemaire et al.**, **2008**; **Lemaire and Gastal**, **1997**). Therefore, biomass is of major importance in in crop growth monitoring. Studies by **Moriondo et al.** (**2007**), **Rembold et al.** (**2013**), and **Marcelis et al.** (**1998**) give examples for quantifying crop growth by measuring daily biomass gains. The accumulated biomass may be multiplied by a harvest index to simulate the final yield.

Data for monitoring crop growth is most valuable when captured with high spatial and temporal resolution to properly detect the variability within an agricultural field. The advantage of using unmanned aerial vehicles (UAVs) for crop growth monitoring is that UAVs fill a niche of observational scale, resolution and height between manned aerial platforms and the ground (**Swain and Zaman**, **2012**). Low distance from the sensed object enables collection of high resolution data and minimizes atmospheric effects in images. A mayor advantage over satellite imagery is the independence of clouds and revisit time and fast data acquisition with real time capability (**Berni et al.**, **2009a**; **Eisenbeiss**, **2009**). Furthermore, high temporal resolution is given through high flexibility in data acquisition (**Aber et al.**, **2010**; **Shahbazi et al.**, **2014**). Those characteristics make UAVs highly suitable for many agricultural applications (**Jensen et al.**, **2007**; **Swain and Zaman**, **2012**). Examples include spraying from unmanned helicopters that is most popular in Japan where more than 10% of paddy fields are sprayed by using this technique (**Nonami et al.**, **2010**).

Generally, the growing interest in UAV systems produces a rapidly growing market with a predicted growth from 5400.0 M€ market value in 2013 up to 6350.0 M€ by 2018 (**MARKETSANDMARKETS**, **2013**). The number of available UAV systems multiplied by three from 2005 to the present (**COLOMINA AND MOLINA**, **2014**) with a relevant increase in civil/commercial platforms (**NONAMI ET AL.**, **2013**). The advice of market researchers is: "*Let them fly and they will create a new remote sensing market in your country*" (**MARKETSANDMARKETS**, **2013**). Trends in UAV technology include autonomous flights and swarm flights with multiple UAVs. Due to a rapid development in microcontroller processing speed and storage capacity the ability of UAVs to perform such complex tasks is increasing (**NONAMI ET AL.**, **2013**; **VALAVANIS AND VACHTSEVANOS**, **2014**). Consequently, sensor development goes in the direction of lighter sensors with high performance. For example, lightweight full-frame hyperspectral cameras, airborne laser scanners and inertial measurement units (IMUs) became available for the use on small UAVs weighing 0.5 to 5 kg with 0.3 to 1.5 h endurance (**BARETH ET AL.**, **2015**; **COLOMINA AND MOLINA**, **2014**; **WALLACE ET AL.**, **2012**). Those developments result in a strong demand for research on robust methodologies in the field of RS and crop monitoring. However, more attention should be paid to development and evaluation of data processing techniques (**SHAHBAZI ET AL.**, **2014**). Data acquisition and data processing for many new sensors are at an experimental stage and improvement is needed to make it available to end users that might be the farmers.

Several authors demonstrate how UAVs in combination with light weight sensors are used for crop monitoring. Crop health is the most popular topic in this context (**SHAHBAZI ET AL.**, **2014**), demonstrated for example by **HUANG ET AL.** (**2010**) for cotton fields, **NEBIKER ET AL.** (**2008**) for vineyards, and **CALDERÓN ET AL.** (**2014**) for opium poppy. Further research investigates water stress for example in orchards and vineyards by using thermal and multispectral sensors (**BALUJA ET AL.**, **2012**; **BELLVERT ET AL.**, **2014**; **BERNI ET AL.**, **2009a**). Existing UAV-based studies on crop growth monitoring include assessing biomass and nitrogen status (**HUNT JR. ET AL.**, **2005**), and deriving vegetation indices to relate them to LAI or nitrogen uptake (**HUNT, JR. ET AL.**, **2010**; **LELONG**, **2008**; **SWAIN AND ZAMAN**, **2012**). In addition, plant height is an important parameter in crop growth monitoring.

Numerous methods for measuring plant height on the ground exist (for example **BUSEMEYER ET AL.**, **2013**; **EHLERT ET AL.**, **2009**), but fail to produce accurate and precise data at high spatial and temporal resolution (**GRENZDÖRFFER AND ZACHARIAS**, **2014**). Additionally, those methods are not suitable for high growing crops like maize and sugarcane as well as irrigated crops like paddy rice. In those

cases, UAVs significantly simplify plant height measurements. EISENBEISS (**2009**) demonstrates digital surface model (DSM) generation in a maize field. Further examples of plant height measurements from UAVs are given by HONKAVAARA ET AL. (**2013**) in wheat and barley, by GRENZDÖRFFER AND ZACHARIAS (**2014**) in wheat and GEIPEL ET AL. (**2014**) in maize. However, studies are missing where plant height is systematically monitored throughout the growing period based on UAV data.

This study utilizes remotely sensed crop surface models (CSMs) to produce high spatial and temporal resolution plant height data. CSMs are 3D models of the canopy surface derived from RS data (HOFFMEISTER ET AL., **2010**). The concept is successfully applied on terrestrial laser scanning (TLS) data (HOFFMEISTER ET AL., **2010**; TILLY ET AL., **2014**). Transferring the CSM concept to UAV data is one key goal of this research.

A second goal is to model crop biomass based on plant height derived from UAV-based CSMs. Today, it is common practice to derive biomass from plant height since crop yield is linked to crop growth and crop yield is directly linked to biomass (SERRANO ET AL., **2000**). LATI ET AL. (**2013b**) estimated biomass from plant volume for single plants. PORDESIMO ET AL. (**2004**) found good relationships between stalk diameter and plant height for biomass estimation in corn stover. CATCHPOLE AND WHEELER (**1992**) give various examples for ground-based biomass estimation from plant height. Moreover, common tractor-based plant height measurement techniques aim at predicting biomass (BUSEMEYER ET AL., **2013**; EHLERT ET AL., **2009**). LUMME ET AL. (**2008**) and TILLY ET AL. (**2014**) estimate biomass using TLS. Following the argumentation that biomass can be estimated from plant height the hypothesis arises if biomass can estimated from UAV-based CSMs.

A third goal is to combine CSMs and vegetation indices. Vegetation indices that use reflectance in the near-infrared are a well-established method for biomass estimation (KUMAR ET AL., **2001**; QI ET AL., **1994**; ROUSE ET AL., **1974**). PERRY AND ROBERTS (**2008**) investigate the relationship of visible band vegetation indices and biomass. UAV-based imagery enables calculation of visible band vegetation indices. It follows that biomass estimation should benefit from combining plant height and vegetation indices. Both vegetation indices from ground-based hyperspectral measurements and UAV-data are suitable for that combination. In conclusion, key research questions are:

- Are UAV-based CSMs suitable for plant height modelling?
- Are UAV-based CSMs suitable for biomass estimation?
- Does a combination of plant height and vegetation indices improve biomass estimation?

## 1.3 Outline

The introduction, **chapter 1**, is followed by a specification of the basic principles and methods used, **chapter 2**. First, ways the estimate biomass from remote sensing data are presented. Secondly, methods for plant height and plant growth measurement are outlined and the principle of crop surface models (CSMs) is described. The next section introduces the method of UAV remote sensing, divided in a general UAV section and a description of 3D surface generation from red-green-blue (RGB) imaging. After that, methods for measuring spectral properties of plants are explained with regard to the focus of this research. The term reflectance is introduced and vegetation indices are presented as a method for expressing and comparing reflectance. **Chapter 2** concludes with a brief introduction to the basic agronomy of barley and rice and a description of the study sites. The study sites are located in Bonn and Rheinbach (Germany) for summer barley and in Jiansanjiang (China) for rice. **Chapters 3** to **7** comprise five research papers with the following content:

In **chapter 3** (**BENDIG ET AL.**, **2014b**) the CSM generation process from RGB imaging is described for the rice study site in China. In this context, CSM generation process is adapted to the conditions of an irrigated rice field.

In **chapter 4** (**BENDIG ET AL.**, **2013**) CSMs to monitor crop growth in summer barley are evaluated. Detected crop growth variability is evaluated with ground-based in-field control surveys of plant height, indicating a strong relationship between CSM-derived plant height and in-field control surveys. Results are verified in an accuracy assessment.

In **chapter 5** (**BENDIG ET AL.**, **2014a**) a biomass model is developed based on CSMs derived from UAV-based images. The CSMs are validated with in-field plant height ground measurements. For fresh and dry biomass estimation five linear regression models are tested in a cross validation. A strong correlation is found between plant height and fresh biomass, and plant height and dry biomass.

In **chapter 6** (**BENDIG ET AL.**, **submitted**) CSM-derived plant height and vegetation indices are evaluated for biomass estimation. Vegetation indices are calculated from hyperspectral data and RGB imagery. Plant height shows the strongest relationship with dry biomass across all growth stages. Visible band vegetation indices have potential for biomass estimation in early growth stages.

In **chapter 7** (**BARETH ET AL.**, **2015**) two UAV-based hyperspectral full-frame cameras are compared with a field spectroradiometer. The images of the hyperspectral full-frame camera are consistent with the measurements from the field spectroradiometer.

The discussion, **chapter 8**, addresses the accuracy of CSMs from UAV-based RGB imaging and general uncertainties in plant height modelling. Further discussion points include both, potentials of biomass estimation from CSMs and combining vegetation indices and CSMs for biomass estimation. Subsequently, additional applications of CSMs are presented. At the end, the methods' and dataset's limits are outlined.

**Chapter 9** concludes significant achievements of this research and summarises future research opportunities.

## 2    Basics and Methods

### 2.1    Biomass Estimation from Remote Sensing Data

The term biomass refers to the weight of living material, usually expressed as dry weight, in all or parts of an organism, population or community (**KUMAR**, **2006**). It is commonly expressed as weight per unit area. Biomass accumulates through photosynthesis when solar radiation is converted into carbon dioxide ($CO_2$) and water ($H_2O$) (**KUMAR ET AL.**, **2001**; **VARGAS ET AL.**, **2002**). Plants grow through photosynthesis and develop plant organs above and below the ground. Grasses like barley and rice develop underground root biomass and above ground biomass. The above ground biomass includes stems, leaves and ears depending on the development stage. Fresh biomass is dried to constant weight to obtain dry biomass. Biomass and biomass growth rate indicate potential crop yield (**SCULLY AND WALLACE**, **1990**; **SHANAHAN ET AL.**, **2001**). Furthermore, biomass is positively correlated with leaf area index (LAI) (**JONES AND VAUGHAN**, **2010**). Biomass maximizes under optimum nutrient, water availability, climate conditions, and pest control (**BEADLE AND LONG**, **1985**).

Crop biomass can be estimated with different techniques. Reflectance measurements base on the instantaneous relationship between spectral reflectance and biomass (**BARET ET AL.**, **1989**). VIs are derived from reflectance data and thus VIs are suitable for crop biomass estimation. Several studies demonstrate the relationship of different vegetation indices (VIs) and biomass on various spatial scales (**GITELSON ET AL.**, **2003**; **HEISKANEN**, **2006**; **LE MAIRE ET AL.**, **2008**). PH is also correlated with biomass and this relationship is commonly used for biomass estimation from tractor-based PH measurements (**BUSEMEYER ET AL.**, **2013**; **EHLERT ET AL.**, **2009**). PH measurement methods are described in **chapter 2.2**.

### 2.2    Plant Height, Plant Growth and Crop Surface Models

In plant modelling, plant height (PH) is defined as the vertical distance from the model's origin to the uppermost point (**LATI ET AL.**, **2013a**). For a plant canopy PH equals the difference between bare soil and the canopy top. Plant growth (PG) is defined by the difference in plant height between two observation dates. Both PH and PG are variables of interest in precision agriculture applications. PH is an important factor in optimizing site specific crop management and harvesting processes like crop yield predictions, precise fertilizer application, and pesticide application (**EHLERT ET AL.**, **2009**; **LATI ET AL.**, **2013a**). Moreover, PH is a key variable in determining yield potential (**GIRMA ET AL.**, **2005**) and in modelling yield losses from lodging (**BERRY ET AL.**, **2003**; **CHAPMAN ET AL.**,

**2014**; CONFALONIERI ET AL., **2011**). Monitoring PG is important since plants undergo intra-annual cycles linked to growth and phenology (ATZBERGER, **2013**).

Both PH and PG are measured by using RS methods. Destructive PH measurement is carried out by clipping the plant and measuring length with a ruler. Non-destructive methods include direct height measurement with laser rangefinders (EHLERT ET AL., **2009, 2008**), ultrasonic sensors (SCOTFORD AND MILLER, **2004**), 3D time-of-flight cameras (BUSEMEYER ET AL., **2013**), light curtains (FENDER ET AL., **2005**; MONTES ET AL., **2011**; SPICER ET AL., **2007**) or electronic capacitance meter, rising plate meter and simple pasture ruler (SANDERSON ET AL., **2001**). The latter are commonly used in rangeland applications. All of the above mentioned sensors and devices are usually mounted on tractors. Measurements cover the areas close to the tractor lanes resulting in limited spatial coverage. Spatial coverage increases when PH is derived from 3D point clouds collected by terrestrial laser scanning (TLS) (HOFFMEISTER ET AL., **2010**; LUMME ET AL., **2008**; TILLY ET AL., **2014**) and airborne laser scanning (HUNT ET AL., **2003**). Another way to derive such 3D point clouds is using UAV-based RGB imaging (see **chapter 2.3.2**). PG is acquired by repeated measurements with the described methods and calculating the difference between observations. When analysing plant canopies, rather PH and PG information of a surface is required than point measurements.

Such information is provided within the concept of crop surface models (CSMs), first introduced by HOFFMEISTER ET AL. (**2010**). By definition CSMs represent the top of the plant canopy at a given point in time (HOFFMEISTER ET AL., **2013**). CSMs are accurately georeferenced and resolution typically ranges from 1 m to 0.01 m. In a CSM, PH results from the plant surface at a point in time $t_i$ minus the ground surface $t_0$ (**Figure 2-1** and **Figure 4-1**). PG is derived by subtracting surfaces at the start and the end of the desired observation period (BENDIG ET AL., **2013**). CSM products include PH and PG maps that enable spatial variability detection (TILLY ET AL., **2014**). Point clouds for CSM generation are acquired through RS techniques like TLS or UAV RS. The latter is described in the following section.
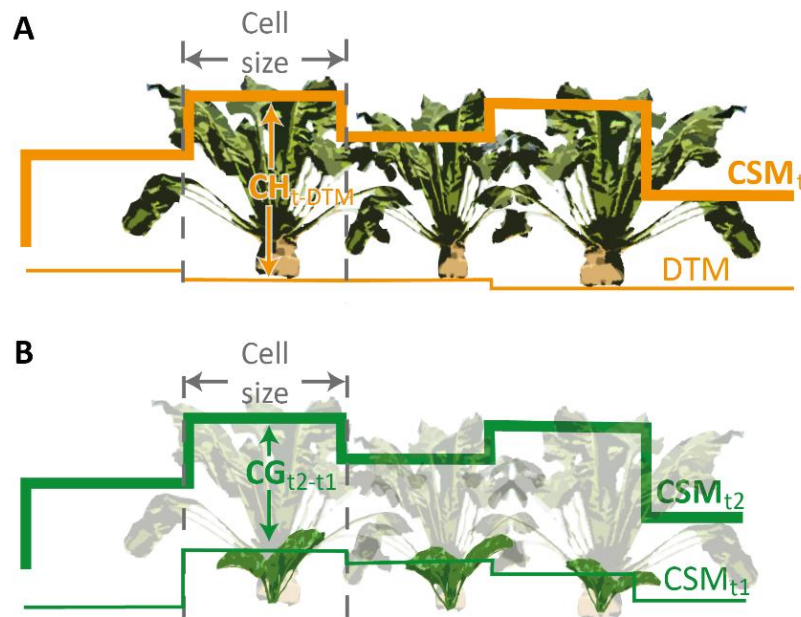
*Figure 2-1: Derivation of Crop Height (CH) and Crop Growth (CG) by the comparison of CSMs and the initial DTM (HOFFMEISTER, 2014).*

## 2.3 UAV Remote Sensing

This study focuses on data from a small UAV for RS by RGB imaging. The following section introduces the basics of UAV RS and DEM generation from UAV-based imaging.

### 2.3.1 UAVs

In recent years, Unmanned Aerial Vehicles (UAVs) became widespread in RS (COLOMINA AND MOLINA, 2014; SHAHBAZI ET AL., 2014). VAN BLYENBURGH (1999) defines UAVs as uninhabited, reusable, motorized aerial vehicles. UAVs rely on microprocessors allowing autonomous flight, nearly without human intervention (NONAMI ET AL., 2010). A data link ensures remote control by a pilot. Autopilots enable autonomous flights along predefined waypoints. Remotely controlled kites, blimps, balloons, fixed wings, helicopter or multi-rotor platforms are referred to as UAVs (EISENBEISS, 2009). Numerous platform classifications exist based on size, weight, range, endurance and power supply (COLOMINA AND MOLINA, 2014). In this study, a small, multi-rotor platform below 5 kg take-off weight with 15 min typical endurance is used. Those platforms are available at low cost (<1000 € to a few 10,000 €) as well as the sensors for RGB imaging (a few 100 € to a few 1000 €). A system consisting of platform, sensor and remote control has the advantages of high

portability, rapid field setup and use, and limited need for highly trained personnel enabling operation in many situations unsuitable for manned platforms (**ABER ET AL.**, **2010**).

*MK-OKTOKOPTER*

The MK-Oktokopter, is a low cost multi-rotor platform that is available for self-assembly (**HISYSTEMS GMBH**, **2013**). The system consists of an aluminium and fibre reinforced plastic airframe, eight brushless motors and propellers, flight control board and navigation control board (**NEITZEL AND KLONOWSKI**, **2011**). Flight and navigation control is facilitated with high-quality gyroscopes, pressure sensor, compass and GPS (**BÄUMKER AND PRZYBILLA**, **2011**). Lithium polymer batteries are used for power supply. With included batteries the UAV weighs less than 2.5 kg. The maximum additional sensor payload is 1 kg. In addition to the UAV itself the UAV-system comprises a remote control and autopilot for waypoint navigation and autonomous flights (**BENDIG ET AL.**, **2013**). Attached sensors are triggered by the remote control. Self-assembly allows for individual system modification like adding plugs to power cables for an easily detachable airframe during transport in a suitcase. Camera holder, gimbal and landing gear are adjusted according to the sensor payload. Furthermore, understanding the system's principle of operation allows for onsite repair during field campaigns (**Figure 2-2**).



*Figure 2-2: UAV-system onsite repair during one of the first field campaigns, Rheinbach, 18 May 2011.*

*UAV SENSORS*

Today, many lightweight sensors are available for use on small UAV-systems for various crop monitoring applications. Sensor systems range from low-cost amateur to professional sensors specially designed for use on UAV-systems. There are visible band cameras (*e.g.* for 3D modelling), multi-spectral and hyperspectral ones (*e.g.* for crop health status) as well as thermal cameras (*e.g.* for plant stress). Additionally, laser scanners and radar systems are available (*e.g.* for 3D modelling) (**COLOMINA AND MOLINA**, **2014**). Weight is the main limiting factor for using a sensor on a UAV. Within the scope of this dissertation low-weight and low-cost sensors are tested on the above described MK-Oktokopter:

- **Visible**: Panasonic Lumix GF3 and GX1 digital consumer-grade cameras (**BENDIG ET AL.**, **2014a**, **2013**)

- **Multispectral**: Tetracam Mini-MCA 4-channel multispectral camera (550, 671, 800, 950 nm) (**BENDIG ET AL.**, **2012**)

- **Thermal**: NEC F30IS thermal imaging system (**BENDIG ET AL.**, **2012**)

- **Hyperspectral**: Cubert UHD185 Firefly (450-950 nm) and Rikola Ltd. hyperspectral camera (500-900 nm) (**BARETH ET AL.**, **2015**)

Results presented in the following chapters concentrate on images obtained from the visible sensors because calibration of data from other sensors is not satisfactorily solved. The Tetracam Mini-MCA needs careful calibration and post-processing of images (**KELCEY AND LUCIEER**, **2012**; **LALIBERTE ET AL.**, **2011**; **VON BUEREN ET AL.**, **2014**). Thermal imaging adds complexity to image interpretation due to lighting conditions, sun angle, local atmospheric conditions (**BERNI ET AL.**, **2009b**). Low image resolution (160x120 pixel for NEC F30IS) poses challenges on image georectification (**HARTMANN ET AL.**, **2012**). Cubert UHD185 Firefly and Rikola Ltd. hyperspectral camera only became available two years ago and had to be integrated in the UAV-system before first data could be recorded in 2013 (**BARETH ET AL.**, **2015**). Therefore, the following section deals with data processing of UAV-based RGB imaging only.

## 2.3.2 DSMs/DEMs from UAV-based RGB Imaging

Two types of models can be derived from UAV-based RGB imaging. By definition, digital surface models (DSMs) or digital terrain models (DTMs) represent the spatial distribution of terrain attributes. Digital elevation models (DEMs) show the spatial distribution of elevations in an arbitrary

datum (**PECKHAM AND JORDAN**, **2007**). Such models are needed for plant height (PH) and plant growth (PG) analysis with CSMs. The DSM/DEM generation process comprises:

- image collection
- image processing
- and product generation.

*IMAGE COLLECTION*

Image collection involves considering the image scale and the area of interest (AOI). The AOI equals the agricultural field to be studied. The scale is the spatial resolution of an image. It is given by the pixel size that is the linear dimension of a pixel (**ABER ET AL.**, **2010**). The area covered by one pixel depends on the height above ground ($H_g$) and the focal length (f) of the camera resulting in the ground sampling distance (GSD) (**Equation 2-1**):

$$GSD = pixel\ size * \frac{H_g}{f}\ \textbf{(2-1)}$$

Images are mostly taken from a vertical vantage point, known as nadir, with a certain overlap. The minimal required forward overlap is 60% and 20-30% side lap between flight strips. Those numbers are common in small format aerial photography (**ABER ET AL.**, **2010**). For UAV campaigns overlaps are usually higher with 80% forward overlap and 60% side lap (**COLOMINA AND MOLINA**, **2014**).

*IMAGE PROCESSING*

Two types of software are generally used for image processing: traditional photogrammetry software or computer vision software. Examples for photogrammetry software are Leica Photogrammetry Suite (LPS) and PhotoModeler. The photogrammetric approach starts with camera calibration, followed by ground control point (GCP) identification and tie point research either automatic or manual depending on the software (**SONA ET AL.**, **2014**). GCPs are points of known ground coordinates that facilitate georeferencing. Additional tie points identified by the software support the process. In a next step, exterior image orientation is estimated based on known interior image orientation. Exterior orientation is defined by X, Y and Z ground coordinates and the UAV's roll, pitch and yaw (**ABER ET AL.**, **2010**). Roll equals the rotation around the X axis, pitch equals the rotation around the Y axis and yaw equals the rotation around the Z axis. Interior image orientation is defined by focal length, principal point location, three radial and two tangential distortion coefficients. Finally a bundle adjustment, the orientation of an image block, is carried out (**REMONDINO ET AL.**, **2014**). Difficulties arise during image georeferencing and bundle adjustment when image positions differ from those common for classical aerial surveys. Leica LPS was initially tested on

data acquired for this study but arising problems during data processing led to a change to computer vision software.

Processing with computer vision is usually faster but reduces the user's control over georeferencing and block formation as well as calculated accuracies (**REMONDINO AND KERSTEN**, **2012**). Nevertheless, results are competitive with those from the photogrammetric approach (**SONA ET AL.**, **2014**). Available software packages include Pix4UAV (Pix4D SA, Switzerland), Bundler and Agisoft PhotoScan Professional (Agisoft LLC, Russia). Agisoft PhotoScan Professional is chosen because it is easy to use and it produces high quality results (**DONEUS ET AL.**, **2011**; **GINI ET AL.**, **2013**; **NEITZEL AND KLONOWSKI**, **2011**; **SONA ET AL.**, **2014**). Image processing with Agisoft PhotoScan is described below (**Figure 2-3**).
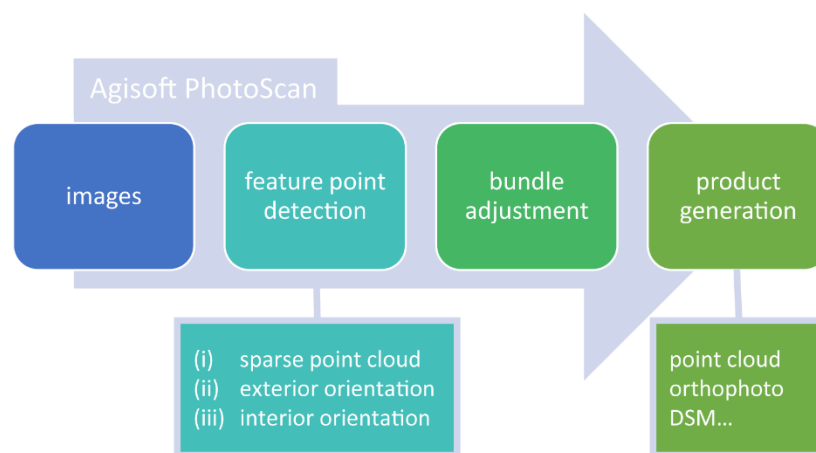


*Figure 2-3: Image processing workflow with Agisoft PhotoScan.*

In a first step, the images are aligned to each other. The alignment is executed using the Structure from Motion (SfM) algorithm (**ULLMAN**, **1979**). SfM reconstructs three-dimensional scene geometry and camera motion from an image sequence taken while moving around the scene (**SZELISKI**, **2010**). The algorithm detects geometrical similarities like object edges, so called image feature points, and subsequently monitors their movement throughout the image sequence (**VERHOEVEN**, **2011**). Products of the first processing step are a sparse point cloud (i), the exterior image orientation (ii) and the interior image orientation (iii). The sparse point cloud (i) is calculated from the information about the image feature points. Calculated camera positions equal the exterior image orientation (ii). In the photogrammetric approach (ii) and (iii) need to be known, which requires a calibrated camera. The advantage of the SfM approach with Agisoft PhotoScan is that it works with images from any uncalibrated digital camera (**SNAVELY ET AL.**, **2008**; **VERHOEVEN ET AL.**, **2012**).

Image information and thus image alignment is improved by using GCPs that are manually or half automatically identified in the images. The software's latest version supports automatic GCP detection.

In a second step the detailed scene geometry is built in a bundle adjustment using dense multi-view stereo (MVS) algorithms (SCHARSTEIN AND SZELISKI, **2002**). Like the image feature points, all pixels are used in this step to reconstruct finer scene details. The reconstruction accuracy may be adjusted by the user. The three dimensional geometry is then represented in a mesh of local coordinates. Local coordinates are transferred into an absolute coordinate system by applying a Helmert similarity transformation (VERHOEVEN ET AL., **2012**).

*PRODUCT GENERATION*

In a third step the desired products are exported for further analysis. Products include point clouds, orthophotos and DSMs. No filtering is applied to the point clouds, thus they contain outliers and noise (AGISOFT LLC, **2013**). Orthophotos are exported in common image formats such as *.JPG or *.TIF with specified coordinate system, image blending mode, and the pixel size where the default value results from the entered flying height. DSM export options are similar to the latter but the default pixel size is defined by chosen accuracy during dense point cloud generation. The DSMs are required for CSM generation (**chapter 2.2**).

## 2.4    Measuring Spectral Properties of Plants

Any RS sensor used in plant studies somehow exploits the spectral properties of plants. Traditionally, RS of agriculture involves timely spectral reflectance information that is linked to the plants through structural, biochemical, and physiological properties (NELLIS ET AL., **2009**; ROBERTS ET AL., **2011**). This section aims at explaining reflectance as well as basic concepts of vegetation indices. Since this study focuses on biomass estimation, a more detailed description of this plant parameter is given.

### 2.4.1 Reflectance

Remote sensing methods employ electromagnetic radiation (EMR) such as light, heat and radio waves for detecting and measuring plant properties (SABINS, **1997**). EMR moves at light velocity in a harmonic wave pattern in different wavelengths. Once EMR hits a matter it is either transmitted, adsorbed, scattered, emitted or reflected. Absorption causes heating and determines the EMR

emission (**Campbell and Wynne**, **2011**). The Stefan-Boltzmann law specifies the relationship between total emitted radiation (W in watts/cm$^2$) of a blackbody and temperature (T in K) (**Equation 2-2**):

$$W = \sigma T^4 \text{ (2-2)}$$

According to this law, the total emitted radiation is proportional to temperature to the power of four, times the Stefan-Boltzmann constant ($\sigma = 5.6697 \times 10^{-8}$). The peak intensity of radiation shifts to shorter wavelengths ($\lambda$ [nm]) with increased temperature (T [K]). The relationship is defined by Wien's displacement law for a blackbody (**Equation 2-3**):

$$\lambda = 2.897.8/T \text{ (2-3)}$$

Short wavelength ultraviolet (UV) EMR <300 nm is absorbed by ozone ($O_3$), and long wavelength EMR <1 cm is absorbed by clouds in the earth's atmosphere. The atmospheric composition varies with place and time and thus EMR hitting the earth surface varies. For this study, RS methods using the reflected part of EMR are of interest.

The reflection is defined as the ratio of reflected energy to incident energy (**Kumar et al.**, **2001**). It is measured with sensors that are either framing systems, known as cameras, or scanning systems, so called single detectors with a narrow field of view (FOV) (**Sabins**, **1997**). A sensor's spectral resolution is defined by the bandwidth that is determined by the wavelength interval recorded at 50% of peak response of the detector. Multispectral sensors typically consist of six to 12 broad bands whereas hyperspectral sensors consist of many (200 or more), narrow bands down to 2 nm or less (**Albertz**, **2007**; **Jones and Vaughan**, **2010**). According to the spectral resolution different plant properties can be studied.

A plant's reflectance curve has typical properties in each spectral domain. The ranges of such domains are differently defined in the literature. The definition by **Kumar et al.** (**2001**) is used below. The biochemical plant constituents include foliar pigments like chlorophyll (Chl), carotene and xanthophyll that absorb light in the visible (VIS) spectrum (400-700 nm). Pigments absorb the UV and VIS with distinct but overlapping absorption features (**Roberts et al.**, **2011**). Reflectance strongly increases in the red edge between 690 and 720 nm. The point of maximum slope is called red edge inflection point. Maximum reflectance is reached at the red edge shoulder around 800 nm. The red edge position may shift due to chlorophyll concentration or LAI. Reflectance in the near-infrared (NIR) region (700-1300 nm) varies with plant species and is dominated by the leaf internal structure. The shortwave infrared (SWIR) region (1300-2500 nm) is characterized by

strong water absorption bands and a resulting lower reflectance compared to the NIR (**KUMAR ET AL.**, **2001**).

Reflectance of vegetation cover changes with the above mentioned biological aspects and the vegetation structure. Water content, age, stress, cover geometry, row spacing and orientation and leaf distribution in the cover alter vegetation reflectance (**BANNARI ET AL.**, **1995**). Furthermore, reflectance is influenced by atmosphere composition, soil properties, soil brightness and colour as well as solar illumination geometry and viewing conditions.

### 2.4.2 Vegetation Indices

Vegetation indices (VIs) are developed to qualitatively and quantitatively evaluate vegetation using spectral measurements in relation to agronomic parameters like biomass or PH (**BANNARI ET AL.**, **1995**). They are commonly used for extracting information from RS data (**JACKSON AND HUETE**, **1991**). Numerous vegetation indices exist in VIS, NIR and SWIR spectral regions. The VIs are classified as broad multispectral indices, narrow hyperspectral indices, and combined indices depending on the width of spectral bands used for calculation. Narrow band indices can be better tuned to capture a specific absorption but need a hyperspectral sensor (**MUTANGA AND SKIDMORE**, **2004**; **ROBERTS ET AL.**, **2011**). Broad band indices can be calculated from many sensors. Most indices are calculated as ratios or normalized differences of two or three bands (**HUNT JR. ET AL.**, **2013**). Plant properties determined from VIs are grouped into structural, biochemical, and physiological properties (**ROBERTS ET AL.**, **2011**). Structural properties include fraction of vegetation cover, green leaf biomass and leaf area index (LAI). Biochemical properties include water, pigments like chlorophyll and plant structural materials like lignin. Physiological indices measure stress-induced changes in the state of xanthophyll, chlorophyll content, fluorescence or leaf moisture (**KUMAR ET AL.**, **2001**).

*VISIBLE DOMAIN VEGETATION INDICES*

VIS vegetation indices ($VI_{VIS}$) use the reflection in the blue (420-480 nm), green (490-570 nm) and red (640-760 nm) part of the spectrum. $VI_{VIS}$ can be calculated from UAV-based RGB images. **Table 2-1** gives an overview of $VI_{VIS}$ mentioned in the literature, while $VI_{VIS}$ developed in this study are listed in **Table 6-2**. The ratio of red to green reflectance is defined as Red Green Index (RGI) or red green ratio (**COOPS ET AL.**, **2006**). The Green Red VI (GRVI) or Normalized Green Red Difference Index (NGRDI) (**TUCKER**, **1979**) exploits the balance between red and green reflectance to distinguish phenology stages of vegetation (**MOTOHKA ET AL.**, **2010**). The GRVI/NGRDI may also be used for biomass estimation (**CHANG ET AL.**, **2005**; **HUNT JR. ET AL.**, **2005**). The Vegetation Atmospherically

Resistant Index (VARI) has proven good estimates of leaf area index (LAI), biomass and moisture stress (**GITELSON ET AL.**, **2003**; **PERRY AND ROBERTS**, **2008**). Moreover, it outperforms the NDVI in fraction of vegetation cover estimation (**GITELSON ET AL.**, **2002**). Crop parameters are assessed using the Green Leaf Index (GLI) and Triangular Greenness Index (TGI) (**HUNT ET AL.**, **2011a**) for leaf chlorophyll content (**HUNT JR. ET AL.**, **2013**) or NGRDI for biomass estimation (**HUNT JR. ET AL.**, **2005**). The Excess Green Index (ExG) (**WOEBBECKE ET AL.**, **1995**) quantifies green vegetation reflectance and is used for weed mapping and mapping of vegetation fraction (**RASMUSSEN ET AL.**, **2013**; **TORRES-SÁNCHEZ ET AL.**, **2014**). Although NIR VIs ($VI_{NIR}$) are widely used, **HUNT ET AL.** (**2013**) assert that higher correlations are found for leaf chlorophyll content and $VI_{VIS}$ than for $VI_{NIR}$.

*Table 2-1: Overview of visible band vegetation indices where R = reflectance (%), $R_B$ = 450-520 nm, $R_G$ = 520-600 nm, $R_R$ = 630-690 nm, λ = reflectance at a particular wavelength (band is ± 5 nm around centre wavelength). \*Multispectral sensor bands or digital camera bands of red, green and blue may be used instead of narrow bands (HUNT JR. ET AL., 2013).*

| VI | Name | Formula | References |
|---|---|---|---|
| RGI | Red Green Index | $\dfrac{R_R}{R_G}$ | (COOPS ET AL., 2006; GAMON AND SURFUS, 1999) |
| GRVI /NGRDI | Green Red Vegetation Index/ Normalized Green Red Difference Index | $\dfrac{R_G - R_R}{R_G + R_R}$ | (HUNT JR. ET AL., 2005; MOTOHKA ET AL., 2010; TUCKER, 1979) |
| VARI | Visible Atmospherically Resistant Index | $\dfrac{R_G - R_R}{R_G + R_R - R_B}$ | (GITELSON ET AL., 2002) |
| GLI | Green Leaf Index | $\dfrac{2 * R_G - R_R - R_B}{2 * R_G + R_R + R_B}$ | (HUNT JR. ET AL., 2013; LOUHAICHI ET AL., 2001) |
| TGI* | Triangular Greenness Index | $-0.5 \begin{pmatrix} (\lambda_r - \lambda_b) - \\ (R_R - R_G) \end{pmatrix} - \begin{pmatrix} (\lambda_r - \lambda_g) - \\ (R_R - R_B) \end{pmatrix}$ | (HUNT ET AL., 2011a) |
| ExG | Excess Green Index | $2 * R_G - R_R - R_B$ | (WOEBBECKE ET AL., 1995) |

*NEAR-INFRARED DOMAIN VEGETATION INDICES*

Most VI equations compare an absorbing wavelength to a non-absorbing wavelength (**ROBERTS ET AL.**, **2011**). Combinations of red, green, blue and NIR or SWIR bands exist depending on the investigated plant properties. Extensive lists of existing $VI_{NIR}$ and $VI_{SWIR}$ are given for example by **BANNARI ET AL.** (**1995**), **MULLA** (**2013**) and **ROBERTS ET AL.** (**2011**). A selection of commonly used $VI_{NIR}$ is presented in the following section (and in **Table 6-1**) based on the work by **GNYP ET AL.** (**2014**) and **HUETE** (**1988**). Simple Ratio (SR), the ratio of NIR to red reflectance (**JORDAN**, **1969**) and Normalized Difference Vegetation Index (NDVI) (**ROUSE ET AL.**, **1974**) are widely used and good predictors for

fresh and dry biomass. However, NDVI saturates with canopy closure during the vegetative growth cycle (heading stage for most crops) with high LAI values and varies with viewing geometry and soil reflectance (**BARET AND GUYOT**, **1991**; **HABOUDANE**, **2004**; **MUTANGA AND SKIDMORE**, **2004**). Moreover, atmospheric effects alter the reflectance (**CARLSON AND RIPLEY**, **1997**). Based on the NDVI, indices are adjusted to reduce the influence of atmosphere and soil. The Soil Adjusted Vegetation Index (SAVI) (**HUETE**, **1988**) contains the constant L that is adjusted according to vegetation density. For the Modified SAVI (MSAVI) the L value is replaced with a variable L function (**QI ET AL.**, **1994**). A simpler version is the optimised SAVI (OSAVI) where L was replaced with a constant value of 0.16 (**RONDEAUX ET AL.**, **1996**). The GnyLi is a new, narrow band index (**GNYP ET AL.**, **2014a**). All of the VIs listed here may be used to predict plant biomass that is discussed in **chapter 5**.

*Table 2-2: Selection of VIS and NIR vegetation indices where R = reflectance (%), $R_R$ = 630-690 nm, $R_{NIR}$ = 700-1300 nm, $R_i$ = reflectance in a narrow band e.g. $R_{1220}$ = 1220 nm, L = constant.*

| VI | Name | Formula | References |
|---|---|---|---|
| SR | Simple Ratio | $$\frac{R_{NIR}}{R_R}$$ | (**JORDAN**, **1969**) |
| NDVI | Normalized Difference Vegetation Index | $$\frac{R_{NIR} - R_R}{R_{NIR} + R_R}$$ | (**ROUSE ET AL.**, **1974**) |
| SAVI | Soil Adjusted Vegetation Index | $$(1 + L)x\frac{R_{800} - R_{670}}{R_{800} + R_{670} + L}$$ | (**HUETE**, **1988**) |
| MSAVI | Modified SAVI | $$0.5\left(2R_{800}+1-\sqrt{(2xR_{800}+1)^2-8(R_{800}-R_{670})}\right)$$ | (**QI ET AL.**, **1994**) |
| OSAVI | Optimised SAVI | $$(1 + 0.16)x\frac{R_{800} - R_{670}}{R_{800} + R_{670} + 0.16}$$ | (**RONDEAUX ET AL.**, **1996**) |
| GnyLi | Named by the developers Gnyp and Li | $$\frac{R_{900}xR_{1050} - R_{955}xR_{1220}}{R_{900}xR_{1050} + R_{955}xR_{1220}}$$ | (**GNYP ET AL.**, **2014a**) |

## 2.5 Agronomy of Barley and Rice

### 2.5.1 Barley

Barley (*Hordeum vulgare L.*) belongs to the grass family and has been cultivated since 5,000 B.C (**LIEBEREI AND REISDORFF**, **2007**). Barley originates from the Asian wild species *H. spontaneum Koch*. Today, barley is mainly cultivated in temperate climate while the producing region spreads from the subtropics to tropical high plateaus for example in the Andes and Himalaya. In 2013, the largest barley producer was Russia (15,39 mt/y), followed by Germany (10,34 mt/y) and France (10,31 mt/y) (**FOOD AND AGRICULTURE ORGANIZATION OF THE UNITED NATIONS**, **2013**).

Generally, barley is distinguished into winter and spring/summer barley. Both forms differentiate in cultivation period, temperature requirement and nutrient content (**LIEBEREI AND REISDORFF**,

**2007**). In the northern hemisphere, spring/summer barley has an average ripening period of 95 days and is suited for lower temperatures and has lower requirements for soil quality. Winter barley requires a cold period to induce flowering, prefers milder climate and has a longer ripening period than spring/summer barley. Spring/summer barley is usually sown in March or April while winter barley is sown in late September. The crop is harvested with yellow ripeness or full ripeness. Grains are used for bread making, as animal food or for beer brewing. Spring/summer barley is predominantly used as malting barley in the beer brewing process.

According to the "Biologische Bundesanstalt, Bundessortenamt und CHemische Industrie" BBCH scale, barley phenology is divided into three growth cycles with 10 principal growth stages (0-9) (**Lancashire et al., 1991**):

- Vegetative cycle: germination (0), leaf development (1) and tillering (2)
- Reproductive cycle: stem elongation (3), booting (4), inflorescence emergence and heading (5), flowering and anthesis (6)
- Post-heading cycle: development of fruit (7), ripening (8) and senescence (9).

Germination (0) is the development of the dry seed until the coleoptile penetrates the soil surface. During leaf development (1) one to nine or more leaves are developed. Stages 2 and 3 can begin before leaf development is completed. Tillering (2) is completed when the maximum number of tillers is reached. A pseudo stem develops during stem elongation (3). This stage ends with flag leaf development and continues with booting (4) of leaf sheath until first awns are visible. Inflorescence emergence and heading (5) end when the spikelets become visible and inflorescence is fully emerged. The beginning of flowering and anthesis (6) is indicated by first visible anthers and ends when all spikelets have flowered. Fruit development (7) follows with grain growth and different grain milk contents. During ripening (8) grains become harder until difficult to divide with a thumbnail. In the final senescence (9) stage, grains are very hard and loosening from the plant until the plant is dead and collapses. Plants growth is highest between leaf development (2) and flowering (6). Hence CSMs are produced during those development stages.

### 2.5.2 Rice

Rice (*Oryza sativa L.*) is a member of the grass family like barley. The plant's origin is not exactly known (**Lieberei and Reisdorff, 2007**). Today the Indian *O. fatua Koen, ex. Trin.* is accepted as the originating species. Rice has been cultivated since 3,000 B.C. Recently, rice is cultivated in the tropics and subtropics between 45° N and 40° S preferably at average temperatures between 20

and 38°C during the growing period. Biggest producers are China (203,29 mt/y), India (159,20 mt/y) and Indonesia (71,28 mt/y) (**FOOD AND AGRICULTURE ORGANIZATION OF THE UNITED NATIONS**, **2013**).

Due to intensive transpiration rice requires high water availability. In most cases rainfall is insufficient and fields need irrigation. Furthermore, rice cultivars are distinguished into tropical and temperate varieties (**LIEBEREI AND REISDORFF**, **2007**). The study site investigated consists of irrigated paddies in a lowland temperate climate. In China, rice seedlings are commonly grown in a greenhouse and later transplanted to the field. The field is then flooded with 15-30 cm of water. After flowering the water table is continuously decreased until the field is dry for harvesting. The growth cycle is 140-150 days long and grains are harvested with yellow ripening.

BBCH development stages are similar to those of barley with a few differences. Germination (0) and leaf development (1) usually take place in the greenhouse and plant development pauses after transplanting to continue again in the field. During tillering (2) a substantial number of tillers and leaves are produced compared to other cereals (**WATANABE ET AL.**, **2005**). Stem elongation (3) starts with the development of a green ring in the stem tissue. Booting (4) starts when the sheath of the flag leaf emerges from the penultimate leaf sheath. Inflorescence emergence and heading (5) start with panicle emergence and no grains loosen during senescence (9) (**LANCASHIRE ET AL.**, **1991**).

## 2.6    Study Sites

### 2.6.1  Barley – Bonn (2012)

*LOCATION*

The barley study site in Bonn is located at the Institute of Crop Science and Resource Conservation – Horticulture Science (Institut für Nutzpflanzenwissenschaften und Ressourcenschutz (INRES) - Gartenbauwissenschaft), University of Bonn, Germany (**Figure 2-5**). The institute is centrally located in the West German city of Bonn at 50°43'47" N, 7°04'29" E at 66 m above sea level. Bonn is located on both banks of the river Rhine with the predominant soil being luvisol from loess and loamy-sandy terrace deposits (**BGR**, **1994**). The climate is temperate with significant rainfall throughout the year (Cfb after Köppen-Geiger climate classification). The average annual temperature is 10°C, rising to average 20°C in July and dropping to average 1°C in January (**LANUV NRW**, **2011**). The average annual rainfall is 600-700 mm spreading relatively evenly over the year. The experiment field is located on flat terrain.
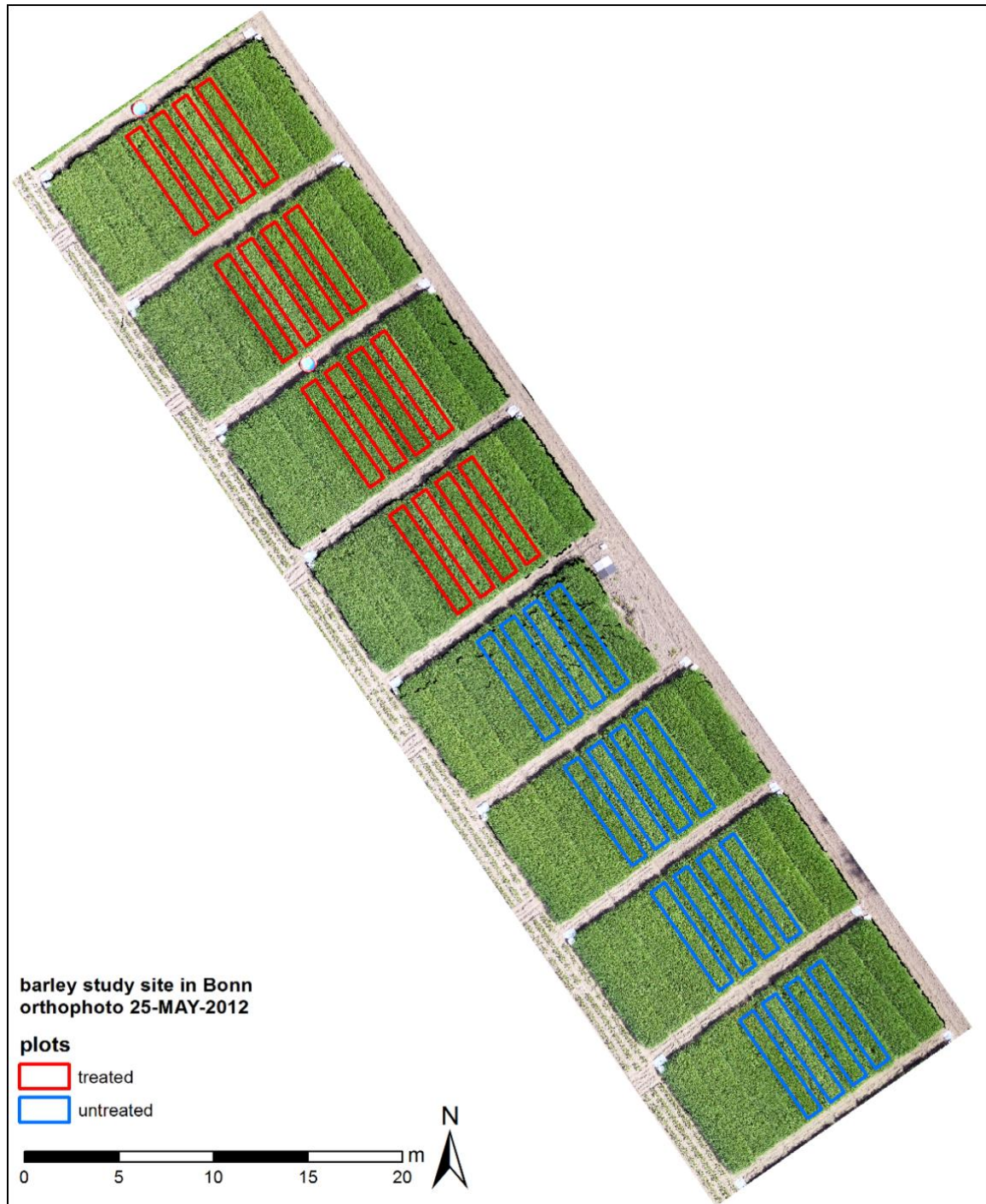
*Figure 2-4: Barley study site in Bonn, orthophoto 25 May 2012 and plots treated and untreated with fungicide.*

EXPERIMENT DESIGN AND FIELD DATA

The experiment consists of 32 plots that are 1.5 x 7 m in size. Four spring/summer barley cultivars are planted in randomized blocks with a sowing density of 320 seeds per m². One half of the field,

with four replications of each cultivar, is treated with a curative fungicide against three common plant diseases. The other half of the field is left untreated (**Figure 2-4**, **Figure 4-2**).

Destructive samples are taken to determine biomass, nitrogen (N)- and chlorophyll content. Additionally, non-destructive sampling of plant height, hyperspectral reflectance data and fluorescence data is conducted throughout the growing period. RGB images are acquired in five UAV flights between 14 May and 23 July 2012.

### 2.6.2 Barley – Rheinbach (2013)

*LOCATION*

The barley study site in Rheinbach is located at the Campus Klein-Altendorf research station for crop sciences of the Agricultural Faculty of the University of Bonn at 50°37'51" N, 6°59'32" E, 186 m above sea level. Klein-Altendorf is located near the township of Rheinbach with 26,600 inhabitants, 17 km southwest of Bonn (**Figure 2-5**). The region belongs to the lower Rhine basin and is known as one of the most important fruit growing regions of Germany. In addition to fruits agricultural crops are grown. Typical crops are sugar beet, wheat and winter barley. The soil is a mostly loamy silt with a high a soil quality (Ackerzahl: 93). The climate is similar to the one Bonn: temperate with significant rainfall throughout the year (Cfb after Köppen-Geiger climate classification). The average annual temperature is 9.2°C, rising to average 18°C in July and dropping to average 0°C in January (**KUNZ AND VÖLKERING**, **2013**; **LANUV NRW**, **2011**). The average annual rainfall is 595 mm spreading relatively evenly over the year.

*EXPERIMENT DESIGN AND FIELD DATA*

The experiment field is the central experimental site for spring/summer barley of the CROP.SENSE.net interdisciplinary research network. Scientists working on the study site non-destructively and quantitatively analyse and screen plant phenotypes throughout their life cycle. The experiment consists of 54 plots that are 3 x 7 m in size (**Figure 5-1**). Two replications of 18 spring/summer barley cultivars, 10 current and eight old cultivars, are planted in randomized blocks. One replication is fertilized with 40 kg N/ha and the other one with 80 kg N/ha. The sowing density is 300 seeds per m² with a 0,104 m row spacing. Each plot consists of a 3 x 5 m measuring area and a 3 x 2 m sampling area. Destructive biomass samples are taken in 36 plots throughout the growing season (see **chapter 5.2.1**). Non-destructive plant height (PH$_{ref}$) samples are taken in

each plot to be compared with CSM-derived PH for reference. Hyperspectral reflectance measurements are taken throughout the growing period. RGB images are acquired in seven UAV flights between 30 April and 23 July 2013.
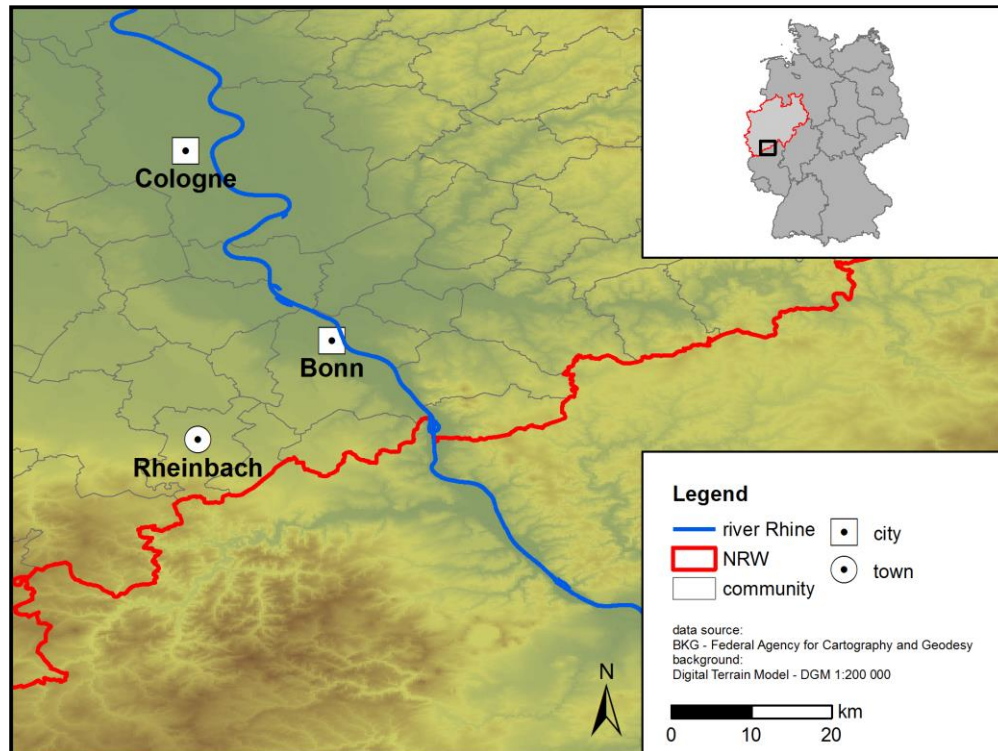


*Figure 2-5: Location of barley study sites in Bonn and Rheinbach, North Rhine-Westphalia (NRW), Germany.*

### 2.6.3 Rice – Jiansanjiang, China (2012)

*LOCATION*

The rice study site in Jiansanjiang is located at the Keyansuo experimental station of the China Agricultural University (CAU) of Beijing at 47° 15' 21" N, 132° 37' 43" E, 59 m above sea level. Jiansanjiang is located in the Heilongjiang Province in the Northeast China plain (**Figure 2-6**). The name Jiansanjiang, indicates the location as situated in an alluvial floodplain between three rivers (three=san, rivers=jiang) (**ZHOU AND LIU**, **2005**). The Sanjiang Plain is one of the largest wetland distributions in China with typical marsh soils, meadow soils and peat soils (**CHINGKWEI AND OU**, **1999**). Continuous land use changes within wetland development transformed the former forested area into an intensely used agricultural area (**WANG AND YANG**, **2001**). Winters are cold and dry while summers are warm and temperate, and characterized by high precipitation during the East Asian Monsoon season (Dwb after Köppen-Geiger climate classification). The average annual

temperature is 3.6°C, rising to average 22°C in July and dropping to average -18°C in January (**GNYP**, **2014**). The average annual rainfall is 400-600 mm, which peaks in July and August.
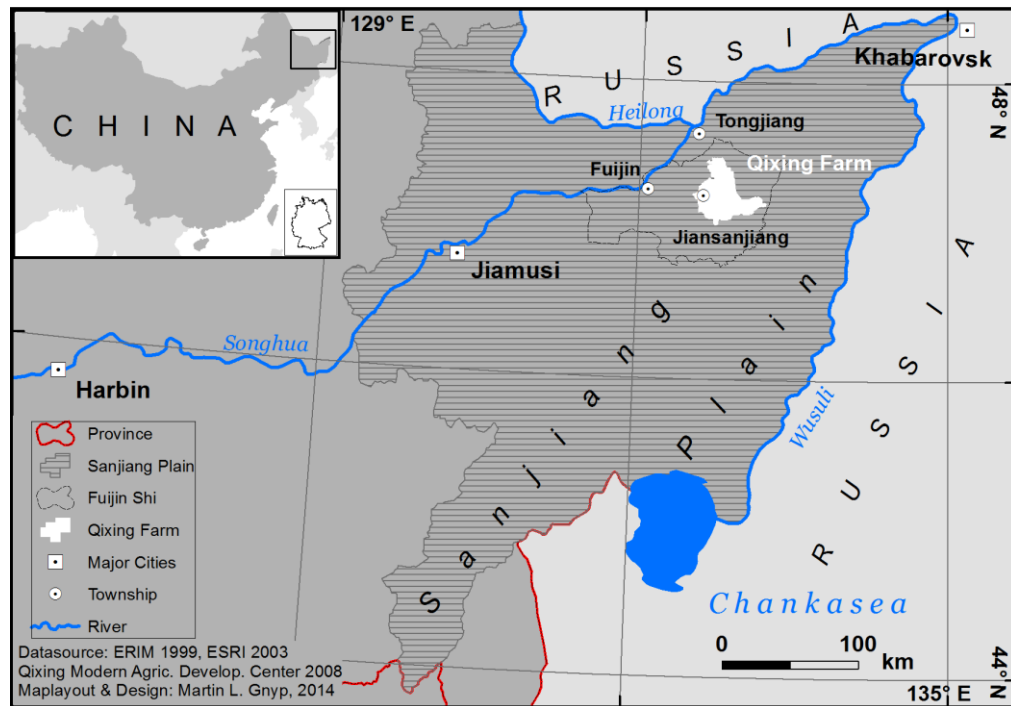


*Figure 2-6: Location of Sanjiang Plain and Jiansanjiang study site (GNYP, 2014).*

*EXPERIMENT DESIGN AND FIELD DATA*

The experiment focuses on monitoring rice plant development in response to N fertilizer treatments. Half of the 54 plots (7 x 8 m) were planted with rice seedlings of cultivar Kongyu131 and the other half with cultivar Longjing21 in May 2012 (see **chapter 3.2.1**). Plots are arranged into three randomized replications of five N fertilizer levels (0-160 kg N/ha) and four N treatments based on sensor measurements (Greenseeker™, CropCircle™) (**CAO ET AL.**, **2013**). The latter are not used in this study. Constant ground water irrigation is carried out during the growing period. Destructive biomass sampling and non-destructive hyperspectral reflectance measurements are taken throughout the growing season. RGB images are acquired in three UAV flights on 04, 07 and 17 July 2012. Additionally, three PH reference measurements are taken in each plot with a ruler and the field was scanned with a terrestrial laser scanner (**TILLY ET AL.**, **2014**).

# 3  Hoch auflösende crop surface models (CSMs) auf der Basis von Stereobildern aus UAV-Befliegungen zur Überwachung von Reiswachstum in Nordostchina

Juliane Bendig [1,*], Maximilian Willkomm [1], Nora Tilly [1], Martin Leon Gnyp [1], Simon Bennertz [1], Victoria I.S. Lenz-Wiedemann [1,2], Georg Bareth [1,2]

Original manuscript is embedded in dissertation format.

1   Institute of Geography, GIS & RS Group, University of Cologne, Albertus-Magnus-Platz, 50923 Cologne

2   ICASD-International Center for Agro-Informatics and Sustainable Development, www.icasd.org

*   Corresponding author, Tel.: +49-221-470-6551; Fax: +49-221-470-4917

E-Mail: juliane.bendig@uni-koeln.de

**Zusammenfassung:** Unmanned Aerial Vehicles ( UAVs ) wurden in den letzten Jahren zu beliebten Plattformen für die Sammlung von mit Fernerkundungsmethoden erhobenen Geodaten (**Hardin and Jensen, 2011b**). Verschiedene Anwendungen in vielen Forschungsbereichen wie Archäologie (**Hendrickx et al., 2011**), Forstwirtschaft oder Geomorphologie (**Martinsanz, 2012**) entwickelten sich. Dieser Beitrag befasst sich mit der Erzeugung von multitemporalen crop surface models (CSMs) mit sehr hoher Auflösung zur Überwachung von Reiswachstum mit günstiger Ausrüstung. Das Konzept der Generierung von multitemporalen CSM mittels Terrestrischem Laserscanning (TLS) wurde bereits von **Hoffmeister et al.**(**2010**) eingeführt. Für diese Studie wurde die Datenerfassung mit einem günstigen und leichten Mini-UAV (< 5kg) durchgeführt. UAVs allgemein und vor allem kleinere, wie das hier vorgestellte System, schließen eine Lücke in der Fernerkundung im Nahbereich (**Berni et al., 2009a**; **Watts et al., 2012**). Im Präzisionsackerbau liefern häufige Erhebungen von Fernerkundungsdaten im Nahbereich, während der Vegetationsperiode, wichtige räumliche Informationen über den Pflanzenzustand. Variabilität im Pflanzenwachstum kann durch Vergleich der CSM in verschiedenen phänologischen Stadien erkannt werden. In diesem Beitrag wird das Verfahren, welches bereits für Gerste genutzt wurde (**Bendig et al., 2013**), auf eine andere Feldfrucht in einer anderen Umgebung angewendet. Das Untersuchungsgebiet ist ein Versuchsfeld für Reis in Nordost-China (Sanjiangebene). Zwei Reissorten wurden dort gepflanzt und

mit unterschiedlichen Mengen Stickstoffdünger behandelt. Im Juli 2012 wurden drei UAV-Kampagnen durchgeführt. Zusätzlich erfolgte die Erhebung weiterer destruktiver und nicht destruktiver Felddaten. Das UAV-System ist ein MK-Okto von Hisystems (www.mikrokopter.de), ausgestattet mit einer hochauflösenden optischen Digitalkamera. Das selbstgebaute und -gewartete System hat eine Nutzlast von bis zu 1 kg, 15 Minuten durchschnittliche Flugdauer und kann bis zu einer Windgeschwindigkeit von unter 19 km/h betrieben werden. Die Erfassung der Stereobilder erfolgte bei einer Flughöhe von 50 m und einer 44% Seit- und 90% Vorwärtsüberlappung. Die Bilder werden in CSM mittels der Structure from Motion (SFM)-basierten Software Agisoft Photo-Scan 0.9.0 prozessiert. Die resultierenden Modelle verfügen über eine Auflösung von 0,02 m. Weitere Datenverarbeitung in Esri ArcGIS® ermöglicht quantitative Vergleiche der Pflanzenhöhen. Die multi-temporalen Datensätze werden auf Basis sogenannter „Versuchsplots" analysiert. Die Ergebnisse können mit den zusätzlichen Felddaten verglichen und kombiniert werden. Die Erfassung von Wuchshöhe mit nicht-invasiven Messverfahren ermöglicht die Analyse der Korrelation zu Biomasse und anderen Pflanzenparametern, die im Feld gemessen werden (**HANSEN AND SCHJOER-RING**, **2003**; **THENKABAIL ET AL.**, **2000**). Die hier vorgestellte Methode kann somit eine wertvolle Ergänzung für die Erkennung solcher Korrelationen liefern.

**Schlüsselwörter:** Landwirtschaft, Biomasse, DGM, multi-temporale Daten, Pflanzenhöhe, Reis, UAV

## Very High Resolution Crop Surface Models (CSMs) from UAV-based Stereo Images for Rice Growth Monitoring In Northeast China

**Abstract:** Unmanned aerial vehicles (UAVs) became popular platforms for the collection of remotely sensed geodata in the last years (**HARDIN AND JENSEN**, **2011b**). Various applications in numerous fields of research like archaeology (**HENDRICKX ET AL.**, **2011**), forestry or geomorphology evolved (**MARTINSANZ**, **2012**). This contribution deals with the generation of very high resolution multi-temporal crop surface models (CSMs) for rice growth monitoring by means of low-cost equipment. The concept of the generation of multi-temporal CSMs using Terrestrial Laserscanning (TLS) has already been introduced by **HOFFMEISTER ET AL.**(**2010**). For this study, data acquisition was performed with a low-cost and low-weight Mini-UAV (< 5kg). UAVs in general and especially smaller ones, like the system presented here, close a gap in small-scale remote sensing (**BERNI ET AL.**, **2009a**; **WATTS ET AL.**, **2012**). In precision agriculture frequent remote sensing on such scales during the vegetation period provides important spatial information on the crop status. Crop growth variability can be detected by comparison of the CSMs in different phenological stages. In

this contribution, the method, that has already been used for barley (**Bendig et al.**, **2013**), is applied to a different crop in a different environment. The study area is an experiment field for rice in Northeast China (Sanjiang Plain). Two rice cultivars were planted and treated with different amounts of N-fertilizer. In July 2012 three UAV-campaigns were carried out. Additionally, further destructive and non-destructive field data were collected. The UAV-system is an MK-Okto by Hisystems (www.mikrokopter.de) equipped with a high resolution optical consumer camera. The self-built and self-maintained system has a payload of up to 1 kg and 15 minutes mean endurance and can be operated up to a wind speed of less than 19 km/h. Stereo images were captured at a flying height of 50 m and a 44% side and 90% forward overlap. The images are processed into CSMs under the use of the Structure from Motion (SfM)-based software Agisoft PhotoScan 0.9.0. The resulting models have a resolution of 0.02 m. Further data processing in Esri ArcGIS® allows for quantitative comparison of the plant heights. The multi-temporal datasets are analysed on a plot size basis. The results can be compared to and combined with the additional field data. Detecting plant height with non-invasive measurement techniques enables analysis of its correlation to biomass and other crop parameters (**Hansen and Schjoerring**, **2003**; **Thenkabail et al.**, **2000**) measured in the field. The method presented here can therefore be a valuable addition for the recognition of such correlations.

**Keywords:** Agriculture, Biomass, DEM, Multi-temporal data, Plant height, Rice, UAV

## 3.1    Introduction

Surveying crop growth during phenological stages is an important component of precision agriculture (**Hansen and Schjoerring**, **2003**; **Thenkabail et al.**, **2000**). Remote sensing has great potential of contributing data for such kind of investigations in the field of precision agriculture (**Mulla**, **2013**). In Northeast China, rice production is an important economic factor and contributes to ensuring the food supply for the local population (**Miao et al.**, **2010**; **Peng et al.**, **2006**). The use of precision agriculture to optimise rice cultivation in this region has high potential. The control of plant growth can help to improve management of the fields. In experiment fields, such as the one in this contribution, the relationship between application of different amounts of N-fertilizer and plant parameters is investigated. These plant parameters can be put in relation to the size of the plant, which is related to the yield. A way to monitor plant growth is the idea of generating multi-temporal crop surface models (CSMs) to allow for comparison of different phenological stages (**Bendig et al.**, **2013**; **Hoffmeister et al.**, **2013**). For each date of data acquisition a model of the

crop surface is generated from highly dense point clouds. The plant growth is obtained by comparison of the surface models for each date. Data collection using a mobile, low-cost and self-maintainable device like a small UAV offers big advantages in this remote region of the world. In addition, the well-managed, small-sized experiment field provides an ideal opportunity to validate the method of CSM generation by a UAV under different conditions than in Germany. The aim of this study is to monitor plant growth using point clouds generated from very high resolution stereo images captured by a UAV-system.

## 3.2 Data Aquisition

### 3.2.1 Study Area and Dataset

The study area is Keyansuo experiment field in China's Sanjiang Plain the northernmost rice growing region in China (**Figure 3-1**). Two cultivars of rice seedlings were transplanted in May of 2012. Ground water was used for constant irrigation during the growing season. Harvest of the crops took place at the end of September. The experiment consisted of 54 small plots with a size of 7 x 8 m, in which three replications of the rice varieties Kongyu131 and Longjing21 were planted in randomized order. Different amounts of N-fertilizer (0-160 kg ha$^{-1}$) were applied (**Figure 3-2**). The total size of the field is 0.39 ha.
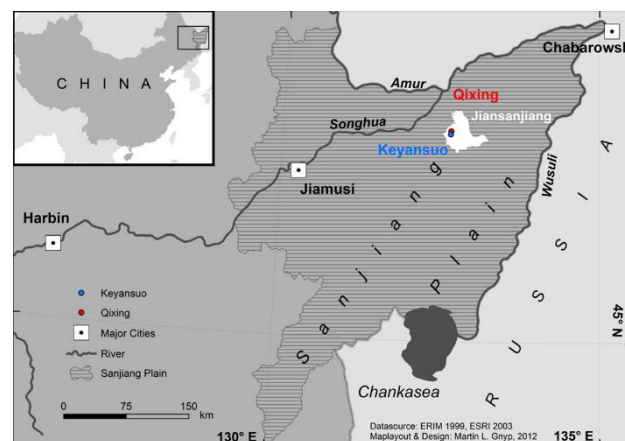


*Figure 3-1: Location of the experiment fields Qixing and Keyansuo, Jiansanjiang Branch Bureau, Heilongjiang Bureau of Agricultural Reclamation, Heilongjiang province, China. (Yu et al., 2013).*
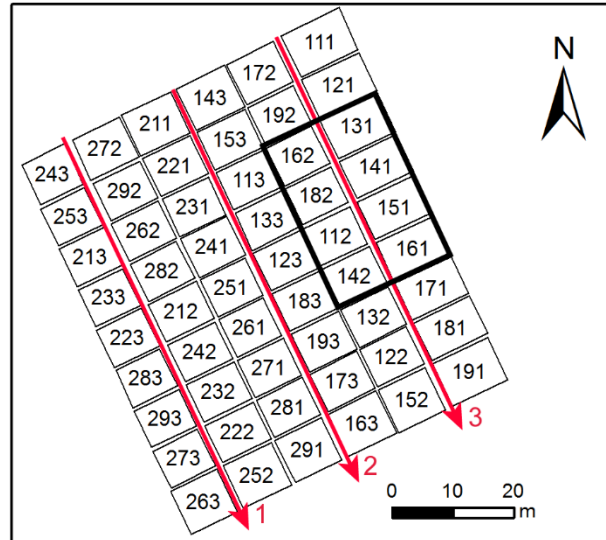
*Figure 3-2: Experiment field in Keyansuo, plot numbering: 1st no.: cultivar (1=Kongyu131, 2=Longjing21), 2nd no.: treatment (1=0, 2=70, 3=100, 4=130, 5=160 kg ha-1, 6-9=other), 3rd no.: replication, red arrows: flight strips 1-3, black rectangle: dataset selection b.*

In July 2012 three UAV-campaigns (04,09,17 July 2012) were carried out. 30 ground control points (GCPs) were distributed evenly across the field to facilitate ground truth. Additional destructive sampling of biomass and non-destructive measurements of plant height, hyperspectral point data using an ASD FieldSpec and 3D point clouds using a terrestrial laser scanner were carried out.

### 3.2.2    Platform

The sensor platform is the MK-Okto by Hisystems (**HISYSTEMS GMBH**, **2013**). The UAV-system was self-built at the study site in 2011. Thus on-site maintenance was possible, which is important in remote areas where spare parts and manufacturer's support might not be available. The frame consists of aluminium and fiberglass reinforced plastics (**Figure 3-3**). The eight brushless outrunner high torque engines are equipped with high performance propellers. The electronics consist of an ARM-processor equipped mainboard and a navigation mainboard with gyroscopes, a pressure sensor and a compass module (**BENDIG ET AL.**, **2012**). Lithium polymer batteries (up to 5000 mAh capacity) are used for the power supply. A 2.4 GHz transmitter remote control (RC) is used for stirring and camera triggering. The maximum payload is 1 kg. The average endurance is 15 minutes (about 0.5 kg payload). The price of the system including spare batteries and RC is approximately 3000 €. The operation is possible up to a wind speed of 19 km h-1 (Beaufort scale number 3 for wind speed).

*Figure 3-3: MK-Okto by Hisystems GmbH mounted with Lumix DMC GF3 optical camera (BENDIG ET AL., 2013).*

### 3.2.3   Sensor

The RGB sensor used in this study is the Panasonic Lumix DMC GF3 in combination with a Lumix G 20 mm (F1.7 ASPH) fixed lens. The weight is 400 g, the sensor resolution is 4016 x 3016 (12 million) pixel (**PANASONIC**, **2013**). Thus capturing very high resolution images of *e.g.* 0.01 m at a 50 m object distance is feasible. The Field of View (FOV) has an extend of 48.5° horizontal and 33.4° vertical, resulting in an image size of 45 x 30 m at a 50 m object distance.

Prior to each flight aperture and exposure time are adjusted and fixed manually according to the current light conditions. The camera gimbal is custom-built and features a mechanical trigger driven by a servomotor. The image acquisition is controlled by the remote control of the UAV-system.

### 3.2.4   Measurement

A number of 30 GCPs were installed on the experiment in a uniform distribution. In order to be able to use the same GCPs during the whole campaign, wooden poles were installed on the dikes. 0.3 x 0.3 m highly visible targets were attached to the poles and served as the GCPs. The GCP positions were measured with a TrimbleProXT GPS with a 1 m accuracy in x-y-z-direction. For technical reasons, no more accurate device was available.

The flights were carried out at a height of 50 m, resulting in three flight strips with a 44% side and 90% forward overlap in order to cover the whole experiment field (**Figure 3-2**). Each flight strip was captured in a separate flight due to the endurance of the UAV-system limited by the battery capacity. The RGB sensor was mounted in a fixed nadir position and orientation.

The flights were carried out in mostly clear sky conditions (0-2 okta) at low wind speed (up to 3.4 m/s) in the early morning between 05:30 and 07:00 am. Due to the uniform time zone in China, the sun rises at about 03:00 am in Jiansanjiang, resulting in high air temperatures in the summer between 25 and 35 °C in the early morning.

### 3.2.5 Data Processing

The data processing workflow is divided into CSM generation using Agisoft PhotoScan 0.9.0 and post processing and analysis in ArcGIS® 10.1. The workflow is presented in **Figure 3-4**. The individual steps of the data analysis are described below.
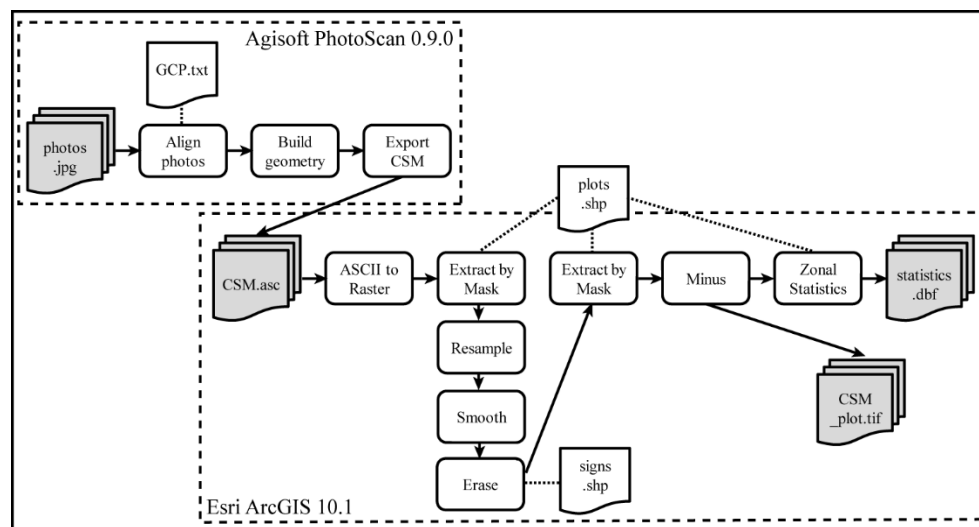


*Figure 3-4: Data Processing workflow for generation of CSM (CSM.asc) from RGB images captured by UAV-system (photos.jpg) in Agisoft PhotoScan 0.9.0 and further processing for analysis in Esri ArcGIS® 10.1.*

### 3.2.5.1 Agisoft PhotoScan

The images captured during the flight campaigns were processed into CSMs using the multi-view 3D reconstruction software Agisoft PhotoScan 0.9.0 (latest version 0.9.1, (**AGISOFT LLC, 2014**). The software utilizes a structure from motion (SfM) algorithm (**VERHOEVEN ET AL., 2012**). This approach allows for computation of the relative projection geometry and 3D points by using only corresponding image features occurring in a series of overlapping images of the area of interest (**SZELISKI, 2010**). The surface geometry is reconstructed by using multi-view stereo (MVS) algorithms (**SCHARSTEIN AND SZELISKI, 2002**; **SEITZ ET AL., 2006**). The software computes a depth estimate, in this case the distance from the camera to the object surface, for nearly every pixel of each view. One view equals one image. The resulting independent depth maps are combined and approximated by a triangular mesh, resulting in a DSM (**VERHOEVEN ET AL., 2012**). The transformation from

local to an absolute UTM coordinates was carried out by assigning the coordinates of the GCPs to the corresponding images. Computation of the CSMs was carried out using the highest possible accuracy resulting in computation times of up to two hours on an 8 GB RAM 64-bit operating system. The dataset for every date was divided into three tiles according to the three flight strips. This allowed for manageable size of datasets. The CSMs with a 0.01 m resolution have 700 points per m² on average. Agisoft offers various ways of exporting the generated CSMs. In this case an ASCII-file was chosen which enabled further processing in ArcGIS®.

### 3.2.5.2 ArcGIS®

Esri's ModelBuilder was used for data processing in ArcGIS® 10.1. The processing steps were split up into three models due to identification signs that had been placed in the plots. Those had to be removed in each dataset by applying a mask.

Model 1 comprises data conversion, masking and resampling (**Figure 3-5**). The *file iterator* was used to process all files (three files for each of the three dates) automatically. The *ASCII to raster* tool was used for data conversion to a floating-point raster for enhanced performance in ArcGIS®. Based on the plot boundaries visible in the CSMs, a shapefile of the *area of interest* (AOI) was constructed. Plant growth at the margins of a field differs from plant growth in the middle of the field due to different environmental conditions such as availability of light. Thus a negative buffer of 0.6 m was applied to the plot boundary shapefile in order to exclude those plants from the analysis. The resulting mask was used as an input for the *Extract by Mask* tool. Results of this step were marked with a "_1" in the filename (**Figure 3-5**). In a next step the *Resample* function with a nearest neighbour interpolation was applied reduce to the cell size of the CSMs to 0.1 m as it is suitable for analysis on a plant level. Outliers in the data were removed by applying the *Focal Statistics* tool with a focal mean of 3 x 3 pixel rectangles. Finally the AOI mask needed to be applied again, as the interpolation and smoothing added some pixel at the boundaries of the dataset.
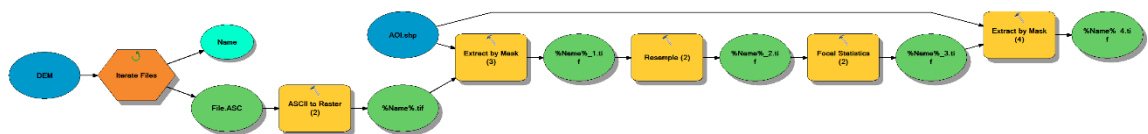


*Figure 3-5: Model 1 in Esri ArcGIS® 10.1 processing workflow – data conversion, masking and resampling.*

In order to remove the identification signs in the field individual shapefiles containing the outlines of the signs were produced for every CSM (see *e.g.* s120717_2 in **Figure 3-6**). The shape of the files varied in every flight strip, due to the different viewing angles. Using the *Erase* tool the AOI mask could be modified for every single CSM (*e.g.* s120717_2e in **Figure 3-6**). In a next step the *Extract by Mask* tool was applied and datasets of the different dates could be subtracted from each other using the *Minus* tool. As a result the relative plant growth in meters between the 09th and 04 July and the 17 and 09 July can be obtained. The concept of CSMs includes generation of absolute plant heights as well as growth monitoring. Due to frequently varying water levels in each of the 54 plots, no ground plane could be generated. In a barley field for example this ground plane can used as a basis for calculation of absolute heights (**BENDIG ET AL.**, **2013**).
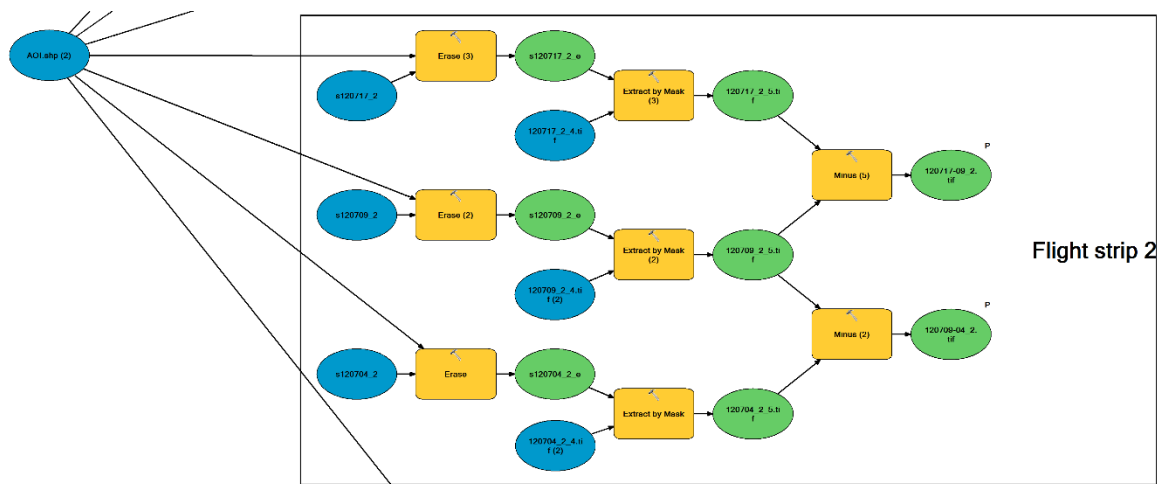


*Figure 3-6: Model 2 in Esri ArcGIS® 10.1 processing workflow – AOI refinement by applying individual masks and dataset subtraction.*
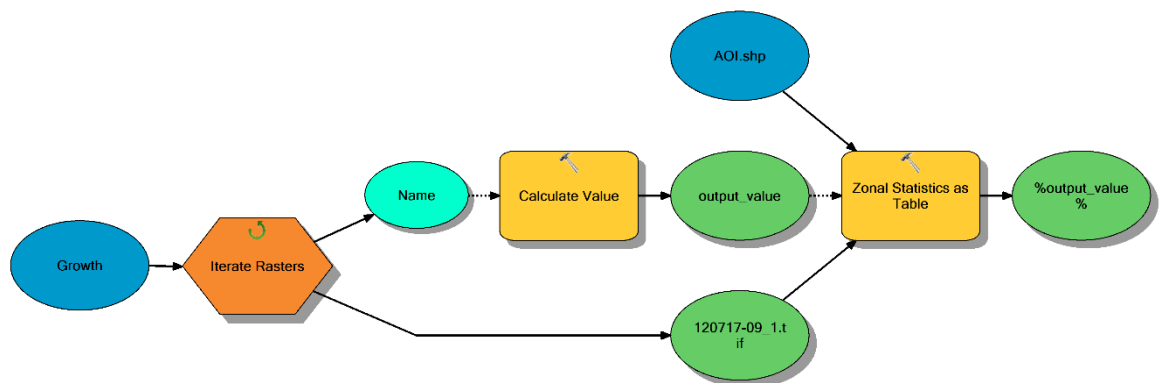


*Figure 3-7: Model 2 in Esri ArcGIS® 10.1 processing workflow – calculation of plant growth on a plot sized basis.*

In a last step, plant growth on a plot sized basis was calculated using the *Zonal Statistics as Table* tool (**Figure 3-7**). The *raster iterator* helped to automate the process. As a result, a *.dbf-table for each dataset containing range of values, minimum, maximum, mean value and standard deviation was generated. The tables were named according to the corresponding raster file using the *Calculate Value* function. Further analysis of the tables was carried out in Microsoft® Excel®.

## 3.3 Results

The results of the CSM generation and the analysis of the plant growth are presented below. Analysis was carried out for three dataset selections (*all values*, *selection a* and *selection b* in **Table 3-1** and **Table 3-2**) and two growth periods (GP1 = 04.-09.07.; GP2 = 09.-17.07.). A visible inspection of the CSMs showed that unrealistic height values existed in parts of single CSMs (GP1: flight strip 1; GP2. flight strip 2) due to the quality of the georeference. The values of the affected plots were removed from the analysis resulting in dataset *selection a* (**Table 3-1**, **Table 3-2**). Furthermore, data at the beginning and the End of the flight strips were removed with only the core part of the field remaining. This resulted in *selection b* (see **Figure 3-2**) containing only the values where the CSMs for GP1 and GP2 showed the most reliable results and were less prone to boundary effects (**Figure 3-10**).

### *3.3.1 Statistics*

The range of overall plant growth (**Table 3-1**) obtained from the CSMs is 1.3 m for the dataset containing *all values* showing negative values of up to -0.5 m. For the *selections a* and *b* show lower values of 0.7 m and 0.5 m apply. Negative values also occur (a: -0.322, b: -0.019). Regarding the mean plant growth, the datasets show differing tendencies. In the dataset with *all values*, the mean plant growth declines between GP1 and GP2 from 0.144 to 0.069 m, while for *selections a* and *b* the growth increases slightly (a: 0.13 to 0.143 m, b: 0.206 to 0.255 m). The standard deviation varies between 0.02 and 0.05 m with a mean of 0.04 m.

**Table 3-2** shows the mean plant growth differentiated by the two cultivars of the experiment field; Kongyu131 and Longying21. In the dataset containing *all values* the growth of Longjing21 (0.157 and 0.121 m) is 31% higher than for Kongyu131 (0.129 and 0.083 m) for both GPs. In dataset *selection a*, growth only differs by less than a centimetre for GP1 but is 0.014 m higher for Kongyu131 in GP2. *Selection b* only contains data for Kongyu131 but has a 78% higher growth of 0.2 m and higher compared to the rest of the values.

*Table 3-1: Descriptive statistics of plant growth [m] derived from CSMs for all data and selected datasets a and b for two growth periods in July 2012.*

| dataset | all values | | selection a | | selection b | |
|---|---|---|---|---|---|---|
| growth | **GP1** | GP2 | GP1 | GP2 | GP1 | GP2 |
| min | -0.433 | -0.514 | -0.322 | -0.284 | -0.019 | 0.078 |
| max | 0.508 | 0.786 | 0.408 | 0.474 | 0.324 | 0.474 |
| range | 0.941 | 1.300 | 0.730 | 0.758 | 0.343 | 0.396 |
| mean | 0.144 | 0.069 | 0.130 | 0.143 | 0.206 | 0.255 |
| std. | 0.040 | 0.051 | 0.037 | 0.040 | 0.026 | 0.036 |

*Table 3-2: Mean plant growth [m] of rice cultivars Kongy131 and Longjing 21 derived from CSMs for all data and selected datasets a and b for two growth periods in July 2012.*

| cultivar | | Kongyu 131 | Longjing 21 | Kongyu 131 | Longjing 21 |
|---|---|---|---|---|---|
| growth | | GP1 | | GP2 | |
| Dataset | *all values* | 0.129 | 0.157 | 0.083 | 0.121 |
| | *selection a* | 0.129 | 0.131 | 0.155 | 0.129 |
| | *selection b* | 0.206 | *no data* | 0.255 | *no data* |

## 3.3.2   Crop Surface Models

The CSM of flight strip to of the 09th of July with a 0.01 m resolution is shown in **Figure 3-8**. 27 of the 54 experiment plots are completely covered in the model. Orange areas indicate high and green areas indicate low heights. The highest areas are located in the centre of the field, while heights decrease towards the north, south and to the west. The pointy objects in red show the positions of the identification signs that had been placed in the field. The water channels used for irrigation at the northern and southern ends of the field are clearly marked by the dark green colour indicating the lowest parts of the CSM.
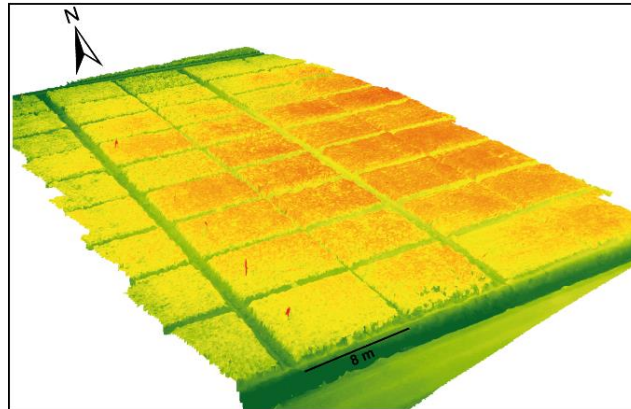
*Figure 3-8: CSM of flight strip 2 of 09 July 2012 – orange areas indicate high and green areas indicate low heights*
*(Esri ArcScene, height 2 times exaggerated).*

### 3.3.3   Crop Growth

A map of the plant growth of GP1 for flight strip 2 is presented in **Figure 3-9**. Values under -0.08 m
are coloured in grey indicating a "negative growth" (see **chapter 3.4** for discussion). Positive values
change from yellow to red, with red indicating the highest growth. Areas with the highest growth
between 0.2 and 0.4 m are located in the centre. Growth is decreasing towards north and south
where the grey areas are located. The trend is similar to the one in **Figure 3-8**.
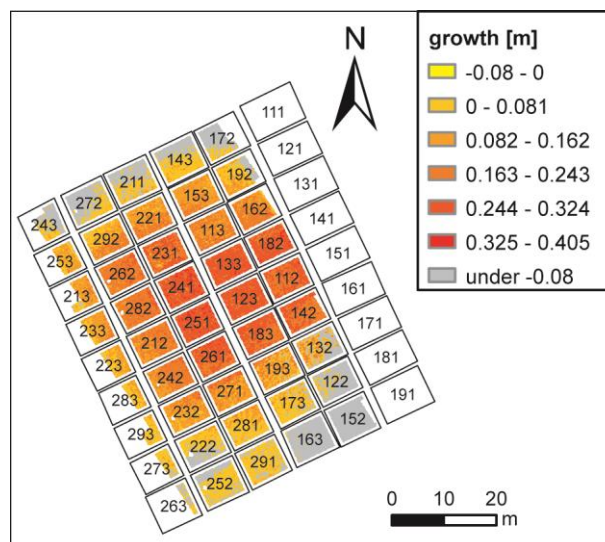


*Figure 3-9: Plant growth in flight strip 2 between 04 and 09 July 2012 (GP1) (Esri ArcMap).*

An example of a detailed plot analysis of dataset *selection b* is given in **Figure 3-10** showing the
plots in centre of flight strip 3. The plant growth for GP1 is shown on the left and for GP2 on the
right. In general, growth for GP1 is lower than for GP2 (compare **Table 3-2**). For GP1 plots 182,
141 and 142 have the highest growth, while plot 171 has the lowest values. GP2 gives a different

impression with plots 131, 182, 141 and 151 showing the highest values and 161 having lowest values. Growth variability in the plots for both GPs can be detected; for example the north western corners of plots 141 and 171 growing stronger than the south eastern corners.
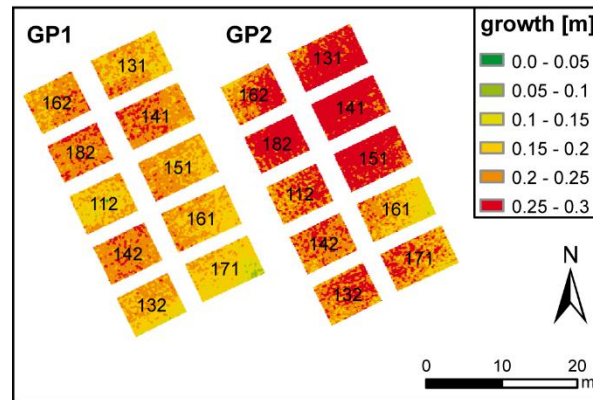


*Figure 3-10: Plant growth of dataset selection b between 04 and 09 July (GP1) and 09 and 17 of July (GP2) 2012 (Esri ArcMap).*

## 3.4 Discussion

The GCPs used during the data acquisition helped during data processing with sufficient visibility and distribution across the experiment field. A strong disadvantage was that for measurement of the GCP positions, only a GPS with a low accuracy of 1 m on all three axes was available. This can be regarded as the main source of error during the process of CSM generation and the results of the whole data analysis.

The flight plan with 44% side and 90% forward overlap and 50 m flying height produced images at very high resolution with sufficient overlap for CSM generation. Comparable studies use similar flight plans with overlaps of 70 to 95% (**Haala and Rothermel, 2012**; **Hartmann et al., 2012**). The area of image acquisition should be extended further across the borders of the field to account for errors at the CSM edges.

Model generation using Agisoft PhotoScan was comfortable and well suited for the task of handling unregistered aerial images. Comparisons by **Neitzel and Klonowski** (**2011**) or **Gini et al.**(**2013**) of similar software using SfM and MVS techniques like Bundler, Patch-based Multi-view Stereo Software Version 2 (PMVS2) and the photogrammetry software Leica Photogrammetry Suite (LPS) stated the good performance of Agisoft PhotoScan.

The further processing in ArcGIS® with ModelBuilder offers the advantage of an adaptable and automated processing chain. The models are clearly structured which make the process easy to

understand for people unfamiliar with the workflow. The fact that only one iterator can be used in the model limits the flexibility to a certain extend. Putting the whole process into a Phyton script would have been an alternative but would not offer such a good overview of the process. A solution could be building a custom made ArcGIS® tool for the whole process. But more experience on processing chains for different datasets is needed first before automating processing to such an extent.

Results of the plant growth analysis show that there is a big range of values of up to one meter (see **Table 3-1**) in the dataset, which is linked to the quality of the resulting CSMs; since range of values in datasets of *selection a* and *b* are considerably lower (**Table 3-1**). The fact that negative values of up to -0.5 m occur in the data evinces the limited quality of the CSMs. Again, the occurrence of such values is directly linked to the low accuracy of the GCP measurement.

Values obtained for the mean plant growth still have a realistic magnitude between 0.06 and 0.26 m (**Table 3-1**) for the regarded phenological stage. This can be stated due to frequent observation of rice fields in this region since 2007 (**YU ET AL., 2013**).

When comparing the two rice cultivars Kongyu131 and Longjing21, no significant differentiation in growth can be observed (**Table 3-2**). Differences are in the magnitude of a few centimetres (*e.g.* 0.129 m compared to 0.157 m). The dataset where *all values* had been used suggests a higher growth for Longjing21, while in *selection a* the growth is higher for Kongyu131 in GP2. In-field measurements showed that Kongyu131 tends to grow slower than Longjing21. This could not be proved from the data in this paper. Either no actual difference in the growth of the two cultivars existed for the regarded GPs (about 1 month) or the quality of the CSMs was not sufficient to show such differences.

When analysing the spatial distribution of growth (**Figure 3-8**, **Figure 3-9**) it can be clearly seen that plant heights are decreasing towards the northern and southern ends of the fields. This could be due to inhomogeneity in the field *i.e.* soil quality or other factors influencing plant growth. Since **Figure 3-9** gives the impression of a radial decrease of growth towards the edges, another reason is more likely: It could be a barrel effect in the CSMs which is resulting in lower heights at the edges of the CSM. This problem can be addressed by extending the area of interest during the flights and by solving the problem of inaccurate registration of the GCPs.

In the centre of the field where this effect is less masking the true infield variability, the variability of growth in the plots can be shown with very high detail (**Figure 3-10**). This proves that the

method is suitable for detection of small-scale variability (here: 0.1 m raster resolution) in plant growth.

## 3.5 Conclusion

Choosing a UAV for monitoring a remote small sized study area like the one presented here, enables multi-temporal data acquisition at very low cost and with high flexibility. This flexibility is especially important for areas which are difficult to access such as irrigated rice fields.

Due to the strong barrel effect influencing the models, no analysis of the different treatments of N-fertilizer (**Figure 3-2**) was performed. This step can be added to the analysis as well as comparison of the derived CSMs with the additional data available such as CSMs from terrestrial laser scanning, hyperspectral reflection data and agronomical data collected for the same time span.

In summary it can be stated that the method of multi-temporal CSM generation from UAV-based data, is applicable to rice. For the reliable modelling of plant growth and a differentiation of cultivars and treatment the model quality needs to be improved, which is possible through improved post processing.

## 3.6 Outlook

Although the platform is performing well, some improvements are possible. A gimbal enabling pitch and roll compensation during the flight was mounted. A camera with a higher image resolution (Panasonic Lumix DMC GX1, 16 M pixel) is used. It is triggered electrically, which has the advantage of a more reliable image acquisition. Another advantage is continuous image acquisition which guarantees an over 95% forward overlap.

The availability of point clouds generated from terrestrial laser scanning offers the chance of using the highly precise local coordinate system for georeferencing of the CSMs resulting in models of significantly higher accuracy. This will greatly improve the usability of the resulting CSMs and offer wider possibilities of data analysis.

## Acknowledgements

# References

AGISOFT LLC, **2014**. Agisoft PhotoScan [WWW Document]. Agisoft PhotoScan. URL http://www.agisoft.com (accessed 10.9.14).

BENDIG, J., BOLTEN, A., BARETH, G., **2012**. Introducing a low-cost mini-UAV for thermal-and multi-spectral-imaging. International Archives of the Photogrammetry, Remote Sensing and Spatial Information Sciences 39, 345–349.

BENDIG, J., BOLTEN, A., BARETH, G., **2013**. UAV-based Imaging for Multi-Temporal, very high Resolution Crop Surface Models to monitor Crop Growth Variability. Photogrammetrie - Fernerkundung - Geoinformation 6, 551–562. doi:10.1127/1432-8364/2013/0200

BERNI, J.A.J., ZARCO-TEJADA, P.J., SUAREZ, L., FERERES, E., **2009a**. Thermal and Narrowband Multispectral Remote Sensing for Vegetation Monitoring From an Unmanned Aerial Vehicle. IEEE Transactions on Geoscience and Remote Sensing 47, 722–738. doi:10.1109/TGRS.2008.2010457

GINI, R., PAGLIARI, D., PASSONI, D., PINTO, L., SONA, G., DOSSO, P., GRENZDÖRFFER, G., BILL, R., **2013**. UAV Photogrammetry: Block triangulation comparisons. International Archives of the Photogrammetry, Remote Sensing and Spatial Information Sciences XL-1/W2, 157–162.

HAALA, N., ROTHERMEL, M., **2012**. Dense Multi-Stereo Matching for High Quality Digital Elevation Models. Photogrammetrie - Fernerkundung - Geoinformation 4, 331–343. doi:10.1127/1432-8364/2012/0121

HANSEN, P.M., SCHJOERRING, J.K., **2003**. Reflectance measurement of canopy biomass and nitrogen status in wheat crops using normalized difference vegetation indices and partial least squares regression. Remote Sensing of Environment 86, 542–553. doi:10.1016/S0034-4257(03)00131-7

HARDIN, P., JENSEN, R., **2011b**. Introduction—Small-Scale Unmanned Aerial Systems for Environmental Remote Sensing. GIScience & Remote Sensing 48, 1–3. doi:10.2747/1548-1603.48.1.1

HARTMANN, W., TILCH, S., EISENBEISS, H., SCHINDLER, K., **2012**. Determination of the UAV position by automatic processing of thermal images. International Archives of the Photogrammetry, Remote Sensing and Spatial Information Sciences XXXIX-B6, 111–116.

HENDRICKX, M., GHEYLE, W., BONNE, J., BOURGEOIS, J., DE WULF, A., GOOSSENS, R., **2011**. The use of stereoscopic images taken from a microdrone for the documentation of heritage – An example from the Tuekta burial mounds in the Russian Altay. Journal of Archaeological Science 38, 2968–2978. doi:10.1016/j.jas.2011.06.013

HISYSTEMS GMBH, **2013**. HiSystems [WWW Document]. URL http://www.hisystems.de (accessed 1.8.13).

HOFFMEISTER, D., BOLTEN, A., CURDT, C., WALDHOFF, G., BARETH, G., **2010**. High-resolution Crop Surface Models (CSM) and Crop Volume Models (CVM) on field level by terrestrial laser scanning, in: Guo, H., Wang, C. (Eds.), SPIE Proceedings of the Sixth International Symposium on Digital Earth: Models, Algorithms, and Virtual Reality. Presented at the Sixth International Symposium on Digital Earth: Models, Algorithms, and Virtual Reality, Beijing, China, p. 78400E–78400E–6. doi:10.1117/12.872315

HOFFMEISTER, D., WALDHOFF, G., CURDT, C., TILLY, N., BENDIG, J., BARETH, G., **2013**. Spatial variability detection of crop height in a single field by terrestrial laser scanning, in: Stafford, J.V. (Ed.), Precision Agriculture '13. Presented at the 9th European Conference on Precision Agriculture, Wageningen Academic Publishers, Lleida, Spain, pp. 267–274.

MARTINSANZ, G.P., **2012**. Special Issue Information: Unmanned Aerial Vehicles (UAVs) based Remote Sensing. Remote Sensing 4.

MIAO, Y., STEWART, B.A., ZHANG, F., **2010**. Long-term experiments for sustainable nutrient management in China. A review. Agronomy for Sustainable Development 31, 397–414. doi:10.1051/agro/2010034

MULLA, D.J., **2013**. Twenty five years of remote sensing in precision agriculture: Key advances and remaining knowledge gaps. Biosystems Engineering 114, 358–371. doi:10.1016/j.biosystemseng.2012.08.009

NEITZEL, F., KLONOWSKI, J., **2011**. Mobile 3D mapping with a low-cost UAV system, in: International Archives of the Photogrammetry, Remote Sensing and Spatial Information Sciences. Presented at the UAV-g 2011, Zurich, Switzerland, pp. 1–6.

PANASONIC, **2013**. Panasonic Lumix GF3 [WWW Document]. URL http://94.23.55.209/index.php/Cameras/Camera-Sensor-Database/Panasonic/Lumix-DMC-GF3 (accessed 1.8.13).

PENG, S., BURESH, R.J., HUANG, J., YANG, J., ZOU, Y., ZHONG, X., WANG, G., ZHANG, F., **2006**. Strategies for overcoming low agronomic nitrogen use efficiency in irrigated rice systems in China. Field Crops Research 96, 37–47. doi:10.1016/j.fcr.2005.05.004

SCHARSTEIN, D., SZELISKI, R., **2002**. A taxonomy and evaluation of dense two-frame stereo correspondence algorithms. International Journal of Computer Vision 47, 7–42. doi:10.1023/A:1014573219977

SEITZ, S.M., CURLESS, B., DIEBEL, J., SCHARSTEIN, D., SZELISKI, R., **2006**. A Comparison and Evaluation of Multi-View Stereo Reconstruction Algorithms, in: 2006 IEEE Computer Society Conference on Computer Vision and Pattern Recognition. Presented at the 2006 IEEE Computer Society Conference on Computer Vision and Pattern Recognition, New York, NY, US, pp. 519–528. doi:10.1109/CVPR.2006.19

SZELISKI, R., **2010**. Computer Vision: Algorithms and Applications. Springer, London, UK.

THENKABAIL, P.S., SMITH, R.B., DE PAUW, E., **2000**. Hyperspectral vegetation indices and their relationships with agricultural crop characteristics. Remote sensing of Environment 71, 158–182. doi:10.1016/S0034-4257(99)00067-X

VERHOEVEN, G., DONEUS, M., BRIESE, C., VERMEULEN, F., **2012**. Mapping by matching: a computer vision-based approach to fast and accurate georeferencing of archaeological aerial photographs. Journal of Archaeological Science 39, 2060–2070. doi:10.1016/j.jas.2012.02.022

WATTS, A.C., AMBROSIA, V.G., HINKLEY, E.A., **2012**. Unmanned Aircraft Systems in Remote Sensing and Scientific Research: Classification and Considerations of Use. Remote Sensing 4, 1671–1692. doi:10.3390/rs4061671

YU, K., LI, F., GNYP, M.L., MIAO, Y., BARETH, G., CHEN, X., **2013**. Remotely detecting canopy nitrogen concentration and uptake of paddy rice in the Northeast China Plain. ISPRS Journal of Photogrammetry and Remote Sensing 78, 102–115. doi:10.1016/j.isprsjprs.2013.01.008

# 4 UAV-based Imaging for Multi-Temporal, very high Resolution Crop Surface Models to monitor Crop Growth Variability

Juliane Bendig [1,*], Andreas Bolten [1], Georg Bareth [1,2]

1 Institute of Geography, GIS & RS Group, University of Cologne, Albertus-Magnus-Platz, 50923 Cologne

2 ICASD-International Center for Agro-Informatics and Sustainable Development, www.icasd.org

* Corresponding author, Tel.: +49-221-470-6551; Fax: +49-221-470-4917

E-Mail: juliane.bendig@uni-koeln.de

**Summary**: This paper describes the generation of multi-temporal crop surface models (CSMs) with very high resolution of <0.05 m. Data collection was carried out with a low-cost and low-weight UAV-system with a weight of less than 5 kg and the possibility of mounting different sensors. Key focus is the detection of crop growth variability and its dependency on cultivar, crop treatment and stress. The study area is a barley experiment field in Bonn in the west of Germany. Four replications of four cultivars of barley were investigated of which half of them where treated with a fungicide. Five UAV-campaigns were carried out during the growing season between early May and late July 2012. Ground control points (GCPs) measured with a HiPer® Pro Topcon DGPS allowed for appropriate ground truth (<0.02 m). Ground based infield control surveys on three dates served as validation of the method. Additionally, various destructive and non-destructive ground data were collected. The stereo images captured were processed into CSMs by using the structure-from-motion (SfM) software Agisoft PhotoScan Professional. Generated plant heights ranged between 0.16 m and 0.983 m. $R^2$ (n = 32) for the correlation between plant heights in the CSM and infield control surveys is 0.69. Lower plant heights were detected in those plots of the field where no fungicide was applied. Height differences between cultivars were observed and increased during growing season. The accuracy assessment of DEMs generated with the proposed UAV-based imaging showed a correlation coefficient of 0.99 (n = 10) between the DGPS GCPs and the DEMs with a mean difference of 0.01 m in z-direction.

**Zusammenfassung**: Monitoring des Pflanzenwachstums mit Hilfe multitemporaler und hoch auflösender Oberflächenmodelle von Getreidebeständen auf Basis von Bildern aus UAV-Befliegungen. Dieser Beitrag beschreibt die Erzeugung von multitemporalen Oberflächenmodellen von Getreidebeständen (crop surface models, CSMs) mit einer sehr hohen Auflösung von <0.05 m. Die Datenerfassung wurde mit einem kostengünstigen UAV-System mit einem Gewicht von weniger als 5 kg durchgeführt, welches die Möglichkeit der Anbringung verschiedener Sensoren bietet. Schwerpunkt war die Detektion der Variabilität im Pflanzenwachstum und die Abhängigkeit von Sorte, Pflanzenbehandlung und Stress. Das Untersuchungsgebiet liegt in Bonn im Westen Deutschlands und besteht aus 32 Testflächen, die mit viermaliger Wiederholung mit je vier Gerstensorten bepflanzt wurden, Die Hälfte der Pflanzen wurde mit einem Fungizid behandelt. Die Untersuchung umfasste fünf UAV-Kampagnen während der Vegetationsperiode zwischen Anfang Mai und Ende Juli 2012. Passpunkte (GCPs), gemessen mit einem HiPer® Pro Topcon DGPS, sorgten für eine entsprechende Georeferenzierung (<0.02 m). Kontrollmessungen im Feld an drei Terminen dienten zur Validierung der Methode. Zusätzlich wurden weitere destruktive und nicht-destruktive Felddaten erhoben. Aus den Stereobildern wurden unter Verwendung der Structure-from-Motion (SfM) Software Agisoft PhotoScan CSMs erzeugt. Die abgeleiteten Pflanzenhöhen lagen zwischen 0.16 m und 0.983 m. Das $R^2$ für die Korrelation zwischen Pflanzenhöhe im CSM und den Kontrollmessungen liegt bei 0.69. Niedrigere Pflanzenhöhen befanden sich in ungespritzten Teilen des Feldes. Höhenunterschiede zwischen den Sorten wurden festgestellt, die sich während der Vegetationsperiode verstärkten. Die Genauigkeitsanalyse des UAV-basierten DEMs zeigte einen Korrelationskoeffizienten von 0.99 zwischen DGPS und DEM, mit einer mittleren Differenz von 0.01 m in Z-Richtung.

**Keywords**: agriculture, crop growth, DEM, plant height, UAV

## 4.1 Introduction

Modelling canopy surfaces is a common application of remote sensing methods. In forestry, stereo photogrammetry or airborne laser scanning (ALS) are used for the extraction of canopy heights and surface modelling (**St-Onge et al., 2008**). Spaceborne sensors like TerraSAR-X combined with TanDEM-X enable stereo radargrammetric modelling of canopy heights (**Perko et al., 2010**).

Precision agriculture can benefit greatly from remote sensing (**Mulla, 2013**). Small experiment fields (<5 ha) like the one presented in this study can be easily monitored using low-weight unmanned aerial vehicles (UAVs). Producing multi-temporal datasets of the whole vegetation period

is essential for obtaining reliable results in such experiments. UAVs are already in use for capturing optical, spectral and thermal information (**Eisenbeiss and Sauerbier**, **2011**; **Grenzdörffer et al.**, **2008**; **Hartmann et al.**, **2012**; **Hunt, Jr. et al.**, **2010**). The UAV-system used in this study is a low-cost multi-sensor system with a weight of less than 5 kg, a so called Mini-UAV (**Eisenbeiss**, **2009**). Using a high resolution RGB consumer camera, stereo images can be captured and processed into digital crop surface models (CSMs) (**Figure 4-1**).

The key focus is to detect differences in plant height depending on cultivar, phenology, crop treatment, or stress. The non-invasive measurement of plant height is important due to its correlation to biomass and other crop parameters (**Hansen and Schjoerring**, **2003**; **Thenkabail et al.**, **2000**). In this context, **Hoffmeister et al.** (**2010**) introduced the concept of multi-temporal CSMs for monitoring plant growth between phenological stages with terrestrial laser scanning. Comparison of the CSMs for different phenological stages allows for the detection of crop growth variability and absolute plant height. This approach of analysing CSMs is shown in **Figure 4-1**. The plant height (PH), *e.g.* at time $t_3$ results from $t_3$ minus $t_0$. The plant growth (PG), for example from time $t_1$ to time $t_3$ results from $t_3$ minus $t_1$.

In this study, the idea of investigating multi-temporal CSMs is transferred to very high resolution CSMs derived from stereo images captured by a UAV.

## 4.2    Data Acquisition

### 4.2.1 *Study Area and Dataset*

The study area is located in the city of Bonn in the west of Germany (**Figure 4-2**). In 2012 the Institute for Agricultural Plants and Resource Protection (INRES) – Horticultural Science established an experiment field with four different cultivars of barley with different resistances to plant diseases.
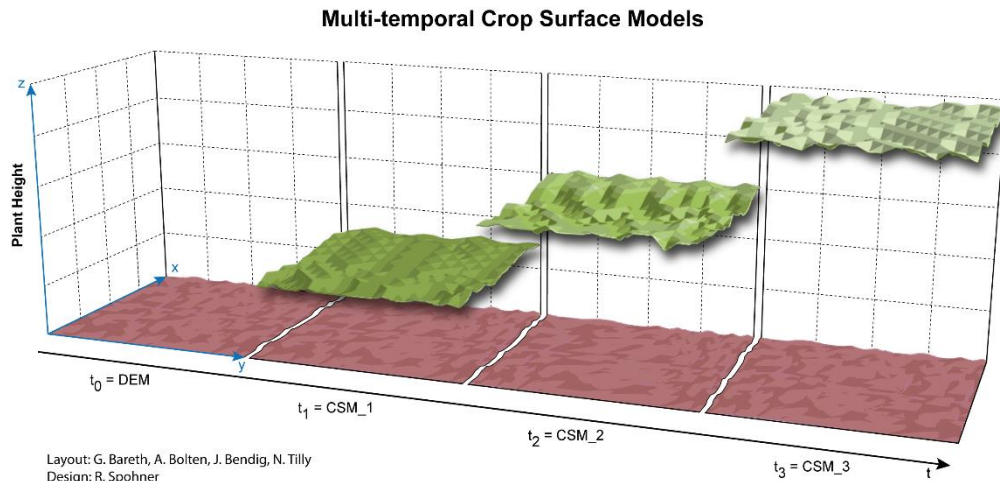
*Figure 4-1: Multi-temporal crop surface models (CSMs).*

The aim of the experiment is to determine the response to natural pathogens using non-destructive measurement techniques. A protective and curative fungicide against three common plant diseases was applied to the control sample plants (grey plots in **Figure 4-2**). All other horticultural activities were left unchanged. Four replications of every cultivar for both treatments were planted in 1.5 m x 7 m plots in a randomised order surrounded by boundary plots which were not used for measurements.
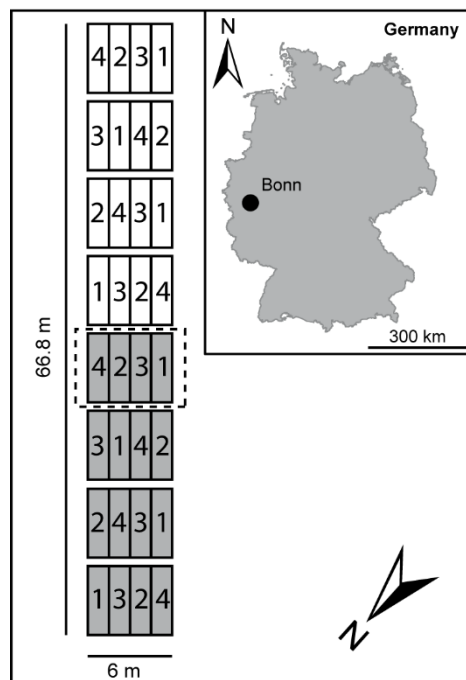


*Figure 4-2: Study area – 4 replications of 4 cultivars of barley (1, 2, 3, 4) planted in randomised order, two treatments. Grey: treated plots, white: untreated plots, dashed line: replication 4 (treated).*

*Figure 4-3: MK-Oktokopter by HiSystems GmbH mounted with RGB sensor.*

The ground based data collection was separated into destructive sampling of biomass, plant N-
and chlorophyll content, and non-destructive data acquisition of plant height, hyperspectral, and
fluorescence data. Field data campaigns were carried out repeatedly during the growing season.
UAV campaigns were conducted on 14.5., 25.5., 5.6, 18.6. and 23.7.12 using an RGB sensor (see
**chapter 4.2.3**). 18 ground control points (GCPs) were established on the corners of the plots for
ground truth. Infield control surveys of the plant heights were carried out on the 25.5., 5.6. and
18.6.12.

## 4.2.2 Platform

The UAV-system is a MK-Oktokopter by HiSystems GmbH (**HiSystems GmbH**, **2013**). It consists of a
point-symmetrical frameset composed of aluminium and glass fibre reinforced plastics (**Figure
4-3**). The total weight of the system including battery is less than 2.5 kg. An additional payload of
up to 1 kg is possible. The cost of the entire system not including the sensor is around 3,000 €. The
eight engines are equipped with high performance propellers.

The electronics include high-quality gyroscopes, a pressure sensor, a compass module and a GPS
module (**Mikrokopter**, **2013a**). Using the open source software MikrokopterTool (**Mikrokopter**,
**2013b**) pre-defined flight routes in a sense of an auto-pilot can be carried out in autonomous flight
mode. Lithium polymer batteries with up to 6,600 mAh capacity enable flight times of around 15
minutes depending on the payload. The additional transmitter channels of the 2.4 GHz transmitter
remote control are used for camera triggering (**Bendig et al.**, **2012**).

## 4.2.3 Sensor

The RGB sensor is a Panasonic Lumix DMC GF3 with a Lumix G 20 mm (F1.7 ASPH) lens. The weight
is 400 g and the sensor resolution is 4016 x 3016 (12 million) pixel (**Panasonic**, **2013**).

The field of view (FOV) of the camera is 48.5° horizontal and 33.4° vertical resulting in an image size of 90 m x 60 m at a distance of 100 m. Aperture and exposure times are adjusted and fixed manually prior to each flight. Due to the manual triggering of the camera an individually adapted camera holder with a mechanical trigger is used and operated by the remote control of the UAV-system.

## 4.2.4 Data Acquisition

Wooden poles with 0.3 m x 0.3 m highly visible targets attached to them were used as GCPs. Those were measured using a HiPer® Pro Topcon DGPS with a horizontal and vertical accuracy of < 0.01 m according to own evaluations (0.02 m according to **Ascos PED**, **2010**). Horizontal coordinates of eight data acquisition points were taken in the field which were used as waypoints for the flight route, resulting in a 50% overlap of the images, covering the whole experimental field in one flight. Several flights were carried out for each field campaign with the sensor mounted in nadir position with constant orientation and flying height. For the Panasonic Lumix DMC GF3 a height of 30 m was chosen resulting in a FOV of 18 m x 27 m and ground resolution of 0.006 m.

For the infield control surveys a ruler was placed next to the plants on three positions in each of the 32 plots to determine the mean plant height per plot with a 0.01 m precision. Plant heights per plot vary 0.1 m on an average.

## 4.2.5 Data Processing

The overall workflow of data processing is presented in **Figure 4-4**. For the generation of the CSM the multi-view 3D reconstruction software Agisoft PhotoScan 0.9.0 (**AGISOFT LLC**, **2014**) was used which is based on a structure-from-motion (SfM) algorithm (**VERHOEVEN**, **2011**). SfM allows for the estimation of the unknown camera positions through comparison of detected image feature points, e. g. object edges, in multiple images (**SZELISKI**, **2010**). Despite of the fact that Agisoft PhotoScan and, in general, the use of SfM algorithms for DEMs derived from UAV-based imagery is becoming more and more popular since 2012, quite little literature on comparable studies has been published. Papers by **NEITZEL AND KLONOWSKI** (**2011**), **VERHOEVEN ET AL.** (**2012**) and **DE REU ET AL.** (**2013**) suggest that the software shall be well suited for such applications.

For each date (except 23.7.) two partly overlapping tiles were generated, one covering the treated plots of the experiment field and one covering the untreated plots. However, a complete model could be generated as well. Due to computation and calculation time, we split the model into two

parts. The point clouds consisted of 12 million points per model on average. As a result, the 4th replication of the untreated plots was covered in both datasets (**Figure 4-5**).
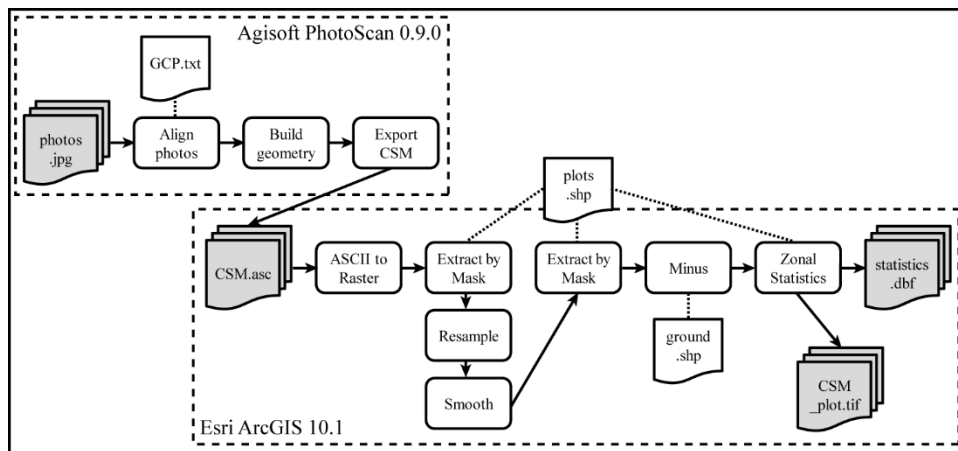


*Figure 4-4: Data Processing workflow for the generation of CSM (CSM.asc) from RGB images captured by UAV (photos.jpg) in Agisoft PhotoScan and further processing for analysis based on each plot in Esri ArcGIS®.*

GCPs were identified manually on each photo and assigned to the coordinates measured by the DGPS (**Figure 4-4**). In a batch process the images were aligned to each other, the CSM was built.

Via an ASCII-file it was transferred to a raster file in Esri ArcGIS® 10.1. A shapefile containing the outlines of the plots, reduced by a 0.3 m inside buffer to reduce plot boundary effects, served as a mask to extract areas of interest (AOI). After that, data were resampled to a raster size of 0.1 m and smoothed by calculating the focal mean of 3 x 3 pixel rectangles. A ground model was constructed from z-data of the GCPs ($t_0$ in **Figure 4-1**). Each CSM was subtracted from the ground plane using the AOI shapefile to obtain plant height per plot. In a last step, general statistics including mean plant height and standard deviation were calculated for each date and plot.

Five datasets were collected during the growing season of which four could be used for analysis. For $t_5$ (23.7.), the CSM could only be generated for parts of the experiment field due to image quality (see **Table 4-1**). Image quality was decreased because of strong wind during data collection and lodging caused by a thunderstorm a few days before. Furthermore, parts of the CSM for $t_3$ (16.5.) and $t_4$ (18.6.) could not be modelled satisfactorily ($t_3$: replications 1–4 treated, replication 2 untreated; $t_4$: replication 4 treated, replication 3 and 1 untreated) resulting in unrealistic values for plant height. Those datasets were partly excluded from the analysis and are referred to as "selected data" in the following (**Table 4-2**, **Figure 4-7**). Results of the analysis are presented for all data and selected data of sufficient quality.

## 4.3   Results

### 4.3.1 Statistics

**Table 4-1** illustrates minimum, maximum, range, mean, and standard deviation (std.) of plant height for the whole experimental field according to date (t) and measurement technique (CSM or infield control survey). Plant heights generated from CSMs range from 0.16 m to 0.983 m over all dates. Ranges for each date vary between 0.149 m and 0.755 m and increase with development of vegetation (range ($t_5$) > range ($t_1$)). The mean plant height increases for $t_1$ to $t_3$ and decreases for $t_4$ to $t_5$. Standard deviation increases continuously with the vegetation development (std. ($t_5$) > std. ($t_1$)). For the infield control surveys, plant heights range between 0.370 m and 1.06 m for all dates ($t_2$ to $t_4$). Ranges for each date vary between 0.17 m and 0.22 m which is significantly lower compared to the CSM heights. Mean plant height increases from $t_2$ to $t_4$ while the standard deviation varies without a trend.

The average difference of mean plant height between CSM and infield control survey is under 0.01 m for $t_2$ and $t_3$ but one magnitude higher for $t_4$. $R^2$ (correlation, n = 32) for both measurement techniques are 0.55 ($t_2$), 0.22 ($t_3$) and 0.71 ($t_4$). The overall correlation is 0.69 (n = 96) for the three dates altogether. For selected data, overall correlation decreases to 0.62 (n = 64), because some values were removed ($R^2$ $t_3$= 0.43 (n = 12), $R^2$ $t_4$ = 0.68 (n = 20)).

*Table 4-1: Descriptive statistics of plant heights (m) derived from CSMs and infield control survey according to date (std. = standard deviation, RMSE = root-mean-square error).*

| | date | $t_1$ 14.5.12 | $t_2$ 25.5.12 | $t_3$ 5.6.12 | $t_4$ 18.6.12 | $t_5$ 23.7.12 |
|---|---|---|---|---|---|---|
| CSM | min | 0.160 | 0.354 | 0.595 | 0.454 | 0.228 |
| | max | 0.309 | 0.512 | 0.905 | 0.874 | 0.983 |
| | range | 0.149 | 0.158 | 0.310 | 0.420 | 0.755 |
| | mean | 0.241 | 0.451 | 0.772 | 0.688 | 0.595 |
| | std. | 0.028 | 0.032 | 0.062 | 0.075 | 0.160 |
| | RMSE | 0.256 | 0.453 | 0.815 | 0.683 | 0.892 |
| infield control survey | min | no data | 0.370 | 0.685 | 0.850 | no data |
| | max | | 0.590 | 0.855 | 1.060 | |
| | range | | 0.220 | 0.170 | 0.210 | |
| | mean | | 0.509 | 0.763 | 0.950 | |
| | std. | | 0.054 | 0.045 | 0.058 | |
| | RMSE | | 0.702 | 0.755 | 0.940 | |

### 4.3.2 Crop Surface Models

In **Figure 4-5** an example of the generated CSM with 0.006 m resolution is presented for $t_2$ (25.5.) starting with replication 1 (treated) in the north. The experiment plots, e. g. red rectangle in **Figure 4-5**, are surrounded by two boundary plots on one side and three on the other side.
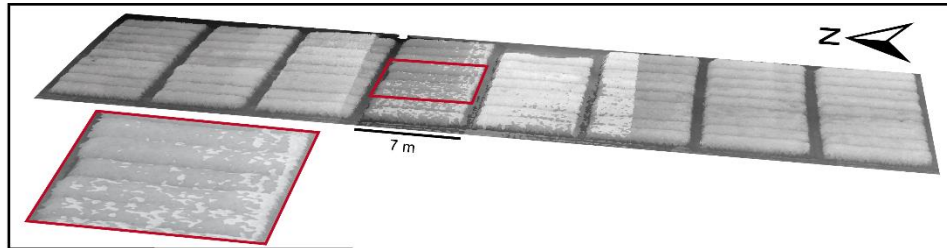


*Figure 4-5: CSM – Overview of study area ($t_2$: 25 May 2012), red rectangle: replication 4 (treated) (Esri ArcScene).*
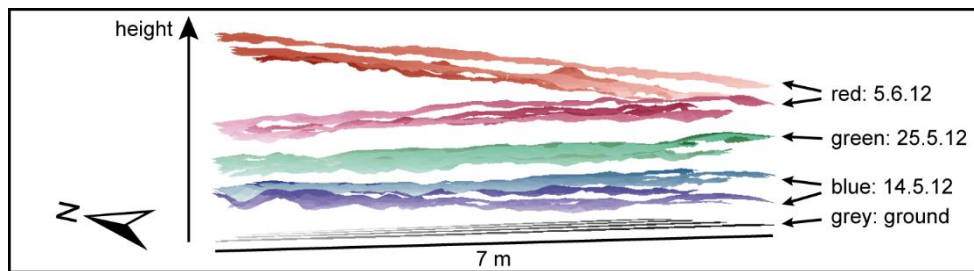


*Figure 4-6: Cross section of CSM – replication 4 (treated): height comparison ($t_0 – t_3$) for two datasets of over-lapping tiles ($t_0$ = grey, $t_1$ = light and dark blue, $t_2$ = light and dark green, $t_3$ = light and dark red) (Esri ArcScene, height 2 times exaggerated).*

The plots can be clearly distinguished from each other and from the surrounding bare soil. Since the model was separated into two tiles, seamlines are visible. Tiles were not merged in order to keep the original data and to facilitate the comparison between the datasets. A closer look at replication 4 (treated) for $t_0$ to $t_3$ (**Figure 4-6**) allows for the detection of possible differences in the datasets. Blue surfaces show plant height for $t_1$ (14.5.). An increasing height difference to the south (mean: 0.08 m, max: 0.18 m) is noticeable. For $t_2$ (25.5.), green surfaces in **Figure 4-6**, the maximum difference is considerably lower with 0.11 m and the mean difference 0.02 m. The red surfaces in **Figure 4-6** of $t_3$ (5.6.) show maximum differences of 0.36 m and a mean of 0.01 m due to the surface on top increasing in height towards north.

### 4.3.3 Plant Height Development

The analysis of plant height and the growth according to cultivar and treatment is presented in **Table 4-2** and **Figure 4-7** for all data and selected data (in brackets).
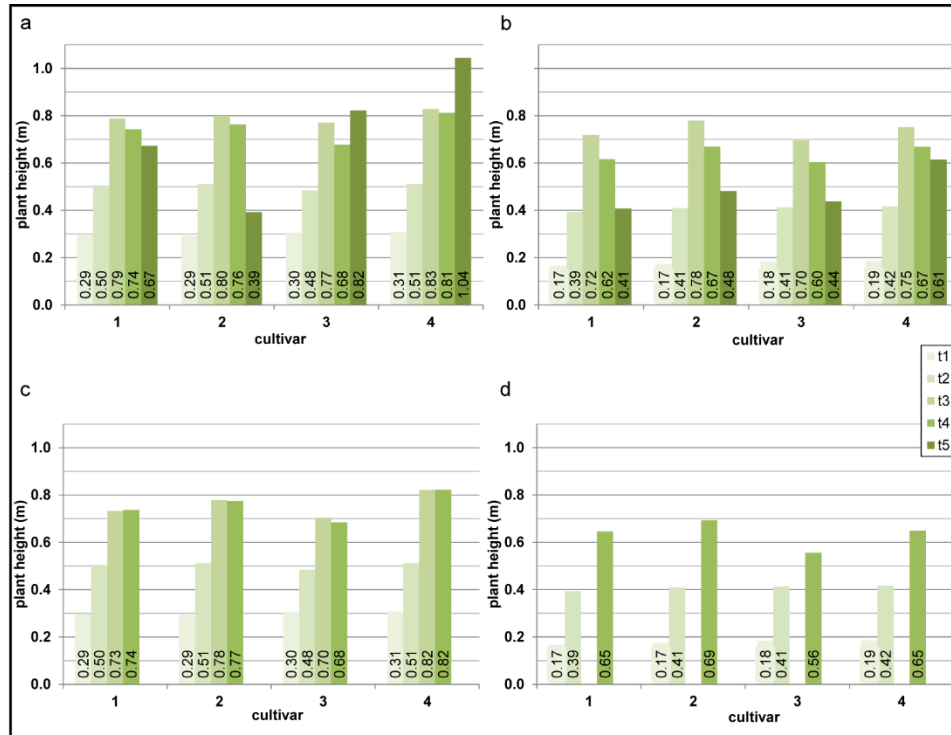


*Figure 4-7: CSM – mean plant height comparison according to date, cultivar and treatment; a: treated (all data), b: untreated (all data), c: treated (selected data), d: untreated (selected data) (for definition of "selected data" see 4.2.5).*



*Figure 4-8: Experimental design of accuracy assessment (left: photo, right: DEM): Reference points are four GCPs, two different sized Peli Cases and 4 corners of the UAV transport box.*

**Figure 4-7** shows that plants in untreated plots are generally smaller than plants in treated plots. Numbers in **Table 4-2** give more details, for example cultivar 1: 0.295 m compared to 0.165 m for $t_1$ minus $t_0$. Looking at column $t_4$ minus $t_0$, plants in untreated plots are 0.109 m (0.118 m) lower on average (mean height treated: 0.749 m (0.755 m) and untreated: 0.639 m (0.636 m)).

In general, height differences increase between cultivars during the growing season, e. g. orange bars compared to green bars in **Figure 4-7a** or **Table 4-2**: 0.016 m for $t_1$ minus $t_0$ compared to 0.135 m for $t_4$ minus $t_0$ for treated plots, all data. Mean heights between cultivars differ by 0.135 m (0.138 m) for treated plots and 0.065 m (0.1 37 m) respectively for untreated plots ($t_4$ minus $t_0$). For $t_4$ minus $t_0$ cultivar 3 has the smallest heights while the cultivar with most growth is cultivar 4 for the treated plots and cultivar 2 for the untreated plots ($t_4$ minus $t_0$).

### 4.3.4 Accuracy Assessment

To determine the quality of DEMs generated from stereo images acquired with the UAV system an accuracy assessment was carried out (**Figure 4-8**). X-, y- and z-coordinates of test targets and four GCPs were measured using DGPS and compared to pixel values in the DEM (flying height 30 m). The test targets were two Peli Cases of different sizes of which each midpoint was measured and the transport box for the UAV (0.75 m x 0.75 m x 0.365 m) of which the four corners were measured. Z-values and differences between DGPS and DEM are presented in **Table 4-3**. Numbers in italic mark differences measured for the four corners of the transport box. The mean height difference is 0.01 m which is in the same order as the accuracy of the DGPS measurement of 0.01 m in z-direction. The differences for the corners of the transport box are above average with 0.02 m which is probably due to the grooved surface of the box. $R^2$ for the correlation between DGPS and DEM is 0.99.

*Table 4-2: Plant height and growths (m) ($t_0$– $t_4$) according to cultivar and treatment. Shading in the last column indicates ranking of the amount of growth according to cultivar (dark = big, bright = small) (for definition of "selected data" see 4.2.5)*

| cultivar | | | date | $t_0$ | $t_1-t_0$ | $t_2-t_1$ | $t_2-t_0$ | $t_3-t_2$ | $t_3-t_1$ | $t_3-t_0$ | $t_4-t_3$ | $t_4-t_2$ | $t_4-t_1$ | $t_4-t_0$ |
|---|---|---|---|---|---|---|---|---|---|---|---|---|---|---|
| 1 | all data | treated | | 0.000 | 0.295 | 0.210 | 0.505 | 0.282 | 0.492 | 0.787 | -0.045 | 0.237 | 0.447 | 0.742 |
| 2 | | | | 0.000 | 0.293 | 0.219 | 0.511 | 0.289 | 0.508 | 0.800 | -0.037 | 0.252 | 0.471 | 0.763 |
| 3 | | | | 0.000 | 0.305 | 0.179 | 0.484 | 0.286 | 0.465 | 0.770 | -0.093 | 0.193 | 0.372 | 0.677 |
| 4 | | | | 0.000 | 0.308 | 0.203 | 0.511 | 0.316 | 0.520 | 0.828 | -0.016 | 0.300 | 0.503 | 0.812 |
| 1 | | untreated | | 0.000 | 0.165 | 0.228 | 0.393 | 0.326 | 0.554 | 0.719 | -0.103 | 0.222 | 0.450 | 0.616 |
| 2 | | | | 0.000 | 0.173 | 0.236 | 0.409 | 0.370 | 0.606 | 0.780 | -0.111 | 0.260 | 0.496 | 0.669 |
| 3 | | | | 0.000 | 0.183 | 0.230 | 0.413 | 0.282 | 0.512 | 0.695 | -0.092 | 0.190 | 0.421 | 0.604 |
| 4 | | | | 0.000 | 0.185 | 0.231 | 0.416 | 0.335 | 0.566 | 0.751 | -0.083 | 0.252 | 0.483 | 0.668 |
| 1 | selected data | treated | | 0.000 | 0.295 | 0.210 | 0.505 | 0.228 | 0.437 | 0.732 | 0.004 | 0.232 | 0.442 | 0.737 |
| 2 | | | | 0.000 | 0.293 | 0.219 | 0.511 | 0.267 | 0.485 | 0.778 | -0.003 | 0.264 | 0.482 | 0.775 |
| 3 | | | | 0.000 | 0.305 | 0.179 | 0.484 | 0.220 | 0.399 | 0.704 | 0.020 | 0.200 | 0.379 | 0.684 |
| 4 | | | | 0.000 | 0.308 | 0.203 | 0.511 | 0.309 | 0.513 | 0.821 | 0.001 | 0.311 | 0.514 | 0.822 |
| 1 | | untreated | | 0.000 | 0.165 | 0.228 | 0.393 | | | | | 0.252 | 0.480 | 0.646 |
| 2 | | | | 0.000 | 0.173 | 0.236 | 0.409 | | no data | | | 0.284 | 0.520 | 0.693 |
| 3 | | | | 0.000 | 0.183 | 0.230 | 0.413 | | | | | 0.143 | 0.373 | 0.556 |
| 4 | | | | 0.000 | 0.185 | 0.231 | 0.416 | | | | | 0.233 | 0.464 | 0.649 |

*Table 4-3: Comparison of heights (m) measured by DGPS and pixel values of DEM for accuracy assessment.*

| DGPS | DEM | Difference |
|---|---|---|
| 126.261 | 126.257004 | 0.003996 |
| 126.151 | 126.164001 | −0.013001 |
| 126.181 | 126.166000 | 0.015000 |
| 126.219 | 126.224998 | −0.005998 |
| 126.529 | 126.504997 | 0.024003 |
| 126.409 | 126.393997 | 0.015003 |
| 126.713 | 126.728996 | *−0.015996* |
| 126.730 | 126.704002 | *0.025998* |
| 126.734 | 126.707001 | *0.026999* |
| 126.716 | 126.691002 | *0.024998* |
| | **mean** | **0.0101002** |

## 4.4 Discussion and Conclusion

The study area, experiment design and validation results underlined the suitability of stereo images from optical cameras mounted on UAV systems for crop growth monitoring. This enables DEM/CSM generation for agricultural purposes (**HOFFMEISTER ET AL.**, **2010**). Other campaigns like

the ones by **GRENZDÖRFFER ET AL.** (**2008**), **HUNT ET AL.** (**2010**) and **LELONG ET AL.** (**2008**) already mentioned the great potential of UAVs in the field of agriculture.

The MK-Oktokopter by HiSystems GmbH low-cost platform produces competitive results to the often used Microdrone MD4-200, Falcon 8 (**EISENBEISS AND SAUERBIER**, **2011**) and other UAVs (*e.g.* **ABER ET AL.**, **2010**; **EISENBEISS ET AL.**, **2005**; **VALLET ET AL.**, **2011**).

Still some improvements will be made in the future: the UAV-system will be equipped with a camera holder that enables pitch and roll compensation during the flight. This ensures the capture of images in nadir position during movement of the UAV-system. A camera with increased resolution will be used (Panasonic Lumix DMC GX1, 16 mio. pixel) in order to increase ground resolution. It can be triggered electrically which makes image acquisition more reliable compared to a mechanical trigger.

Size, design, texture and number of the GCPs were suitable for the study since they could be clearly identified in the images. With increasing density and height of vegetation the visibility of the GCPs at the chosen placement was obstructed by plants in some cases. To enhance data quality GCPs will be placed in unobstructed positions. The accuracy of the GCPs could be slightly improved by using a total station as **HARWIN AND LUCIEER** (**2012**) found out, but would make data collection more time consuming.

Flight planning including flight route generation and data acquisition points enabled capturing images of the whole study area. For $t_3$, $t_4$ and $t_5$ weather conditions during data collection, mainly wind, influenced the quality of the CSMs. Generally weather conditions limit the applicability of a UAV-system for data collection.

The overlap of 50% between the images will be increased in the future in order to cover the study area from numerous positions leading to a greater variety of viewing perspectives. **HAALA AND ROTHERMEL** (**2012**) used 80% overlap, stating that using additional stereo pairs enhances the point clouds, especially in previously occluded areas. Another study by **HARTMANN ET AL.** (**2012**) suggest 90% overlap leading to 0.01 m horizontal and 0.03 m vertical accuracy.

Different settings were tested in Agisoft PhotoScan showing that model quality increased with the amount of photos used for model generation. This is also stated by **ROBERTS ET AL.** (**2011**). The number of photos taken during the flights will be increased in the future because higher accuracy is expected. The inclusion of photos that were discarded before due to insufficient sharpness,

exposure or coverage of the area did not decrease the model quality but on the contrary led to increased model quality in some cases.

Dividing the model of the study area into two tiles led to datasets with manageable data size and provided the opportunity of model comparison. The comparison showed satisfying results for good quality data (*e.g.* $t_2$, **Figure 4-6**) with a mean difference of z-values of 0.02 m. An error of this magnitude corresponds to the results of the accuracy assessment which shows a mean error of 0.01 m. **Harwin and Lucieer** (**2012**) achieved an accuracy of 0.025 cm – 0.04 cm with a DGPS at a comparable flying height of 40 m – 50 m. Taking other sources of error into account like inaccuracies caused by moving plants during data acquisition or inaccuracy of the DGPS, the resulting CSMs enable plant growth monitoring with very high accuracy.

The comparison of plant heights derived from CSM and infield control surveys showed that for $t_4$ the range of values is twice as large in the CSM (0.42 m) compared to the infield control survey (0.21 m). This is mainly due to the underestimation of heights in the model especially in the southern part of the field where the untreated plots are located. In this part of the field the range of height values is about 0.06 m larger compared to the northern part of the field. The same is true for the mean height difference between CSM and infield control survey compared to treated plots. Two possible sources of error might account for those differences: The CSMs become more complex with progressing phenology as differences in plant heights increase. This makes modelling difficult as only one viewing perspective (nadir) was chosen and some areas might not have been covered sufficiently. **Harwin and Lucieer** (**2012**) suggest data collection from different perspectives. This would further increase the time required for data collection. Continuous acquisition of nadir images using the electrical trigger could address this problem avoiding time consuming measurements.

A second reason is the accuracy of infield control surveys. Determining average plant height is difficult due to high variability of heights in a plot and the fact that plants are moving by wind. A higher number of samples for the control surveys could help to increase accuracy.

**Figure 4-6** shows that with the method presented in this study it is possible to derive multi-temporal CSMs similar to the concept presented in **Figure 4-1**. The transferability of the concept used for a TLS (**Hoffmeister et al., 2010**) to a different platform, the UAV, is possible. The partial models show a similar surface profile, if the quality of the raw data is sufficient (problematic are: $t_3$, $t_4$ and $t_5$).

The statistical analysis of the models showed detectable differences between growth according to the cultivar and the treatment. When plants were treated with fungicides, the overall plant height was 15% higher compared to untreated plants. The plant heights of cultivar 3 were 14% lower compared to better growing cultivars 2 and 4.

## 4.5   Outlook

In the planned field campaign of 2013, the results obtained from the CSM analysis will be combined with data captured by a multispectral (Tetracam's MiniMCA) and a thermal sensor (NEC F30IS) (**BENDIG ET AL.**, **2012**). Thus additional spectral and thermal patterns will be analysed between plant height, which is linked to biomass, vegetation indices, derived from multispectral data (**HUNT, JR. ET AL.**, **2010**), and plant temperature (**BERNI ET AL.**, **2009a**), derived from thermal data. Additionally, the approach will be applied to different crops with varying growth patterns like rice, sugar beet and maize in 2013 in order to investigate the transferability of the concept of multi-temporal CSMs.

## Acknowledgements

# References

ABER, J.S., MARZOLFF, I., RIES, J., **2010**. Small-Format Aerial Photography: Principles, techniques and geoscience applications. Elsevier, Amsterdam, Netherlands.

AGISOFT LLC, **2014**. Agisoft PhotoScan [WWW Document]. Agisoft PhotoScan. URL http://www.agisoft.com (accessed 10.9.14).

ASCOS PED, **2010**. Der präzise Echtzeitdienst [WWW Document]. URL http://www.ascos.de/up-loads/tx_v3downloads/Produktblatt_PED_2010.pdf (accessed 1.10.13).

BENDIG, J., BOLTEN, A., BARETH, G., **2012**. Introducing a low-cost mini-UAV for thermal-and multi-spectral-imaging. International Archives of the Photogrammetry, Remote Sensing and Spatial Information Sciences 39, 345–349.

BERNI, J.A.J., ZARCO-TEJADA, P.J., SUAREZ, L., FERERES, E., **2009a**. Thermal and Narrowband Multispectral Remote Sensing for Vegetation Monitoring From an Unmanned Aerial Vehicle. IEEE Transactions on Geoscience and Remote Sensing 47, 722–738. doi:10.1109/TGRS.2008.2010457

DE REU, J., PLETS, G., VERHOEVEN, G., DE SMEDT, P., BATS, M., CHERRETTÉ, B., DE MAEYER, W., DECONYNCK, J., HERREMANS, D., LALOO, P., VAN MEIRVENNE, M., DE CLERCQ, W., **2013**. Towards a three-dimensional cost-effective registration of the archaeological heritage. Journal of Archaeological Science 40, 1108–1121. doi:10.1016/j.jas.2012.08.040

EISENBEISS, H., **2009**. UAV photogrammetry (dissertation). ETH, Zurich, Switzerland.

EISENBEISS, H., SAUERBIER, M., **2011**. Investigation of uav systems and flight modes for photogrammetric applications: Investigation of UAV systems and flight modes. The Photogrammetric Record 26, 400–421. doi:10.1111/j.1477-9730.2011.00657.x

EISENBEISS, H., SAUERBIER, M., ZHANG, L., GRUEN, A., **2005**. Mit dem Modellhelikopter über Pinchango Alto. Geomatik Schweiz 103, 510–515.

GRENZDÖRFFER, G.J., ENGEL, A., TEICHERT, B., **2008**. The photogrammetric potential of low-cost UAVs in forestry and agriculture. The International Archives of the Photogrammetry, Remote Sensing and Spatial Information Sciences 31, 1207–1214.

HAALA, N., ROTHERMEL, M., **2012**. Dense Multi-Stereo Matching for High Quality Digital Elevation Models. Photogrammetrie - Fernerkundung - Geoinformation 4, 331–343. doi:10.1127/1432-8364/2012/0121

HANSEN, P.M., SCHJOERRING, J.K., **2003**. Reflectance measurement of canopy biomass and nitrogen status in wheat crops using normalized difference vegetation indices and partial least squares regression. Remote Sensing of Environment 86, 542–553. doi:10.1016/S0034-4257(03)00131-7

HARTMANN, W., TILCH, S., EISENBEISS, H., SCHINDLER, K., **2012**. Determination of the UAV position by automatic processing of thermal images. International Archives of the Photogrammetry, Remote Sensing and Spatial Information Sciences 111–116.

HARWIN, S., LUCIEER, A., **2012**. Assessing the Accuracy of Georeferenced Point Clouds Produced via Multi-View Stereopsis from Unmanned Aerial Vehicle (UAV) Imagery. Remote Sensing 4, 1573–1599. doi:10.3390/rs4061573

HISYSTEMS GMBH, **2013**. HiSystems [WWW Document]. URL http://www.hisystems.de (accessed 1.8.13).

HOFFMEISTER, D., BOLTEN, A., CURDT, C., WALDHOFF, G., BARETH, G., **2010**. High-resolution Crop Surface Models (CSM) and Crop Volume Models (CVM) on field level by terrestrial laser scanning, in: Guo, H., Wang, C. (Eds.), SPIE Proceedings of the Sixth International Symposium on Digital Earth: Models, Algorithms, and Virtual Reality. Presented at the Sixth International Symposium on Digital Earth: Models, Algorithms, and Virtual Reality, Beijing, China, p. 78400E–78400E–6. doi:10.1117/12.872315

HUNT, JR., E.R., HIVELY, W.D., FUJIKAWA, S.J., LINDEN, D.S., DAUGHTRY, C.S.T., MCCARTY, G.W., **2010**. Acquisition of NIR-Green-Blue Digital Photographs from Unmanned Aircraft for Crop Monitoring. Remote Sensing 2, 290–305. doi:10.3390/rs2010290

LELONG, C.C.D., **2008**. Assessment of Unmanned Aerial Vehicles Imagery for Quantitative Monitoring of Wheat Crop in Small Plots. Sensors 8, 3557–3585. doi:10.3390/s8053557

MIKROKOPTER, **2013a**. NaviCtrl_2.0 [WWW Document]. URL http://www.mikrokopter.de/ucwiki/NaviCtrl_2.0 (accessed 1.8.13).

MIKROKOPTER, **2013b**. MikroKopterTool-OSD [WWW Document]. URL http://www.mikrokopter.de/ucwiki/en/MikroKopterTool-OSD (accessed 1.8.13).

MULLA, D.J., **2013**. Twenty five years of remote sensing in precision agriculture: Key advances and remaining knowledge gaps. Biosystems Engineering 114, 358–371. doi:10.1016/j.biosystemseng.2012.08.009

NEITZEL, F., KLONOWSKI, J., **2011**. Mobile 3D mapping with a low-cost UAV system, in: International Archives of the Photogrammetry, Remote Sensing and Spatial Information Sciences. Presented at the UAV-g 2011, Zurich, Switzerland, pp. 1–6.

PANASONIC, **2013**. Panasonic Lumix GF3 [WWW Document]. URL http://94.23.55.209/index.php/Cameras/Camera-Sensor-Database/Panasonic/Lumix-DMC-GF3 (accessed 1.8.13).

PERKO, R., RAGGAM, H., GUTJAHR, K., SCHARDT, M., **2010**. Analysis of 3D Forest Canopy Height Models Resulting from Stereo-Radargrammetric Processing of TerraSAR-X Images, in: Proceedings of the 30th EARSeL Symposium, Remote Sensing for Science, Education, and Natural and Cultural Heritage, Paris, France. p. 8.

ROBERTS, D., ROTH, K., PERROY, R., **2011**. Hyperspectral Vegetation Indices, in: Thenkabail, P.S., Huete, A. (Eds.), Hyperspectral Remote Sensing of Vegetation. CRC Press, Boca Raton, FL, US, pp. 309–328.

ST-ONGE, B., VEGA, C., FOURNIER, R.A., HU, Y., **2008**. Mapping canopy height using a combination of digital stereo-photogrammetry and lidar. International Journal of Remote Sensing 29, 3343–3364. doi:10.1080/01431160701469040

SZELISKI, R., **2010**. Computer Vision: Algorithms and Applications. Springer, London, UK.

THENKABAIL, P.S., SMITH, R.B., DE PAUW, E., **2000**. Hyperspectral vegetation indices and their relationships with agricultural crop characteristics. Remote sensing of Environment 71, 158–182. doi:10.1016/S0034-4257(99)00067-X

VALLET, J., PANISSOD, F., STRECHA, C., TRACOL, M., **2011**. Photogrammetric Performance of an Ultra Light Weight Swinglet "UAV," in: International Archives of the Photogrammetry, Remote Sensing and Spatial Information Sciences. Presented at the UAV-g 2011, Zurich, Switzerland, p. 6.

VERHOEVEN, G., **2011**. Taking computer vision aloft - archaeological three-dimensional reconstructions from aerial photographs with photoscan. Archaeological Prospection 18, 67–73. doi:10.1002/arp.399

VERHOEVEN, G., DONEUS, M., BRIESE, C., VERMEULEN, F., **2012**. Mapping by matching: a computer vision-based approach to fast and accurate georeferencing of archaeological aerial photographs. Journal of Archaeological Science 39, 2060–2070. doi:10.1016/j.jas.2012.02.022

# 5   Estimating Biomass of Barley Using Crop Surface Models (CSMs) Derived from UAV-Based RGB Imaging

Juliane Bendig [1,*], Andreas Bolten [1], Simon Bennertz [1], Janis Broscheit [1], Silas Eichfuss [1],

Georg Bareth [1,2]

Original manuscript is embedded in dissertation format.

1   Institute of Geography, GIS & RS Group, University of Cologne, Albertus-Magnus-Platz, 50923 Cologne

2   ICASD-International Center for Agro-Informatics and Sustainable Development, www.icasd.org

*   Corresponding author, Tel.: +49-221-470-6551; Fax: +49-221-470-4917

E-Mail: juliane.bendig@uni-koeln.de

**Abstract:** Crop monitoring is important in precision agriculture. Estimating above-ground biomass helps to monitor crop vitality and to predict yield. In this study, we estimated fresh and dry biomass on a summer barley test site with 18 cultivars and two nitrogen (N)-treatments using the plant height (PH) from crop surface models (CSMs). The super-high resolution, multi-temporal (1 cm/pixel) CSMs were derived from red, green, blue (RGB) images captured from a small unmanned aerial vehicle (UAV). Comparison with PH reference measurements yielded an $R^2$ of 0.92. The test site with different cultivars and treatments was monitored during "Biologische Bundesanstalt, Bundessortenamt und CHemische Industrie" (BBCH) Stages 24–89. A high correlation was found between PH from CSMs and fresh biomass ($R^2 = 0.81$) and dry biomass ($R^2 = 0.82$). Five models for above-ground fresh and dry biomass estimation were tested by cross-validation. Modelling biomass between different N-treatments for fresh biomass produced the best results ($R^2 = 0.71$). The main limitation was the influence of lodging cultivars in the later growth stages, producing irregular plant heights. The method has potential for future application by non-professionals, *e.g.*, farmers.

**Keywords:** UAV; optical; remote sensing; RGB; 3D; biomass estimation; crop surface model; plant height; summer barley; precision agriculture

## 5.1   Introduction

Monitoring crops throughout the vegetation period is one prerequisite for precision agriculture (**Laudien and Bareth, 2006**; **Mulla, 2013**). In addition to natural factors, like water availability or soil quality, knowledge about the health status, nutrient supply and effects of agricultural management practices helps when estimating the predicted yield of a field (**Adamchuk et al., 2010**; **Goyne et al., 1996**; **Shanahan et al., 2001**). Such knowledge can be obtained from crop parameters, such as plant height (PH), biomass, plant nitrogen content, soil nitrogen content and LAI, amongst other variables (**Jensen et al., 1990**; **Thenkabail et al., 2000**). Biomass plays an important role in yield prediction and for management optimization. For the latter, the nitrogen nutrition index (NNI), the ratio of measured and critical nitrogen (N) content, is commonly used as a tool for determining the ideal amount of N needed to maximize yield while preventing over-fertilization (**Chen et al., 2010**; **Lemaire and Gastal, 1997**). The relationship between biomass and N concentration is used in the N dilution curve, from which the critical N content is derived (**Lemaire et al., 2008**; **Lemaire and Gastal, 1997**). Hence, biomass is a crucial parameter for calculating the NNI.

The NNI input values can be measured either destructively or non-destructively by remote sensing. Biomass can be estimated through spectral reflectance measurements (**Kumar et al., 2001**) from space (**Koppe et al., 2012**; **Migdall et al., 2009**), from the air (**Hoyos-Villegas and Fritschi, 2013**; **Jang et al., 2006**; **Yang et al., 2008**) or from the ground (**Gnyp et al., 2014a**; **Jensen et al., 1990**; **Li et al., 2010b**; **Sakamoto et al., 2012**). However, these measurements often involve sophisticated and expensive equipment that needs careful calibration. Alternatively, PH is also positively correlated with crop biomass (**Lati et al., 2013a**). In combination with a non-vegetation ground model, PH can be obtained by quantifying the height of a canopy using crop surface models (CSMs) (**Bendig et al., 2013**; **Hoffmeister et al., 2013, 2010**). The suitability of terrestrial laser scanning (TLS) for biomass estimation is demonstrated by **Tilly et al.** (**2014**, **2012**) for paddy rice and for sugar beet by **Hoffmeister et al.** (**2011b**). A good correlation between PH and grain yield in barley, oat and wheat is given by **Lumme et al.** (**2008**) and by **Ehlert et al.** (**2009**) in oilseed rape, winter rye, winter wheat and grassland. Besides laser scanning approaches, 3D geometry information from an unmanned aerial vehicle (UAV), in combination with a high-resolution digital camera, is used for CSM generation. UAVs, sometimes referred to as remotely-piloted aerial systems (RPAS) or unmanned aerial systems (UAS), are the emerging tools to be used for small-scale remote sensing (**Colomina and Molina, 2014**; **Sakamoto et al., 2012**; **Zarco-Tejada, 2008**). A few

studies exist for biomass estimation, *i.e.*, (**Hunt et al., 2011b**; **Jensen et al., 2007**), using UAV-based near-infrared imaging. Comparisons of UAVs with airborne platforms (for larger areas) and TLS show competitive results (**Lumme et al., 2008**; **Tilly et al., 2012**). In an agricultural context, UAVs have been used, for example, for crop status analysis using near-infrared or thermal data (**Agüera et al., 2011**; **Baluja et al., 2012**; **Berni et al., 2009b**) or crop mapping. This study uses UAV-based data from a small-scale summer barley field experiment to evaluate how successfully CSMs can predict biomass.

## 5.2 Materials and Methods

### 5.2.1 Test Site: Campus Klein-Altendorf, 2013

The study site is located at the Campus Klein-Altendorf agricultural research station (50°37′N, 6°59′E, altitude 186 m), 40 km south of Cologne, Germany. The summer barley experiment consists of 18 barley cultivars, of which ten are new cultivars and eight are old cultivars (**Figure 5-1**). They were randomized over 54 plots with a size of 3 × 7-m, a 300-plants/$m^2$ seeding density and a 0.104-m row spacing. The plots were fertilized with either 40 or 80 kg N/ha. Each plot was divided into a 3 × 5-m measuring area and a 3 × 2-m sampling area. Destructive biomass sampling was carried out for two replicas (40 and 80 kg N/ha) of each variety (number of samples (n) = 36). Additionally, the reference plant height ($PH_{ref}$) was measured manually in each plot (n = 10). Ground control points (GCPs) were distributed evenly across the field, making them easily identifiable in the images. The GCPs were made of 0.3 × 0.3-m laminated card board, which was attached to wooden poles that were fixed in the ground. We then measured the position with a differential global positioning system (DGPS, HiPer® Pro Topcon, Tokyo, Japan) with 0.01-m horizontal and vertical precision.
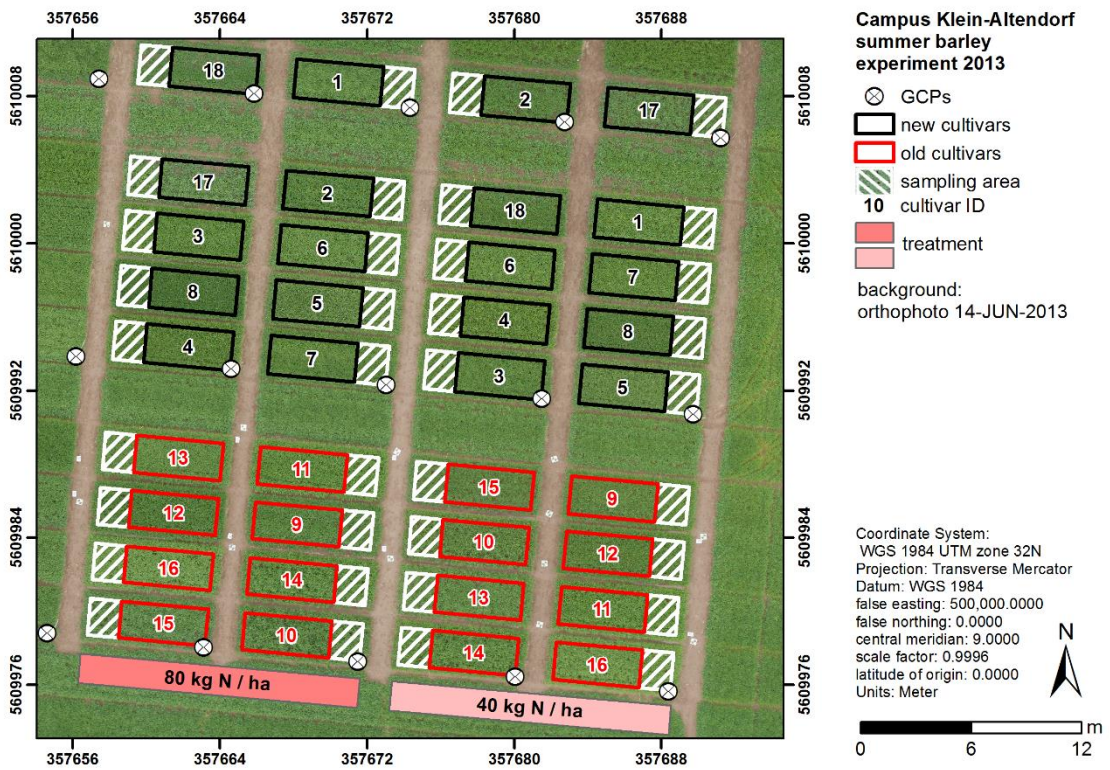
*Figure 5-1: Test site: summer barley experiment at Campus Klein-Altendorf agricultural research station in 2013. GCPs, ground control points used for crop surface model (CSM) generation.*

### 5.2.2 Biomass Sampling

Destructive above-ground biomass sampling of 0.04 m$^2$ was carried out within the sampling areas of each plot (**Figure 5-1**). The roots were clipped, samples were cleaned and stem, leaves and ears were weighed separately on the same day for fresh biomass measurement. For obtaining dry biomass, the samples were then dried at 70 °C for 120 h, and each plant organ was weighed again separately. The values were rescaled to kg per m$^2$. The sampling took place either on the same day or on the day before or after the UAV flights (**Table 5-1**). The biomass sampling area was excluded from the CSM calculation.

*Table 5-1: Details of unmanned aerial vehicle (UAV) flight campaigns (CSM resolution 0.01 m) and destructive biomass sampling.*

| Type | Date | Number of Images Collected | BBCH [1] | Point Density (pt./m²) | Ø Image Overlap [2] |
|---|---|---|---|---|---|
| UAV (ground model) | 30 April 2013 | 216 | | | |
| UAV | 14 May 2013 | 378 | | 2878 | >9 |
| Biomass | 14 May 2013 | | tillering (21–27) | | |
| UAV | 28 May 2013 | 783 | | 2675 | >9 |
| Biomass | 28 May 2013 | | tillering-stem elongation (25–35) | | |
| UAV | 14 June 2013 | 363 | | 2958 | >9 |
| Biomass | 12 June 2013 | | booting (41–47) | | |
| UAV | 25 June 2013 | 300 | | 3452 | >9 |
| Biomass | 25 June 2013 | | inflorescence emergence, heading (51–59) | | |
| UAV | 8 July 2013 | 342 | | 2836 | >9 |
| Biomass | 9 July 2013 | | development of fruit (71–75) | | |
| UAV | 23 July 2013 | 265 | | 2653 | >9 |
| Biomass | 22 July 2013 | | development of fruit-ripening (77–89) | | |

[1] "Biologische Bundesanstalt, Bundessortenamt und CHemische Industrie" (BBCH); [2] the number of images covering the same part of the area of interest (AOI).

## 5.2.3 Platform

In this study, we used the multi-rotor MK-Oktokopter developed by HiSystems (see **BENDIG ET AL.** (**2013**) for details). The payload capacity is 1 kg. The flight duration varies between 5–15 min, depending on the batteries and payload chosen. The red, green, blue (RGB) optical sensor was mounted on a gimbal that maintained a near nadir camera position. The gimbal position is adjusted to the pitch and roll movement that is measured by the onboard gyroscopes of the airframe (**BENDIG ET AL., 2013**; **TURNER ET AL., 2014a**). During the flight, position, altitude and flying speed were automatically logged to a memory card. The MK-tool autopilot was used to set the flight waypoints.

## 5.2.4 Sensor

RGB imagery was collected with a Panasonic Lumix GX1 digital camera (16 Megapixels, 4608 × 3464, with a Lumix G 20 mm (F1.7 aspheric (ASPH)) fixed lens). The angular field of view is 55.8° horizontal × 38.9° vertical, resulting in 0.009-m ground sampling distance (GSD) at 50 m above ground level. A cable connects the camera to the flight control of the MK-Oktokopter, which enables triggering via the remote control. The camera is set to continuous data capture at 2 frames per second (fps) with fixed aperture and exposure according to the light conditions and saves images to a secure digital (SD) memory card.

## 5.2.5 Generating CSMs

Generating crop surface models requires (a) mosaicking of the collected images, (b) point cloud generation, and (c) digital surface model (DSM) export. Here, the DSM represents the crop surface and is referred to as CSM hereafter. It has to be subtracted from a ground model (**Table 5-1**, **Figure 5-2**) in order to obtain (d) the PH. For Steps a–c, we use Agisoft PhotoScan Professional, a structure from motion (SfM) (**VERHOEVEN**, **2011**) software that performs a bundle adjustment based on matching features between the images. The result is a 3D reconstruction of the geometry that enables export of a CSM, in our case, a 0.01-m resolution *TIF-file (**Figure 5-2**; **LUCIEER ET AL.**, **2014**; **TURNER ET AL.**, **2012**). For enhanced absolute spatial accuracy, the GCPs were imported into PhotoScan prior to (b), where they were projected to all images automatically after being placed in a single image (**BAIOCCHI ET AL.**, **2013**). We then manually verified and adjusted the positions if necessary. Finally, the CSM is exported in *TIF-image format.

Further processing was carried out in Esri ArcGIS® 10.2.1. The CSM was clipped with the 36 plots, which form the area of interest (AOI). To account for boundary effects, the plots were reduced by 0.3 m on each end, and the areas where destructive biomass sampling was performed were excluded. In the next step, the CSM is subtracted from the ground model to obtain the PH. The mean PH was calculated for each plot (**Figure 5-2, Table 5-2**) and used for the biomass estimation with a regression model. This process is repeated for the CSM of each date. The workflow for deriving PH from CSMs is described in detail in **BENDIG ET AL.** (**2013**). An example of the ground model and the CSM for two sample dates is presented in **Figure 5-2**, as well as the derived PH.
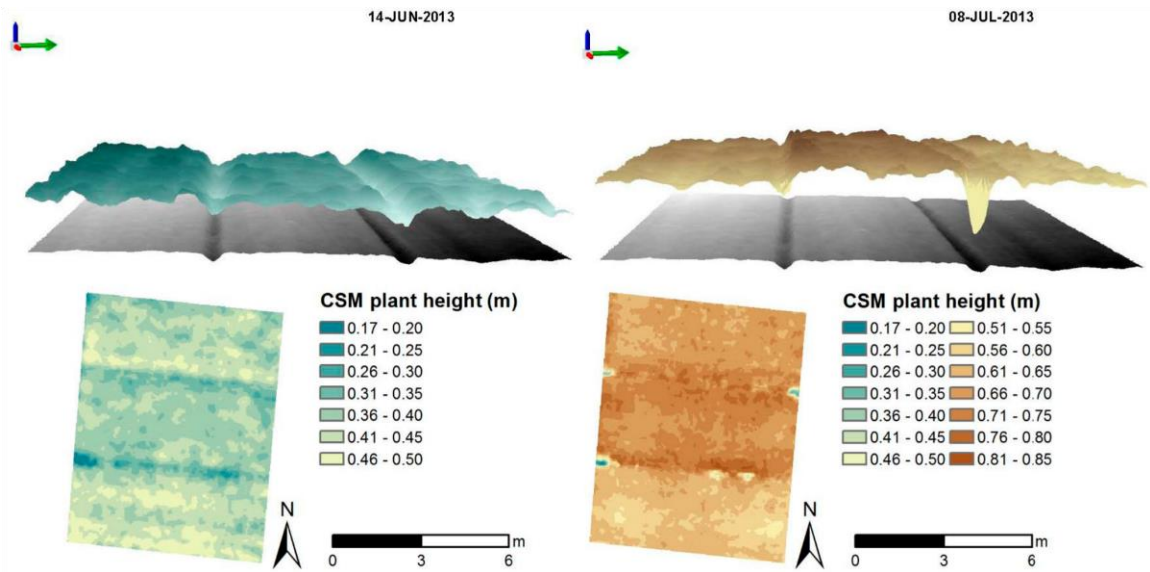
*Figure 5-2: CSM over ground model (top) and derived plant height (bottom) of Plots 8, 7 and 1 (from left to right) of the eastern row of the test site for 14 June and 8 July 2013.*

*Table 5-2: Descriptive statistics of CSM plant height ($PH_{CSM}$), ground reference plant height ($PH_{ref}$) (linear regression) and above-ground fresh and dry biomass (exponential regression) for all plots (n = 216). SE = standard error; n = number of samples.*

|  | $PH_{ref}$ (m) | $PH_{CSM}$ (m) | Fresh Biomass(kg/m²) | Dry Biomass (kg/m²) |
|---|---|---|---|---|
| Min | 0.14 | −0.03 | 0.22 | 0.03 |
| Max | 1.00 | 0.80 | 8.29 | 2.70 |
| Mean | 0.55 | 0.43 | 3.24 | 0.81 |
| SE | 0.25 | 0.25 | 1.96 | 0.68 |
| n | 216 | 216 | 216 | 216 |

## 5.2.6 Statistical Analyses

The correlation and regression analyses were carried out in Microsoft® Excel® 2013 and IBM® SPSS® Statistics 22.0.0.0. The mean PH per plot obtained from the CSM ($PH_{CSM}$) was evaluated against the mean PH obtained from the reference ground measurements ($PH_{ref}$). The result is presented in a scatter plot together with a linear regression equation.

For the biomass estimation, the multi-temporal dataset (n = 216) was divided into five different calibration and validation datasets (**Table 5-3**). Exponential regression equations were derived for $PH_{CSM}$ *versus* fresh biomass and $PH_{CSM}$ *versus* dry biomass for the calibration datasets and evalu-

ated by their coefficient of determination ($R^2$). The resulting regression models from the calibration datasets were applied to the validation datasets and analysed by linear correlation between observed biomass and predicted biomass. The results are compared based on the root mean square error (RMSE), relative error (RE in %) and standard error (SE), which equals the standard deviation (**Table 5-4**).

*Table 5-3: Coefficients of determination ($R^2$) for PH (CSM and ground reference, linear regression) and above-ground fresh and dry biomass (exponential regression) for all plots (n = 216); lin. = linear, exp. = exponential; p < 0.0001 for all $R^2$.*

| $R^2$ | $PH_{ref}$ (m) | $PH_{CSM}$ (m) | Fresh Biomass (kg/m²) | Dry Biomass (kg/m²) |
|---|---|---|---|---|
| $PH_{ref}$ (m) | 1 | | | |
| $PH_{CSM}$ (m) | 0.92 (lin.) | 1 | | |
| fresh biomass (kg/m²) | 0.76 (exp.) | 0.81 (exp.) | 1 | |
| dry biomass (kg/m²) | 0.79 (exp.) | 0.82 (exp.) | 0.67 (lin.) | 1 |

## 5.3 Results

### 5.3.1 Plant Height and Biomass Samples

The test site was flown seven times between 30 April and 23 July 2013, at 50 m above ground level, of which the first dataset served as the non-vegetative ground model. Descriptions of the dataset are given in **Table 5-1**. Destructive biomass sampling was carried out for "Biologische Bundesanstalt, Bundessortenamt und CHemische Industrie" (BBCH) Stages 21–89 that equal the tillering until ripening stage. From 25 June onwards, lodging occurred in the plots with four of the old cultivars (10, 11, 12 and 14 in **Figure 5-1**).

*Table 5-4: Regression characteristics of observed versus predicted biomass. M1: 70% calibration, 30% validation; M2a: model for 40 kg N/m² applied on plots treated with 80 kg N/m²; M2b: model for 80 kg N/m² applied on plots treated with 40 kg N/m²; M3a: model for old cultivars applied on new cultivars; M3b: model of new cultivars applied on old cultivars. n = sample number of validation dataset; SE = standard error; R² = coefficient of determination; with p < 0.0001; RMSE = root mean square error; RE = relative error.*

| Calibration/Validation Dataset | Regression Model | n | SE (kg/m²) | R² | RMSE (kg/m²) | RE (%) |
|---|---|---|---|---|---|---|
| **Fresh Biomass** | | | | | | |
| M1: 70%/30% | BIOM = 0.642 × exp(PH × 3.082) | 66 | 3.21 | 0.71 | 1.95 | 60.87 |
| M2a: 40/80 kg N/m² | BIOM = 0.534 × exp(PH × 3.411) | 108 | 3.46 | 0.61 | 2.35 | 67.72 |
| M2b: 80/40 kg N/m² | BIOM = 0.741 × exp(PH × 2.858) | 108 | 2.97 | 0.71 | 1.60 | 54.04 |
| M3a: old/new cultivars | BIOM = 0.690 × exp(PH × 3.080) | 120 | 3.49 | 0.61 | 2.15 | 61.50 |
| M3b: new/old cultivars | BIOM = 0.591 × exp(PH × 3.135) | 96 | 2.87 | 0.72 | 1.77 | 61.79 |
| **Dry Biomass** | | | | | | |
| M1: 70%/30% | BIOM = 0.073 × exp(PH × 4.309) | 66 | 0.77 | 0.60 | 0.59 | 76.50 |
| M2a: 40/80 kg N/m² | BIOM = 0.057 × exp(PH × 4.922) | 108 | 0.98 | 0.49 | 0.83 | 84.61 |
| M2b: 80/40 kg N/m² | BIOM = 0.083 × exp(PH × 3.960) | 108 | 0.61 | 0.61 | 0.42 | 68.41 |
| M3a: old/new cultivars | BIOM = 0.081 × exp(PH × 4.242) | 120 | 0.67 | 0.39 | 0.54 | 79.88 |
| M3b: new/old cultivars | BIOM = 0.063 × exp(PH × 4.469) | 96 | 0.83 | 0.68 | 0.64 | 76.28 |
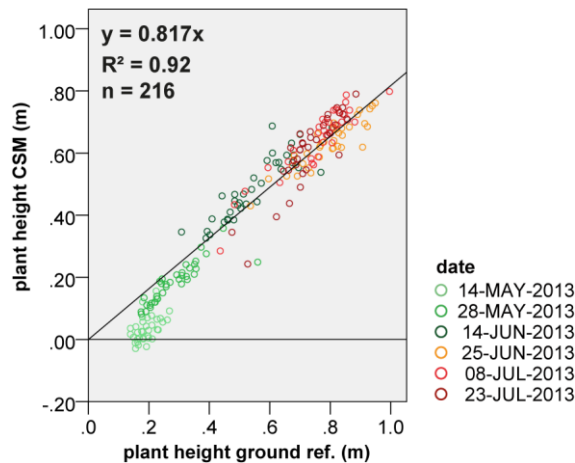


*Figure 5-3: Scatter plot for $PH_{ref}$ and $PH_{CSM}$ for all plots (n = 216). R² = coefficient of determination; p < 0.0001 for all R².*

We compared the PH derived from the CSM ($PH_{CSM}$) to the reference measurements on the ground ($PH_{ref}$) (**Table 5-2**, **Figure 5-3**). In general, $PH_{CSM}$ is about 0.1 m lower than $PH_{ref}$, since the CSM represents the entire relief of the crop surface, not only the highest points of the plants (see the Discussion). The coefficients of determination are classified hereafter as high ($R^2 > 0.7$), medium

(0.5 < $R^2$ < 0.7) and low ($R^2$ < 0.5). A high linear correlation of $R^2$ = 0.92 is observed between $PH_{CSM}$ and $PH_{ref}$ (**Figure 5-3**). The overall standard errors (SEs) are similar for the $PH_{CSM}$ and the $PH_{ref}$ with 0.25 m.

The average fresh (and dry) biomass ranges between 0.2 and 8.3 (0.03 and 2.70) kg/m$^2$ with an SE of 1.96 (0.68) kg/m$^2$. The exponential regression between $PH_{CSM}$ and $PH_{ref}$ and fresh biomass shows a high correlation of $R^2$ = 0.81 and 0.76. The correlation is similar for dry biomass with an $R^2$ of 0.82 and 0.79.

## 5.3.2 Biomass Modelling

### 5.3.2.1 Model Development

In the first step, five exponential regression models between observed fresh and dry biomass and $PH_{CSM}$ were developed and evaluated by their coefficients of determination ($R^2$) (**Figure 5-4**). For Model 1 (M1), the data were split into a 70% calibration and 30% validation dataset by picking a randomized calibration dataset of 25 out of 36 samples for each date. For Models 2a and 2b, the data were split into a calibration dataset of 40 kg N/m$^2$ (M2a) and 80 kg N/m$^2$ (M2b). The calibration dataset for Model 3a (M3a) consists of the old cultivars, and for Model 3b (M3b), it consists of the new cultivars. M1 yielded an $R^2$ of 0.79 for fresh biomass and 0.81 for dry biomass. M2a has a correlation of 0.84 for fresh biomass and 0.87 for dry biomass. For M2b, the correlation is 0.79 for fresh biomass and dry biomass. M3a produced an $R^2$ of 0.78 for fresh and 0.73 for dry biomass and M3b 0.84 and 0.89. Note that all models are based on a different number of samples varying from 96 to 150 according to the experimental design. As we can see from **Figure 5-4**, the values tend to scatter increasingly for the later sampling dates.

### 5.3.2.2 Model Application

In a second step, the derived regression models from the calibration datasets were applied to the validation datasets for all models (M1–M3b) (**Figure 5-5**). The correlation between observed biomass and predicted biomass is displayed in **Table 5-4** and **Figure 5-5**. As we can see, the prediction of fresh biomass had the highest $R^2$ values in the models, M3b (0.72), M2b (0.71) and M1 (0.70). The models M2a and M3a show medium correlations (0.61). In combination with the RMSE, RE and SE error measures, the model M2b performs best (RMSE = 1.6 kg/m$^2$, RE = 54.04%, SE = 2.97). Model M2a fits worst with an RMSE of 2.35 kg/m$^2$, an RE of 67.72% and an SE
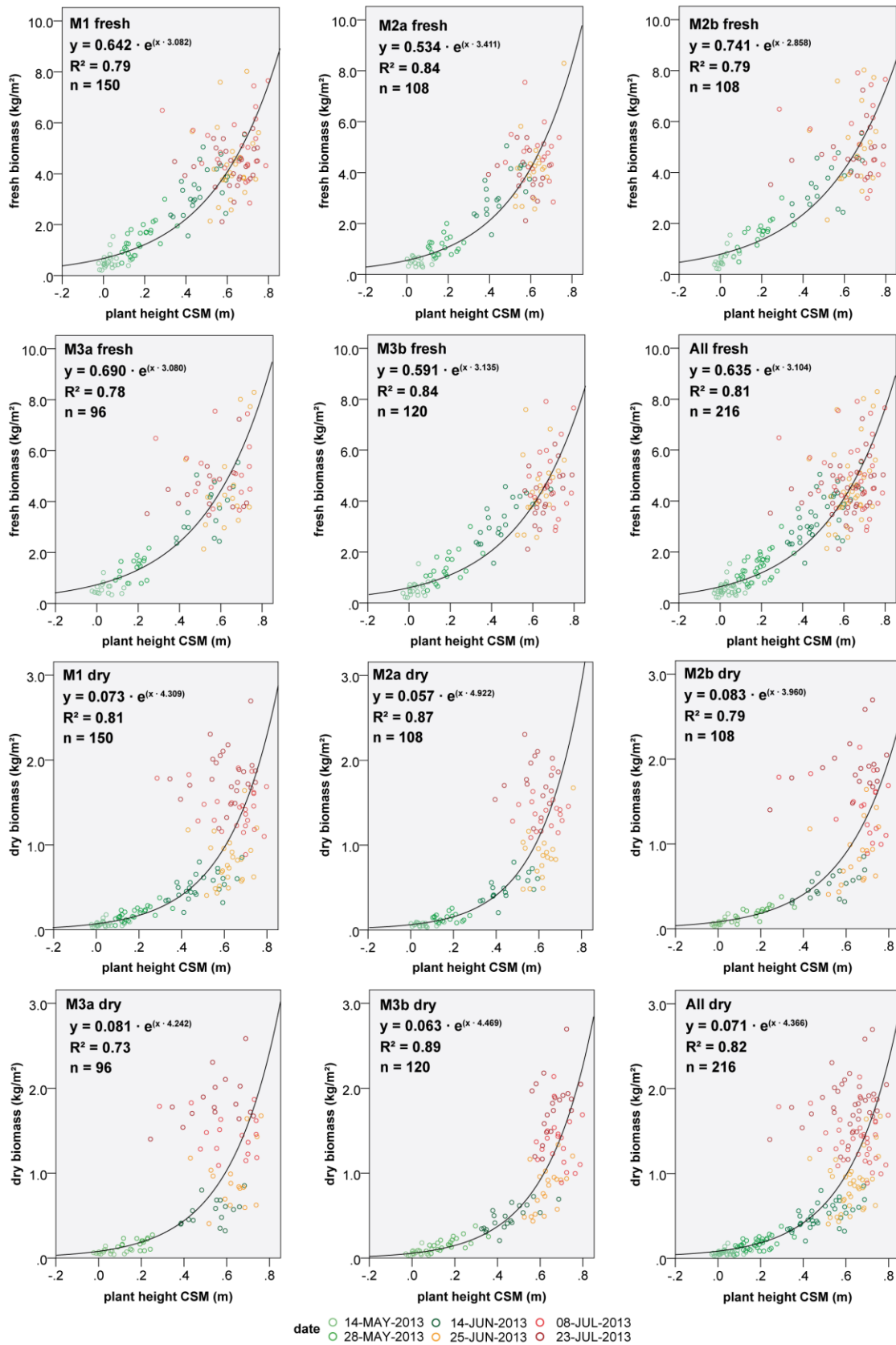
*Figure 5-4: Cross-validation relationship of fresh/dry biomass and CSM$_{PH}$ for calibration datasets. Model 1 (M1): 70%; M2a: 40 kg N/m²; M2b: 80 kg N/m²; M3a: old cultivars; M3b: new cultivars and all values; p < 0.0001 for all R².*
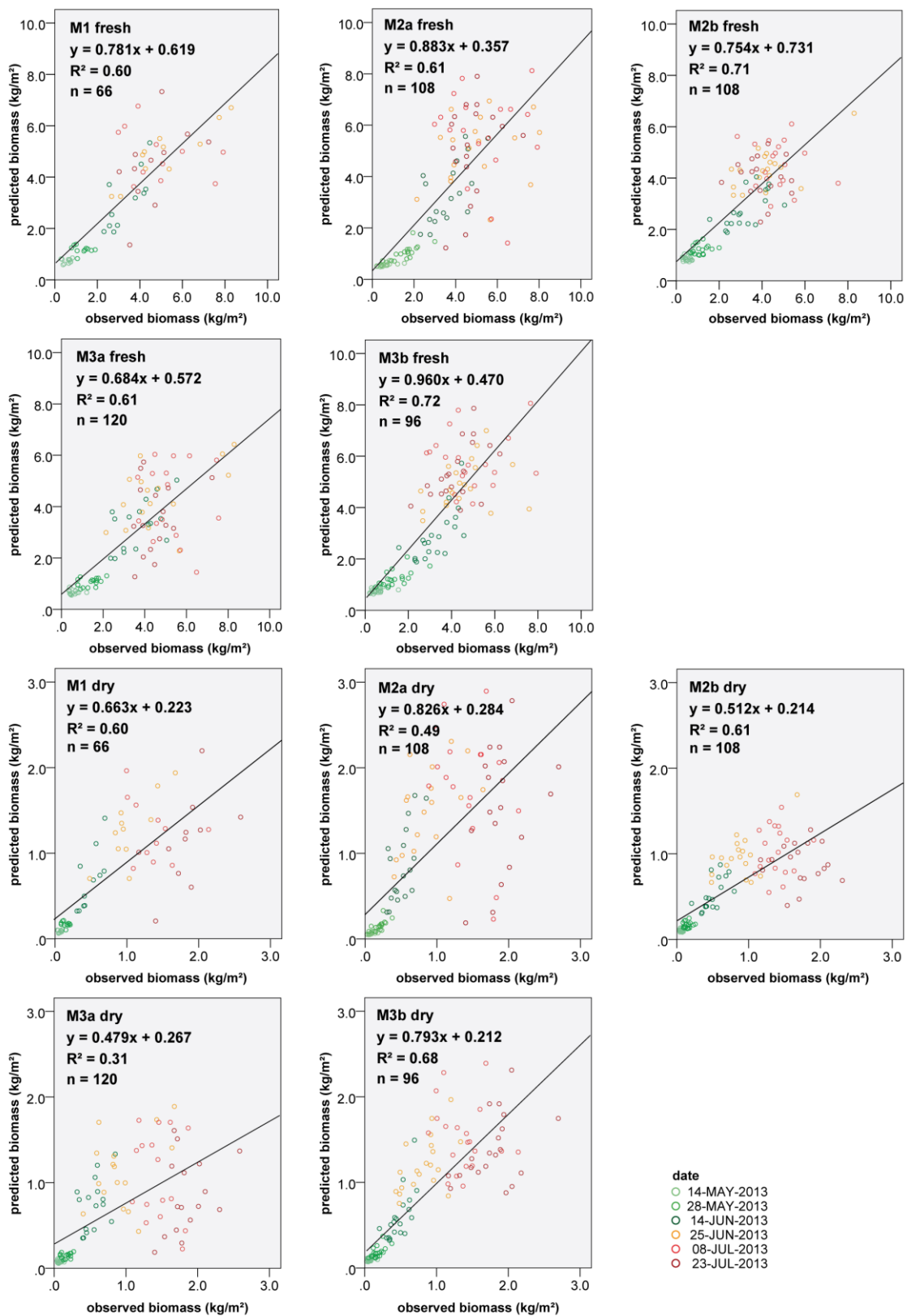
*Figure 5-5: Cross-validation scatter plots for observed fresh and dry biomass versus predicted biomass derived from validation datasets M1–M3b (details in Table 5-4); p < 0.0001 for all R².*

of 3.46 kg/m². Again, the scattering of values increases with progressing vegetation stages. For the dry biomass, M3b, M2b and M1 show a medium $R^2$ (0.68, 0.61 and 0.60), while the other models have a low correlation (0.49, 0.39). The regression characteristics show that M2b fits best to the biomass samples (RMSE = 0.42 kg/m², RE = 68.41%, SE = 0.61), and M2a fits worst (RMSE = 0.83 kg/m², RE = 84.61%, SE = 0.98 kg/m²). The fit for the dry biomass models is 5 to 10% lower than that of the fresh models for each model.

## 5.4 Discussion

The CSM plant height ($PH_{CSM}$) strongly correlates with the reference measurements ($PH_{ref}$) ($R^2$ = 0.92). For comparison, **Ehlert et al.** (**2008**) achieved a coefficient of determination of 0.93–0.99 in oilseed rape, winter rye and winter wheat using a ground-based, non-destructive laser rangefinder. **Busemeyer et al.** (**2013**) state an $R^2$ of 0.97 in triticale using breed vision, a multi-sensor ground-based measuring platform consisting of a laser distance sensor, an ultrasonic sensor, a light curtain and a hyperspectral camera. However, ground-based methods can only be used in the accessible parts of a field and, thus, require interpolation (**Grenzdörffer and Zacharias**, **2014**).

In this study, the $PH_{CSM}$ represents the mean plant height (PH) of all 0.01-m pixels in a plot. As a result, not only the top of the plant, for example the ears, is measured, but also the lower parts, like the leaves. Consequently, the detail of $PH_{CSM}$ is higher than $PH_{ref}$, because $PH_{CSM}$ contains more than one pixel per plant and, thus, not only the maximum height. In this context, the method for the PH reference measurements in the field should be discussed. Manual PH measurement is often subjective when the height is varying in a plot (**Scotford and Miller**, **2004**). The results indicate that measuring 10 randomly chosen single plants does not produce a representative mean of the plot. To solve the problem, a transect could be measured every 0.05 m to better cover the canopy's heterogeneity. Another important factor is the influence of crop movement through wind. From our experience, wind primarily causes a shift in the x-y-direction and does not significantly influence PH measurements. The main constraint of the dataset is the lodging cultivars. A way to mitigate the effect of lodging can be to use the average maximum PH instead of the average mean PH. However, the objective of measuring PH by UAV-based imaging was satisfactorily reached.

CSMs allow spatial variation in PH, plant growth and, accordingly, biomass and yield to be identified. This ability is positive in comparison to point-wise sampling (**Laudien and Bareth**, **2006**), where a high number of samples would be needed to allow for a comparable analysis. Even in

small-scale field studies of <1 ha, the number of samples that can be collected in a manageable amount of time is limited. The number of samples might influence the comparison of point-wise biomass sampling and spatially measured CSM-derived biomass. In this study, the sampling area did not influence the model development, since it was separated from the measuring area.

The regression models for biomass estimation show that all models perform differently. The highest $R^2$ occurs for fresh biomass in M3b ($R^2$ 0.72, RE 61.79%) and M2b ($R^2$ 0.71, RE 54.04%). The model quality for the dry biomass is generally lower, as is reflected in the high relative errors ranging between 68 and 85%. The models' main limiting factors are the four lodging cultivars, 10, 11, 12 and 14. Note that Cultivars 10, 11 12 and 14 belong to the class of old cultivars. The scatter plot in **Figure 5-6** shows the general exponential trend of the non-lodging plots (blue dots) and the scattering lodging plots (red dots). We removed the lodging cultivars from model M1 and achieved an $R^2$ of 0.88 compared to 0.81 for the relationship between dry biomass and $PH_{CSM}$. Similarly, for model validation, $R^2$ increases from 0.60 to 0.64. This observation can explain the big differences between M3a and M3b, where the dataset was divided into old and new cultivars. Therefore, the best performing model, M3b, for fresh biomass is possibly influenced by the lodging effect.
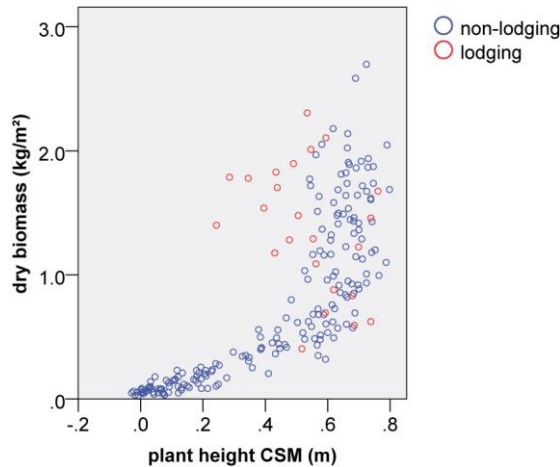


*Figure 5-6: Scatter plot for dry biomass versus CSM_PH: lodging and non-lodging plots; n = 216.*

Comparable results from UAV-based imaging are currently limited to the study by **GRENZDÖRFFER AND ZACHARIAS** (**2014**). They found relationships of 0.6 and 0.76 between PH and yield in a grassland experiment. Most other studies focus on terrestrial laser scanning (TLS). **TILLY ET AL.** (**2014**) estimated biomass with an $R^2$ of 0.90 in a comparison between a field experiment and a farmer's field for paddy rice. In the study by **LUMME ET AL.** (**2008**), a comparison of PH and estimated grain yield in barley, oat and wheat using a laser scanner mounted on a rack led to an $R^2$ between 0.88

and 0.95. The results indicate that TLS yields higher accuracies in biomass estimation. However, the number of samples was slightly lower in the study by **TILLY ET AL. (2014)** (n = 72, n = 90) obtained in a shorter observation period (21 June–19 July 2011) with only three measurements and only three cultivars, as opposed to 18 in this study. **LUMME ET AL. (2008)** used three types of crops with five treatments (n = 15) in six scans during the growing period. Furthermore, no lodging was reported for the comparative studies. Lodging and differences in plant development of the cultivars clearly influence biomass and PH. The results presented here need to be evaluated for field scale studies of multiple years to verify transferability. Several factors, such as water supply and temperature, soil type and status, the type of crop and the phenology, which are commonly considered in crop growth models (**CLEVERS AND JONGSCHAAP, 2001**; **CONFALONIERI ET AL., 2011**), are not investigated here.

Both methods, the UAV-based CSM and the TLS-based CSM, produce highly detailed point clouds. Comparisons of TLS *versus* the UAV-based SfM approach show that competitive results can be achieved for excavation sites (**DONEUS ET AL., 2011**), dike inspection (SE 0.022–0.04 m) (**NAUMANN ET AL., 2014**) and landslides (RMSE 0.31 m) (**NIETHAMMER ET AL., 2012**), although the point density is considerably lower for the UAV-based approach. On the other hand, **HÖFLE (2014)** suggests that occlusion effects of TLS are possibly avoided in the UAV approach. Data collected with UAVs might be less accurate, but UAVs offer the advantage of a fast, inexpensive and highly-flexible data collection method that can easily cover larger areas. Data acquisition of 1 ha takes about 2 h with TLS and 20 min with a UAV, assuming that the allowed time for ground control measurement and data analysis is equal. Purchasing a suitable laser scanner costs about 40,000 €, while a low-cost UAV-system can be bought from 4000 €, including an RGB sensor (Mk-Oktokopter, including autopilot (1500 €), GPS (300 €), battery (200 € each), remote control (MX-20 HoTT; 450 €), gimbal (MK HiSight SLR2; 450 €), sensor (Panasonic Lumix DMC GX1; 460 €) and lens (Panasonic Lumix G F1, 7/20 mm; 365 €) = 3725 €). Since autopilots and automated take-off and landing mechanisms make data acquisition with a UAV feasible without intensive training, they will become directly applicable for a farmer or non-professional service providers (**SWAIN ET AL., 2010**) in the future.

In this study, uncertainties occur both in PH modelling and biomass modelling. The main constraint of the dataset are the lodging cultivars. Lodging causes a lower average PH than expected (**Figure 5-6**) and, thus, weakens the relationship between biomass and PH (*i.e.*, $R^2$ = 0.61 compared to 0.64 for dry biomass M1). In addition, it appears from **Figure 5-4** that scattering increases after PH reaches 0.5 m. This height is reached at the heading stage (**Table 5-1**). The standard error of $PH_{CSM}$

varies between 0.007 and 0.019 m across growth stages and does show an increasing trend. Thus, a reason for the increased scattering is the higher SE in obtained destructively measured biomass. The SE doubles from 0.025 to 0.053 kg/m$^2$ when it reaches the heading stage. Therefore, it seems that growth stages influence the prediction accuracy due to increasing spatial variability. Generally, the robustness of the method must be further investigated, as we only used data from a single experiment in one year.

## 5.5    Conclusions and Outlook

In this study, we introduced a simple method for estimating biomass based on plant height derived from crop surface models. First, it was demonstrated that unmanned aerial vehicle (UAV)-based red, green, blue (RGB) optical images are highly suitable for deriving barley plant height (PH) from multi-temporal crop surface models (CSMs) with a super high resolution of 1 cm on the field scale. The PH can be modelled with a very high accuracy for different growth stages using UAV-based high resolution images (R$^2$ = 0.92). The CSMs cover more details than point-wise ground measurements, where a lower mean PH per plot is obtained.

In the second step, a new method for estimating crop biomass based on PH was tested. Five linear models for estimating above-ground fresh and dry biomass were developed and tested through cross-validation. The models explain 61%–72% of the fresh and 39%–68% of the dry summer barley biomass variability in a controlled field experiment with 18 cultivars and two treatments throughout the vegetation period (May to July, 2013). The coefficients of determination (R$^2$ = 0.31–0.72) demonstrate that PH derived from UAV-based images is a suitable indicator for biomass. The model quality is limited through the lodging of four cultivars and increased biomass scattering after the booting stage. The results presented here need to be evaluated in multiple-year field-scale studies to ensure model robustness and transferability.

Improvements should be made in UAV-based image collection by using an inertial measurement unit (IMU) in combination with a global positioning system (GPS) on the MK-Oktokopter. The combination enables direct georeferencing of the images with cm accuracy. That way, the ground control points can be omitted, which speeds up both the data collection and the data processing. The first studies (ELING ET AL., **2014**, **2013**; PFEIFER ET AL., **2012**; TURNER ET AL., **2014b**) show that this approach is close to operational use (COLOMINA AND MOLINA, **2014**). In a next step, the results from this study will be combined with (hyper-) spectral measurements for the calculation of vegetation indices. Vegetation indices can serve for the estimation of plant parameters, like chlorophyll or

nitrogen concentration (**GNYP ET AL.**, **2014a**; **YU ET AL.**, **2012**). The first results from UAV-based hyperspectral full-frame imaging have been published (**BARETH ET AL.**, **2015**; **HONKAVAARA ET AL.**, **2013**). Furthermore, vegetation indices in the visible domain have potential in crop monitoring (**HUNT JR. ET AL.**, **2013**, **2005**). Ultimately, the analysis of single growth stages should be performed.

## Acknowledgments

## Author Contributions

Simon Bennertz, Janis Broscheit and Silas Eichfuss collected the biomass samples, measured plant height in the field and processed the weight analysis in the laboratory. Simon Bennertz performed BBCH measurements. Juliane Bendig conducted the UAV campaigns, processed the CSMs, executed the biomass modelling and wrote the manuscript. Andreas Bolten assisted in the statistical analysis and the figure design. Georg Bareth provided expertise on biomass modelling and co-prepared the manuscript. Editorial contributions to the manuscript were made by Andreas Bolten and Georg Bareth.

## Conflicts of Interest

The authors declare no conflict of interest.

## References

ADAMCHUK, V.I., FERGUSON, R.B., HERGERT, G.W., **2010**. Soil Heterogeneity and Crop Growth, in: Oerke, E.-C., Gerhards, R., Menz, G., Sikora, R.A. (Eds.), Precision Crop Protection - the Challenge and Use of Heterogeneity. Springer, Dordrecht, Netherlands, pp. 3–16.

AGÜERA, F., CARVAJAL, F., PÉREZ, M., **2011**. Measuring sun-flower nitrogen status from an unmanned aerial vehicle-based system and an on the ground device. ISPRS-International Archives of the Photogrammetry, Remote Sensing and Spatial Information Sciences XXXVIII-1/C22, 33–37.

BAIOCCHI, V., DOMINICI, D., ELAIOPOULOS, M., MASSIMI, V., MORMILE, M., ROSCIANO, E., **2013**. UAV flight plan software: first implementation of UP23d, in: Lasaponara, R., Masini, N., Biscione, M. (Eds.), Proceedings of the 33th EARSeL Symposium Towards Horizon 2020: Earth Observation and Social Perspectives. Presented at the 33th EARSeL Symposium Towards Horizon 2020: Earth Observation and Social Perspectives, Matera, Italy.

BALUJA, J., DIAGO, M.P., BALDA, P., ZORER, R., MEGGIO, F., MORALES, F., TARDAGUILA, J., **2012**. Assessment of vineyard water status variability by thermal and multispectral imagery using an unmanned aerial vehicle (UAV). Irrigation Science 6, 511–522.

BARETH, G., BENDIG, J., AASEN, H., GNYP, M.L., BOLTEN, A., JUNG, A., MICHELS, R., SOUKKAMÄKI, J., **2015**. Low-weight and UAV-based hyperspectral full-frame cameras for monitoring crops: spectral comparison with portable spectroradiometer measurements. Photogrammetrie - Fernerkundung - Geoinformation accepted.

BENDIG, J., BOLTEN, A., BARETH, G., **2013**. UAV-based Imaging for Multi-Temporal, very high Resolution Crop Surface Models to monitor Crop Growth Variability. Photogrammetrie - Fernerkundung - Geoinformation 6, 551–562. doi:10.1127/1432-8364/2013/0200

BERNI, J.A.J., ZARCO-TEJADA, P.J., SUÁREZ, L., GONZÁLEZ-DUGO, V., FERERES, E., **2009b**. Remote sensing of vegetation from UAV platforms using lightweight multispectral and thermal imaging sensors. International Archives of Photogrammetry, Remote Sensing and Spatial Information Sciences 38, 6.

BUSEMEYER, L., MENTRUP, D., MÖLLER, K., WUNDER, E., ALHEIT, K., HAHN, V., MAURER, H.P., REIF, J.C., WÜRSCHUM, T., MÜLLER, J., RAHE, F., RUCKELSHAUSEN, A., **2013**. BreedVision - A Multi-Sensor Platform for Non-Destructive Field-Based Phenotyping in Plant Breeding. Sensors 13, 2830–2847. doi:10.3390/s130302830

CHEN, P., HABOUDANE, D., TREMBLAY, N., WANG, J., VIGNEAULT, P., LI, B., **2010**. New spectral indicator assessing the efficiency of crop nitrogen treatment in corn and wheat. Remote Sensing of Environment 114, 1987–1997. doi:10.1016/j.rse.2010.04.006

CLEVERS, J.P.G.W., JONGSCHAAP, R., **2001**. Imaging Spectrometry For Agricultural Applications, in: Meer, F.D. van der, Jong, S.M.D. (Eds.), Imaging Spectrometry, Remote Sensing and Digital Image Processing. Kluwer Academic Publishers, Dordrecht, Netherlands, pp. 157–199.

COLOMINA, I., MOLINA, P., **2014**. Unmanned aerial systems for photogrammetry and remote sensing: A review. ISPRS Journal of Photogrammetry and Remote Sensing 92, 79–97. doi:10.1016/j.isprsjprs.2014.02.013

CONFALONIERI, R., BREGAGLIO, S., ROSENMUND, A.S., ACUTIS, M., SAVIN, I., **2011**. A model for simulating the height of rice plants. European Journal of Agronomy 34, 20–25. doi:10.1016/j.eja.2010.09.003

DONEUS, M., VERHOEVEN, G., FERA, M., BRIESE, C., KUCERA, M., NEUBAUER, W., **2011**. From deposit to point cloud: a study of low-cost computer vision approaches for the straightforward documentation of archaeological excavations, in: Pavelka, K. (Ed.), Proceedings of the XXIIIrd International CIPA Symposium. Presented at the XXIIIrd International CIPA Symposium, Prague, Czech Republic, pp. 81–88.

EHLERT, D., ADAMEK, R., HORN, H.-J., **2009**. Laser rangefinder-based measuring of crop biomass under field conditions. Precision Agriculture 10, 395–408. doi:10.1007/s11119-009-9114-4

EHLERT, D., HORN, H.-J., ADAMEK, R., **2008**. Measuring crop biomass density by laser triangulation. Computers and Electronics in Agriculture 61, 117–125. doi:10.1016/j.compag.2007.09.013

ELING, C., KLINGBEIL, L., WIELAND, M., KUHLMANN, H., **2013**. A precise position and attitude determination system for lighweight unmanned aerial vehicles. International Archives of Photogrammetry, Remote Sensing and Spatial Information Sciences XL-1/W2, 113–118. doi:10.5194/isprsarchives-XL-1-W2-113-2013

ELING, C., KLINGBEIL, L., WIELAND, M., KUHLMANN, H., **2014**. Direct Georeferencing of Micro Aerial Vehicles – System Design, System Calibration and First Evaluation Tests. Photogrammetrie - Fernerkundung - Geoinformation 4, 227–237. doi:10.1127/1432-8364/2014/0200

GNYP, M.L., BARETH, G., LI, F., LENZ-WIEDEMANN, V.I.S., KOPPE, W., MIAO, Y., HENNIG, S.D., JIA, L., LAUDIEN, R., CHEN, X., ZHANG, F., **2014a**. Development and implementation of a multiscale biomass model using hyperspectral vegetation indices for winter wheat in the North China Plain. International Journal of Applied Earth Observation and Geoinformation 33, 232–242. doi:10.1016/j.jag.2014.05.006

GOYNE, P.J., MEINKE, H., MILROY, S.P., HAMMER, G.L., HARE, J.M., **1996**. Development and use of a barley crop simulation model to evaluate production management strategies in north-eastern Australia. Crop and Pasture Science 47, 997–1015.

GRENZDÖRFFER, G., ZACHARIAS, P., **2014**. Bestandeshöhenermittlung landwirtschaftlicher Kulturen aus UAS-Punktwolken, in: Proceedings of the 34. Wissenschaftlich-Technische Jahrestagung Der DGPF. Presented at the DGPF Tagung, Hamburg, Germany, p. 8.

HOFFMEISTER, D., BOLTEN, A., CURDT, C., WALDHOFF, G., BARETH, G., **2010**. High-resolution Crop Surface Models (CSM) and Crop Volume Models (CVM) on field level by terrestrial laser scanning, in: Guo, H., Wang, C. (Eds.), SPIE Proceedings of the Sixth International Symposium on Digital Earth: Models, Algorithms, and Virtual Reality. Presented at the Sixth International Symposium on Digital Earth: Models, Algorithms, and Virtual Reality, Beijing, China, p. 78400E–78400E–6. doi:10.1117/12.872315

HOFFMEISTER, D., CURDT, C., TILLY, N., BENDIG, J., BARETH, G., **2011b**. 3D change detection of different sugar-beet types by multi-temporal terrestrial laser scanning, in: Proceeding of: Int. Symposium on Remote Sensing and GIS Methods for Change Detection and Spatio-Temporal Modelling (CDSM). Presented at the Int. Symposium on remote sensing and GIS methods for change detection and spatio-temporal modelling (CDSM), Hong Kong, China, p. 5.

HOFFMEISTER, D., WALDHOFF, G., CURDT, C., TILLY, N., BENDIG, J., BARETH, G., **2013**. Spatial variability detection of crop height in a single field by terrestrial laser scanning, in: Stafford, J.V. (Ed.), Precision Agriculture '13. Presented at the 9th European Conference on Precision Agriculture, Wageningen Academic Publishers, Lleida, Spain, pp. 267–274.

HÖFLE, B., **2014**. Radiometric Correction of Terrestrial LiDAR Point Cloud Data for Individual Maize Plant Detection. IEEE Geoscience and Remote Sensing Letters 1, 94–98. doi:10.1109/LGRS.2013.2247022

HONKAVAARA, E., SAARI, H., KAIVOSOJA, J., PÖLÖNEN, I., HAKALA, T., LITKEY, P., MÄKYNEN, J., PESONEN, L., **2013**. Processing and Assessment of Spectrometric, Stereoscopic Imagery Collected Using a Lightweight UAV Spectral Camera for Precision Agriculture. Remote Sensing 5, 5006–5039. doi:10.3390/rs5105006

HOYOS-VILLEGAS, V., FRITSCHI, F.B., **2013**. Relationships Among Vegetation Indices Derived from Aerial Photographs and Soybean Growth and Yield. Crop Science 53, 2631–2642. doi:10.2135/cropsci2013.02.0126

HUNT, E.R., HIVELY, W.D., MCCARTY, G.W., DAUGHTRY, C.S.T., FORRESTAL, P.J., KRATOCHVIL, R.J., CARR, J.L., ALLEN, N.F., FOX-RABINOVITZ, J.R., MILLER, C.D., **2011**. NIR-Green-Blue High-Resolution Digital

Images for Assessment of Winter Cover Crop Biomass. GIScience & Remote Sensing 48, 86–98. doi:10.2747/1548-1603.48.1.86

HUNT JR., E.R., CAVIGELLI, M., DAUGHTRY, C.S.T., MCMURTREY III, J.E., WALTHALL, C.L., **2005**. Evaluation of Digital Photography from Model Aircraft for Remote Sensing of Crop Biomass and Nitrogen Status. Precision Agriculture 6, 359–378. doi:10.1007/s11119-005-2324-5

HUNT JR., E.R., DORAISWAMY, P.C., MCMURTREY, J.E., DAUGHTRY, C.S.T., PERRY, E.M., AKHMEDOV, B., **2013**. A visible band index for remote sensing leaf chlorophyll content at the canopy scale. International Journal of Applied Earth Observation and Geoinformation 21, 103–112. doi:10.1016/j.jag.2012.07.020

JANG, G.-S., SUDDUTH, K.A., HONG, S.Y., KITCHEN, N.R., PALM, H.L., **2006**. Relating hyperspectral image bands and vegetation indices to corn and soybean yield. Korean Journal of Remote Sensing 22, 183–197.

JENSEN, A., LORENZEN, B., ØSTERGAARD, H.S., HVELPLUND, E.K., **1990**. Radiometric estimation of biomass and nitrogen content of barley grown at different nitrogen levels. International Journal of Remote Sensing 11, 1809–1820. doi:10.1080/01431169008955131

JENSEN, T., APAN, A., YOUNG, F., ZELLER, L., **2007**. Detecting the attributes of a wheat crop using digital imagery acquired from a low-altitude platform. Computers and Electronics in Agriculture 59, 66–77. doi:10.1016/j.compag.2007.05.004

KOPPE, W., GNYP, M.L., HENNIG, S.D., LI, F., MIAO, Y., CHEN, X., JIA, L., BARETH, G., **2012**. Multi-Temporal Hyperspectral and Radar Remote Sensing for Estimating Winter Wheat Biomass in the North China Plain. Photogrammetrie - Fernerkundung - Geoinformation 3, 281–298. doi:10.1127/1432-8364/2012/0117

KUMAR, L., SCHMIDT, K., DURY, S., SKIDMORE, A., **2001**. Imaging Spectrometry and Vegetation Science, in: Meer, F.D. van der, Jong, S.M.D. (Eds.), Imaging Spectrometry, Remote Sensing and Digital Image Processing. Kluwer Academic Publishers, Dordrecht, Netherlands, pp. 111–155.

LATI, R.N., FILIN, S., EIZENBERG, H., **2013a**. Estimating plant growth parameters using an energy minimization-based stereovision model. Computers and Electronics in Agriculture 98, 260–271. doi:10.1016/j.compag.2013.07.012

LAUDIEN, R., BARETH, G., **2006**. Multitemporal Hyperspectral Data Analysis for Regional Detection of Plant Diseases by using a Tractor- and an Airborne-based Spectrometer. Photogrammetrie - Fernerkundung - Geoinformation 3, 217–227.

LEMAIRE, G., GASTAL, F., **1997**. N Uptake and Distribution in Plant Canopies, in: Lemaire, D.G. (Ed.), Diagnosis of the Nitrogen Status in Crops. Springer, Berlin, Germany, pp. 3–43.

LEMAIRE, G., JEUFFROY, M.-H., GASTAL, F., **2008**. Diagnosis tool for plant and crop N status in vegetative stage. European Journal of Agronomy 28, 614–624. doi:10.1016/j.eja.2008.01.005

LI, F., MIAO, Y., HENNIG, S.D., GNYP, M.L., CHEN, X., JIA, L., BARETH, G., **2010b**. Evaluating hyperspectral vegetation indices for estimating nitrogen concentration of winter wheat at different growth stages. Precision Agriculture 11, 335–357. doi:10.1007/s11119-010-9165-6

LUCIEER, A., TURNER, D., KING, D.H., ROBINSON, S.A., **2014**. Using an Unmanned Aerial Vehicle (UAV) to capture micro-topography of Antarctic moss beds. International Journal of Applied Earth Observation and Geoinformation 27, 53–62. doi:10.1016/j.jag.2013.05.011

LUMME, J., KARJALAINEN, M., KAARTINEN, H., KUKKO, A., HYYPPÄ, J., HYYPPÄ, H., JAAKKOLA, A., KLEEMOLA, J., **2008**. Terrestrial laser scanning of agricultural crops. The International Archives of the Photogrammetry, Remote Sensing and Spatial Information Sciences 37, 563–566.

MIGDALL, S., BACH, H., BOBERT, J., WEHRHAN, M., MAUSER, W., **2009**. Inversion of a canopy reflectance model using hyperspectral imagery for monitoring wheat growth and estimating yield. Precision Agriculture 10, 508–524. doi:10.1007/s11119-009-9104-6

MULLA, D.J., **2013**. Twenty five years of remote sensing in precision agriculture: Key advances and remaining knowledge gaps. Biosystems Engineering 114, 358–371. doi:10.1016/j.biosystemseng.2012.08.009

NAUMANN, M., BILL, R., NIEMEYER, F., NITSCHKE, E., **2014**. Deformation analysis of dikes using Unmanned Aerial Systems (UAS), in: Proceedings of the South Baltic Conference on Dredged Materials in Dike Construction. Presented at the South Baltic Conference on Dredged Materials in Dike Construction, Rostock, Germany, pp. 119–126.

NIETHAMMER, U., JAMES, M.R., ROTHMUND, S., TRAVELLETTI, J., JOSWIG, M., **2012**. UAV-based remote sensing of the Super-Sauze landslide: Evaluation and results. Engineering Geology 128, 2–11. doi:10.1016/j.enggeo.2011.03.012

PFEIFER, N., GLIRA, P., BRIESE, C., **2012**. Direct georeferencing with on board navigation components of light weight UAV platforms, in: Proceedings of the XXII ISPRS Congress. Technical Commission VII. ISPRS. Presented at the XXII ISPRS Congress, Melbourne, Australia, pp. 487–492.

SAKAMOTO, T., GITELSON, A.A., NGUY-ROBERTSON, A.L., ARKEBAUER, T.J., WARDLOW, B.D., SUYKER, A.E., VERMA, S.B., SHIBAYAMA, M., **2012**. An alternative method using digital cameras for continuous monitoring of crop status. Agricultural and Forest Meteorology 154-155, 113–126. doi:10.1016/j.agrformet.2011.10.014

SCOTFORD, I.M., MILLER, P.C.H., **2004**. Combination of Spectral Reflectance and Ultrasonic Sensing to monitor the Growth of Winter Wheat. Biosystems Engineering 87, 27–38. doi:10.1016/j.biosystemseng.2003.09.009

SHANAHAN, J.F., SCHEPERS, J.S., FRANCIS, D.D., VARVEL, G.E., WILHELM, W.W., TRINGE, J.M., SCHLEMMER, M.R., MAJOR, D.J., **2001**. Use of remote-sensing imagery to estimate corn grain yield. Agronomy Journal 93, 583–589. doi:10.2134/agronj2001.933583x

SWAIN, K.C., THOMSON, S.J., JAYASURIYA, H.P.W., **2010**. Adoption of an unmanned helicopter for low-altitude remote sensing to estimate yield and total biomass of a rice crop. Transactions of the ASAE 53, 21.

THENKABAIL, P.S., SMITH, R.B., DE PAUW, E., **2000**. Hyperspectral vegetation indices and their relationships with agricultural crop characteristics. Remote sensing of Environment 71, 158–182. doi:10.1016/S0034-4257(99)00067-X

TILLY, N., HOFFMEISTER, D., CAO, Q., HUANG, S., LENZ-WIEDEMANN, V.I.S., MIAO, Y., BARETH, G., **2014**. Multitemporal crop surface models: accurate plant height measurement and biomass estimation with terrestrial laser scanning in paddy rice. Journal of Applied Remote Sensing 8, 083671–083671. doi:10.1117/1.JRS.8.083671

TILLY, N., HOFFMEISTER, D., LIANG, H., CAO, Q., LIU, Y., LENZ-WIEDEMANN, V., MIAO, Y., BARETH, G., **2012**. Evaluation of terrestrial laser scanning for rice growth monitoring. International Archives of the Photogrammetry, Remote Sensing and Spatial Information Science XXXIX-B7, 351–356.

TURNER, D., LUCIEER, A., MALENOVSKÝ, Z., KING, D., ROBINSON, S., **2014a**. Spatial Co-Registration of Ultra-High Resolution Visible, Multispectral and Thermal Images Acquired with a Micro-UAV over Antarctic Moss Beds. Remote Sensing 6, 4003–4024. doi:10.3390/rs6054003

TURNER, D., LUCIEER, A., WALLACE, L., **2014b**. Direct Georeferencing of Ultrahigh-Resolution UAV Imagery. IEEE Transactions on Geoscience and Remote Sensing 52, 2738–2745. doi:10.1109/TGRS.2013.2265295

TURNER, D., LUCIEER, A., WATSON, C., **2012**. An Automated Technique for Generating Georectified Mosaics from Ultra-High Resolution Unmanned Aerial Vehicle (UAV) Imagery, Based on Structure from Motion (SfM) Point Clouds. Remote Sensing 4, 1392–1410. doi:10.3390/rs4051392

VERHOEVEN, G., **2011**. Taking computer vision aloft - archaeological three-dimensional reconstructions from aerial photographs with photoscan. Archaeological Prospection 18, 67–73. doi:10.1002/arp.399

YANG, C., EVERITT, J.H., BRADFORD, J.M., **2008**. Yield estimation from hyperspectral imagery using spectral angle mapper (SAM). Transactions of the ASABE 51, 729–737.

YU, K., LENZ-WIEDEMANN, V., LEUFEN, G., HUNSCHE, M., NOGA, G., CHEN, X., BARETH, G., **2012**. Assessing hyperspectral vegetation indices for estimating leaf chlorophyll concentration of summer barley. ISPRS Ann. Photogramm. Remote Sens. Spat. Inf. Sci 1-7, 89–94.

ZARCO-TEJADA, P.J., **2008**. A new era in remote sensing of crops with unmanned robots. SPIE Newsroom 2–4. doi:10.1117/2.1200812.1438

# 6 Combining UAV-based Crop Surface Models, Visible and Near Infrared Vegetation Indices for Biomass Monitoring in Barley

JULIANE BENDIG [1,*], KANG YU [1], HELGE AASEN [1], ANDREAS BOLTEN [1], SIMON BENNERTZ [1], JANIS BROSCHEIT [1],
MARTIN L. GNYP [1,2,3], GEORG BARETH [1,3]

Submitted in: International Journal of Earth Observation and Geoinformation

Original manuscript is embedded in dissertation format.

1   Institute of Geography, GIS & RS Group, University of Cologne, Albertus-Magnus-Platz, 50923
    Cologne

2   Research Centre Hanninghof, Yara International ASA, Hanninghof 35, 48249 Dülmen, Germany

3   ICASD-International Center for Agro-Informatics and Sustainable Development,
    www.icasd.org

*   Corresponding author, Tel.: +49-221-470-6551; Fax: +49-221-470-4917

E-Mail: juliane.bendig@uni-koeln.de

**Abstract:** In this study we combined selected vegetation indices (VIs) and plant height information to estimate biomass in a summer barley experiment. The VIs were calculated from ground-based hyperspectral data and unmanned aerial vehicle (UAV)-based red-green-blue (RGB) imaging. In addition, the plant height information was obtained from UAV-based multi-temporal crop surface models (CSMs). The test site is a summer barley experiment comprising 18 cultivars and two nitrogen treatments located in Western Germany. We calculated five VIs from hyperspectral data, of which the GnyLi showed the highest correlation ($R^2$=0.83) with dry biomass. In addition, we calculated three visible band VIs: the Green Red Vegetation Index (GRVI), the modified GRVI (MGRVI) and the Red-Green-Blue VI (RGBVI), whereas the MGRVI and the RGBVI are newly developed VI. We found that the visible band VIs have potential for biomass prediction prior to heading stage. A robust estimate for biomass was obtained from the plant height models ($R^2$=0.80-0.82). In a cross validation test, we compared plant height, selected VIs and their combination with plant height information. Combining VIs and plant height information by using multiple linear regression or multiple non-linear regression models performed better than the VIs alone. However, only in

two cases the relationship was stronger than for the plant height alone. All visible band VIs produced varying results both in the model development and in the model application. Especially the performance of the GRVI and the newly developed RGBVI should be further investigated. In summary, the results indicate that plant height is competitive with VIs for biomass estimation in summer barley. Moreover, visible band VIs might be a useful addition to biomass estimation. The main limitation is that the visible band VIs work for early growing stages only. There should be more studies examining these simple and cost effective methods to provide improved applicability.

**Keywords:** vegetation indices; visible; UAV; remote sensing; biomass estimation; crop surface model

## 6.1   Introduction

It is a well-known fact that biomass estimation is crucial for yield prediction of crops (OERKE ET AL., 2010). Crop parameters, like biomass, are frequently used to assess crop health status, nutrient supply and effects of agricultural management practices (ADAMCHUK ET AL., 2010). For management optimization, the nitrogen nutrition index (NNI) plays a key role (CHEN ET AL., 2010; TREMBLAY ET AL., 2011). Biomass is needed for calculating the NNI (LEMAIRE AND GASTAL, 1997). A well-established method for biomass estimation is the calculation of vegetation indices (VIs) in the near-infrared region (NIR) (QI ET AL., 1994; ROUSE ET AL., 1974), here defined as the range between 700 and 1300 nm (KUMAR ET AL., 2001). Field spectroradiometers are commonly used for the collection of hyperspectral reflectance data that are used for such calculations (CLEVERS AND JONGSCHAAP, 2001; KUMAR ET AL., 2001; ROYO AND VILLEGAS, 2011). An alternative possibility is to model biomass using plant height information. LUMME ET AL. (2008) and TILLY ET AL. (2014) demonstrated the suitability of the method in wheat, oat, barley and paddy rice. Plant height information is most useful when it is available at high spatial and temporal resolution. The method of multi-temporal crop surface models (CSMs) derived from 3D point clouds delivers the desired high resolution. The method was studied for different crops by HOFFMEISTER ET AL. (2013, 2010) for sugar beet, TILLY ET AL. (2014) for paddy rice and BENDIG ET AL. (2014a, 2013) for summer barley. For small fields of a few hectares, suitable data collection platforms can be ground-based like terrestrial laser scanners (HOFFMEISTER ET AL., 2013; KRAUS, 2004; TILLY ET AL., 2014) or airborne like unmanned aerial vehicles (UAVs) (BENDIG ET AL., 2014a, 2013). Through the availability of high resolution consumer digital cameras, red-green-blue (RGB) aerial imaging with cm-resolution can easily be obtained using UAVs (D' OLEIRE-OLTMANNS ET AL., 2012; LUCIEER ET AL., 2014; NEITZEL AND KLONOWSKI, 2011). At the same time, the emergence of structure from motion (SfM)-based software (DANDOIS AND ELLIS,

**2010**; **Verhoeven**, **2011**) speeded up data processing for 3D point clouds and super high detail orthophotos. Visible band VIs (VI$_{VIS}$) may be calculated from the orthophotos as demonstrated by **Hunt et al.** (**2014**; **2005**). **Motohka et al.** (**2010**) use RGB-imagery obtained from a tower. However, such studies are rarely done for small-scale field trials. Near-infrared VIs (VI$_{NIR}$) are more widely used because of the deviation between red and NIR reflection in green vegetation (**Bannari et al.**, **1995**). In addition, smaller, but significant spectral differences in the visible bands exist, caused by biochemical plant constituents such as chlorophyll (**Hatfield et al.**, **2008**; **Roberts et al.**, **2011**). Consequently, it is worthwhile investigating if VI$_{VIS}$ can compete with VI$_{NIR}$ at biomass estimation. Furthermore, the VI$_{VIS}$ and the plant height information can be obtained from the same dataset suggesting to combine both parameters to possibly improve biomass estimation. According to **Koppe et al.** (**2013**), a combination of parameters can improve the model quality of biomass prediction. Similarly, this approach can be transferred to this study. In this paper we shall investigate the possibilities of using VI$_{NIR}$ calculated from hyperspectral reflectance data and VI$_{VIS}$ calculated from non-calibrated RGB images in combination with CSM-based plant height information.

## 6.2 Materials and Methods

### 6.2.1 Test Site

The study site is based at the Campus Klein-Altendorf agricultural research station (50°37′N, 6°59′E, altitude 186 m), located 40 km south of Cologne, Germany. In 2013, 18 summer barley (*hordeum vulgare*) cultivars were planted, of which 10 were new cultivars and eight are old cultivars (**Figure 6-1**, **Bendig et al.**, **2014a**). They were treated with two levels of nitrogen fertilizer (40 and 80 kg N/ha). The experiment is organized in 54 (we used 36) small 3×7 m plots with a randomised order of the cultivars. Seedlings were planted with 300 plants/m² and a row spacing of 0,104 m. In addition, the plots are divided into a 3×5 m measuring area for PH and reflectance measurements and a 3×2 m sampling area for destructive biomass sampling. Biomass samples were taken frequently from April to July in 36 of the plots. For the UAV image collection, ground control points (GCPs) were evenly distributed across the field (**Figure 6-1**). The positions were taken using a HiPer® Pro Topcon DGPS (Topcon Corporation, Tokyo, Japan) with 0.01 m horizontal and vertical precision. Later, the GCPs were identified in the images and used for georeferencing.
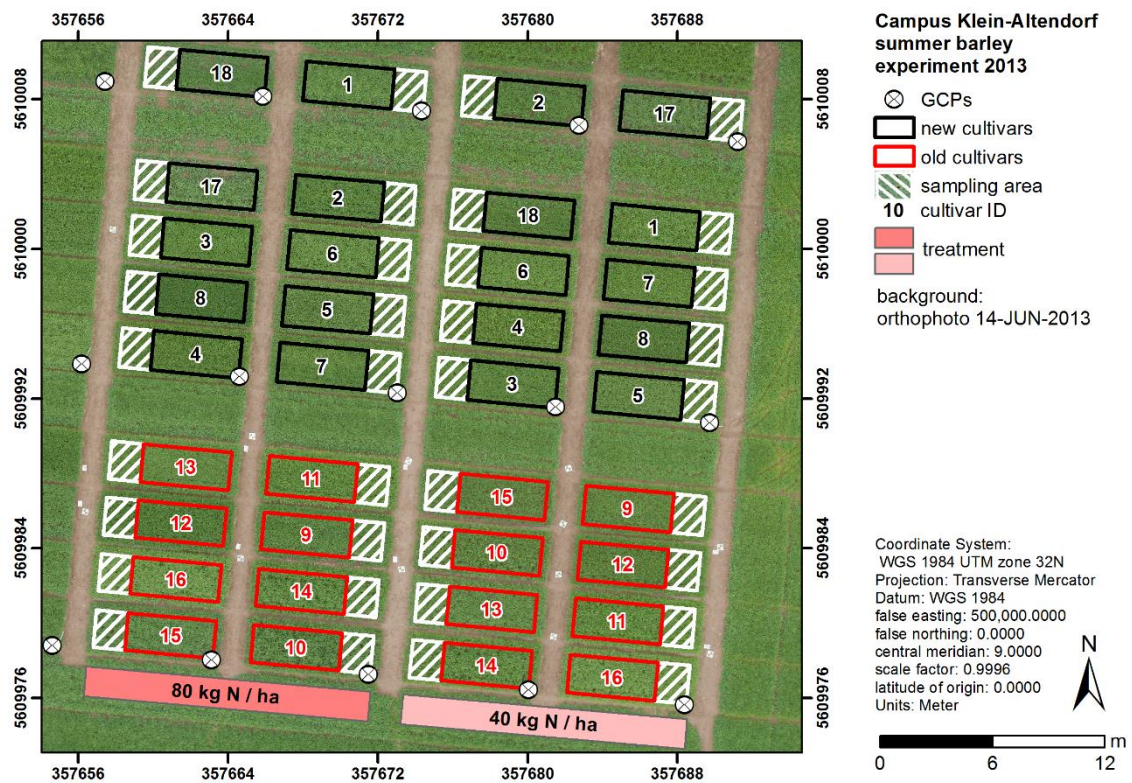
*Figure 6-1: Test site: summer barley experiment at Campus Klein-Altendorf agricultural research station in 2013 (BENDIG ET AL., 2014a); GCPs = ground control points used for crop surface model (CSM) generation.*

### 6.2.2 Biomass Sampling and BBCH Measurements

A destructive sample of 0.2×0.2 m above ground biomass was taken in the sampling area for each date (**Figure 6-1**). The sampling dates were within one day before or after the UAV campaigns and the field spectroradiometer measurements. For the fresh biomass, the samples were cleaned, the roots were clipped and stem, leaves and ears were weighed. In a next step, the samples were dried at 70°C for 120 h and dry biomass is weighed again for each plant organ. The weights are extrapolated to kg/m² for analysis. Plant growth stages were determined according to the "Biologische Bundesanstalt, Bundessortenamt und CHemische Industrie" (BBCH) scale (**LANCASHIRE ET AL., 1991**) along with PH measurements. Three plant representatives for the crop stand were chosen for each plot.

### 6.2.3 UAV-based Data Collection

The UAV used in this study is a multi-rotor MK-Oktokopter by HiSystems GmBH (**BENDIG ET AL., 2013**). It is equipped with an RGB-sensor, a 16 Megapixel Panasonic Lumix GX1 (F1.7 aspheric

(ASPH) fixed 20 mm lens) digital camera that is attached to the UAV on a gimbal. The gimbal compensates for the UAV movement (pitch and roll) during the flight and guarantees close to nadir image collection (**BENDIG ET AL., 2014a**). To trigger the sensor, we used the UAV's remote control. Images are captured at 2 frames per second (fps) with the camera set to a fixed aperture and exposure time at 50 m above ground level (AGL). An autopilot was used for waypoint navigation to achieve the desired coverage of the AOI. On 30 April 2013, a non-vegetation ground model was recorded in a flight. Data from six flights (15 May, 28 May, 14 June, 25 June, 08 July and 23 July) were used for the plant height derived from the CSM (PH$_{CSM}$).

## 6.2.4  Field Spectroradiometer Measurements

Barley canopy reflectance was sensed with an ASD FieldSpec3 spectroradiometer (Analytical Spectral Devices, Inc., Boulder, CO, USA). The FieldSpec3 is a passive field device that is dependent on solar or artificial illumination. The spectroradiometer acquired the reflectance in the wavelength domain of 350-2500 nm with three detectors, one for the visible near-infrared (VNIR: 350-1000 nm) and two for shortwave-infrared (SWIR1: 1001-1830 nm, SWIR2: 1831-2500 nm). Each detector is equipped with 19 silica glass fibres. The FieldSpec3 has a 1.4 nm sampling interval in the VNIR and 2 nm sampling interval in the SWIR. For continuous measurements of the same footprint, the spectroradiometer's fibre probe was fixed on an orthogonal construction with a 1 m sensor-canopy distance (d) (**LAUDIEN AND BARETH, 2006**), and the same field of view of 25° (a) was used. Hence, the acquisition geometry is described by (d) and (a), resulting in a 0.155 m² sample area with a 44 cm diameter at the barley canopy surface. The hyperspectral data were automatically subdivided into 1 nm narrow band using a self-driven method of the ASD.

Reflectance measurements were taken between 11 a.m. and 2 p.m. local mean time under solar illumination at the study site. Calibration measurements were carried out with a Spectralon (polytetrafluoroethylene (PTFE)) reference panel (white colour) and a dark current at least every 10-15 minutes, depending on illumination changes. In the ASD RS3 software, twenty sample counts were set for a calibration and ten samples counts for the reflectance measures at each scanning position of the barley canopy. Within one experimental plot, six scanning positions with representative plant growth were selected randomly and the six reflectance measurements were averaged to one value.

### 6.2.5 Plant Height generation from CSM

In a first step, the collected images were mosaiced in the structure from motion (SfM)-based software Agisoft PhotoScan Professional (**Verhoeven, 2011**). For georeferencing the mosaic, the GCP positions were imported and projected to the images after once placed on one image (**Lucieer et al., 2014**). Additionally, the positions are checked and adjusted manually. The software uses matching features in the images to perform a bundle adjustment and the point cloud generation (**Sona et al., 2014**). Finally, a digital surface model in *TIF image format is exported, which contains the crop surface model (CSM) information at a 0.01 m resolution. In addition, orthophotos are generated using the software's 'mosaicing blending mode'. In this mode, the software uses the pixel value of the most appropriate photo, in the case of overlapping photos, to calculate the orthophoto (**Agisoft LLC, 2014**). The orthophoto is then exported in *TIF image format at 0.01 m resolution for the $VI_{VIS}$ calculations.

For the derivation of the $PH_{CSM}$, we used the workflow in Esri ArcGIS® 10.2.1 described in **Bendig et al.** (**2013**). An area of interest (AOI) is defined by the outline of the measuring area of the plots, which is buffered by a 0.3 m inside buffer to exclude the plot boundaries and the sampling area. To get information of the PH, each CSM (for each date) was subtracted from a non-vegetation ground model (**Bendig et al., 2014a**). In a last step, the mean $PH_{CSM}$ for each plot was averaged for each date.

### 6.2.6 Vegetation Indices

#### 6.2.6.1 Near-Infrared Vegetation Indices

In this study we examined the correlation of different near-infrared vegetation indices ($VI_{NIR}$) which are reported to be well correlated with biomass or leaf area index (LAI) (**Thenkabail et al., 2000**). These are the normalized difference vegetation index (NDVI), the soil adjusted vegetation index (SAVI), modified SAVI (MSAVI) and optimized SAVI (OSAVI) (**Table 6-1**). The NDVI (**Rouse et al., 1974**) is the most popular VI (**Pettorelli, 2013**) but its applicability is limited by atmospheric influences, soil reflectance in the spectra and saturation with the occurrence of high biomass values in later growth stages (**Carlson and Ripley, 1997**; **Haboudane, 2004**). The SAVI (**Huete, 1988**), MSAVI (**Qi et al., 1994**) and OSAVI (**Rondeaux et al., 1996**) are based on the NDVI but include correction factors for the soil reflection in the spectra. In addition, we calculated the GnyLi (**Gnyp et al., 2014a**) that is based on the normalised ratio index (NRI) equation (**Thenkabail et al., 2000**). The GnyLi exploits the difference of two reflection and absorption features around 900 and

1200 nm. The reflection peak at 900 nm is caused by the intercellular plant structure, while the reflection minimum between 970 and 1200 nm is affected by plant moisture, cellulose, starch and lignin (**CURRAN**, **1989**; **PU ET AL.**, **2003**). In contrast to NDVI, SAVI, MSAVI and OSAVI, the GnyLi is calculated from narrow bands in the NIR domain only.

*Table 6-1: Near-infrared vegetation indices ($VI_{NIR}$) used in this study where R = reflectance (%), $R_R$ = red (630-690 nm), $R_{NIR}$ = near-infrared (700-1300 nm), $R_i$ = reflectance in a narrow band e.g. $R_{1220}$ = 1220 nm, L = constant (Huete, 1988)*

| VI | Name | Formula | References |
|---|---|---|---|
| NDVI | Normalized Difference Vegetation Index | $$\dfrac{R_{NIR} - R_R}{R_{NIR} + R_R}$$ | (ROUSE ET AL., 1974) |
| SAVI | Soil Adjusted Vegetation Index | $$(1 + L)x\dfrac{R_{800} - R_{670}}{R_{800} + R_{670} + L}$$ | (HUETE, 1988) |
| MSAVI | Modified SAVI | $$0.5\left(2R_{800}{+}1{-}\sqrt{(2xR_{800}{+}1)^2{-}8(R_{800}{-}R_{670})}\right)$$ | (QI ET AL., 1994) |
| OSAVI | Optimized Soil-Adjusted Vegetation Index | $$(1 + 0.16)x\dfrac{R_{800} - R_{670}}{R_{800} + R_{670} + 0.16}$$ | (RONDEAUX ET AL., 1996) |
| GnyLi | Named by the developers Gnyp and Li | $$\dfrac{R_{900}xR_{1050} - R_{955}xR_{1220}}{R_{900}xR_{1050} + R_{955}xR_{1220}}$$ | (GNYP ET AL., 2014a) |

### 6.2.6.2 Visible Band Vegetation Indices

Three $VI_{VIS}$ were calculated from the orthophotos (**Table 6-2**) based on the NDVI equation (**MOTOHKA ET AL.**, **2010**; **TUCKER**, **1979**). The green red vegetation index (GRVI) (**TUCKER**, **1979**) is used as a phenology indicator and has potential for biomass estimation (**CHANG ET AL.**, **2005**; **HUNT JR. ET AL.**, **2005**). Advantageous is the exploitation of the high reflection of plants in the green (around 540 nm) and the absorption in the red and blue part of the visible spectrum (400-700 nm) through plant chlorophylls (**GAO**, **2006**; **GITELSON ET AL.**, **2002**; **MOTOHKA ET AL.**, **2010**). Squaring the reflectance helps to amplify the differences between red, green and blue reflectance. Based on these assumptions, we developed two new VIs. The modified GRVI (MGRVI) is defined as the normalized difference of the squared green reflectance and the squared red reflectance. To capture reflec-

tance differences due to chlorophyll a-absorption (420, 490 and 660 nm) and chlorophyll b-absorption (435, 643 nm) (**KUMAR ET AL., 2001**), we further introduced the new Red-Green-Blue Vegetation Index (RGBVI). The RGBVI is defined as the normalized difference of the squared green reflectance and the product of blue×red reflectance (**Table 6-2**).

*Table 6-2: Visible band vegetation indices (VI$_{VIS}$) used in this study where R = reflectance (%), R$_R$ = red, R$_G$ = green, R$_B$ = blue. Red, Green and Blue are the DN in the respective channels extracted from the orthophotos.*

| VI | Name | Formula | References |
|---|---|---|---|
| GRVI | Green Red Vegetation Index | $\dfrac{R_G - R_R}{R_G + R_R}$ | (**TUCKER, 1979**) |
| MGRVI | Modified Green Red Vegetation Index | $\dfrac{(R_G)^2 - (R_R)^2}{(R_G)^2 + (R_R)^2}$ | introduced here |
| RGBVI | Red Green Blue Vegetation Index | $\dfrac{(R_G)^2 - (R_B * R_R)}{(R_G)^2 + (R_B * R_R)}$ | introduced here |

To calculate the VI$_{VIS}$ we processed the above mentioned orthophotos in Esri ArcGIS® 10.2.1 by using the program's ModelBuilder. We extracted the extract digital numbers (DN) for each band (red, green and blue) by converting the *.TIF files to float files (*.FLT) (**Figure 6-2**). The equations in **Table 6-2** served as input to the raster calculator that was used to calculate the VI$_{VIS}$. To obtain the mean for each plot, we used the command 'zonal statistics as table'. We repeated the process for each VI$_{VIS}$ and each orthophoto by employing an iterator.
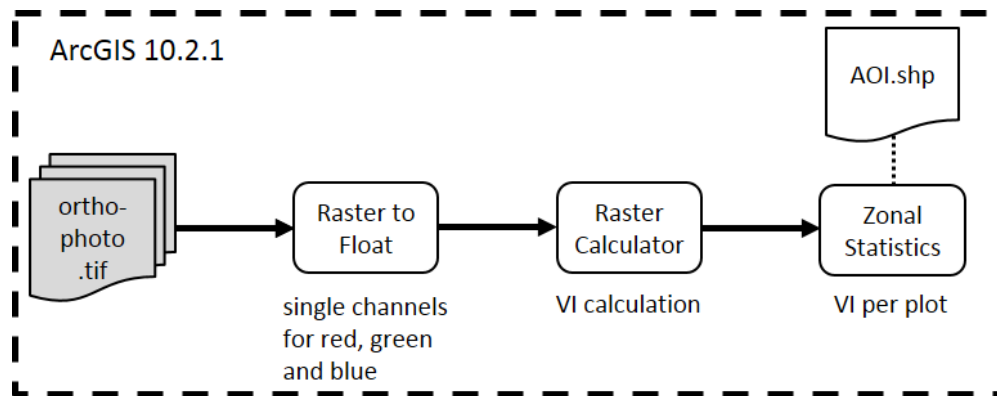


*Figure 6-2: Workflow for VI$_{VIS}$ calculation. (AOI = old and new cultivars in Table 6-2).*

### 6.2.7 Statistical Analyses

The statistical analyses were executed in Microsoft® Excel® 2013 and IBM® SPSS® Statistics 22.0.0.0. Depending on the growth stages, we calculated a simple linear regression or exponential regression (**HANSEN AND SCHJOERRING, 2003**) for dry biomass and the VIs and PH$_{CSM}$ (**Table 6-3**). To

investigate the influence of combing VIs and $PH_{CSM}$ we computed a multiple linear regression
(MLR) was calculated in addition. Previous studies have shown that the relationships between the
biomass and VIs or PH are often nonlinear (**THENKABAIL ET AL., 2000**). Therefore, a multiple non-
linear regression (MNLR) model was employed additionally to estimate the biomass. The nonlin-
ear model is a quadratic regression model (**BERTHOLD AND HAND, 2006**) using two variables and it
takes the form of the following equation (**Equation 6-1**),

$$y = \beta_0 + \beta_1 x_{PH} + \beta_2 x_{VI} + \beta_3 x_{PH} x_{VI} + \beta_4 x_{PH}^2 + \beta_5 x_{VI}^2 \ \textbf{(6-1)}$$

where y is the biomass, and $x_{PH}$ and $x_{VI}$ are the $PH_{CSM}$ and VI values, respectively. The model coef-
ficients ($\beta_0,…,\beta_5$) were determined for the nonlinear regression model based on the calibration
dataset. All processes of the nonlinear model were implemented in the SPSS software package.

## 6.3    Results

### 6.3.1    Plant Height and Biomass Samples

On each flight date between 200 and 800 photos of the field were taken, resulting in a point den-
sity between 2653 and 3452 (pt./m²) and a mean of >9 images covering the same part of the AOI.
To cover the AOI, we undertook two consecutive flights with an average 5 min flight time per flight
on each date around 9 a.m. local mean time (2 p.m. on 14 July). Lighting conditions were homo-
geneous for all flights except 25th June. On 25th June, the lighting conditions changed between
flight one and flight two. We excluded images from the second flight to maintain radiation homo-
geneity. From 25 June onwards, lodging occurred in the plots with cultivars 10, 11, 12 and 14
(**Figure 6-1**, details in (**BENDIG ET AL., 2014a**)), resulting in lower PH and reflection changes in the
affected plots. The average measured $PH_{CSM}$ varies between 0.14 to 1.00 m with a standard error
(SE) of 0.25 m. The biomass samples of plots 7 and 46 on 08 July were identified as erroneous and
therefore excluded from further analysis. The averaged dry biomass ranges from 0.03 to 2.70
kg/m² with a SE of 0.68 kg/m².

### 6.3.2    Biomass Modelling

#### 6.3.2.1   Model Development

Biomass modelling was carried out from 15 May until 08 July 2013 ('all data'). On 23 July, the
ripening crop substantially yellowed (BBCH Stages 77-89) and was thus unsuitable for biomass
estimation from VIs. The results presented below are divided into 'all data' (n = 178) and 'pre
heading' (n = 108), with 'pre heading' covering 15 May until 16 June 2013, due to significantly

changing performance of the $VI_{VIS}$ with the beginning of the heading stage. The general relationship between dry biomass and the VIs or the $PH_{CSM}$ has an exponential trend in the 'all data' class and a linear trend in the 'pre heading' class.

The coefficients of determination ($R^2$) for the exponential regression (ER) and linear regression (LR) between the $PH_{CSM}$ and dry biomass and VIs and dry biomass are presented in **Table 6-3**. We classified $R^2$ in high (> 0.7), medium (0.5 <$R^2$< 0.7) and low (<0.5) correlation. In the ER 'all data' class, high correlations were found between $PH_{CSM}$ ($R^2$ = 0.85) and the GnyLi ($R^2$ = 0.83). All other combinations yielded medium correlations (SAVI, MSAVI and OSAVI, $R^2$ = 0.54-0.6) or low correlations (NDVI, GRVI, MGRVI, RGBVI, $R^2$ = 0.12-0.41). In the LR of 'pre heading' growth stages we found a high correlation between dry biomass and $PH_{CSM}$ ($R^2$ = 0.85) and GnyLi ($R^2$ = 0.71). All other relationships were medium (SAVI, MSAVI, GRVI, MGRVI, $R^2$ = 0.51-0.62) or low (NDVI, RGBVI, $R^2$ = 0.39-0.47).

*Table 6-3: Coefficient of determination ($R^2$) and root mean square error (RMSE) for regression between dry biomass and either CSM derived plant height ($PH_{CSM}$) or near-infrared ($VI_{NIR}$) or visible band ($VI_{VIS}$) vegetation indices where n = number of samples; ER = exponential regression and LR = linear regression.*

| VI/PH$_{CSM}$ *versus* dry biomass | | exponential regression (ER) | | | | linear regression (LR) | | | |
|---|---|---|---|---|---|---|---|---|---|
| | | all data n = 178 | | pre heading n = 108 | | all data n = 178 | | pre heading n = 108 | |
| | | $R^2$ | RMSE (kg/m²) | $R^2$ | RMSE (kg/m²) | $R^2$ | RMSE (kg/m²) | $R^2$ | RMSE (kg/m²) |
| PH$_{CSM}$ | | 0.85 | 0.324 | 0.81 | 0.112 | 0.65 | 0.311 | 0.85 | 0.083 |
| VI$_{NIR}$ | GnyLi | 0.83 | 0.350 | 0.76 | 0.119 | 0.62 | 0.326 | 0.71 | 0.113 |
| | NDVI | 0.40 | 0.515 | 0.61 | 0.162 | 0.16 | 0.484 | 0.39 | 0.164 |
| | SAVI | 0.59 | 0.468 | 0.70 | 0.144 | 0.30 | 0.441 | 0.51 | 0.147 |
| | MSAVI | 0.60 | 0.466 | 0.70 | 0.144 | 0.32 | 0.437 | 0.52 | 0.146 |
| | OSAVI | 0.54 | 0.481 | 0.68 | 0.148 | 0.25 | 0.457 | 0.47 | 0.153 |
| VI$_{VIS}$ | GRVI | 0.13 | 0.596 | 0.79 | 0.117 | 0.00 | 0.528 | 0.62 | 0.130 |
| | MGRVI | 0.13 | 0.596 | 0.79 | 0.117 | 0.00 | 0.528 | 0.61 | 0.131 |
| | RGBVI | 0.41 | 0.439 | 0.67 | 0.156 | 0.33 | 0.434 | 0.47 | 0.153 |

### 6.3.2.2 Model Application

Based on the results from **Table 6-3**, $PH_{CSM}$, GnyLi, MSAVI, GRVI and RGBVI were selected for model application. The dataset was divided into a calibration and validation dataset. The validation dataset consisted of the randomly selected cultivars 1, 6, 13 and 18 (two old and two new cultivars), while the remaining cultivars served for the calibration. We developed exponential regression and multiple non-linear regression (MNLR) models for the 'all data' class and linear regression and multiple linear regression (MLR) models for the 'pre heading' class. The calibration

models (**Table 6-4**) were then applied to the validation datasets and evaluated by the relation between observed and predicted biomass (**Figure 6-3**, **Figure 6-4**).

*Table 6-4: Cross-validation relationships between observed and predicted biomass (kg/m²) for selected vegetation indices, PH$_{CSM}$ respectively and combinations of both; ER = exponential regression; MLR = multiple linear regression, LR = linear regression; MNLR = multiple non-linear regression; n = number of samples; SE = standard error; R² = coefficient of determination; RMSE = root mean square error; RE = relative error.*

| observed *versus* predicted biomass | | | regression model | n | SE (kg/m²) | R² | RMSE (kg/m²) | RE (%) |
|---|---|---|---|---|---|---|---|---|
| All data | ER | PH$_{CSM}$ | BIOM = 0.070×exp(PH$_{CSM}$×4.155) | 40 | 0.56 | 0.80 | 0.24 | 44.61 |
| | | GnyLi | BIOM = 0.025×exp(GnyLi×11.757) | 40 | 0.52 | 0.65 | 0.30 | 56.45 |
| | | MSAVI | BIOM = 0.001×exp(MSAVI×6.436) | 40 | 0.40 | 0.22 | 0.46 | 86.84 |
| | | GRVI | BIOM = 0.187×exp(GRVI×5.594) | 40 | 0.39 | 0.00 | 0.53 | 99.87 |
| | | RGBVI | BIOM = 0.062×exp(RGBVI×3.553) | 40 | 0.47 | 0.59 | 0.32 | 61.18 |
| | MNLR | GnyLi+PH$_{CSM}$ | BIOM = 0.073+(1.206×PH$_{CSM}$)+(-2.678×GnyLi) +(-11.109×(PH$_{CSM}$×GnyLi)) +(2.743×PH$_{CSM}$²)+(21.811×GnyLi²) | 40 | 0.59 | 0.74 | 0.26 | 48.86 |
| | | MSAVI+PH$_{CSM}$ | BIOM = 1.321+(4.243×PH$_{CSM}$)+(-3.910×MSAVI) +(-4.403×(PH$_{CSM}$× MSAVI)) +(2.050×PH$_{CSM}$²)+(2.865×MSAVI²) | 40 | 0.60 | 0.77 | 0.25 | 47.87 |
| | | GRVI+PH$_{CSM}$ | BIOM = 0.052+(3.146×PH$_{CSM}$)+(-2.229×GRVI) +(-3.172×(PH$_{CSM}$×GRVI)) +(-1.200× PH$_{CSM}$²)+(1.439×GRVI²) | 40 | 0.58 | 0.74 | 0.26 | 49.10 |
| | | RGBVI+PH$_{CSM}$ | BIOM = 0.404+(1.664×PH$_{CSM}$)+(-2.332×RGBVI) +(0.275×(PH$_{CSM}$×RGBVI)) +(-0.285× PH$_{CSM}$²)+(2.508×RGBVI²) | 40 | 0.61 | 0.84 | 0.21 | 40.69 |
| Pre heading | LR | PH$_{CSM}$ | BIOM=1.009×PH+0.018 | 24 | 0.22 | 0.81 | 0.09 | 45.01 |
| | | GnyLi | BIOM=2.651×GnyLi-0.196 | 24 | 0.24 | 0.74 | 0.10 | 51.30 |
| | | MSAVI | BIOM=1.074×MSAVI-0.651 | 24 | 0.23 | 0.72 | 0.11 | 55.34 |
| | | GRVI | BIOM=2.240×GRVI-0.032 | 24 | 0.24 | 0.76 | 0.10 | 54.22 |
| | | RGBVI | BIOM=0.878×RGBVI-0.140 | 24 | 0.23 | 0.64 | 0.10 | 53.21 |
| | MLR | GnyLi+PH$_{CSM}$ | BIOM =0.909×PH$_{CSM}$+0.324×GnyLi-0.014 | 24 | 0.22 | 0.82 | 0.09 | 44.43 |
| | | MSAVI+PH$_{CSM}$ | BIOM =1.139×PH$_{CSM}$-0.220×MSAVI+0.174 | 24 | 0.22 | 0.78 | 0.09 | 44.24 |
| | | GRVI+PH$_{CSM}$ | BIOM =1.077×PH$_{CSM}$-0.206×GRVI+0.029 | 24 | 0.22 | 0.79 | 0.09 | 45.01 |
| | | RGBVI+PH$_{CSM}$ | BIOM =1.111×PH$_{CSM}$-0.158×RGBVI+0.067 | 24 | 0.22 | 0.78 | 0.09 | 45.79 |
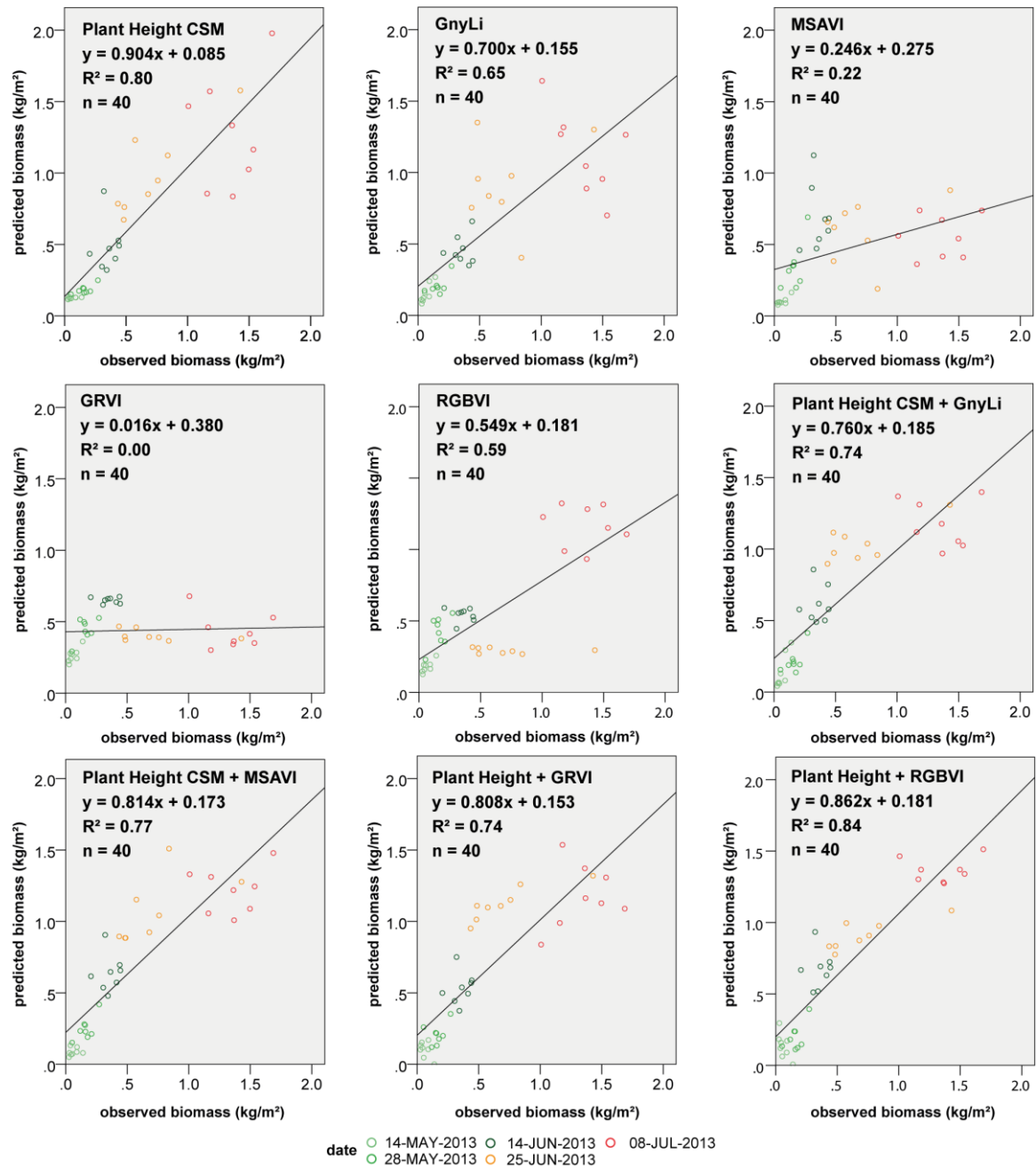
*Figure 6-3: 'All data' class cross-validation scatter plots for observed dry biomass versus predicted biomass derived
from validation datasets listed in Table 6-4; p < 0.0001 for all R².*
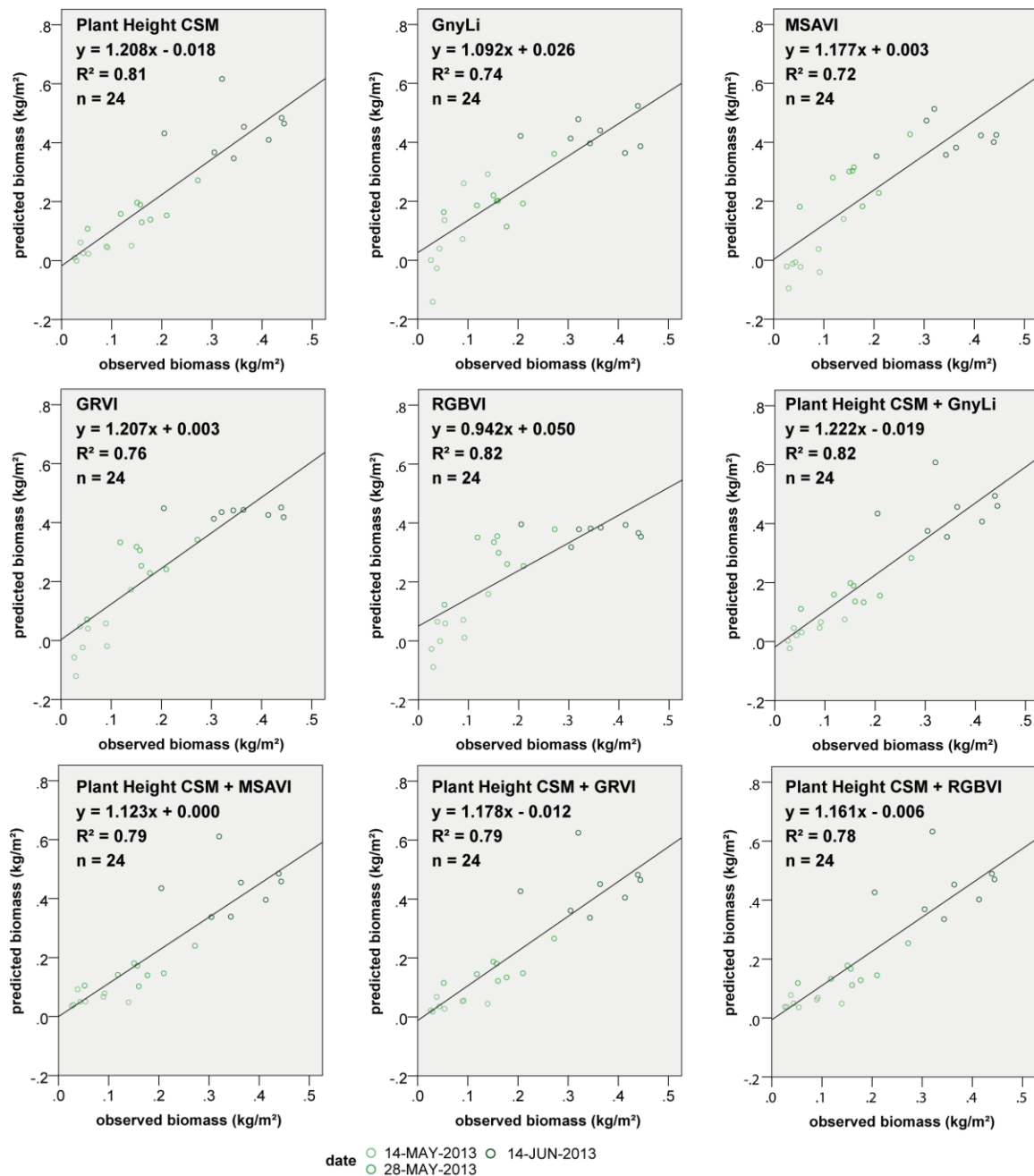
*Figure 6-4: 'Pre heading' class cross-validation scatter plots for observed dry biomass versus predicted biomass derived from validation datasets listed in Table 6-4; p < 0.0001 for all R².*

In the 'all data' class (**Figure 6-3**), the $PH_{CSM}$ model had a high fit with $R^2$ = 0.80 and a low relative error (RE) of 44.61%. Comparably high fits were found for the MNLR model combinations of GnyLi+$PH_{CSM}$ ($R^2$ = 0.74, RE = 48.86%) and MSAVI+$PH_{CSM}$ ($R^2$ = 0.77, RE = 47.86%) and RGBVI+$PH_{CSM}$ ($R^2$ = 0.84, RE = 40.69%). Correlations in the 'pre heading' dataset (**Figure 6-4**) were all above 0.64 with RE under 55.34%. The highest fit occurred for the GnyLi+$PH_{CSM}$ MLR model ($R^2$ = 0.82, RE = 44.43%).

## 6.4 Discussion

The primary aim of this study is to evaluate UAV-based RGB imaging and two of its products: the plant height (PH) and $VI_{VIS}$. Both are available at cm-resolution. We compared the performance in biomass estimation of PH, $VI_{VIS}$, high spectral resolution $VI_{NIR}$ from point measurements, and the combination of the VIs with PH. It appears from the results in **Table 6-3** and **Table 6-4** that CSM-derived plant height ($PH_{CSM}$) and GnyLi are the most robust parameters for biomass estimation in summer barley, while $PH_{CSM}$ performs slightly better than GnyLi. In addition, combinations of $PH_{CSM}$ with $VI_{VIS}$ or $VI_{NIR}$ performed better than the VIs alone. In early growth stages, only the combination of GnyLi+$PH_{CSM}$ ($R^2 = 0.82$) yielded a slightly higher $R^2$ than the $PH_{CSM}$ ($R^2 = 0.81$). Although, the RGBVI+$PH_{CSM}$ produces a higher $R^2$ than the $PH_{CSM}$ across all growth stages, this result should be regarded with caution. The performances of the $VI_{VIS}$ vary significantly between model development and model application. Thus, strong relationships in model applications might be produced randomly. Generally, the statistically more complex MLR and MNLR produce robust results, but a more significant effect was expected. Positive examples for combining remotely sensed information from different sources are found in the literature (KOPPE ET AL., **2013**; LIU ET AL., **2006**). Most studies comparable to this one either investigate the relationship between PH and biomass (EHLERT ET AL., **2008**; LUMME ET AL., **2008**) or the relationship between VIs and biomass (HUNT JR. ET AL., **2005**; MOTOHKA ET AL., **2010**; TUCKER, **1979**). GEIPEL ET AL. (**2014**) investigated yield prediction from UAV-based CSMs and $VI_{VIS}$ for early growth stages in maize. They found a slightly higher correlation between yield and $PH_{CSM}$ in combination with one of three tested $VI_{VIS}$.

Of the $VI_{NIR}$ investigated here, the GnyLi clearly outperformed the NDVI-based indices. This result is consistent with a multi-scale study for winter wheat, where the GnyLi outperformed 14 other indices (GNYP ET AL., **2014a**). The NDVI-based indices perform lower, due to the well-known saturation effect. Similar results are reported by (BARET AND GUYOT, **1991**; GNYP ET AL., **2014a**; HABOUDANE, **2004**; MUTANGA AND SKIDMORE, **2004**). According to the statistics, the GRVI and MGRVI showed no correlation and the RGBVI produced a low correlation to the biomass after the booting stage (14 June 2013). Nevertheless, high positive correlations were found until booting stage, which is important for fertilizer management to improve crop yield. Management recommendations show that summer barley is commonly fertilized after seeding and at the tillering stage (MUNZERT AND FRAHM, **2006**). Additionally, CHANG ET AL. (**2005**) state that booting stage is best suited for

yield prediction using canopy reflectance. Similarly, studies in different crops and grasses by **Mo-
tohka et al.** (**2010**), **Hunt et al.** (**2005**) and **Tucker** (**1979**) demonstrate that the applicability of $VI_{VIS}$
is limited to certain growth stages.

Generally, there are noteworthy constraints in the $VI_{VIS}$ generation method. We collected images
with fixed aperture and exposure setting but we calculated the $VI_{VIS}$ from an image mosaic gener-
ated by Agisoft PhotoScan Professional using the 'mosaic blending mode' (see **chapter 6.2.5**). As
a result, there is no radiometric correction for changes in lighting conditions between single pho-
tos. Changing light incidence introduces bidirectional reflectance distribution function (BRDF) ef-
fects, even in close to nadir imaging (**Grenzdörffer and Niemeyer**, **2011**). Capturing the whole AOI
in one image can partly eliminate the problem. Furthermore, no calibration between the images
was possible because no object of known reflectance was present, like *e.g.* calibration panels or
colored tarpaulins. Moreover, no investigation was made of the exact wavelengths covered by the
red, green and blue bands of the digital camera. A calibration of digital numbers (DN) in the images
with a monochromatic light source is highly recommended (**Hunt Jr. et al.**, **2005**). Ultimately,
multi-year studies are required to evaluate and improve the method for obtaining $VI_{VIS}$ from UAV-
based RGB imagery.

Practically speaking, the data collection for hyperspectral reflectance data with a field spectrora-
diometer is more complex and time-consuming than the data collection with a UAV-system. A
field spectroradiometer produces point data, while UAV-based imaging has the advantage of cap-
turing more productively infield variability. Moreover, a field spectroradiometer is a sensitive and
expensive instrument which requires special training of users. A spectroradiometer's main ad-
vantage is the high spectral resolution of calibrated spectra. On the other hand an out-of-the-box
UAV-system can be operated by a larger user group at a low cost. Besides, two parameters are
acquired with an 800€ sensor which almost performs as good as the $VI_{NIR}$.

## 6.5    Conclusions and Outlook

The foregoing discussion has attempted to examine the suitability of plant height and vegetation
indices in the visible and near-infrared region in their suitability for biomass prediction in a sum-
mer barley experiment. We conclude that the GnyLi is a suitable indicator for biomass as well as
UAV-derived plant height from crop surface models. The GRVI and newly developed MGRVI and
RGBVI visible band vegetation indices are promising, also in combination with plant height. But
the indices need to be further explored due to varying performance, especially in later growth

stages. Contrary to expectation, the combination of vegetation indices and plant height did not significantly improve the model performance. A validation with data from multiple years and different crops is needed. Keeping in mind that results are most valuable when obtained in a simple, timely manner, the simple linear regression or exponential regression may be favoured over more complex models like the multiple linear/non-linear regression. With regard to the tradeoff between cost for the sensor and complexity of the reflectance measurement, it is more productive to use a combination of a UAV with a non-calibrated optical camera. This observation does not supersede hyperspectral measurements with high spectral resolution beyond the visible domain. Hyperspectral full frame cameras for UAVs are a promising development and combine advantages of high spectral and spatial resolution, opening up new possibilities in crop monitoring.

## Acknowledgments

## References

ADAMCHUK, V.I., FERGUSON, R.B., HERGERT, G.W., **2010**. Soil Heterogeneity and Crop Growth, in: Oerke, E.-C., Gerhards, R., Menz, G., Sikora, R.A. (Eds.), Precision Crop Protection - the Challenge and Use of Heterogeneity. Springer, Dordrecht, Netherlands, pp. 3–16.

AGISOFT LLC, **2014**. Agisoft PhotoScan [WWW Document]. Agisoft PhotoScan. URL http://www.agisoft.com (accessed 10.9.14).

BANNARI, A., MORIN, D., BONN, F., HUETE, A.R., **1995**. A review of vegetation indices. Remote Sensing Reviews 13, 95–120. doi:10.1080/02757259509532298

BARET, F., GUYOT, G., **1991**. Potentials and limits of vegetation indices for LAI and APAR assessment. Remote Sensing of Environment 35, 161–173. doi:10.1016/0034-4257(91)90009-U

BENDIG, J., BOLTEN, A., BARETH, G., **2013**. UAV-based Imaging for Multi-Temporal, very high Resolution Crop Surface Models to monitor Crop Growth Variability. Photogrammetrie - Fernerkundung - Geoinformation 6, 551–562. doi:10.1127/1432-8364/2013/0200

BENDIG, J., BOLTEN, A., BENNERTZ, S., BROSCHEIT, J., EICHFUSS, S., BARETH, G., **2014a**. Estimating Biomass of Barley Using Crop Surface Models (CSMs) Derived from UAV-Based RGB Imaging. Remote Sensing 6, 10395–10412. doi:10.3390/rs61110395

BERTHOLD, M.R., HAND, D., **2006**. Intelligent Data Analysis, 2nd ed. Springer, Berlin, Germany.

CARLSON, T.N., RIPLEY, D.A., **1997**. On the relation between NDVI, fractional vegetation cover, and leaf area index. Remote Sensing of Environment 62, 241–252. doi:10.1016/S0034-4257(97)00104-1

CHANG, K.-W., SHEN, Y., LO, J.-C., **2005**. Predicting Rice Yield Using Canopy Reflectance Measured at Booting Stage. Agronomy Journal 97, 872. doi:10.2134/agronj2004.0162

CHEN, P., HABOUDANE, D., TREMBLAY, N., WANG, J., VIGNEAULT, P., LI, B., **2010**. New spectral indicator assessing the efficiency of crop nitrogen treatment in corn and wheat. Remote Sensing of Environment 114, 1987–1997. doi:10.1016/j.rse.2010.04.006

CLEVERS, J.P.G.W., JONGSCHAAP, R., **2001**. Imaging Spectrometry For Agricultural Applications, in: Meer, F.D. van der, Jong, S.M.D. (Eds.), Imaging Spectrometry, Remote Sensing and Digital Image Processing. Kluwer Academic Publishers, Dordrecht, Netherlands, pp. 157–199.

CURRAN, P.J., **1989**. Remote sensing of foliar chemistry. Remote Sensing of Environment 30, 271–278. doi:10.1016/0034-4257(89)90069-2

DANDOIS, J.P., ELLIS, E.C., **2010**. Remote Sensing of Vegetation Structure Using Computer Vision. Remote Sensing 2, 1157–1176. doi:10.3390/rs2041157

D' OLEIRE-OLTMANNS, S., MARZOLFF, I., PETER, K., RIES, J., **2012**. Unmanned Aerial Vehicle (UAV) for Monitoring Soil Erosion in Morocco. Remote Sensing 4, 3390–3416. doi:10.3390/rs4113390

EHLERT, D., HORN, H.-J., ADAMEK, R., **2008**. Measuring crop biomass density by laser triangulation. Computers and Electronics in Agriculture 61, 117–125. doi:10.1016/j.compag.2007.09.013

GAO, J., **2006**. Canopy chlorophyll estimation with hyperspectral remote sensing (dissertation). Kansas State University, Manhattan, Kansas, US.

GEIPEL, J., LINK, J., CLAUPEIN, W., **2014**. Combined Spectral and Spatial Modeling of Corn Yield Based on Aerial Images and Crop Surface Models Acquired with an Unmanned Aircraft System. Remote Sensing 6, 10335–10355. doi:10.3390/rs61110335

GITELSON, A.A., KAUFMAN, Y.J., STARK, R., RUNDQUIST, D., **2002**. Novel algorithms for remote estimation of vegetation fraction. Remote Sensing of Environment 80, 76–87. doi:10.1016/s0034-4257(01)00289-9

GNYP, M.L., BARETH, G., LI, F., LENZ-WIEDEMANN, V.I.S., KOPPE, W., MIAO, Y., HENNIG, S.D., JIA, L., LAUDIEN, R., CHEN, X., ZHANG, F., **2014a**. Development and implementation of a multiscale biomass

model using hyperspectral vegetation indices for winter wheat in the North China Plain. International Journal of Applied Earth Observation and Geoinformation 33, 232–242. doi:10.1016/j.jag.2014.05.006

GRENZDÖRFFER, G.J., NIEMEYER, F., **2011**. UAV based BRDF-measurements of agricultural surfaces with PFIFFIKUS. International Archives of the Photogrammetry, Remote Sensing and Spatial Information Sciences XXXVIII-1/C22, 229–234.

HABOUDANE, D., **2004**. Hyperspectral vegetation indices and novel algorithms for predicting green LAI of crop canopies: Modeling and validation in the context of precision agriculture. Remote Sensing of Environment 90, 337–352. doi:10.1016/j.rse.2003.12.013

HANSEN, P.M., SCHJOERRING, J.K., **2003**. Reflectance measurement of canopy biomass and nitrogen status in wheat crops using normalized difference vegetation indices and partial least squares regression. Remote Sensing of Environment 86, 542–553. doi:10.1016/S0034-4257(03)00131-7

HATFIELD, J.L., GITELSON, A.A., SCHEPERS, J.S., WALTHALL, C.L., **2008**. Application of Spectral Remote Sensing for Agronomic Decisions. Agronomy Journal 100, S117–S131. doi:10.2134/agronj2006.0370c

HOFFMEISTER, D., BOLTEN, A., CURDT, C., WALDHOFF, G., BARETH, G., **2010**. High-resolution Crop Surface Models (CSM) and Crop Volume Models (CVM) on field level by terrestrial laser scanning, in: Guo, H., Wang, C. (Eds.), SPIE Proceedings of the Sixth International Symposium on Digital Earth: Models, Algorithms, and Virtual Reality. Presented at the Sixth International Symposium on Digital Earth: Models, Algorithms, and Virtual Reality, Beijing, China, p. 78400E–78400E–6. doi:10.1117/12.872315

HOFFMEISTER, D., WALDHOFF, G., CURDT, C., TILLY, N., BENDIG, J., BARETH, G., **2013**. Spatial variability detection of crop height in a single field by terrestrial laser scanning, in: Stafford, J.V. (Ed.), Precision Agriculture '13. Presented at the 9th European Conference on Precision Agriculture, Wageningen Academic Publishers, Lleida, Spain, pp. 267–274.

HUETE, A.R., **1988**. A soil-adjusted vegetation index (SAVI). Remote Sensing of Environment 25, 295–309. doi:10.1016/0034-4257(88)90106-X

HUNT, E., DAUGHTRY, C., MIRSKY, S., HIVELY, W., **2014**. Remote Sensing With Simulated Unmanned Aircraft Imagery for Precision Agriculture Applications. IEEE Journal of Selected Topics in Applied Earth Observations and Remote Sensing. doi:10.1109/JSTARS.2014.2317876

HUNT JR., E.R., CAVIGELLI, M., DAUGHTRY, C.S.T., MCMURTREY III, J.E., WALTHALL, C.L., **2005**. Evaluation of Digital Photography from Model Aircraft for Remote Sensing of Crop Biomass and Nitrogen Status. Precision Agriculture 6, 359–378. doi:10.1007/s11119-005-2324-5

KOPPE, W., GNYP, M.L., HÜTT, C., YAO, Y., MIAO, Y., CHEN, X., BARETH, G., **2013**. Rice monitoring with multi-temporal and dual-polarimetric TerraSAR-X data. International Journal of Applied Earth Observation and Geoinformation 21, 568–576. doi:10.1016/j.jag.2012.07.016

KRAUS, K., **2004**. Photogrammetrie: Geometrische Informationen aus Photographien und Laserscanneraufnahmen, 7th ed. Walter de Gruyter, Berlin, Germany.

KUMAR, L., SCHMIDT, K., DURY, S., SKIDMORE, A., **2001**. Imaging Spectrometry and Vegetation Science, in: Meer, F.D. van der, Jong, S.M.D. (Eds.), Imaging Spectrometry, Remote Sensing and Digital Image Processing. Kluwer Academic Publishers, Dordrecht, Netherlands, pp. 111–155.

LANCASHIRE, P.D., BLEIHOLDER, H., BOOM, T.V.D., LANGELÜDDEKE, P., STAUSS, R., WEBER, E., WITZENBERGER, A., **1991**. A uniform decimal code for growth stages of crops and weeds. Annals of Applied Biology 119, 561–601. doi:10.1111/j.1744-7348.1991.tb04895.x

LAUDIEN, R., BARETH, G., **2006**. Multitemporal Hyperspectral Data Analysis for Regional Detection of Plant Diseases by using a Tractor- and an Airborne-based Spectrometer. Photogrammetrie - Fernerkundung - Geoinformation 3, 217–227.

LEMAIRE, G., GASTAL, F., **1997**. N Uptake and Distribution in Plant Canopies, in: Lemaire, D.G. (Ed.), Diagnosis of the Nitrogen Status in Crops. Springer, Berlin, Germany, pp. 3–43.

LIU, L., WANG, J., BAO, Y., HUANG, W., MA, Z., ZHAO, C., **2006**. Predicting winter wheat condition, grain yield and protein content using multi-temporal EnviSat-ASAR and Landsat TM satellite images. International Journal of Remote Sensing 27, 737–753. doi:10.1080/01431160500296867

LUCIEER, A., TURNER, D., KING, D.H., ROBINSON, S.A., **2014**. Using an Unmanned Aerial Vehicle (UAV) to capture micro-topography of Antarctic moss beds. International Journal of Applied Earth Observation and Geoinformation 27, 53–62. doi:10.1016/j.jag.2013.05.011

LUMME, J., KARJALAINEN, M., KAARTINEN, H., KUKKO, A., HYYPPÄ, J., HYYPPÄ, H., JAAKKOLA, A., KLEEMOLA, J., **2008**. Terrestrial laser scanning of agricultural crops. The International Archives of the Photogrammetry, Remote Sensing and Spatial Information Sciences 37, 563–566.

MOTOHKA, T., NASAHARA, K.N., OGUMA, H., TSUCHIDA, S., **2010**. Applicability of Green-Red Vegetation Index for Remote Sensing of Vegetation Phenology. Remote Sensing 2, 2369–2387. doi:10.3390/rs2102369

MUNZERT, M., FRAHM, J., **2006**. Pflanzliche Erzeugung: Grundlagen des Acker- und Pflanzenbaus und der Guten fachlichen Praxis, Grundlagen der Verfahrenstechnik, Produktions- und Verfahrenstechnik für Kulturpflanzen, Dauergrünland, Sonderkulturen, Nachwachsende Rohstoffe, Ökologischer Landbau, Naturschutz und Landschaftspflege, 12th ed. BLV, Munich, Germany.

MUTANGA, O., SKIDMORE, A.K., **2004**. Narrow band vegetation indices overcome the saturation problem in biomass estimation. International Journal of Remote Sensing 25, 3999–4014. doi:10.1080/01431160310001654923

NEITZEL, F., KLONOWSKI, J., **2011**. Mobile 3D mapping with a low-cost UAV system, in: International Archives of the Photogrammetry, Remote Sensing and Spatial Information Sciences. Presented at the UAV-g 2011, Zurich, Switzerland, pp. 1–6.

OERKE, E.-C., GERHARDS, R., MENZ, G., SIKORA, R.A. (EDS.), **2010**. Precision Crop Protection - the Challenge and Use of Heterogeneity. Springer, Dordrecht, Netherlands.

PETTORELLI, N., **2013**. The Normalized Difference Vegetation Index. Oxford University Press, Oxford, UK.

PU, R., GE, S., KELLY, N.M., GONG, P., **2003**. Spectral absorption features as indicators of water status in coast live oak (Quercus agrifolia) leaves. International Journal of Remote Sensing 24, 1799–1810. doi:10.1080/01431160210155965

QI, J., CHEHBOUNI, A., HUETE, A.R., KERR, Y.H., SOROOSHIAN, S., **1994**. A modified soil adjusted vegetation index. Remote Sensing of Environment 48, 119–126. doi:10.1016/0034-4257(94)90134-1

ROBERTS, D., ROTH, K., PERROY, R., **2011**. Hyperspectral Vegetation Indices, in: Thenkabail, P.S., Huete, A. (Eds.), Hyperspectral Remote Sensing of Vegetation. CRC Press, Boca Raton, FL, US, pp. 309–328.

RONDEAUX, G., STEVEN, M., BARET, F., **1996**. Optimization of soil-adjusted vegetation indices. Remote Sensing of Environment 55, 95–107. doi:10.1016/0034-4257(95)00186-7

ROUSE, J.W., HAAS, R.H., SCHELL, J.A., DEERING, D.W., **1974**. Monitoring Vegetation Systems in the Great Plains with Erts. NASA Special Publication 351, 309.

ROYO, C., VILLEGAS, D., **2011**. Field Measurements of Canopy Spectra for Biomass Assessment of Small-Grain Cereals, in: Matovic, M.D. (Ed.), Biomass - Detection, Production and Usage. InTech, Rijeka, Croatia, pp. 27–52.

SONA, G., PINTO, L., PAGLIARI, D., PASSONI, D., GINI, R., **2014**. Experimental analysis of different software packages for orientation and digital surface modelling from UAV images. Earth Science Informatics 7, 97–107. doi:10.1007/s12145-013-0142-2

THENKABAIL, P.S., SMITH, R.B., DE PAUW, E., **2000**. Hyperspectral vegetation indices and their relationships with agricultural crop characteristics. Remote sensing of Environment 71, 158–182. doi:10.1016/S0034-4257(99)00067-X

TILLY, N., HOFFMEISTER, D., CAO, Q., HUANG, S., LENZ-WIEDEMANN, V.I.S., MIAO, Y., BARETH, G., **2014**. Multitemporal crop surface models: accurate plant height measurement and biomass estimation with terrestrial laser scanning in paddy rice. Journal of Applied Remote Sensing 8, 083671–083671. doi:10.1117/1.JRS.8.083671

TREMBLAY, N., FALLON, E., ZIADI, N., **2011**. Sensing of crop nitrogen status: Opportunities, tools, limitations, and supporting information requirements. HortTechnology 21, 274–281.

TUCKER, C.J., **1979**. Red and photographic infrared linear combinations for monitoring vegetation. Remote Sensing of Environment 8, 127–150. doi:10.1016/0034-4257(79)90013-0

VERHOEVEN, G., **2011**. Taking computer vision aloft - archaeological three-dimensional reconstructions from aerial photographs with photoscan. Archaeological Prospection 18, 67–73. doi:10.1002/arp.399

# 7 Low-Weight and UAV-based Hyperspectral Full-frame Cameras for Monitoring Crops: Spectral Comparison with Portable Spectroradiometer Measurements

Georg Bareth [1,6,*], Helge Aasen [1], Juliane Bendig [1], Martin Leon Gnyp [1,2], Andreas Bolten [1], András Jung [3], René Michels [4], Jussi Soukkamäki [5]

1   Institute of Geography, GIS & RS Group, University of Cologne, Albertus-Magnus-Platz, 50923 Cologne

2   Research Centre Hanninghof, Yara International ASA, Hanninghof 35, 48249 Dülmen, Germany

3   Institute of Geography, University of Leipzig, Johannisallee 19, 04103 Leipzig, Germany

4   Cubert GmbH, Real Time Spectral Imaging, Helmholtzstraße 12, 89081 Ulm, Germany

5   Rikola LTD., Kaitoväylä 1, 90570 Oulu, Finland

6   ICASD-International Center for Agro-Informatics and Sustainable Development, www.icasd.org

*   Corresponding author, Tel.: +49-221-470-6265; Fax: +49-221-470-8838

E-Mail: g.bareth@uni-koeln.de

**Summary:** The non-destructive monitoring of crop growth status with field-based or tractor-based multi- or hyperspectral sensors is a common practice in precision agriculture. The demand is given for flexible, easy to use, and field scale systems with super-high resolution (< 20 cm) or on single plant scale to provide knowledge on in-field variability of crop status for management purposes. Satellite- and airborne systems are usually not able to provide the spatial and temporal resolution for such purposes within a low-cost approach. The developments in the area of Unmanned Aerial Vehicles (UAV) equipped with hyperspectral sensor systems may be suited to fill that niche. In this contribution, we introduce two hyperspectral full-frame cameras weighing less than 1 kg which can be mounted to low-weight UAVs (< 3 kg). The first results of a campaign in June/July 2013 are

presented and the derived spectra from the hyperspectral images are compared to related spectra collected with a portable spectroradiometer. The first results are promising.

**Zusammenfassung:** Leichte und UAV-getragene hyperspektrale, bildgebende Kameras zur Beobachtung von landwirtschaftlichen Pflanzenbeständen: spektraler Vergleich mit einem tragbaren Feldspektrometer. Die nicht-destruktive Beobachtung von Pflanzenwachstum mit feldbasierten oder traktorbasierten multi- oder hyperspektralen Sensoren ist eine gängige Praxis in der Präzisionslandwirtschaft. Um Wissen über die Variabilität des Pflanzenzustands im Feld für Managementzwecke bereitzustellen, werden flexible, multitemporal einsetzbare und einfach zu bedienende Systeme zur Erfassung ganzer Felder mit extrem hoher Auflösung (< 20 cm) oder für Einzelpflanzen benötigt. Satelliten- und flugzeuggetragene Systeme sind in der Regel nicht in der Lage, diese räumliche und zeitliche Auflösung für solche Anwendungen bereitzustellen bzw. dies wäre mit einem nicht vertretbaren finanziellen Aufwand verbunden. Die Entwicklungen im Bereich der Unmanned Aerial Vehicles (UAV) sowie der hyperspektralen Sensortechnik scheinen genau diese Nische zu füllen. In diesem Beitrag stellen wir zwei hyperspektrale Kameras mit einem Gewicht von weniger als 1 kg vor, die mit leichten UAVs (< 3 kg) geflogen werden können. Wir präsentieren die ersten Ergebnisse einer Kampagne im Juni/Juli 2013 und vergleichen die aus den hyperspektralen Bildern abgeleiteten Spektren mit entsprechenden Spektren eines tragbaren Feldspektrometers. Die ersten Ergebnisse sind vielversprechend.

**Keywords**: UAV, sensors, hyperspectral, change detection, agriculture, CSM, plant height, 3D, vegetation index, crops

## 7.1 Introduction

In Precision Agriculture (PreAg), sensor-based monitoring of crops to derive plant growth parameters and yield are in the focus of research to support proper crop management (MULLA, **2013**). Therefore, the applications of remote and proximal sensing methods are key technologies in PreAg (OERKE ET AL., **2010**). Besides monitoring crops, sensing technologies are also widely used for measuring soil and environmental parameters (WHELAN AND TAYLOR, **2013**). Hyperspectral remote and proximal sensing is intensively investigated for the detection of crop nitrogen (N) content, biomass, yield and crop stress (KOPPE ET AL., **2012**; LI ET AL., **2010a**; OERKE ET AL., **2010**; THENKABAIL ET AL., **2000**; YU ET AL., **2013**). In general, the remote sensing approaches described in the literature are satellite- or airborne (manned airplanes). For proximal sensing approaches, portable field spectrometer are used for canopy or leaf-level sensing (GNYP ET AL., **2014b**; YU ET AL., **2013**).

In the last years, efforts have been undertaken to make hyperspectral data more frequently available and sensing methods for a specific crop growth stage were investigated (Aasen et al., **2014**; Gnyp et al., **2013**). The latter is a pre-condition for monitoring plant growth behavior by multi-temporal campaigns during phenology which enables the detection of abiotic and biotic stresses (Laudien et al., **2006**; Laudien and Bareth, **2006**).

For the consideration of specific phenological stages in non-destructive sensing approaches, a very flexible platform is needed. Usually, satellite- or airborne sensors cannot provide such multi-temporal data within a fixed time slot of a few days (Zhang & Kovacs 2012). Besides the demand for high temporal resolution in crop monitoring approaches, a high spatial resolution is in the focus of PreAg resulting in increased knowledge on within-field variability of crop growth. Unmanned Aerial Vehicles (UAVs) also known as Unmanned Aerial Systems (UAS) or Remotely-Piloted Aerial Systems (RPAS) are remote sensing platforms combining very high flexibility in temporal scale and very high resolution in spatial scale (Zhang and Kovacs, **2012**). The potential of UAV-based imaging in agricultural applications is already well described by Zhang and Kovacs (**2012**), Calderón et al. (**2013**), Zarco-Tejada et al. (**2012**) and others.

The fast technological progress and developments are not only found for UAV platforms, but also for sensor development (Bareth et al., **2011**; Bendig and Bareth, **2014**). Electronic devices continuously minimised in the last years resulting in low-weight UAVs and low-weight sensors being very capable, integrated remote sensing platforms (Colomina and Molina, **2014**). Hence, in 2013 two new hyperspectral, full-frame imaging spectrometers were introduced, the Cubert UHD185 "Firefly" (www.cubert-gmbh.de) and the Rikola Hyperspectral Camera (www.rikola.fi), and in 2014 the BaySpec OCI-1000 (www.bayspec.com). All three low-weight (< 1 kg) cameras cover the spectral VIS/NIR domain but use different technologies. The Rikola and the Cubert sensors were flown in a first campaign in June/July 2013. The objectives of this contribution are (i) to introduce the two hyperspectral frame cameras, which document a new milestone in hyperspectral imaging spectroscopy, and (ii) to compare spectra from the images acquired by UAV-campaigns on barley field experiments with spectra measured with the fieldspectroradiometer FieldSpec3 by ASD (www.asdi.com).

## 7.2 Study Area, UAV, and Sensors

The field experiment is located on the research farm of Bonn University, called Campus Klein-Altendorf, which is outside of the city of Bonn in Klein-Altendorf. The field campaigns were carried

out within the Crop.Sense.net project's activity, coordinated by the Institute of Crop Science and Resource Conservation of Bonn University (www.cropsense.de). Crop.Sense.net is one of the BMBF Networks of Excellence in Agricultural and Nutrition Research, which are funded by the German Ministry for Education and Research (BMBF) and by the European Union Funds for regional development. In Klein-Altendorf, the central field experiments of Crop.Sense.net for barley and sugar beet have been conducted. For this study, multi-temporal UAV campaigns were flown over barley in 2013. The experiment covers 36 plots (each 3 by 7 m) with 18 barley varieties and two nitrogen treatments (40 and 80 kg/ha). For this first spectral comparison and evaluation, only selected plots (plot numbers 41, 42, and 43) are investigated.

For the UAV campaigns, a HiSystems MK Oktokopter was flown which is a low-cost (< 2000 €) and low-weight UAV (< 1.5 kg). The latter is an important fact due to the aviation regulations in Germany which allow commercial and non-commercial imaging campaigns with UAVs weighing less than 5 kg. The MK Oktokopter has a payload of up to 1 kg and a flight endurance of approx. 15 min. It can be auto-piloted by using waypoints. The UAV platform is described in detail by **BENDIG ET AL. (2013)**. Two hyperspectral full-frame cameras were mounted to the UAV and were flown separately after each other over the same experimental fields. In **Figure 7-1 (top)**, the MK Oktokopter is shown before take-off with the mounted Rikola Hyperspectral Camera (RHC), which is based on Piezo-Actuated Fabry-Perot Interferometer (FPI) (**MÄKELÄINEN ET AL.**, **2013**). FPI enables tunable wavelength settings resulting in a time lag for each wavelength (**MÄKELÄINEN ET AL.**, **2013**). The wavelength is produced by a tunable air gap (vacuum) between two optical layers (**HONKAVAARA ET AL.**, **2013**). Therefore, the spectral wavelength is a function of the size of the air gap. The tuning of the air gap results in an individual image acquisition for each spectral band with a CMOSIS CMOS image sensor recording 1 megapixel (**MÄKELÄINEN ET AL.**, **2013**). The RHC covers the spectral region between 400 nm to 950 nm. Before take-off, the RHC can be calibrated against a white reference panel. The images are saved onboard on an SD card.

The Cubert UHD185 Firefly is designed and developed by the Institute of Laser Technologies in Medicine and Metrology at the University of Ulm and the Cubert GmbH, Germany. The camera records hyperspectral full-frames with 137 bands in a spectral range of 450 - 950 nm. A silicium CCD chip captures an image with 1000 by 970 grayscale pixels as well as 50 by 50 hyperspectral pixels. At a flying altitude of 30 m the grayscale image has a ground resolution of about 1 cm and a pure hyperspectral ground resolution of about 20 cm. However, the latter may be pan-sharpened by the software of the manufacturer to the resolution of the grayscale image. The footprint

of each scene at 30 m sensor to canopy distance is about 10.3 m. In **Figure 7-1** (**bottom**), the UAV-mounted UHD185 is shown. As the RHC, the UHD185 may be calibrated against a white reference panel (**Figure 7-1, middle**). The typical integration time to capture a full hyperspectral data cube is 1 ms (clear sky). The UHD185 has to be flown with a mini-computer (MC) which records the data. Additionally, the MC runs the server application by which the Camera can be remotely controlled via WiFi.

The two cameras are differently remote controlled during flight with an UAV. While the measurement of the RHD is controlled by an initialization file which has to be created before the flight, the UHD185 is controlled by the mini-pc with a server application, which may be configured and con-



*Figure 7-1: top: MK Oktokopter is prepared for a flight campaign with the Rikola Hyperspectral Camera, middle: Cubert UHD185 Firefly is calibrated against a white panel before take-off, bottom: UHD185 in the air mounted on a MK Oktokopter.*

trolled through WiFi. Depending on the user's needs one of the systems might be beneficial. Additionally, both interfaces are currently still under development and thus, will not be further presented here.

For ground truth data collection, destructive samplings of biomass, plant N- and chlorophyll content, and non-destructive samplings of plant height, hyperspectral, and fluorescence data were performed. Those samplings were continuously carried out during phenology. Canopy reflectance was measured in the barley experiment in 2013 with an ASD FieldSpec3 Pro (Analytical Spectral Devices, Inc., Boulder, CO, USA). The FieldSpec3 (FS3) measures the reflectance between 350 and 2500 nm with a sampling interval of 1.4 nm in the visible near-infrared (VNIR) domain and with 2 nm in the shortwave infrared (SWIR) spectral region. The reflectance was measured at a height of 1 m above canopy without a fore optic resulting in a 25° field of view to minimize the background signals of soil (**Figure 7-2**). FieldSpec3 campaigns were conducted between 11 am and 2 pm local mean time around solar noon. A condition for the measurements is a mostly cloudless sky. A white spectralon panel was used for continuous calibrations. The same reference panel was also used for the RHC and UHD185 calibration (compare **Figure 7-1**, **middle**). For each plot, a total of six to eight FieldSpec3 spectra were randomly taken to represent a mean plot reflectance.



*Figure 7-2: Sampling hyperspectral ground truth with an ASD FieldSpec3.*

## 7.3 Spectral Comparisons

The first UAV campaigns with the UHD185 and the RHC were carried out on June 14, 2013 (**Figure 7-3**). Both hyperspectral frame imagers operated successfully in air after mounting them to the MK Oktokopter. To compare the spectral results for both camera systems with the FS3 spectra, images were taken at 30 m above ground level covering a maximum of three plots per image. The spatial resolution is as stated above.

*Figure 7-3: RGB image with the UHD185 covering three barley plots (3 by 7 m each), 14 June 2013.*

Directly after the UAV-based image acquisition the hyperspectral field measurements were taken. For each plot, ten measurements of the FS3 were averaged at six to eight positions (**Figure 7-4**). The measurements were taken from the core of the plots to exclude border effects. The spectra were than averaged to represent the plot's mean reflectance. In **Figure 7-4**, a false color image of the UHD185 data is displayed showing the potential locations of the six FS3 measurements.
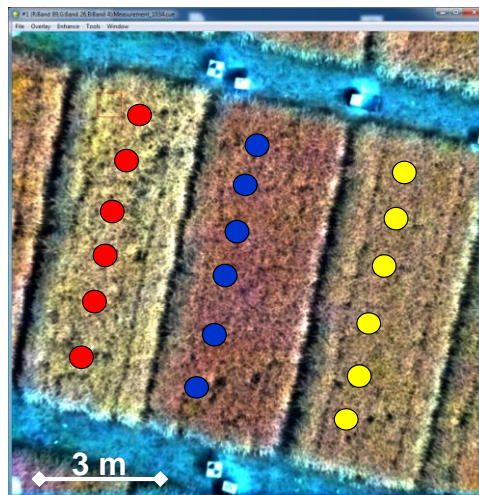


*Figure 7-4: Six randomized FieldSpec3 spectra were taken for each plot on 14 June 2013.*

For retrieving the mean plot spectra of the hyperspectral images, polygons with an inner buffer of 0.3 m were digitized to reduce border effects. Spatial statistics were computed for all pixels within a plot polygon to derive mean spectra. In **Figure 7-5**, the polygons are visualized for the three plots, each covering approx. 130,000 pixels of the UHD185 hyperspectral image.
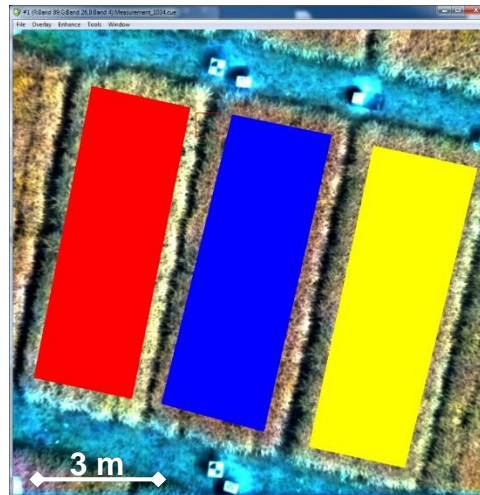
*Figure 7-5: Digitized polygons to calculate spatial statistics for each plot from UHD185 hyperspectral image for 14 June 2013.*

While the polygons in **Figure 7-5** represent the true area for calculating the spatial statistics, the circles of the single hyperspectral field measurements shown in **Figure 7-4** do not represent the true location. The latter were captured as shown in **Figure 7-2** but the locations were randomly selected excluding areas of destructive biomass sampling.
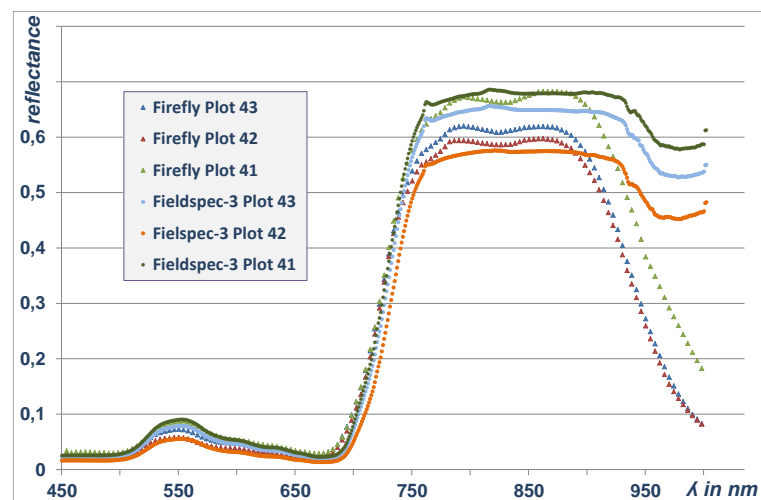


*Figure 7-6: FieldSpec3 spectra versus UHD185 spectra for plots 41, 42, and 43 on 14 June 2013.*

The mean spectra from the UHD185 image shown in **Figure 7-5** and the corresponding mean spectra from FS3 are plotted in **Figure 7-6**. The lines with the denser dotted points represent the FS3 data with higher spectral resolution compared to the UHD185 data with a lower spectral resolu-

tion. The magnitude of reflectance is similar and corresponds well. However, in the NIR, differences in the shape of the spectra are visible. Additionally, a decline of reflection in the UHD185 spectra is obvious for wavelengths longer than 900 nm.

To get an impression of the usability of the sensors for vegetation indices (VIs) two common vegetation indices, the Optimized Soil-Adjusted Vegetation Index (OSAVI) and the Normalized Difference Vegetation Index (NDVI), were calculated for the FS3 and UHD185. NDVI is widely used in remote sensing while OSAVI reduces the soil background signals (**RONDEAUX ET AL., 1996**). The first impression of similar spectral pattern and magnitude are confirmed for NDVI-like VIs. The OSAVI from FS3 data and UHD185 spectra are shown in **Figure 7-9** for the investigated plots. They do not show a significant difference having UHD185/FS3 OSAVI values of 0.87/0.88, 0.86/0.87, and 0.85/0.88 for plots 41, 42, and 42, respectively. Similar results were produced for NDVI calculations (**Figure 7-11**).
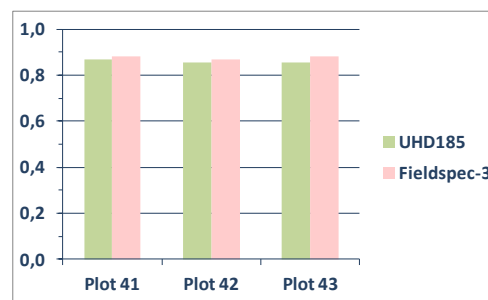


*Figure 7-7: OSAVI for the investigated plots from FieldSpec3 and UHD185 spectra for 14 June 2013.*
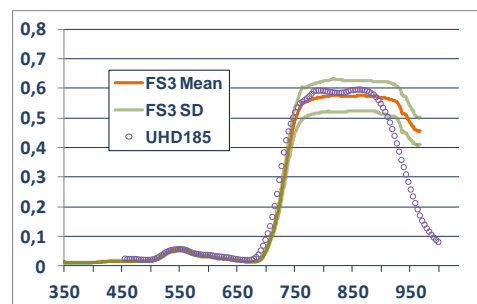


*Figure 7-8: Mean FieldSpec3 spectrum for plot 42 with standard deviation (SD) and mean UHD185 spectrum for 14 June 2013.*

Additionally, the differences in the spectra between the two sensors are partly within the standard deviation (SD) of the FS3 measurements. As an example, the FS3 spectrum with the SD for plot 42 is displayed in **Figure 7-8**. When compared to the UHD185 spectra, it is visible that in the NIR

region the instruments are within SD. The latter is not true for the red edge domain and the wavelengths longer than 900 nm. A small spectral shift to the shorter wavelength is observable resulting in large differences when calculating simple ratio VIs from bands in the VIS spectral region.

Similar spectral properties can be described for the UAV campaign with the UHD185 on June 19 2013 (**Figure 7-9**). In general, lower spectral magnitudes can be observed for plots 42 and 43 in the NIR domain with both sensors while magnitude and overall pattern of the UHD185 fit to the FieldSpec3 measurements. Plot 41 was not investigated due to insufficient coverage. Additionally, the aforementioned shift of the UHD185 occurs again in the red edge domain towards shorter wavelength and the performance from 900 nm onwards is poor.
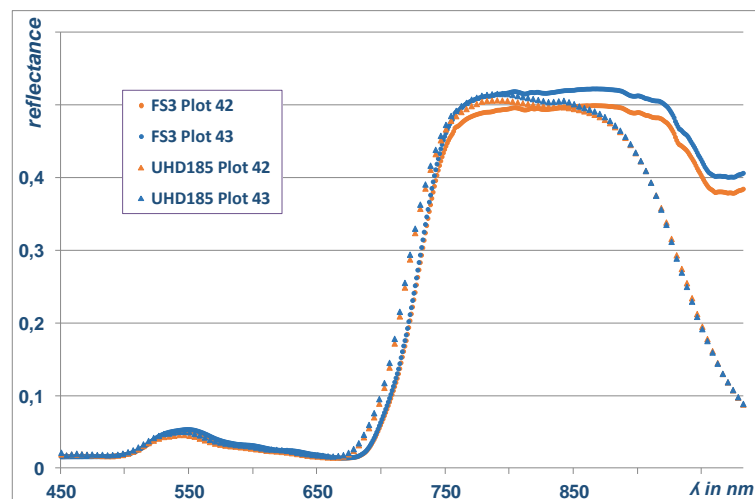


*Figure 7-9: FieldSpec3 and UHD185 spectra for plots 42 and 43 on 19 June 2013.*

Finally, very different spectral patterns occur on 08 July 2013 (**Figure 7-10**). It is clearly visible that the FS3 spectra show a very different NIR pattern due to beginning of senescence. This decrease in reflectance between 750 nm and 800 nm is not captured by the UHD185. Additionally, the spectra show higher differences in the VIS domain while the overall magnitudes are still comparable but much weaker than before. The spectral shift towards shorter wavelength is again a characteristic for the red edge spectral regions and for the poor performance above 900nm.
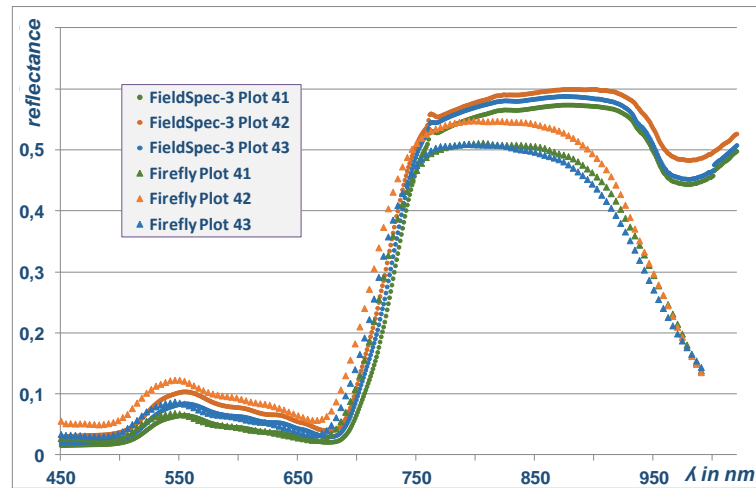
*Figure 7-10: FieldSpec3 spectra versus UHD185 spectra for plots 41, 42, and 43 on 08 July 2013.*

The Rikola hyperspectral camera (RHC) operates on a different technology, using a Piezo-Actuated Fabry-Perot Interferometer (FPI). In moving sensor platforms, a spatial shift of each spectral band might be the consequence and must be solved by image matching techniques. As described above, the RHC enables imaging of selected wavelengths. According to well described VIs (**GNYP ET AL.**, **2013**; **LAUDIEN ET AL.**, **2006**; **LI ET AL.**, **2010a**; **YU ET AL.**, **2013**), we chose eight wavelengths for the UAV campaign on 14 June 2013: 505 nm, 552 nm, 604 nm, 674 nm, 741 nm, 745 nm, 770 nm, and 803 nm. To calculate VIs from the RHC image we used the same polygon as for the image of the UHD185 (**Figure 7-5**).

The NDVI values calculated from the RHC (**Figure 7-11**) are lower than for the UHD185 and the FS3. The reason for this is not clear at this stage, because the RHC was calibrated against the reference panel, too. But the NDVI values are in an order and pattern as expected and the UHD185 showed weaker performances against the FieldSpec3 measurements on other dates. The higher spatial resolution of the RHC's hyperspectral sensor is documented in the calculated NDVI image shown in **Figure 7-12**.
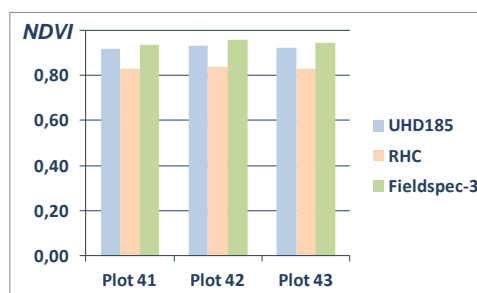


*Figure 7-11: Calculated NDVI for the investigated plots for 14 June 2013.*
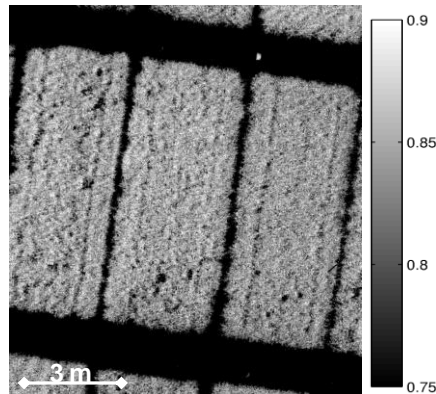
*Figure 7-12: Calculated NDVI for the RHC image taken on 14 June 2013.*

## 7.4    Discussion and Conclusions

In this study, we flew the Rikola Hyperspectral Camera (RHC) and the Cubert UHD185 Firefly with a low-weight and low-cost UAV. Both cameras worked well, had some minor handling problems in the field, and the flight campaigns successfully delivered hyperspectral data. The spectral calibration in the field against a white reference panel was possible for both sensors. While the UHD185 was strong in capturing the whole spectrum within one image, the RHC had a higher spatial resolution in the selected hyperspectral wavelength resulting in a lower spectral resolution. While the RHC was only flown once together with the Rikola Company, the UHD185 was flown in multiple campaigns.

For both cameras the spectral calibration is still an issue. While the spectral pattern and magnitudes are in order of the field measurements, the first comparison with field spectra show clearly a lack of understanding in the spectral calibration of the sensors. Additionally, the UHD185 and the RHC were flown in different image acquisition modes. Future research of using the two cameras must focus on the hyperspectral image properties in terms of BDRF and calibration. Because of the latter the results stated in this paper should be seen as a first indicator of the suitability of hyperspectral full-frame cameras for precision agriculture applications. Despite the differences between the FS3 measurements and the hyperspectral full-frame sensors in some of the measurements the results show the potential of this new technology. Similar comparison approach between ASD Hand-held 2 and UAV-based sensors, such as Mini MCA6 (Tetracam) and STS spectrometer (Ocean Optics), were performed by von BUEREN ET AL. (**2014**), but only in the spectral domain of 350-850 nm. The spectra from the different sensors showed similar magnitudes and

patterns. However, further research need to investigate a best practice for full-frame UAV hyper-spectral sensors to generate robust and reproducible data. Both sensors operated well in the air and recorded the data as configured. Due to the small field of view of both sensors capturing the right footprint was a challenge. The latter may be solved with improved knowledge of the sensor and optimized flying trajectories.

The new technological designs of both hyperspectral sensors result in a low weight and enable hyperspectral imaging campaigns with UAV at a take-off weight below 5 kg. In Germany, this is important due to aviation regulations, since the application procedure for permissions are easier than for heavier UAVs. Apart from the mentioned critical points, both sensors open a new era of hyperspectral imaging. The flexibility of low-weight UAVs enable a temporal resolution which could not been realized in the past by (manned) aerial- or satellite-borne imaging. The same is true for the spatial resolution. Super-high resolutions of < 2 cm are possible on field scale and up to a few square kilometers, even in 3D (**BENDIG ET AL.**, **2013**). Using stereophotogrammetric or structure for motion image analysis techniques with precise RTK measured ground control points, DEMs or in general surface models can be obtained in in a resolution and precision of less than 2 cm. In **Figure 7-13**, such a 3D hyperspectral surface is shown for 14 June 2013.
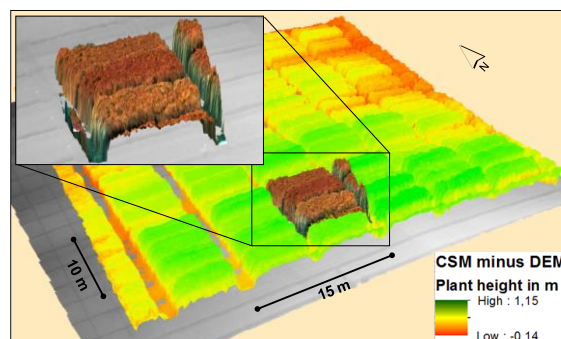


*Figure 7-13: 3D hyperspectral surface with a spatial resolution of 2 cm.*

The combination of 3D imaging techniques and hyperspectral imaging enables the precise and accurate monitoring of crop growth during phenology. The analysis of multi-temporal Crop Surface Models (CSMs) (**BENDIG ET AL.**, **2013**; **TILLY ET AL.**, **2014**) enables the precise monitoring of plant height and plant growth while hyperspectral analysis derive physiological plant parameters like chlorophyll or nitrogen content and others. Exactly this is needed for PreAg in terms of monitoring crop growth behavior, crop vitality, and crop stress. The first data analyses are very promising and

can be regarded as a new technological statement of sensor development, which will be a multiplier for applications not only in the field of crop monitoring.

## Acknowledgements

## References

AASEN, H., GNYP, M.L., MIAO, Y., BARETH, G., **2014**. Automated Hyperspectral Vegetation Index Retrieval from Multiple Correlation Matrices with HyperCor. Photogrammetric Engineering & Remote Sensing 80, 785–795. doi:10.14358/PERS.80.8.785

BARETH, G., BOLTEN, A., BENDIG, J., **2011**. Potentials for low-cost Mini-UAVs, in: Lenz-Wiedemann, V., Bareth, G. (Eds.), Kölner Geographische Arbeiten 92. Presented at the Workshop on Remote Sensing Methods for Change Detection and Process Modelling, Geographisches Institut der Universität zu Köln, Cologne, Germany, pp. 1–8. doi:10.5880/TR32DB.KGA92.2.

BENDIG, J., BARETH, G., **2014**. Preface, in: Bendig, J., Bareth, G. (Eds.), Kölner Geographische Arbeiten 94. Presented at the Workshop on UAV-based Remote Sensing Methods for Monitoring Vegetation, Cologne, Germany, pp. 1–2. doi:10.5880/TR32DB.KGA94.1

BENDIG, J., BOLTEN, A., BARETH, G., **2013**. UAV-based Imaging for Multi-Temporal, very high Resolution Crop Surface Models to monitor Crop Growth Variability. Photogrammetrie - Fernerkundung - Geoinformation 6, 551–562. doi:10.1127/1432-8364/2013/0200

CALDERÓN, R., NAVAS-CORTÉS, J.A., LUCENA, C., ZARCO-TEJADA, P.J., **2013**. High-resolution airborne hyperspectral and thermal imagery for early detection of Verticillium wilt of olive using fluorescence, temperature and narrow-band spectral indices. Remote Sensing of Environment 139, 231–245. doi:10.1016/j.rse.2013.07.031

COLOMINA, I., MOLINA, P., **2014**. Unmanned aerial systems for photogrammetry and remote sensing: A review. ISPRS Journal of Photogrammetry and Remote Sensing 92, 79–97. doi:10.1016/j.isprsjprs.2014.02.013

GNYP, M.L., MIAO, Y., YUAN, F., USTIN, S.L., YU, K., YAO, Y., HUANG, S., BARETH, G., **2014b**. Hyperspectral canopy sensing of paddy rice aboveground biomass at different growth stages. Field Crops Research 155, 42–55. doi:10.1016/j.fcr.2013.09.023

GNYP, M.L., YU, K., AASEN, H., YAO, Y., HUANG, S., MIAO, Y., BARETH, G., **2013**. Analysis of Crop Reflectance for Estimating Biomass in Rice Canopies at Different Phenological Stages. Photogrammetrie - Fernerkundung - Geoinformation 4, 351–365. doi:10.1127/1432-8364/2013/0182

HONKAVAARA, E., SAARI, H., KAIVOSOJA, J., PÖLÖNEN, I., HAKALA, T., LITKEY, P., MÄKYNEN, J., PESONEN, L., **2013**. Processing and Assessment of Spectrometric, Stereoscopic Imagery Collected Using a Lightweight UAV Spectral Camera for Precision Agriculture. Remote Sensing 5, 5006–5039. doi:10.3390/rs5105006

KOPPE, W., GNYP, M.L., HENNIG, S.D., LI, F., MIAO, Y., CHEN, X., JIA, L., BARETH, G., **2012**. Multi-Temporal Hyperspectral and Radar Remote Sensing for Estimating Winter Wheat Biomass in the North China Plain. Photogrammetrie - Fernerkundung - Geoinformation 3, 281–298. doi:10.1127/1432-8364/2012/0117

LAUDIEN, R., BARETH, G., **2006**. Multitemporal Hyperspectral Data Analysis for Regional Detection of Plant Diseases by using a Tractor- and an Airborne-based Spectrometer. Photogrammetrie - Fernerkundung - Geoinformation 3, 217–227.

LAUDIEN, R., BÜRCKY, K., DOLUSCHITZ, R., BARETH, G., **2006**. Aufbau einer webgestützten Spektralbibliothek zur Analyse hyperspektraler Daten von mit Rhizoctonia solani inokulierten Zuckerrüben (Establishment of a web-based spectral database for the analysis of hyperspectral data from Rhizoctonia solani-inoculated sugar beet). Zuckerindustrie 131, 164–170.

LI, F., MIAO, Y., CHEN, X., ZHANG, H., JIA, L., BARETH, G., **2010a**. Estimating winter wheat biomass and nitrogen status using an active crop sensor. Intelligent Automation and Soft Computing 16, 1219–1228.

Mäkeläinen, A., Saari, H., Hippi, I., Sarkeala, J., Soukkamäki, J., **2013**. 2D Hyperspectral frame imager camera data in photogrammetric mosaicking, in: International Archives of Photogrammetry, Remote Sensing and Spatial Information Sciences. Presented at the UAV-g 2013, Rostock, Germany, pp. 263–267.

Mulla, D.J., **2013**. Twenty five years of remote sensing in precision agriculture: Key advances and remaining knowledge gaps. Biosystems Engineering 114, 358–371. doi:10.1016/j.biosystemseng.2012.08.009

Oerke, E.-C., Gerhards, R., Menz, G., Sikora, R.A. (Eds.), **2010**. Precision Crop Protection - the Challenge and Use of Heterogeneity. Springer, Dordrecht, Netherlands.

Rondeaux, G., Steven, M., Baret, F., **1996**. Optimization of soil-adjusted vegetation indices. Remote Sensing of Environment 55, 95–107. doi:10.1016/0034-4257(95)00186-7

Thenkabail, P.S., Smith, R.B., De Pauw, E., **2000**. Hyperspectral vegetation indices and their relationships with agricultural crop characteristics. Remote sensing of Environment 71, 158–182. doi:10.1016/S0034-4257(99)00067-X

Tilly, N., Hoffmeister, D., Cao, Q., Huang, S., Lenz-Wiedemann, V.I.S., Miao, Y., Bareth, G., **2014**. Multitemporal crop surface models: accurate plant height measurement and biomass estimation with terrestrial laser scanning in paddy rice. Journal of Applied Remote Sensing 8, 083671–083671. doi:10.1117/1.JRS.8.083671

Von Bueren, S., Burkart, A., Hueni, A., Rascher, U., Tuohy, M., Yule, I., **2014**. Comparative validation of UAV based sensors for the use in vegetation monitoring. Biogeosciences Discussions 11, 3837–3864. doi:10.5194/bgd-11-3837-2014

Whelan, B., Taylor, J., **2013**. Precision Agriculture for Grain Production Systems. Csiro Publishing, Collingwood, VIC, Australia.

Yu, K., Li, F., Gnyp, M.L., Miao, Y., Bareth, G., Chen, X., **2013**. Remotely detecting canopy nitrogen concentration and uptake of paddy rice in the Northeast China Plain. ISPRS Journal of Photogrammetry and Remote Sensing 78, 102–115. doi:10.1016/j.isprsjprs.2013.01.008

Zarco-Tejada, P.J., González-Dugo, V., Berni, J.A.J., **2012**. Fluorescence, temperature and narrowband indices acquired from a UAV platform for water stress detection using a micro-hyperspectral imager and a thermal camera. Remote Sensing of Environment 117, 322–337. doi:10.1016/j.rse.2011.10.007

Zhang, C., Kovacs, J.M., **2012**. The application of small unmanned aerial systems for precision agriculture: a review. Precision Agriculture 13, 693–712. doi:10.1007/s11119-012-9274-5

## 8   Discussion

This dissertation focuses on the introduction of a new method for quantifying variability in agricultural production by monitoring plant growth and crop biomass. Biomass is an important indicator for the final yield. Measurements during the growing season allow recommendations for improved management practices and higher yields that are part of the objectives in precision agriculture. The foregoing chapters stepwise describe how plant height and biomass are derived from UAV-based crop surface models (CSMs) using red-green-blue (RGB) imaging. Results are presented in three published papers and two manuscripts that describe the CSM generation process for plant height (PH) modelling (**chapters 3 and 4**) and its application for biomass estimation (**chapter 5**). Biomass is modelled from PH and vegetation indices (VIs) (**chapter 6**). Visible band VIs (VI$_{VIS}$) are calculated from uncalibrated UAV-based red-green-blue (RGB) images. In addition, VIs in the near-infrared range (VI$_{NIR}$) are calculated from ground-based hyperspectral measurements with a spectroradiometer. Potentials for calculating VI$_{NIR}$ from UAV-based imaging are demonstrated in **chapter 7** by presenting first results from UAV-based hyperspectral imaging.

The following discussion first deepens aspects of PH modelling with UAV-based CSMs based on the experiences from this work's field studies. One discussion point is the accuracy of CSMs from UAV-based RGB imaging using structure from motion (SfM) software. The second part addresses general uncertainties in plant height (PH) modelling. The subsequent sections examine the potentials of biomass estimation from CSMs and more specifically the combination of VIs and CSMs for biomass estimation. The discussion is completed by a presentation of further applications of CSMs, based on additional results from the datasets described in **chapter 2.6**, and a section on limits of the methods and dataset.

### 8.1   Accuracy of Crop Surface Models from UAV-based RGB Imaging

The results in **chapters 3** and **4** demonstrate that PH is modelled with high accuracy from CSMs using structure from motion (SfM) software. Experience from several years field studies shows that the CSM quality depends on: a sufficient amount of images, sufficient overlap between images, sufficient ground cover that is about 20% larger than the area of interest (AOI), and precisely measured and clearly visible ground control points (GCPs). Furthermore, the bare earth ground model quality is crucial because it defines the surface that is subtracted from the CSMs. Another lesson learned is that CSM quality increases with the number of images used for modelling, which is verified by **HAALA AND ROTHERMEL** (**2012**) and **HARTMANN ET AL.** (**2012**). Different than expected,

image quality properties like sharpness, adequate exposure and constant nadir orientation influence CSM quality less than the image count. Removing low quality images does lead to increased model quality. The above mentioned observations may be quantified by accuracy assessments of the CSM quality (**Table 4-3**). The comparison in **Table 8-1** clarifies how accuracy is influenced by the amount of images, image overlap and quality of GCP measurement. **Table 8-1** depicts differences between data from the Rheinbach study site and the Jiansanjiang study site based on GCP errors in x, y and z-direction, the number of images used for CSM calculation, and the average image overlap.

*Table 8-1: Spatial accuracy comparison of the Rheinbach (barley) and Jiansanjiang (rice) study site: errors (m), projections, pixel error, image number and average image overlap for crop surface models (CSMs). Ground control points (GCPs) measured by (differential) global positioning system ((D)GPS) or terrestrial laser scanning (TLS). *number of images covering the same part of area of interest (AOI).*

| GCP measurement | dataset | X error | Y error | Z error | projec-tions | error (pix) | image number | Ø image overlap* |
|---|---|---|---|---|---|---|---|---|
| DGPS | 15-May-2013 Rheinbach | 0.012 | 0.018 | 0.024 | 183 | 0.449 | 378 | >9 |
| GPS | 04-Jun-2012 Jiansanjiang | 0.183 | 0.193 | 0.308 | 141 | 5.274 | 24 | 4 |
| TLS | 04-Jun-2012 Jiansanjiang | 0.192 | 0.216 | 0.223 | 150 | 0.605 | 26 | 5 |

Position errors are 1-2 cm for the 378 images in the Rheinbach dataset. The average image overlap for this dataset is more than nine images per part of the AOI. In comparison, position errors are one magnitude bigger in the Jiansanjiang dataset with 18-30 cm and only 24 images. Consequently, there is less overlap of 4 images per part of the AOI. It has to be considered that the GCPs are measured with 1 m precision in Jiansanjiang (see **chapter 3.2.1**) due to limited global positioning system (GPS) device availability. To improve the CSM quality, GCP coordinates were substituted with new coordinates taken from a TLS point cloud with 1 cm accuracy. The resulting positioning errors in x- and y-direction remain in the same order with 19-22 cm but the error in z-direction drops from 0.31 to 0.22 cm. The visual comparison of the two models in **Figure 8-1** reveals how CSM quality increases. No artefacts from single images are visible (**Figure 8-1**, **right**). Additionally, the radial barrel or bowl effect with increasing height towards the CSM edges disappears (**Figure 8-1**, **left**). The barrel/bowl effect is a non-linear parabolic distortion in the model that leads to overestimation of heights on the model edges (**OUÉDRAOGO ET AL.**, **2014**). **UNGER ET AL.** (**2014**), **QUÉDRAOGO ET AL.** (**2014**) and users on the Agisoft forum (**AGISOFT FORUM**, **2014**) report on

this general systematic error when using Agisoft PhotoScan. However, the comparison in **Figure 8-1** shows that precise GCP coordinates help to remove that effect. To avoid systematic errors in the CSMs, GCP coordinates measured by differential GPS (DGPS) are the minimum requirement. GCP measurement with a total station would further improve the CSM quality (**HARWIN AND LUCIEER**, **2012**). Omitting the GCPs altogether by directly obtaining exterior image orientation from an on-board inertial measurement unit (IMU) (**CHIANG ET AL.**, **2012**; **COLOMINA AND MOLINA**, **2014**) will avoid the GCP accuracy problem. As a side effect the direct georeferencing will speed up data processing and even facilitate in-flight data processing (**ELING ET AL.**, **2014**; **XIANG AND TIAN**, **2011**). In summary, carefully planned image collection is the basis for high accuracy CSMs. For the following section, a good quality CSM is assumed, and its suitability for PH measurements is discussed.
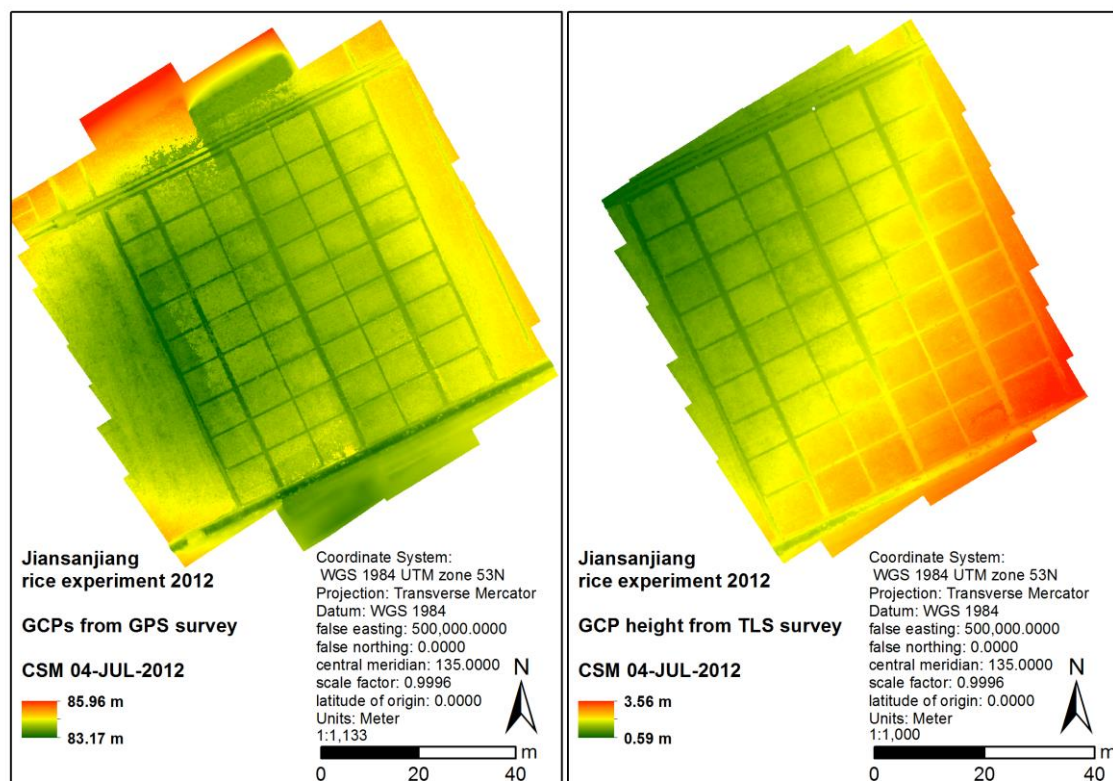


*Figure 8-1: CSM of rice study site in Jiansanjiang, China, 07 July 2012, left: GCP coordinates from low accuracy GPS and right: GCP coordinates from TLS point cloud (local coordinate system).*

## 8.2    Uncertainties in Plant Height Modelling

The question that arises when 3D models are used is: Does the model represent reality? In some cases there is a relatively simple answer to that question for example when the model represents a building. PH is not stable and there is no unambiguous answer to the question of how high a plant is at a given point in time. Plants move with the wind and the PH of certain crops varies significantly with their water stress level, for example in sugar beets (**GRENZDÖRFFER AND ZACHARIAS**, **2014**; **MUNZERT AND FRAHM**, **2006**). In other cases, the management practices of the field influence the suitability of a CSM for PH and plant growth (PG) estimation. In the Jiansanjiang dataset for rice (**chapter 3**) PH and PG are particularly difficult to model when no bare earth ground model is available before field irrigation. Water tables are constantly varying between and within the plots so that assuming an average water table is not an option. Therefore, absolute PH is difficult to obtain in rice. Classifying points in ground and vegetation or terrain filtering methods (**DANDOIS AND ELLIS**, **2013**) may be an option in such cases to work around the subtraction of a ground model. **GEIPEL ET AL.** (**2014**) successfully interpolate a ground model using Agisoft PhotoScan's recently integrated point classification tool. However, the approach will not work in a dense canopy where only few ground areas are visible in the images. **GRENZDÖRFFER AND ZACHARIAS** (**2014**) additionally report that software settings need to be adjusted for each dataset to obtain satisfactory results, which decreases the approach's grade of automation.

Moreover, the analysis of plant canopies, such as the unit of an experimental plot, reveals that even within a small area a high variation of PH occurs (**Figure 5-2**). **JONES AND VAUGHAN** (**2010**) suggest to adjust the sample number to the occurring variability and to divide the assessment sites from the training sites. Transferred to the PH reference measurements, this means that the number of samples would have had to be raised once the lodging occurred. Thus lodging introduces higher PH variability in each plot. In addition, the PH reference measurements are carried out and averaged over the entire plot and then compared with the PH of the CSM. Besides, additional uncertainty arises from the different people who conduct the reference measurements. Each person spontaneously picks different plants in a different distribution and reads heights from a ruler with different precision and from different angles. Therefore, manual PH control measurements may be used for CSM comparison as demonstrated in **chapters 4** and **5**, but should not be considered more representative than the CSM. For example it has been observed in **chapters 4** and **5** that PH from the CSM is lower than manually measured PH. This discrepancy indicates that PH modelled from CSM may provide a more truthful impression of the average canopy height.

Comparisons with the techniques presented in **chapter 2.2** could prove this hypothesis. **GRENZDÖRFFER AND ZACHARIAS (2014)** argue that the aim is to determine an exact spatially measured variable for PH rather than exactly measuring a single plants height. CSMs deliver exactly that, if PH is averaged over a spatial unit like an experimental plot.

## 8.3    Potentials of Biomass Estimation from Crop Surface Models

The previous chapter identifies CSMs as suitable for determining PH. Subsequently, this section discusses the suitability of PH to estimate biomass. The results in **chapter 5** demonstrate a significant relationship between PH and biomass of $R^2$ = 0.73-0.89 for different modelling scenarios. In the model application $R^2$ varies between 0.31 and 0.72. The results indicate that PH has potential in relation to modelling crop biomass. However, there are influencing factors on the model quality that need to be discussed. One factor is plant lodging. Removing the lodging varieties from the dataset yields an increased relationship between dry biomass and PH of $R^2$ = 0.89 in comparison to $R^2$ = 0.81 for the M1 model (70% calibration, 30% validation). The same accounts for model validation where $R^2$ increases from 0.60 to 0.64, as depicted in **Figure 8-2**. Similar observations are made for example by **JENSEN ET AL. (1990)** who report that lodging influences biomass and nitrogen estimation from radiometric measurements in barley. In summary, the model's prediction accuracy decreases when PH decreases due to crop lodging while the biomass might still be accumulating.
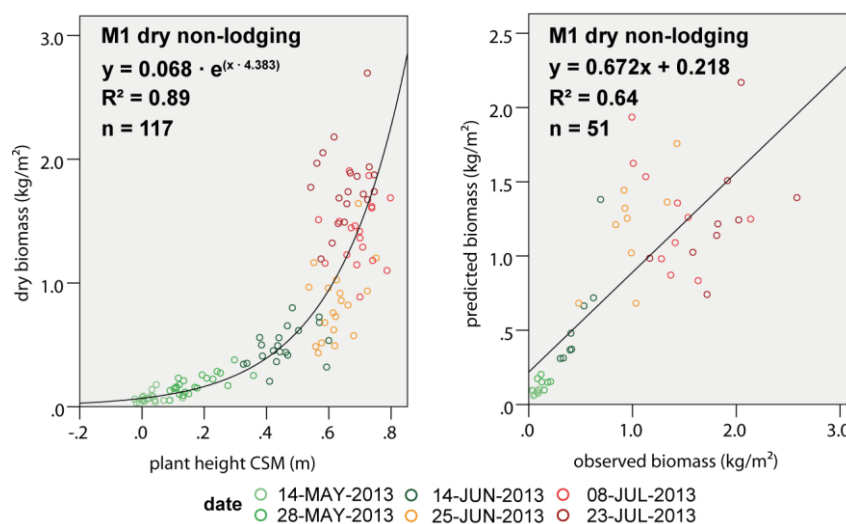


*Figure 8-2: Biomass modelling for M1 (70% calibration, 30% validation) without lodging cultivars (compare chapter 5.4); Left: Relationship between dry biomass and PH for the calibration dataset; Right: Cross-validation scatter plots for observed fresh and dry biomass versus predicted biomass.*

Additionally, the Rheinbach experimental field comprises 18 cultivars and two nitrogen treatments resulting in biomass variability among the cultivars and the treatments. With this heterogeneity in mind, the results are promising for a model that predicts biomass across the varying cultivars. **MERZ AND CHAPMAN** (**2011**) argue that variations in crop development among cultivars are often more subtle than those between treatments and thus difficult to assess. In this study's experiment, the number of cultivars (18) is significantly higher than the number of treatments (two). Consequently, variations among cultivars are more obvious than those between the treatments. For comparison, **SWAIN AND ZAMAN** (**2012**) yield an $R^2$ of 0.76 for biomass (n = 15) in an experiment with five different N-treatments, modelled from multispectral imaging (ADC Tetrcam$^{TM}$) in rice.

The graphs in **Figure 5-4** depict that there is a stronger correlation between $PH_{CSM}$ and fresh biomass than between $PH_{CSM}$ and dry biomass. Most studies examine the relationship between dry biomass and another variable since the dry biomass is closely linked to crop yield. However, the plant growth pattern has greater similarity with the pattern of fresh biomass throughout the growth stages. **Figure 8-3** illustrates how $PH_{CSM}$ and fresh biomass increase until 08 July and then slightly decrease, whereas the dry biomass slowly but constantly increases. The reasons for those phenomena lie in the phenology. The crops stop growing with after 08 July at fruit development stage (**Table 5-1**) and start to dry out (**CAMPBELL AND WYNNE**, **2011**). Conversely, it means that dry biomass estimation from CSMs will not work after a certain growth stage.

| | 14-MAY | 28-MAY | 14-JUN | 25-JUN | 08-JUL | 23-JUL |
|---|---|---|---|---|---|---|
| mean fresh biomass | 0.58 | 1.39 | 3.46 | 4.61 | 5.05 | 4.37 |
| mean dry biomass | 0.07 | 0.18 | 0.51 | 0.88 | 1.41 | 1.81 |
| mean plant height CSM | 0.04 | 0.18 | 0.49 | 0.63 | 0.65 | 0.61 |
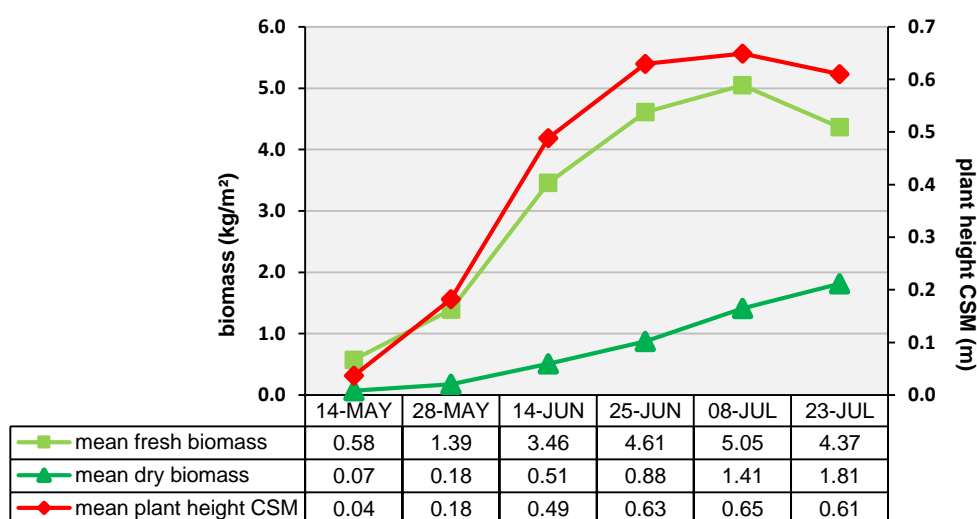
*Figure 8-3: Mean fresh biomass, dry biomass and PH$_{CSM}$ for each date of the summer barley study site Campus Klein-Altendorf, Rheinbach.*

Discussing the potentials of biomass estimation from CSMs, other methods for obtaining biomass models from PH should be taken into account as briefly discussed in **chapter 5.4**. Comparisons with terrestrial laser scanning (TLS) are obviously due to the similarly achievable spatial and temporal resolution. However, in practice it is found that the CSM comparison requires a thorough analysis of the underlying mechanisms of the TLS and UAV CSMs. Data for a suitable comparison is available for the Rheinbach study site but differs in the details of data analysis. For example different non-vegetation ground models are used in the datasets. In addition, the mean maximum PH per plot is calculated from the TLS data (**TILLY ET AL.**, **2014**), whereas the mean average PH is calculated from the UAV data (**chapter 4.2.5**). Furthermore, the underlying preprocessing steps for both datasets need to be examined. Therefore, the dataset comparison is beyond the scope of this study.

Future sensor development goes towards the newly emerging field of UAV-based laser scanning (**LIN ET AL.**, **2011**; **WALLACE ET AL.**, **2012**) with new lightweight laser scanners recently becoming available like the 2.2 kg YellowScan (**L'AVION JAUNE S.A.R.L.**, **2014**) with integrated GPS and the 3.6-3.85 kg VUX-1 (**RIEGL LASER MEASUREMENT SYSTEMS GMBH**, **2014a**) that will be integrated in the soon available RiCOPTER (**RIEGL LASER MEASUREMENT SYSTEMS GMBH**, **2014b**) out of the box UAV-system.

## 8.4 Combining Vegetation Indices and Crop Surface Models for Biomass Estimation

This chapter addresses two aspects: the calculation of $VI_{VIS}$ from UAV-based imagery and the combination with PH from the CSMs. Biomass modelling from two or more combined variables is common practice in remote sensing (**KOPPE ET AL.**, **2013**; **LIU ET AL.**, **2006**). But a literature review shows that it is a novelty in UAV-based high spatial and temporal resolution studies of crops. There are a number of studies in which VIs are derived from UAV-based imaging (**BELLVERT ET AL.**, **2014**; **SUÁREZ ET AL.**, **2010**; **TURNER ET AL.**, **2011**; **ZARCO-TEJADA ET AL.**, **2005**). However, those studies rarely address biomass monitoring like the study by **SWAIN ET AL.** (**2010**), who found a strong relationship ($R^2 = 0.73$) between Normalized Difference Vegetation Index (NDVI) and biomass in rice. An example for using $VI_{VIS}$ to model biomass is demonstrated by **HUNT EL AL.** (**2005**) who investigate correlations of the Green Red Vegetation Index (GRVI) and biomass in alfalfa ($R^2 = 0.47$), soybean ($R^2 = 0.39$) and corn ($R^2 = 0.88$). **BALLESTEROS ET AL.** (**2014**) give another example, not for biomass but leaf area index (LAI), where a strong correlation is found between LAI and Vegetation Atmospherically Resistant Index (VARI) in a two year study in maize ($R^2 = 0.89$) and onion ($R^2 = 0.84$). Combining VIs and PH have only been addressed once for yield estimation in a study by **GEIPEL ET AL.**

(**2014**). They use the VI$_{VIS}$ to determine a crop coverage factor and combined it with PH in a multiple linear regression (R² up to 0.74). In other words, the analysis in **chapter 6** can be considered innovative and examples are found in the literature that identify VI$_{VIS}$ as suitable for biomass monitoring (**CHANG ET AL., 2005**).

Another novelty of **chapter 6** are the two newly developed VI$_{VIS}$, the modified GRVI (MGRVI) and the Red-Green-Blue VI (RGBVI). Both produce a similar pattern in relation to biomass, since they are based on the difference between green reflectance and either red, or red and blue reflectance. However, the relationship's strength largely depends on the modelling approach and the time window chosen for the analysis. The scatter plot of RGBVI *versus* dry biomass (**Figure 8-4**) shows vertical clusters with strikingly low RGBVI values on 25 June and two clusters on 08 July. In other words it indicates that there is neither a linear, nor an exponential relationship between RGBVI and dry biomass on those two dates. Comparable studies in different crops by **MOTOHKA ET AL.** (**2010**), **HUNT ET AL.** (**2005**) and **TUCKER** (**1979**) support the hypothesis that VI$_{VIS}$ are best suited for early growth stages (see **chapter 6.4**).
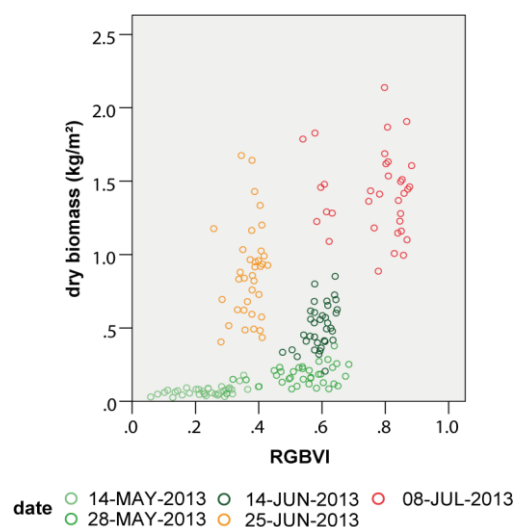


*Figure 8-4: Scatter plot for dry biomass versus RGBVI of the summer barley study site Campus Klein-Altendorf, Rheinbach; n = 178.*

While it is possible that the pattern in **Figure 8-4** is exclusively a result of differences in canopy reflectance, another explanation is more likely. The fact that the data is used uncalibrated and mosaicked in an orthophoto induces spectral uncertainty. In the case of airborne data collection by UAVs, bidirectional reflectance difference function (BRDF) effects (**GRENZDÖRFFER AND NIEMEYER, 2011**), and reflectance differences due to changing irradiance influence the resulting image (**GUILLEN-CLIMENT ET AL., 2012**). A simple solution for uncertainty in lighting conditions is to capture a

single image of the whole area of interest (AOI) in cases in which sufficient ground resolution can be maintained. When using RGB imagery for $VI_{VIS}$ calculation, it is important to keep exposure settings fixed during the flight or to use ground targets for calibration (**HUNT JR. ET AL.**, **2005**).

Compared to ground-based spectroradiometers, $VI_{VIS}$ from UAV-based RGB imagery are noisier and thus less spectrally exact (**SAMSEEMOUNG ET AL.**, **2012**). However, the advantage of spatial information opposed to point-wise measurements might partly outweigh the uncertainties. In this context, the recent development of lightweight hyperspectral full frame cameras is highly promising (**chapter 7**). Since the hyperspectral full frame cameras have a sufficient spatial resolution for CSMs calculation (currently about 1 megapixel), a fusion of spectral and spatial information in 3D-hyperspectral CSMs is obvious (**Figure 7-13**). New opportunities for combining VIs and CSM-derived PH emerge from those technological innovations.

## 8.5    Additional Applications of UAV-based Imaging and Crop Surface Models

In addition to biomass estimation, CSMs are useful for further applications in precision agriculture and plant breeding. In plant breeding, monitoring PH on a plot level is highly demanded for phenotyping or plant phenomics that is defined as the measurement of plant phenotype *i.e.* physical plant characteristics (**MERZ AND CHAPMAN**, **2011**). Phenotyping is realised in extensive crop breeding trials that are expensive to monitor (**CHAPMAN ET AL.**, **2014**). Speeding up the data collection and data analysis process by using UAV-based imaging would reduce the time for delivering new cultivars. A simple map demonstrates the potential of CSMs for phenotyping, generated from one of the $VI_{VIS}$ calculated within the scope of this study. **Figure 8-5** depicts the summer barley study site in Rheinbach on 14 June 2013. The plot colours are based on 18 RGBVI (**chapter 6.2.6.2**) classes with a natural breaks classification. According to **Figure 8-5**, 10 of the 18 cultivars fall in adjacent classes, indicating a potential for cultivar discrimination based on the RGBVI. It is interesting to note that those results are obtained solely from RGB-imaging and a simple $VI_{VIS}$ calculation. However, more extensive testing is needed to identify the most suitable growth stage and a more sophisticated classification for such analysis. Furthermore, tests should be executed across multiple years, changing locations, and for different crops.
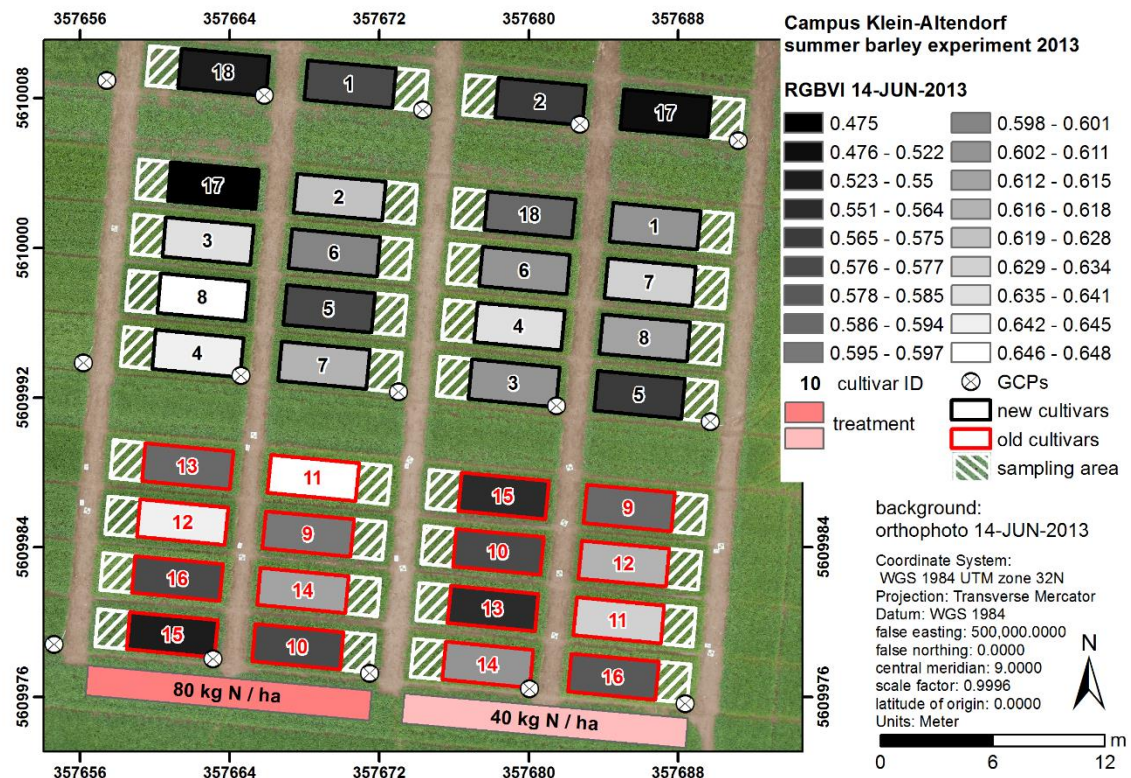
*Figure 8-5: Cultivar discrimination based on RGBVI at the summer barley study site Campus Klein-Altendorf, Rheinbach, 14 June 2013, GCPs = ground control points used for CSM generation.*

A second application of CSMs can be the monitoring of crop lodging that is desired in phenotyping trials. It is important to identify and quantify lodging since it is a major cause of yield loss (**BERRY AND SPINK**, **2012**). Lodging in summer barley is caused by high precipitation shortly before, and during stem elongation stage, making the crop prone to leaf diseases (**MUNZERT AND FRAHM**, **2006**). Additionally, the plant's centre of gravity, which is a function of PH, may be used to calculate lodging risk (**BAKER ET AL.**, **1998**). Lodging can be quantified using CSMs by determining the point in time of occurrence and the extent of crop lodging based on PH thresholds. Such knowledge leads to the deduction of cultivar-related growth patterns that may be considered in cultivar selection and field management. UAV-based RS and derived CSMs can significantly speed up the data collection of the crop lodging status with high spatial and temporal resolution. **LIU ET AL.** (**2014**) suggest an object-oriented approach to detect lodging areas based on reflectance and texture analysis. **CHAPMAN ET AL.** (**2014**) demonstrate automated lodging detection by determining a threshold for height variance per plot and extracting the canopy's average height of lodged and standing fractions. Following the approach by **CHAPMAN ET AL.** (**2014**), a map with two PH classes is generated again from the Rheinbach study site in **Figure 8-6**. The map shows the orthophoto and

PH for 08 July 2013, since lodging occurs from heading stage onwards. Lodging areas can be identified by visual inspection of the orthophoto. Those areas correspond with the red areas marking PH of 0.5 m or lower. Lodging varieties are the old cultivars 10, 11, 12 and 14. Additionally, the lodged area per plot can be extracted.



*Figure 8-6: Lodging detection based on PH at the summer barley study site Campus Klein-Altendorf, Rheinbach, 08 July 2013, GCPs = ground control points used for CSM generation.*

A third important variable in phenotyping is the establishment rate, the ground cover of the crop in early growth stages (**Acquaah**, **2012**). A crop is considered as established when it is safe from juvenile mortality and no longer in need of special protection (**Schlegel, 2009**). Maps of crop cover can easily by derived from UAV-based imaging and help to quantify crop establishment. As an example, **Woebekke et al.** (**1995**) distinguish plants (weed) from soil by using the Excess Green Index calculated from RGB imagery. **Torres-Sánchez et al.** (**2014**) evaluate UAV-based RGB imagery for the mapping of vegetation fraction of a wheat field. To derive a crop cover for the Rheinbach study site, the RGBVI on 14 May 2013 is grouped into two classes in **Figure 8-7**. An RGBVI of 0.174 and higher indicates that the area is covered by crop canopy.
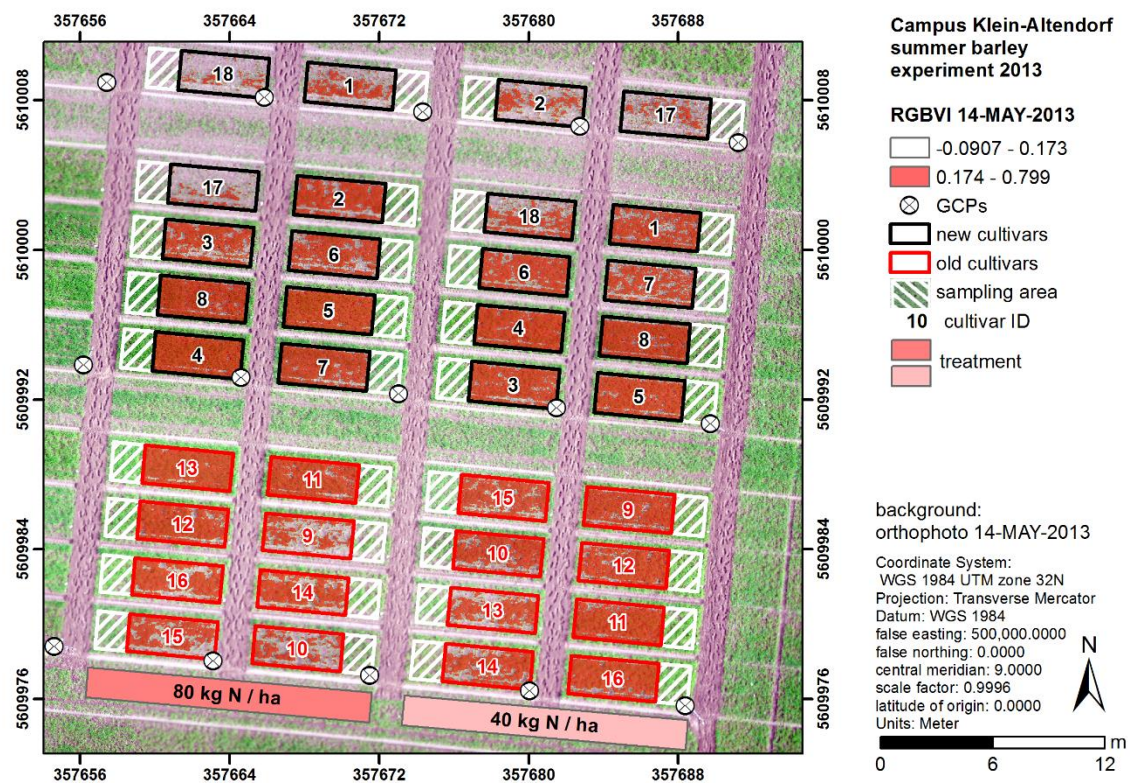
*Figure 8-7: Crop cover based on RGBVI at the summer barley study site Campus Klein-Altendorf, Rheinbach, 14 May 2013, GCPs = ground control points used for CSM generation.*

Ultimately, the spatial distribution of plants is the information of interest. Similar information is required in variable rate technology (VRT). In the field of precision agriculture, VRT for seeding, fertilization, irrigation or plant protection is one of the most advanced precision agriculture techniques (OERKE ET AL., 2010; WHELAN AND TAYLOR, 2013). Spatially related information about crop growth status is of major importance before VRT application and for monitoring the effects of VRT application (ZHANG AND KOVACS, 2012). CSMs provide such spatial information that may be visualized in zonal maps of crop growth status, delivering important data for precision agriculture applications (SEELAN ET AL., 2003; YANG ET AL., 2006). Closely linked to the plants' spatial distribution are attempts to recognize shape, texture and colour properties to classify species into crop or weed categories (SAMSEEMOUNG ET AL., 2012). Such classifications are executed by using object based image analysis (OBIA) and VIs (PEÑA ET AL., 2013; TORRES-SÁNCHEZ ET AL., 2013). In summary, there are a number of additional applications of CSMs in the fields of phenotyping and precision agriculture that need to be explored yet.

## 8.6    Limits of the Method and Dataset

As previously discussed, a model can only be as good as its input data. In the context of UAV-based imaging, careful flight planning is crucial. For crop monitoring throughout the growing season, data should be recorded at least every two weeks. It can be difficult to meet both, the requirements for good quality datasets and a sufficient spatial resolution when weather conditions are unfavourable. Thus the environment may limit the achievable accuracy for example in exposed positions. The MK-Oktokopter used in this study is operable up to about 25 km/h wind speed that is easily reached on windy days even in sheltered positions. Secondly, UAV systems are usually not rainproof with few exceptions like the microdrone md4-1000 (**MICRODRONES, 2014**). For imaging applications it would not make sense to fly in the rain. But if a system is not waterproof, it means that extra care needs to be taken when operating in wet environments such as irrigated rice fields or close to larger water bodies. Another limitation may lie in the nature of airborne systems. In the event of a major crash, the platform and sensor could be destroyed resulting in loss of expensive equipment. However, experience shows that the MK-Oktokopter can be considered as a stable, widely used platform (**BAIOCCHI ET AL.**, 2013; **DANDOIS AND ELLIS**, 2013; **PFEIFER ET AL.**, 2012; **VON BUEREN ET AL.**, 2014). Another limit is the endurance of small UAVs and thus its flight radius. Small study sites up to a few hectare can easily be covered but monitoring bigger fields requires a platform change (**COLOMINA AND MOLINA**, 2014). Changing to a fixed-wing UAV means longer endurance but different flight qualities for example the inability to hover in the air, platform instability and higher ground speed (**ABER ET AL.**, 2010; **NONAMI ET AL.**, 2010). Apart from flight endurance and resulting area coverage, georeferencing poses limits on the area to be observed. As long as GCPs are required those need to be installed in the field and measured, which is time-consuming. Ultimately, legal restrictions may limit the usage of UAV-systems. **HARDIN AND JENSEN** (**2011a**) even regard it as the main obstacle that stops the technology from spreading. Currently, the legal framework for UAV operation is complicated, highly heterogeneous and undetermined in many countries and even within the German federal states. National and international authorities are working on a uniform legal regulation for UAV operation (**EVERAERTS**, 2009). In 2013, roadmaps have been released by the US Federal Aviation Administration (FAA) and European RPAS Steering group (ERSG) that aim to develop and unify regulations (**COLOMINA AND MOLINA**, 2014).

Apart from the platform used for data collection, there are open questions in the data processing with Agisoft PhotoScan. Underlying mechanisms for georeferencing, bundle block adjustment and the calculated accuracies included in the processing reports are not well documented (**SONA ET AL.**,

**2014**). Point cloud quality and interpolation methods, and the orthophoto mosaicking (**chapter 6.4**) may only be controlled to a certain extent due to limited customisation options (**Verhoeven, 2011**). Thus, interpreting and comparing results is difficult.

In regard to biomass estimation, there are limits of achievable model quality on experimental sites. First of all, experimental sites need to be well managed. Good management means that care is taken for even seeding, treatment and irrigation, where desired. As an example, if in-field variability only mirrors uneven fertilizer application, it is hard to distinguish growth patterns of different cultivars. Although comparisons with destructive samples are worthwhile, those samples can be erroneous. Biomass may be lost during packaging, cleaning and weighing. Such inaccuracies would even themselves out with a high number of samples. But destructive sampling is time-consuming, labour-intensive and expensive, thus the number of samples is restricted by the aforementioned factors. Furthermore, the dataset collected for this study only covers one field for one year. The derived biomass models are of local value and cannot be considered robust until they have been tested over several years and in different locations. In addition, the method should be tested on similar crops like wheat and rice, crops with different growth patterns, like sugarcane and maize, and in other fields where biomass plays an important role like greenland farming. The method might require adjustment to be transferable to high growing crops such as sugarcane and maize. Moreover, the relationship between biomass and PH as well as VIs is firstly empirical and secondly indirect und thus naturally limits the achievable accuracy of biomass estimation in a field (**Kumar et al., 2001**). Lastly, a simple biomass model does not account for additional causes of variability like climate, soil and the like (see **chapter 1**). Some of those factors are commonly included in crop growth models such as water and nitrogen (N) availability (**Moriondo et al., 2007**), temperature, soil type and status (**Clevers and Jongschaap, 2001**; **Confalonieri et al., 2011**).

# 9   Conclusions and Future Challenges

On completion of the discussion, the following conclusions can be drawn: first, crop monitoring with UAVs is possible at high spatial and temporal resolution and thus provides a valuable contribution to variability detection in agricultural production. The concept of multi-temporal crop surface models is successfully transferred to UAV-based RGB imaging. Although the method has its constraints, it is highly suitable for accurate plant height and plant growth modelling when applied correctly. Secondly, the method is suitable for biomass estimation which is supported by comparisons with biomass estimation from vegetation indices. It should be noted that the quality of the estimation depends on the accuracy of the crop surface model. Thirdly, the question whether biomass estimation benefits from a combination of UAV-derived plant height and visible band vegetation indices cannot be answered completely. Obtaining visible band vegetation indices from UAV-based RGB imaging is promising but requires further research for the successful implementation. The main constraint is the use of uncalibrated images. Thus, from the results of this study it is not clear that the combination of plant height and visible band vegetation indices significantly improves biomass estimation. In summary, the main advantages of UAV-based RGB imaging are high spatial resolution data, in short processing time at relatively low cost. Consequently, systematic monitoring of plant height and biomass is possible throughout the growing season.

With regard to the available literature it follows that there are only a few studies that thoroughly investigate the relationship between biomass and PH for crops on a high-resolution canopy scale. Even less studies address visible band vegetation indices from UAV-based imaging and their relation to biomass. Crop surface models (CSMs) from UAV-based RGB imaging combine both approaches by providing 3D and spectral information, thus avoiding alignment problems between the data and saving data collection and processing time. Therefore, studies should focus on time-efficient methods like UAV-based CSMs and orthophotos. UAV-based RGB imaging fulfils key aspects of a remote sensing technique for precision agriculture applications (JONES AND VAUGHAN, **2010**): timeliness, relevant spatial resolution for the available field management options, accurate estimation of relevant parameters, and reasonable costs. A critical point is the accuracy that can only be quantified and improved by extensive studies. UAV applications in remote sensing and precision agriculture are at an early stage of research and thus progression in sensor and platform development, and automation in data collection and data processing will increase the method's accuracy, practicability and automation.

Since the beginning of this study the availability of affordable out-of-the-box systems has increased, as well as the battery power and thus the size and payload of UAVs. Affordable, easy to use systems such as the DJI Phantom allow RGB imaging for inexperienced pilots. Evolving applications of hyperspectral line scanners and full-frame cameras, UAV-borne laser scanners and UAV swarm flights have great potential for new insights in the use of vegetation indices and high resolution 3D data. However, UAV-based remote sensing methods can only have an impact on real world scenarios if they are available to a broad scientific audience and, even more important, to the public. Experience shows, that there is lacking exchange even between scientists working in remote sensing and scientists working in plant breeding, phenotyping and weed research (CHAPMAN ET AL., **2014**; RASMUSSEN ET AL., **2013**). Future development of UAV-based remote sensing would greatly benefit from a strong network of remote sensing experts and plant experts. Additional interchange with farmers would further reveal the needs in practical farming as suggested in the learning community approach by SEELAN ET AL. (**2003**). Consequently, crop monitoring with UAVs should be made available to non-professionals like farmers or local service providers to facilitate area-wide application. Numerous companies provide UAV systems and services. Among them are newly emerging companies, established providers of remote sensing technologies and even well-known logistics companies. Thus future dissemination of UAVs in PA is most likely. Modern farmers are part of the smartphone and Facebook generation, and direct beneficiaries of the rapid development of available sensors and computational resources at dropping prices. On-demand mapping from UAV-based data for the farmer's smartphone is not just a dream of the future. Admittedly, technology insensitive agriculture can only be applied where adequate knowhow and infrastructure is available. Thus, the benefits for the world's less developed regions depend on how effectively the technology will be tailored to the local conditions. At a general level, the reliable estimate of plant height and biomass contributes to more effective yields. A productive agriculture is essential against the background of the aforementioned increasing population when natural resources are becoming vulnerable at the same time.

## References*Chapters 1,2,8,9

ABER, J.S., MARZOLFF, I., RIES, J., **2010**. Small-Format Aerial Photography: Principles, techniques and geoscience applications. Elsevier, Amsterdam, Netherlands.

ACQUAAH, G., **2012**. Principles of Plant Genetics and Breeding, 2nd ed. John Wiley & Sons, Ltd, Oxford, UK.

ADAMCHUK, V.I., FERGUSON, R.B., HERGERT, G.W., **2010**. Soil Heterogeneity and Crop Growth, in: Oerke, E.-C., Gerhards, R., Menz, G., Sikora, R.A. (Eds.), Precision Crop Protection - the Challenge and Use of Heterogeneity. Springer, Dordrecht, Netherlands, pp. 3–16.

AGISOFT FORUM, **2014**. Agisoft forum: search results for bowl effect. [WWW Document]. URL http://www.agisoft.com/forum/index.php?action=search2 (accessed 10.12.14).

AGISOFT LLC, **2013**. Agisoft PhotoScan User Manual - Professional Edition, Version 1.0.

ALBERTZ, J., **2007**. Einführung in die Fernerkundung. Grundlagen und Interpretation von Luft- und Satellitenbildern, 3rd ed. WBG, Darmstadt, Germany.

ATZBERGER, C., **2013**. Advances in Remote Sensing of Agriculture: Context Description, Existing Operational Monitoring Systems and Major Information Needs. Remote Sensing 5, 949–981. doi:10.3390/rs5020949

BAIOCCHI, V., DOMINICI, D., ELAIOPOULOS, M., MASSIMI, V., MORMILE, M., ROSCIANO, E., **2013**. UAV flight plan software: first implementation of UP23d, in: Lasaponara, R., Masini, N., Biscione, M. (Eds.), Proceedings of the 33th EARSeL Symposium Towards Horizon 2020: Earth Observation and Social Perspectives. Presented at the 33th EARSeL Symposium Towards Horizon 2020: Earth Observation and Social Perspectives, Matera, Italy.

BAKER, C.J., BERRY, P.M., SPINK, J.H., SYLVESTER-BRADLEY, R., GRIFFIN, J.M., SCOTT, R.K., CLARE, R.W., **1998**. A Method for the Assessment of the Risk of Wheat Lodging. Journal of Theoretical Biology 194, 587–603. doi:10.1006/jtbi.1998.0778

BALLESTEROS, R., ORTEGA, J.F., HERNÁNDEZ, D., MORENO, M.A., **2014**. Applications of georeferenced high-resolution images obtained with unmanned aerial vehicles. Part II: application to maize and onion crops of a semi-arid region in Spain. Precision Agriculture 15, 593–614. doi:10.1007/s11119-014-9357-6

BALUJA, J., DIAGO, M.P., BALDA, P., ZORER, R., MEGGIO, F., MORALES, F., TARDAGUILA, J., **2012**. Assessment of vineyard water status variability by thermal and multispectral imagery using an unmanned aerial vehicle (UAV). Irrigation Science 6, 511–522.

BANNARI, A., MORIN, D., BONN, F., HUETE, A.R., **1995**. A review of vegetation indices. Remote Sensing Reviews 13, 95–120. doi:10.1080/02757259509532298

BARET, F., GUYOT, G., **1991**. Potentials and limits of vegetation indices for LAI and APAR assessment. Remote Sensing of Environment 35, 161–173. doi:10.1016/0034-4257(91)90009-U

BARET, F., GUYOT, G., MAJOR, D.J., **1989**. Crop biomass evaluation using radiometric measurements. Photogrammetria 43, 241–256. doi:10.1016/0031-8663(89)90001-X

BARETH, G., BENDIG, J., AASEN, H., GNYP, M.L., BOLTEN, A., JUNG, A., MICHELS, R., SOUKKAMÄKI, J., **2015**. Low-weight and UAV-based hyperspectral full-frame cameras for monitoring crops: spectral comparison with portable spectroradiometer measurements. Photogrammetrie - Fernerkundung - Geoinformation accepted.

BÄUMKER, M., PRZYBILLA, H.-J., **2011**. Investigations on the accuracy of the navigation data of unmanned aerial vehicles using the example of the system mikrokopter, in: International Archives of Photogrammetry, Remote Sensing and Spatial Information Sciences. Presented at the UAV-g 2011, Zurich, Switzerland, p. 6.

BEADLE, C.L., LONG, S.P., **1985**. Photosynthesis — is it limiting to biomass production? Biomass 8, 119–168. doi:10.1016/0144-4565(85)90022-8

BELLVERT, J., ZARCO-TEJADA, P.J., GIRONA, J., FERERES, E., **2014**. Mapping crop water stress index in a "Pinot-noir" vineyard: comparing ground measurements with thermal remote sensing imagery from an unmanned aerial vehicle. Precision Agriculture 15, 361–376. doi:10.1007/s11119-013-9334-5

BENDIG, J., BOLTEN, A., BARETH, G., **2012**. Introducing a low-cost mini-UAV for thermal-and multi-spectral-imaging. International Archives of the Photogrammetry, Remote Sensing and Spatial Information Sciences 39, 345–349.

BENDIG, J., BOLTEN, A., BARETH, G., **2013**. UAV-based Imaging for Multi-Temporal, very high Resolution Crop Surface Models to monitor Crop Growth Variability. Photogrammetrie - Fernerkundung - Geoinformation 6, 551–562. doi:10.1127/1432-8364/2013/0200

BENDIG, J., BOLTEN, A., BENNERTZ, S., BROSCHEIT, J., EICHFUSS, S., BARETH, G., **2014a**. Estimating Biomass of Barley Using Crop Surface Models (CSMs) Derived from UAV-Based RGB Imaging. Remote Sensing 6, 10395–10412. doi:10.3390/rs61110395

BENDIG, J., WILLKOMM, M., TILLY, N., GNYP, M.L., BENNERTZ, S., LENZ-WIEDEMANN, I.S., BARETH, G., MIAO, Y., **2014b**. Hochauflösende Crop Surface Models (CSM) auf der Basis von Stereobildern aus UAV-Befliegungen zur Überwachung von Reiswachstum in Nordostchina. gis.Science 01, 1–9.

BENDIG, J., YU, K., AASEN, H., BOLTEN, A., BENNERTZ, S., BROSCHEIT, J., GNYP, M.L., BARETH, G., **submitted**. Combining UAV-based Crop Surface Models, Visible and Near Infrared Vegetation Indices for Biomass Monitoring in Barley. International Journal of Applied Earth Observation and Geoinformation.

BERNI, J.A.J., ZARCO-TEJADA, P.J., SUAREZ, L., FERERES, E., **2009a**. Thermal and Narrowband Multispectral Remote Sensing for Vegetation Monitoring From an Unmanned Aerial Vehicle. IEEE Transactions on Geoscience and Remote Sensing 47, 722–738. doi:10.1109/TGRS.2008.2010457

BERNI, J.A.J., ZARCO-TEJADA, P.J., SUÁREZ, L., GONZÁLEZ-DUGO, V., FERERES, E., **2009b**. Remote sensing of vegetation from UAV platforms using lightweight multispectral and thermal imaging sensors. International Archives of Photogrammetry, Remote Sensing and Spatial Information Sciences 38, 6.

BERRY, P.M., SPINK, J., **2012**. Predicting yield losses caused by lodging in wheat. Field Crops Research 137, 19–26. doi:10.1016/j.fcr.2012.07.019

BERRY, P.M., STERLING, M., BAKER, C.J., SPINK, J., SPARKES, D.L., **2003**. A calibrated model of wheat lodging compared with field measurements. Agricultural and Forest Meteorology 119, 167–180. doi:10.1016/S0168-1923(03)00139-4

BGR, **1994**. Bundesanstalt für Geowissenschaften und Rohstoffe: Bodenübersichtskarte der Bundesrepublik Deutschland 1:1.000.000 (BÜK1000DE).

BONGIOVANNI, R., LOWENBERG-DEBOER, J., **2004**. Precision Agriculture and Sustainability. Precision Agriculture 5, 359–387. doi:10.1023/B:PRAG.0000040806.39604.aa

BUSEMEYER, L., MENTRUP, D., MÖLLER, K., WUNDER, E., ALHEIT, K., HAHN, V., MAURER, H.P., REIF, J.C., WÜRSCHUM, T., MÜLLER, J., RAHE, F., RUCKELSHAUSEN, A., **2013**. BreedVision - A Multi-Sensor Platform for Non-Destructive Field-Based Phenotyping in Plant Breeding. Sensors 13, 2830–2847. doi:10.3390/s130302830

CALDERÓN, R., MONTES-BORREGO, M., LANDA, B.B., NAVAS-CORTÉS, J.A., ZARCO-TEJADA, P.J., **2014**. Detection of downy mildew of opium poppy using high-resolution multi-spectral and thermal imagery acquired with an unmanned aerial vehicle. Precision Agriculture 15, 639–661. doi:10.1007/s11119-014-9360-y

CAMPBELL, J.B., WYNNE, R.H., **2011**. Introduction to Remote Sensing, 5th ed. The Guilford Press, New York, U.S.

CAO, Q., MIAO, Y., WANG, H., HUANG, S., CHENG, S., KHOSLA, R., JIANG, R., **2013**. Non-destructive estimation of rice plant nitrogen status with Crop Circle multispectral active canopy sensor. Field Crops Research 154, 133–144. doi:10.1016/j.fcr.2013.08.005

CARLSON, T.N., RIPLEY, D.A., **1997**. On the relation between NDVI, fractional vegetation cover, and leaf area index. Remote Sensing of Environment 62, 241–252. doi:10.1016/S0034-4257(97)00104-1

CATCHPOLE, W.R., WHEELER, C.J., **1992**. Estimating plant biomass: A review of techniques. Australian Journal of Ecology 17, 121–131. doi:10.1111/j.1442-9993.1992.tb00790.x

CHANG, K.-W., SHEN, Y., LO, J.-C., **2005**. Predicting Rice Yield Using Canopy Reflectance Measured at Booting Stage. Agronomy Journal 97, 872. doi:10.2134/agronj2004.0162

CHAPMAN, S., MERZ, T., CHAN, A., JACKWAY, P., HRABAR, S., DRECCER, M., HOLLAND, E., ZHENG, B., LING, T., JIMENEZ-BERNI, J., **2014**. Pheno-Copter: A Low-Altitude, Autonomous Remote-Sensing Robotic Helicopter for High-Throughput Field-Based Phenotyping. Agronomy 4, 279–301. doi:10.3390/agronomy4020279

CHIANG, K.-W., TSAI, M.-L., CHU, C.-H., **2012**. The Development of an UAV Borne Direct Georeferenced Photogrammetric Platform for Ground Control Point Free Applications. Sensors 12, 9161–9180. doi:10.3390/s120709161

CHINGKWEI, L., OU, S. (EDS.), **1999**. Soils of China. Science Press, Beijing, China.

CLEVERS, J.P.G.W., JONGSCHAAP, R., **2001**. Imaging Spectrometry For Agricultural Applications, in: Meer, F.D. van der, Jong, S.M.D. (Eds.), Imaging Spectrometry, Remote Sensing and Digital Image Processing. Kluwer Academic Publishers, Dordrecht, Netherlands, pp. 157–199.

COHEN, W.B., MAIERSPERGER, T.K., GOWER, S.T., TURNER, D.P., **2003**. An improved strategy for regression of biophysical variables and Landsat ETM+ data. Remote Sensing of Environment 84, 561–571. doi:10.1016/S0034-4257(02)00173-6

COLOMINA, I., MOLINA, P., **2014**. Unmanned aerial systems for photogrammetry and remote sensing: A review. ISPRS Journal of Photogrammetry and Remote Sensing 92, 79–97. doi:10.1016/j.isprsjprs.2014.02.013

CONFALONIERI, R., BREGAGLIO, S., ROSENMUND, A.S., ACUTIS, M., SAVIN, I., **2011**. A model for simulating the height of rice plants. European Journal of Agronomy 34, 20–25. doi:10.1016/j.eja.2010.09.003

COOPS, N.C., JOHNSON, M., WULDER, M.A., WHITE, J.C., **2006**. Assessment of QuickBird high spatial resolution imagery to detect red attack damage due to mountain pine beetle infestation. Remote Sensing of Environment 103, 67–80. doi:10.1016/j.rse.2006.03.012

DANDOIS, J.P., ELLIS, E.C., **2013**. High spatial resolution three-dimensional mapping of vegetation spectral dynamics using computer vision. Remote Sensing of Environment 136, 259–276. doi:10.1016/j.rse.2013.04.005

DONEUS, M., VERHOEVEN, G., FERA, M., BRIESE, C., KUCERA, M., NEUBAUER, W., **2011**. From deposit to point cloud: a study of low-cost computer vision approaches for the straightforward documentation of archaeological excavations, in: Pavelka, K. (Ed.), Proceedings of the XXIIIrd International CIPA Symposium. Presented at the XXIIIrd International CIPA Symposium, Prague, Czech Republic, pp. 81–88.

EHLERT, D., ADAMEK, R., HORN, H.-J., **2009**. Laser rangefinder-based measuring of crop biomass under field conditions. Precision Agriculture 10, 395–408. doi:10.1007/s11119-009-9114-4

EHLERT, D., HORN, H.-J., ADAMEK, R., **2008**. Measuring crop biomass density by laser triangulation. Computers and Electronics in Agriculture 61, 117–125. doi:10.1016/j.compag.2007.09.013

EISENBEISS, H., **2009**. UAV photogrammetry (dissertation). ETH, Zurich, Switzerland.

ELING, C., KLINGBEIL, L., WIELAND, M., KUHLMANN, H., **2014**. Direct Georeferencing of Micro Aerial Vehicles – System Design, System Calibration and First Evaluation Tests. Photogrammetrie - Fernerkundung - Geoinformation 4, 227–237. doi:10.1127/1432-8364/2014/0200

EVERAERTS, J., **2009**. New Platforms - Unconventional Platforms (Unmanned Aircraft Systems) for Remote Sensing (final report No. 56), Official publications of the EuroSDR. Euro SDR, Frankfurt am Main, Germany.

FENDER, F., HANKKENEN, M., LINZ, A., RUCKELSHAUSEN, A., SPICER, M., **2005**. Messende Lichtgitter und Multispektralkameras als bildgebende Systeme zur Pflanzenerkennung. Bornimer Agrartechnische Berichte 40, 7–16.

FOLEY, J.A., RAMANKUTTY, N., BRAUMAN, K.A., CASSIDY, E.S., GERBER, J.S., JOHNSTON, M., MUELLER, N.D., O'CONNELL, C., RAY, D.K., WEST, P.C., BALZER, C., BENNETT, E.M., CARPENTER, S.R., HILL, J., MONFREDA, C., POLASKY, S., ROCKSTRÖM, J., SHEEHAN, J., SIEBERT, S., TILMAN, D., ZAKS, D.P.M., **2011**. Solutions for a cultivated planet. Nature 478, 337–342. doi:10.1038/nature10452

FOOD AND AGRICULTURE ORGANIZATION OF THE UNITED NATIONS, **2013**. FAO statistical yearbook 2013: World food and agriculture. Rome, Italy.

GAMON, J.A., SURFUS, J.S., **1999**. Assessing leaf pigment content and activity with a reflectometer. New Phytologist 143, 105–117. doi:10.1046/j.1469-8137.1999.00424.x

GEBBERS, R., ADAMCHUK, V.I., **2010**. Precision Agriculture and Food Security. Science 327, 828–831. doi:10.1126/science.1183899

GEIPEL, J., LINK, J., CLAUPEIN, W., **2014**. Combined Spectral and Spatial Modeling of Corn Yield Based on Aerial Images and Crop Surface Models Acquired with an Unmanned Aircraft System. Remote Sensing 6, 10335–10355. doi:10.3390/rs61110335

GINI, R., PAGLIARI, D., PASSONI, D., PINTO, L., SONA, G., DOSSO, P., GRENZDÖRFFER, G., BILL, R., **2013**. UAV Photogrammetry: Block triangulation comparisons. International Archives of the Photogrammetry, Remote Sensing and Spatial Information Sciences XL-1/W2, 157–162.

GIRMA, K., MARTIN, K.L., ANDERSON, R.H., ARNALL, D.B., BRIXEY, K.D., CASILLAS, M.A., CHUNG, B., DOBEY, B.C., KAMENIDOU, S.K., KARIUKI, S.K., KATSALIROU, E.E., MORRIS, J.C., MOSS, J.Q., ROHLA, C.T., SUDBURY, B.J., TUBANA, B.S., RAUN, W.R., **2005**. Mid-Season Prediction of Wheat-Grain Yield Potential Using Plant, Soil, and Sensor Measurements. Journal of Plant Nutrition 29, 873–897. doi:10.1080/01904160600649187

GITELSON, A.A., KAUFMAN, Y.J., STARK, R., RUNDQUIST, D., **2002**. Novel algorithms for remote estimation of vegetation fraction. Remote Sensing of Environment 80, 76–87. doi:10.1016/s0034-4257(01)00289-9

GITELSON, A.A., VIÑA, A., ARKEBAUER, T.J., RUNDQUIST, D.C., KEYDAN, G., LEAVITT, B., **2003**. Remote estimation of leaf area index and green leaf biomass in maize canopies. Geophysical Research Letters 30, 1248. doi:10.1029/2002GL016450

GNYP, M.L., **2014**. Evaluating and developing methods for non-destructive monitoring of biomass and nitrogen in wheat and rice using hyperspectral remote sensing (dissertation). University of Cologne, Köln, Germany.

GNYP, M.L., BARETH, G., LI, F., LENZ-WIEDEMANN, V.I.S., KOPPE, W., MIAO, Y., HENNIG, S.D., JIA, L., LAUDIEN, R., CHEN, X., ZHANG, F., **2014a**. Development and implementation of a multiscale biomass model using hyperspectral vegetation indices for winter wheat in the North China Plain. International Journal of Applied Earth Observation and Geoinformation 33, 232–242. doi:10.1016/j.jag.2014.05.006

GRENZDÖRFFER, G.J., NIEMEYER, F., **2011**. UAV based BRDF-measurements of agricultural surfaces with PFIFFIKUS. International Archives of the Photogrammetry, Remote Sensing and Spatial Information Sciences XXXVIII-1/C22, 229–234.

GRENZDÖRFFER, G., ZACHARIAS, P., **2014**. Bestandeshöhenermittlung landwirtschaftlicher Kulturen aus UAS-Punktwolken, in: Proceedings of the 34. Wissenschaftlich-Technische Jahrestagung Der DGPF. Presented at the DGPF Tagung, Hamburg, Germany, p. 8.

GUILLEN-CLIMENT, M.L., ZARCO-TEJADA, P.J., BERNI, J. A. J., NORTH, P.R.J., VILLALOBOS, F.J., **2012**. Mapping radiation interception in row-structured orchards using 3D simulation and high-resolution

airborne imagery acquired from a UAV. Precision Agriculture 13, 473–500. doi:10.1007/s11119-012-9263-8

HAALA, N., ROTHERMEL, M., **2012**. Dense Multi-Stereo Matching for High Quality Digital Elevation Models. Photogrammetrie - Fernerkundung - Geoinformation 4, 331–343. doi:10.1127/1432-8364/2012/0121

HABOUDANE, D., **2004**. Hyperspectral vegetation indices and novel algorithms for predicting green LAI of crop canopies: Modeling and validation in the context of precision agriculture. Remote Sensing of Environment 90, 337–352. doi:10.1016/j.rse.2003.12.013

HANSEN, P.M., SCHJOERRING, J.K., **2003**. Reflectance measurement of canopy biomass and nitrogen status in wheat crops using normalized difference vegetation indices and partial least squares regression. Remote Sensing of Environment 86, 542–553. doi:10.1016/S0034-4257(03)00131-7

HARDIN, P., JENSEN, R., **2011a**. Small-Scale Unmanned Aerial Vehicles in Environmental Remote Sensing: Challenges and Opportunities. GIScience & Remote Sensing 48, 99–111. doi:10.2747/1548-1603.48.1.99

HARTMANN, W., TILCH, S., EISENBEISS, H., SCHINDLER, K., **2012**. Determination of the UAV position by automatic processing of thermal images. International Archives of the Photogrammetry, Remote Sensing and Spatial Information Sciences XXXIX-B6, 111–116.

HARWIN, S., LUCIEER, A., **2012**. Assessing the Accuracy of Georeferenced Point Clouds Produced via Multi-View Stereopsis from Unmanned Aerial Vehicle (UAV) Imagery. Remote Sensing 4, 1573–1599. doi:10.3390/rs4061573

HATFIELD, J.L., GITELSON, A.A., SCHEPERS, J.S., WALTHALL, C.L., **2008**. Application of Spectral Remote Sensing for Agronomic Decisions. Agronomy Journal 100, S117–S131. doi:10.2134/agronj2006.0370c

HEISKANEN, J., **2006**. Estimating aboveground tree biomass and leaf area index in a mountain birch forest using ASTER satellite data. International Journal of Remote Sensing 27, 1135–1158. doi:10.1080/01431160500353858

HISYSTEMS GMBH, **2013**. HiSystems [WWW Document]. URL http://www.hisystems.de (accessed 1.8.13).

HOFFMEISTER, D., **2014**. Feasibility studies of terrestrial laser scanning in coastal geomorphology, agronomy, and geoarchaeology (dissertation). University of Cologne, Köln, Germany.

HOFFMEISTER, D., BOLTEN, A., CURDT, C., WALDHOFF, G., BARETH, G., **2010**. High-resolution Crop Surface Models (CSM) and Crop Volume Models (CVM) on field level by terrestrial laser scanning, in: Guo, H., Wang, C. (Eds.), SPIE Proceedings of the Sixth International Symposium on Digital Earth: Models, Algorithms, and Virtual Reality. Presented at the Sixth International Symposium on Digital Earth: Models, Algorithms, and Virtual Reality, Beijing, China, p. 78400E–78400E–6. doi:10.1117/12.872315

HOFFMEISTER, D., WALDHOFF, G., CURDT, C., TILLY, N., BENDIG, J., BARETH, G., **2013**. Spatial variability detection of crop height in a single field by terrestrial laser scanning, in: Stafford, J.V. (Ed.), Precision Agriculture '13. Presented at the 9th European Conference on Precision Agriculture, Wageningen Academic Publishers, Lleida, Spain, pp. 267–274.

HONKAVAARA, E., SAARI, H., KAIVOSOJA, J., PÖLÖNEN, I., HAKALA, T., LITKEY, P., MÄKYNEN, J., PESONEN, L., **2013**. Processing and Assessment of Spectrometric, Stereoscopic Imagery Collected Using a Lightweight UAV Spectral Camera for Precision Agriculture. Remote Sensing 5, 5006–5039. doi:10.3390/rs5105006

HUANG, Y., THOMSON, S.J., LAN, Y., MAAS, S.J., **2010**. Multispectral imaging systems for airborne remote sensing to support agricultural production management. International Journal of Agricultural and Biological Engineering 3, 50–62. doi:10.3965/j.issn.1934-6344.2010.01.0-0

HUETE, A.R., **1988**. A soil-adjusted vegetation index (SAVI). Remote Sensing of Environment 25, 295–309. doi:10.1016/0034-4257(88)90106-X

HUNT, E.R., DAUGHTRY, C.S.T., EITEL, J.U.H., LONG, D.S., **2011**. Remote Sensing Leaf Chlorophyll Content Using a Visible Band Index. Agronomy Journal 103, 1090. doi:10.2134/agronj2010.0395

HUNT, E.R., EVERITT, J.H., RITCHIE, J.C., MORAN, M.S., BOOTH, D.T., ANDERSON, G.L., CLARK, P.E., SEYFRIED, M.S., **2003**. Applications and research using remote sensing for rangeland management. Photogrammetric Engineering & Remote Sensing 69, 675–693.

HUNT JR., E.R., CAVIGELLI, M., DAUGHTRY, C.S.T., MCMURTREY III, J.E., WALTHALL, C.L., **2005**. Evaluation of Digital Photography from Model Aircraft for Remote Sensing of Crop Biomass and Nitrogen Status. Precision Agriculture 6, 359–378. doi:10.1007/s11119-005-2324-5

HUNT JR., E.R., DORAISWAMY, P.C., MCMURTREY, J.E., DAUGHTRY, C.S.T., PERRY, E.M., AKHMEDOV, B., **2013**. A visible band index for remote sensing leaf chlorophyll content at the canopy scale. International Journal of Applied Earth Observation and Geoinformation 21, 103–112. doi:10.1016/j.jag.2012.07.020

HUNT, JR., E.R., HIVELY, W.D., FUJIKAWA, S.J., LINDEN, D.S., DAUGHTRY, C.S.T., MCCARTY, G.W., **2010**. Acquisition of NIR-Green-Blue Digital Photographs from Unmanned Aircraft for Crop Monitoring. Remote Sensing 2, 290–305. doi:10.3390/rs2010290

JACKSON, R.D., HUETE, A.R., **1991**. Interpreting vegetation indices. Preventive Veterinary Medicine 11, 185–200. doi:10.1016/S0167-5877(05)80004-2

JENSEN, A., LORENZEN, B., ØSTERGAARD, H.S., HVELPLUND, E.K., **1990**. Radiometric estimation of biomass and nitrogen content of barley grown at different nitrogen levels. International Journal of Remote Sensing 11, 1809–1820. doi:10.1080/01431169008955131

JENSEN, T., APAN, A., YOUNG, F., ZELLER, L., **2007**. Detecting the attributes of a wheat crop using digital imagery acquired from a low-altitude platform. Computers and Electronics in Agriculture 59, 66–77. doi:10.1016/j.compag.2007.05.004

JONES, H.G., VAUGHAN, R.A., **2010**. Remote Sensing of Vegetation: Principles, Techniques, and Applications. Oxford University Press, Oxford, UK.

JORDAN, C.F., **1969**. Derivation of Leaf-Area Index from Quality of Light on the Forest Floor. Ecology 50, 663–666. doi:10.2307/1936256

KELCEY, J., LUCIEER, A., **2012**. Sensor Correction of a 6-Band Multispectral Imaging Sensor for UAV Remote Sensing. Remote Sensing 4, 1462–1493. doi:10.3390/rs4051462

KOPPE, W., GNYP, M.L., HÜTT, C., YAO, Y., MIAO, Y., CHEN, X., BARETH, G., **2013**. Rice monitoring with multi-temporal and dual-polarimetric TerraSAR-X data. International Journal of Applied Earth Observation and Geoinformation 21, 568–576. doi:10.1016/j.jag.2012.07.016

KUMAR, H.D., **2006**. Agricultural Ecology. APH Publishing, New Delhi, India.

KUMAR, L., SCHMIDT, K., DURY, S., SKIDMORE, A., **2001**. Imaging Spectrometry and Vegetation Science, in: Meer, F.D. van der, Jong, S.M.D. (Eds.), Imaging Spectrometry, Remote Sensing and Digital Image Processing. Kluwer Academic Publishers, Dordrecht, Netherlands, pp. 111–155.

KUNZ, A., VÖLKERING, G., **2013**. Campus Klein-Altendorf Versuchsfeldfuehrer 2013.

LALIBERTE, A.S., GOFORTH, M.A., STEELE, C.M., RANGO, A., **2011**. Multispectral Remote Sensing from Unmanned Aircraft: Image Processing Workflows and Applications for Rangeland Environments. Remote Sensing 3, 2529–2551. doi:10.3390/rs3112529

LANCASHIRE, P.D., BLEIHOLDER, H., BOOM, T.V.D., LANGELÜDDEKE, P., STAUSS, R., WEBER, E., WITZENBERGER, A., **1991**. A uniform decimal code for growth stages of crops and weeds. Annals of Applied Biology 119, 561–601. doi:10.1111/j.1744-7348.1991.tb04895.x

LANUV NRW, **2011**. Landesamt für Natur, Umwelt und Verbraucherschutz: Klimaatlas Nordrhein-Westfalen [WWW Document]. Klimaatlas Nordrhein-Westfalen. URL http://www.klimaatlas.nrw.de/site/nav2/KarteMG.aspx (accessed 8.22.14).

LATI, R.N., FILIN, S., EIZENBERG, H., **2013a**. Estimating plant growth parameters using an energy minimization-based stereovision model. Computers and Electronics in Agriculture 98, 260–271. doi:10.1016/j.compag.2013.07.012

LATI, R.N., MANEVICH, A., FILIN, S., **2013b**. Three-dimensional image-based modelling of linear features for plant biomass estimation. International Journal of Remote Sensing 34, 6135–6151. doi:10.1080/01431161.2013.793870

L'AVION JAUNE S.A.R.L., **2014**. YellowScan UAV lidar [WWW Document]. YellowScan. URL http://yellowscan.lavionjaune.com/ (accessed 10.29.14).

LELONG, C.C.D., **2008**. Assessment of Unmanned Aerial Vehicles Imagery for Quantitative Monitoring of Wheat Crop in Small Plots. Sensors 8, 3557–3585. doi:10.3390/s8053557

LE MAIRE, G., FRANÇOIS, C., SOUDANI, K., BERVEILLER, D., PONTAILLER, J.-Y., BRÉDA, N., GENET, H., DAVI, H., DUFRÊNE, E., **2008**. Calibration and validation of hyperspectral indices for the estimation of broadleaved forest leaf chlorophyll content, leaf mass per area, leaf area index and leaf canopy biomass. Remote Sensing of Environment 112, 3846–3864. doi:10.1016/j.rse.2008.06.005

LEMAIRE, G., GASTAL, F., **1997**. N Uptake and Distribution in Plant Canopies, in: Lemaire, D.G. (Ed.), Diagnosis of the Nitrogen Status in Crops. Springer, Berlin, Germany, pp. 3–43.

LEMAIRE, G., JEUFFROY, M.-H., GASTAL, F., **2008**. Diagnosis tool for plant and crop N status in vegetative stage. European Journal of Agronomy 28, 614–624. doi:10.1016/j.eja.2008.01.005

LIEBEREI, R., REISDORFF, C., **2007**. Nutzpflanzenkunde: Nutzbare Gewächse der gemäßigten Breiten, Subtropen und Tropen, 7th ed. Thieme, Stuttgart, Germany.

LILLESAND, T.M., KIEFER, R.W., CHIPMAN, J.W., **2008**. Remote sensing and image interpretation. John Wiley & Sons, Hoboken, NJ, U.S.

LIN, Y., HYYPPA, J., JAAKKOLA, A., **2011**. Mini-UAV-Borne LIDAR for Fine-Scale Mapping. IEEE Geoscience and Remote Sensing Letters 8, 426–430. doi:10.1109/LGRS.2010.2079913

LIU, H.Y., YANG, G.J., ZHU, H.C., **2014**. The Extraction of Wheat Lodging Area in UAV's Image Used Spectral and Texture Features. Applied Mechanics and Materials 651-653, 2390–2393. doi:10.4028/www.scientific.net/AMM.651-653.2390

LIU, L., WANG, J., BAO, Y., HUANG, W., MA, Z., ZHAO, C., **2006**. Predicting winter wheat condition, grain yield and protein content using multi-temporal EnviSat-ASAR and Landsat TM satellite images. International Journal of Remote Sensing 27, 737–753. doi:10.1080/01431160500296867

LOUHAICHI, M., BORMAN, M.M., JOHNSON, D.E., **2001**. Spatially located platform and aerial photography for documentation of grazing impacts on wheat. Geocarto International 16, 65–70.

LUMME, J., KARJALAINEN, M., KAARTINEN, H., KUKKO, A., HYYPPÄ, J., HYYPPÄ, H., JAAKKOLA, A., KLEEMOLA, J., **2008**. Terrestrial laser scanning of agricultural crops. The International Archives of the Photogrammetry, Remote Sensing and Spatial Information Sciences 37, 563–566.

MARCELIS, L.F.M., HEUVELINK, E., GOUDRIAAN, J., **1998**. Modelling biomass production and yield of horticultural crops: a review. Scientia Horticulturae 74, 83–111. doi:10.1016/S0304-4238(98)00083-1

MARKETSANDMARKETS, **2013**. Unmanned Aerial Vehicle (UAV) Market (2013-2018) [WWW Document]. MarketsandMarkets, Dallas, TX, US. URL http://www.marketsandmarkets.com/Market-Reports/unmanned-aerial-vehicles-uav-market-662.html (accessed 9.16.14).

MERZ, T., CHAPMAN, S., **2011**. Autonomous unmanned helicopter system for remote sensing missions in unknown environments, in: International Archives of the Photogrammetry, Remote Sensing and Spatial Information Sciences. Presented at the UAV-g 2011, Zurich, Switzerland, pp. 14–16.

MICRODRONES, **2014**. microdrones - md4-1000 [WWW Document]. Microdrones md4-1000: the tough workhorse. URL http://www.microdrones.com/en/products/md4-1000/at-a-glance/ (accessed 10.7.14).

MISTELE, B., SCHMIDHALTER, U., **2008**. Spectral measurements of the total aerial N and biomass dry weight in maize using a quadrilateral-view optic. Field Crops Research 106, 94–103. doi:10.1016/j.fcr.2007.11.002

MONTES, J.M., TECHNOW, F., DHILLON, B.S., MAUCH, F., MELCHINGER, A.E., **2011**. High-throughput non-destructive biomass determination during early plant development in maize under field conditions. Field Crops Research 121, 268–273. doi:10.1016/j.fcr.2010.12.017

MORIONDO, M., MASELLI, F., BINDI, M., **2007**. A simple model of regional wheat yield based on NDVI data. European Journal of Agronomy 26, 266–274. doi:10.1016/j.eja.2006.10.007

MOTOHKA, T., NASAHARA, K.N., OGUMA, H., TSUCHIDA, S., **2010**. Applicability of Green-Red Vegetation Index for Remote Sensing of Vegetation Phenology. Remote Sensing 2, 2369–2387. doi:10.3390/rs2102369

MUELLER, N.D., GERBER, J.S., JOHNSTON, M., RAY, D.K., RAMANKUTTY, N., FOLEY, J.A., **2012**. Closing yield gaps through nutrient and water management. Nature 490, 254–257. doi:10.1038/nature11420

MULLA, D.J., **2013**. Twenty five years of remote sensing in precision agriculture: Key advances and remaining knowledge gaps. Biosystems Engineering 114, 358–371. doi:10.1016/j.biosystemseng.2012.08.009

MUNZERT, M., FRAHM, J., **2006**. Pflanzliche Erzeugung: Grundlagen des Acker- und Pflanzenbaus und der Guten fachlichen Praxis, Grundlagen der Verfahrenstechnik, Produktions- und Verfahrenstechnik für Kulturpflanzen, Dauergrünland, Sonderkulturen, Nachwachsende Rohstoffe, Ökologischer Landbau, Naturschutz und Landschaftspflege, 12th ed. BLV, Munich, Germany.

MUTANGA, O., SKIDMORE, A.K., **2004**. Narrow band vegetation indices overcome the saturation problem in biomass estimation. International Journal of Remote Sensing 25, 3999–4014. doi:10.1080/01431160310001654923

NEBIKER, S., ANNEN, A., SCHERRER, M., OESCH, D., **2008**. A light-weight multispectral sensor for micro uav—opportunities for very high resolution airborne remote sensing. The International Archives of the Photogrammetry, Remote Sensing and Spatial Information Sciences 37, 1193–2000.

NEITZEL, F., KLONOWSKI, J., **2011**. Mobile 3D mapping with a low-cost UAV system, in: International Archives of the Photogrammetry, Remote Sensing and Spatial Information Sciences. Presented at the UAV-g 2011, Zurich, Switzerland, pp. 1–6.

NELLIS, M.D., PRICE, K.P., RUNDQUIST, D., **2009**. Remote Sensing of Cropland Agriculture, in: Warner, T.A., Nellis, M.D., Foody, G.M. (Eds.), The SAGE Handbook of Remote Sensing. SAGE Publications Ltd., London, UK, pp. 368–383.

NONAMI, K., KARTIDJO, M., YOON, K.-J., BUDIYONO, A., **2013**. Autonomous Control Systems and Vehicles: Intelligent Unmanned Systems. Springer, New York, U.S.

NONAMI, K., KENDOUL, F., SUZUKI, S., WANG, W., NAKAZAWA, D., **2010**. Autonomous Flying Robots: Unmanned Aerial Vehicles and Micro Aerial Vehicles. Springer, Tokyo, Japan.

OERKE, E.-C., GERHARDS, R., MENZ, G., SIKORA, R.A. (EDS.), **2010**. Precision Crop Protection - the Challenge and Use of Heterogeneity. Springer, Dordrecht, Netherlands.

OLIVER, M., BISHOP, T., MARCHANT, B., **2013**. Precision Agriculture for Sustainability and Environmental Protection. Routledge, Abingdon, UK.

OUÉDRAOGO, M.M., DEGRÉ, A., DEBOUCHE, C., LISEIN, J., **2014**. The evaluation of unmanned aerial system-based photogrammetry and terrestrial laser scanning to generate DEMs of agricultural watersheds. Geomorphology 214, 339–355. doi:10.1016/j.geomorph.2014.02.016

PECKHAM, R.J., JORDAN, G., **2007**. Digital Terrain Modelling: Development and Applications in a Policy Support Environment. Springer, Berlin, Germany.

PEÑA, J.M., TORRES-SÁNCHEZ, J., DE CASTRO, A.I., KELLY, M., LÓPEZ-GRANADOS, F., **2013**. Weed Mapping in Early-Season Maize Fields Using Object-Based Analysis of Unmanned Aerial Vehicle (UAV) Images. PLoS ONE 8, e77151 1–12. doi:10.1371/journal.pone.0077151

PERRY, E.M., ROBERTS, D.A., **2008**. Sensitivity of Narrow-Band and Broad-Band Indices for Assessing Nitrogen Availability and Water Stress in an Annual Crop. Agronomy Journal 100, 1211–1219. doi:10.2134/agronj2007.0306

PFEIFER, N., GLIRA, P., BRIESE, C., **2012**. Direct georeferencing with on board navigation components of light weight UAV platforms, in: Proceedings of the XXII ISPRS Congress. Technical Commission VII. ISPRS. Presented at the XXII ISPRS Congress, Melbourne, Australia, pp. 487–492.

PINTER, P.J., HATFIELD, J.L., SCHEPERS, J.S., BARNES, E.M., MORAN, M.S., DAUGHTRY, C.S., UPCHURCH, D.R., **2003**. Remote sensing for crop management. Photogrammetric Engineering & Remote Sensing 69, 647–664.

PORDESIMO, L.O., EDENS, W.C., SOKHANSANJ, S., **2004**. Distribution of aboveground biomass in corn stover. Biomass and Bioenergy 26, 337–343. doi:10.1016/S0961-9534(03)00124-7

QI, J., CHEHBOUNI, A., HUETE, A.R., KERR, Y.H., SOROOSHIAN, S., **1994**. A modified soil adjusted vegetation index. Remote Sensing of Environment 48, 119–126. doi:10.1016/0034-4257(94)90134-1

RASMUSSEN, J., NIELSEN, J., GARCIA-RUIZ, F., CHRISTENSEN, S., STREIBIG, J.C., **2013**. Potential uses of small unmanned aircraft systems (UAS) in weed research. Weed Research 53, 242–248. doi:10.1111/wre.12026

RAUN, W.R., JOHNSON, G.V., **1999**. Improving Nitrogen Use Efficiency for Cereal Production. Agronomy Journal 91, 357–363. doi:10.2134/agronj1999.00021962009100030001x

REMBOLD, F., ATZBERGER, C., SAVIN, I., ROJAS, O., **2013**. Using Low Resolution Satellite Imagery for Yield Prediction and Yield Anomaly Detection. Remote Sensing 5, 1704–1733. doi:10.3390/rs5041704

REMONDINO, F., KERSTEN, T.P., **2012**. Low-cost und open-source Lösungen für die automatisierte Generierung von 3D-Punkt- wolken – ein kritischer Überblick. Terrestrisches Laserscanning 2012, Schriftenreihe des DVW 69, 63–80.

REMONDINO, F., SPERA, M.G., NOCERINO, E., MENNA, F., NEX, F., **2014**. State of the art in high density image matching. Photogram Rec 29, 144–166. doi:10.1111/phor.12063

RIEGL LASER MEASUREMENT SYSTEMS GMBH, **2014a**. RIEGL - VUX-1 Datasheet [WWW Document]. RIEGL - Laser Measurement Systems. URL http://www.riegl.com/uploads/tx_pxriegldownloads/DataSheet_VUX-1_2014-09-18_PRELIMINARY.pdf (accessed 10.29.14).

RIEGL LASER MEASUREMENT SYSTEMS GMBH, **2014b**. RIEGL - UAS/UAV Scanning [WWW Document]. RIEGL - Laser Measurement Systems. URL http://www.riegl.com/products/uasuav-scanning/ (accessed 10.29.14).

ROBERTS, D., ROTH, K., PERROY, R., **2011**. Hyperspectral Vegetation Indices, in: Thenkabail, P.S., Huete, A. (Eds.), Hyperspectral Remote Sensing of Vegetation. CRC Press, Boca Raton, FL, US, pp. 309–328.

RONDEAUX, G., STEVEN, M., BARET, F., **1996**. Optimization of soil-adjusted vegetation indices. Remote Sensing of Environment 55, 95–107. doi:10.1016/0034-4257(95)00186-7

ROUSE, J.W., HAAS, R.H., SCHELL, J.A., DEERING, D.W., **1974**. Monitoring Vegetation Systems in the Great Plains with Erts. NASA Special Publication 351, 309.

SABINS, F.F., **1997**. Remote sensing, 3rd. ed. ed. W.H. Freeman, New York, NY.

SAMSEEMOUNG, G., SONI, P., JAYASURIYA, H.P.W., SALOKHE, V.M., **2012**. Application of low altitude remote sensing (LARS) platform for monitoring crop growth and weed infestation in a soybean plantation. Precision Agriculture 13, 611–627. doi:10.1007/s11119-012-9271-8

Sanderson, M.A., Rotz, C.A., Fultz, S.W., Rayburn, E.B., **2001**. Estimating forage mass with a commercial capacitance meter, rising plate meter, and pasture ruler. Agronomy Journal 93, 1281–1286.

Scharstein, D., Szeliski, R., **2002**. A taxonomy and evaluation of dense two-frame stereo correspondence algorithms. International Journal of Computer Vision 47, 7–42. doi:10.1023/A:1014573219977

Schlegel, R.H.J., **2009**. Dictionary of Plant Breeding, Second Edition. CRC Press, Boca Raton, FL, US.

Scotford, I.M., Miller, P.C.H., **2004**. Combination of Spectral Reflectance and Ultrasonic Sensing to monitor the Growth of Winter Wheat. Biosystems Engineering 87, 27–38. doi:10.1016/j.biosystemseng.2003.09.009

Scully, B.T., Wallace, D.H., **1990**. Variation in and relationship of biomass, growth rate, harvest index, and phenology to yield of common bean. Journal of the American Society for Horticultural Science 115, 218–225.

Seelan, S.K., Laguette, S., Casady, G.M., Seielstad, G.A., **2003**. Remote sensing applications for precision agriculture: A learning community approach. Remote Sensing of Environment, IKONOS Fine Spatial Resolution Land Observation 88, 157–169. doi:10.1016/j.rse.2003.04.007

Serrano, L., Filella, I., Pen˜uelas, J., **2000**. Remote Sensing of Biomass and Yield of Winter Wheat under Different Nitrogen Supplies. Crop Science 40, 723. doi:10.2135/cropsci2000.403723x

Shahbazi, M., Théau, J., Ménard, P., **2014**. Recent applications of unmanned aerial imagery in natural resource management. GIScience & Remote Sensing 51, 339–365.

Shanahan, J.F., Schepers, J.S., Francis, D.D., Varvel, G.E., Wilhelm, W.W., Tringe, J.M., Schlemmer, M.R., Major, D.J., **2001**. Use of remote-sensing imagery to estimate corn grain yield. Agronomy Journal 93, 583–589. doi:10.2134/agronj2001.933583x

Snavely, N., Seitz, S.M., Szeliski, R., **2008**. Modeling the World from Internet Photo Collections. International Journal of Computer Vision 80, 189–210. doi:10.1007/s11263-007-0107-3

Sona, G., Pinto, L., Pagliari, D., Passoni, D., Gini, R., **2014**. Experimental analysis of different software packages for orientation and digital surface modelling from UAV images. Earth Science Informatics 7, 97–107. doi:10.1007/s12145-013-0142-2

Spicer, M., Ruckelshausen, A., Dzinaj, T., Linz, A., **2007**. Sensor System, Method, and Computer Program Product for Plant Phenotype Measurement in Agricultural Environments. Patent No.: WO/2007/016407.

Srinivasan, A., Srinivasan, A.E., **2006**. Handbook of Precision Agriculture: Principles and Applications. Food Products Pr, Bringhamton, NY, U.S.

Suárez, L., Zarco-Tejada, P.J., González-Dugo, V., Berni, J.A.J., Sagardoy, R., Morales, F., Fereres, E., **2010**. Detecting water stress effects on fruit quality in orchards with time-series PRI airborne imagery. Remote Sensing of Environment 114, 286–298. doi:10.1016/j.rse.2009.09.006

Swain, K.C., Thomson, S.J., Jayasuriya, H.P.W., **2010**. Adoption of an unmanned helicopter for low-altitude remote sensing to estimate yield and total biomass of a rice crop. Transactions of the ASAE 53, 21–27.

Swain, K.C., Zaman, Q.U., **2012**. Rice Crop Monitoring with Unmanned Helicopter Remote Sensing Images, in: Fatoyinbo, L. (Ed.), Remote Sensing of Biomass - Principles and Applications. InTech, Rijeka, Croatia.

Szeliski, R., **2010**. Computer Vision: Algorithms and Applications. Springer, London, UK.

Tilly, N., Hoffmeister, D., Cao, Q., Huang, S., Lenz-Wiedemann, V.I.S., Miao, Y., Bareth, G., **2014**. Multitemporal crop surface models: accurate plant height measurement and biomass estimation with terrestrial laser scanning in paddy rice. Journal of Applied Remote Sensing 8, 083671–083671. doi:10.1117/1.JRS.8.083671

Torres-Sánchez, J., López-Granados, F., De Castro, A.I., Peña-Barragán, J.M., **2013**. Configuration and Specifications of an Unmanned Aerial Vehicle (UAV) for Early Site Specific Weed Management. PLoS ONE 8, e58210 1–15. doi:10.1371/journal.pone.0058210

Torres-Sánchez, J., Peña, J.M., de Castro, A.I., López-Granados, F., **2014**. Multi-temporal mapping of the vegetation fraction in early-season wheat fields using images from UAV. Computers and Electronics in Agriculture 103, 104–113. doi:10.1016/j.compag.2014.02.009

Tucker, C.J., **1979**. Red and photographic infrared linear combinations for monitoring vegetation. Remote Sensing of Environment 8, 127–150. doi:10.1016/0034-4257(79)90013-0

Turner, D., Lucieer, A., Watson, C., **2011**. Development of an Unmanned Aerial Vehicle (UAV) for hyper resolution vineyard mapping based on visible, multispectral, and thermal imagery, in: Proceedings of 34th International Symposium on Remote Sensing of Environment. Presented at the 34th International Symposium on Remote Sensing of Environment, Sydney, Australia, p. 4.

Ullman, S., **1979**. The Interpretation of Structure from Motion. Proceedings of the Royal Society of London. Series B. Biological Sciences 203, 405–426. doi:10.1098/rspb.1979.0006

Unger, J., Reich, M., Heipke, C., **2014**. UAV-based photogrammetry: monitoring of a building zone. ISPRS - International Archives of the Photogrammetry, Remote Sensing and Spatial Information Sciences XL-5, 601–606. doi:10.5194/isprsarchives-XL-5-601-2014

Valavanis, K.P., Vachtsevanos, G.J., **2014**. Handbook of Unmanned Aerial Vehicles. Springer, New York, U.S.

Van Blyenburgh, P., **1999**. UAVs: an overview. Air & Space Europe 1, 43–47. doi:10.1016/S1290-0958(00)88869-3

Van Keulen, H., Goudriaan, J., Seligman, N.G., **1989**. Modelling the effects of nitrogen on canopy development and crop growth, in: Russell, G., Marshall, B., Jarvis, P.G. (Eds.), Plant Canopies: Their Growth, Form and Function. Cambridge University Press, Cambridge, UK, pp. 83–104.

Vargas, L.A., Andersen, M.N., Jensen, C.R., Jørgensen, U., **2002**. Estimation of leaf area index, light interception and biomass accumulation of Miscanthus sinensis "Goliath" from radiation measurements. Biomass and Bioenergy 22, 1–14. doi:10.1016/S0961-9534(01)00058-7

Verhoeven, G., **2011**. Taking computer vision aloft - archaeological three-dimensional reconstructions from aerial photographs with photoscan. Archaeological Prospection 18, 67–73. doi:10.1002/arp.399

Verhoeven, G., Doneus, M., Briese, C., Vermeulen, F., **2012**. Mapping by matching: a computer vision-based approach to fast and accurate georeferencing of archaeological aerial photographs. Journal of Archaeological Science 39, 2060–2070. doi:10.1016/j.jas.2012.02.022

Von Bueren, S., Burkart, A., Hueni, A., Rascher, U., Tuohy, M., Yule, I., **2014**. Comparative validation of UAV based sensors for the use in vegetation monitoring. Biogeosciences Discussions 11, 3837–3864. doi:10.5194/bgd-11-3837-2014

Wallace, L., Lucieer, A., Watson, C., Turner, D., **2012**. Development of a UAV-LiDAR System with Application to Forest Inventory. Remote Sensing 4, 1519–1543. doi:10.3390/rs4061519

Wang, Y., Yang, Y., **2001**. Effects of agriculture reclamation on the hydrologic characteristics in the Sanjiang Plain, China. Chinese Geographical Science 11, 163–167. doi:10.1007/s11769-001-0037-x

Watanabe, T., Hanan, J.S., Room, P.M., Hasegawa, T., Nakagawa, H., Takahashi, W., **2005**. Rice Morphogenesis and Plant Architecture: Measurement, Specification and the Reconstruction of Structural Development by 3D Architectural Modelling. Annals of Botany 95, 1131–1143. doi:10.1093/aob/mci136

Whelan, B., Taylor, J., **2013**. Precision Agriculture for Grain Production Systems. Csiro Publishing, Collingwood, VIC, Australia.

Woebbecke, D.M., Meyer, G.E., Bargen, K.V., Mortensen, D.A., **1995**. Color Indices for Weed Identification Under Various Soil, Residue, and Lighting Conditions. Transactions of the ASAE 38, 259–269. doi:10.13031/2013.27838

Xiang, H., Tian, L., **2011**. Method for automatic georeferencing aerial remote sensing (RS) images from an unmanned aerial vehicle (UAV) platform. Biosystems Engineering 108, 104–113. doi:10.1016/j.biosystemseng.2010.11.003

Yang, C., Everitt, J.H., Bradford, J.M., **2006**. Comparison of QuickBird Satellite Imagery and Airborne Imagery for Mapping Grain Sorghum Yield Patterns. Precision Agriculture 7, 33–44. doi:10.1007/s11119-005-6788-0

Yao, H., Tang, L., Tian, L., Brown, R., Bhatnagar, D., Cleveland, T., **2011**. Using Hyperspectral Data in Precision Farming Applications, in: Hyperspectral Remote Sensing of Vegetation. CRC Press, Boca Raton, FL, US, pp. 591–608.

Zarco-Tejada, P.J., Berjon, A., Lopezlozano, R., Miller, J., Martin, P., Cachorro, V., Gonzalez, M., Defrutos, A., **2005**. Assessing vineyard condition with hyperspectral indices: Leaf and canopy reflectance simulation in a row-structured discontinuous canopy. Remote Sensing of Environment 99, 271–287. doi:10.1016/j.rse.2005.09.002

Zhang, C., Kovacs, J.M., **2012**. The application of small unmanned aerial systems for precision agriculture: a review. Precision Agriculture 13, 693–712. doi:10.1007/s11119-012-9274-5

Zhang, N., Wang, M., Wang, N., **2002**. Precision agriculture—a worldwide overview. Computers and Electronics in Agriculture 36, 113–132. doi:10.1016/S0168-1699(02)00096-0

Zhou, Z., Liu, T., **2005**. The current status, threats and protection way of Sanjiang Plain wetland, Northeast China. Journal of Forestry Research 16, 148–152. doi:10.1007/BF02857910

## List of Figures and Tables

## Appendix A: Eigenanteil zu Kapitel 3

| | |
|---|---|
| Titel | Hochauflösende Crop Surface Models (CSM) auf der Basis von Stereobildern aus UAV-Befliegungen zur Überwachung von Reiswachstum in Nordostchina |
| Autoren | **Juliane Bendig (75%)**, Maximilian Willkomm (2%), Nora Tilly (2%), Martin Leon Gnyp (2%), Simon Bennertz (2%), Victoria I. S. Lenz-Wiedemann (5%), Georg Bareth (5%), Yuxin Miao (5%) und Cao Qiang (2%) (Erstautorenschaft) |
| Status | veröffentlicht |
| Verlag | GIS.Science |
| Publikationsjahr | 2014 |
| Band und Seitenangabe | 1: 1-9 |
| DOI | |

| | |
|---|---|
| Eigenanteil | Planung, Organisation und Durchführung der Flugkampagnen in Nordost China (Juni-Juli 2012) |
| | Datenerhebung im Gelände: Befliegungen mit einem Mini UAV (Unmanned Aerial Vehicle), Vermessung von Ground Control Points (GCPs) mit GPS, Mitarbeit bei Messungen der Pflanzenhöhe und Biomassebeprobung im Feld |
| | Aufarbeitung der gemessenen Pflanzenhöhen und GPS Daten |
| | Prozessieren der UAV Daten |
| | Schreiben des Manuskriptes |
| | Erstellung von Abbildungen und Tabellen |
| | Review/Korrekturlesen des Manuskriptes |

An dieser Publikation habe ich maßgeblich von Feldmessungen und Datenverarbeitung bis hin zur Datenanalyse und Konzeption und Ausarbeitung der Publikation mitgewirkt. Der Eigenanteil an dieser Publikation ist oben im Detail aufgeführt.

## Appendix B: Eigenanteil zu Kapitel 4

| | |
|---|---|
| Titel | UAV-based Imaging for Multi-Temporal, very high Resolution Crop Surface Models to monitor Crop Growth Variability |
| Autoren | Bendig, J. (65%), Bolten, A. (20%) und Bareth, G. (15%) (Erstautorenschaft) |
| Status | veröffentlicht |
| Verlag | PFG (Photogrammetrie Fernerkundung Geoinformation) |
| Publikationsjahr | 2013 |
| Band und Seitenangabe | 6: 551-562 |
| DOI | 10.1127/1432-8364/2013/0200 |
| | |
| Eigenanteil | Planung, Organisation und Durchführung der Flugkampagnen in Bonn (April-Juli 2012) (mit A. Bolten 50/50 %) |
| | Datenerhebung im Gelände: Befliegungen mit einem Mini UAV (Unmanned Aerial Vehicle), Vermessung von Ground Control Points (GCPs) mit GPS, Mitarbeit bei Messungen der Pflanzenhöhe im Feld |
| | Aufarbeitung der gemessenen Pflanzenhöhen und GPS Daten |
| | Prozessieren der UAV Daten |
| | Schreiben des Manuskriptes |
| | Erstellung von Abbildungen und Tabellen |
| | Review/Korrekturlesen des Manuskriptes |

An dieser Publikation habe ich maßgeblich von Feldmessungen und Datenverarbeitung bis hin zur Datenanalyse und Konzeption und Ausarbeitung der Publikation mitgewirkt. Der Eigenanteil an dieser Publikation ist oben im Detail aufgeführt.

## Appendix C: Eigenanteil zu Kapitel 5

| | |
|---|---|
| Titel | Estimating Biomass of Barley Using Crop Surface Models (CSMs) Derived from UAV-Based RGB Imaging |
| Autoren | **Juliane Bendig (70%)**, Andreas Bolten (5%), Simon Bennertz (3%), Janis Broscheit (3%), Silas Eichfuss (3%) und Georg Bareth (16%) (Erstautorenschaft) |
| Status | veröffentlicht |
| Verlag | Remote Sensing |
| Publikationsjahr | 2014 |
| Band und Seitenangabe | 6: 10395–10412 |
| DOI | 10.3390/rs61110395 |
| | |
| Eigenanteil | Planung, Organisation und Durchführung der Flugkampagnen in Klein-Altendorf südlich von Bonn (April-Juli 2013) |
| | Datenerhebung im Gelände: Befliegungen mit einem Mini UAV (Unmanned Aerial Vehicle), Vermessung von Ground Control Points (GCPs) mit GPS, Mitarbeit bei Messungen der Pflanzenhöhe im Feld |
| | Aufarbeitung der gemessenen Pflanzenhöhen, GPS Daten und Biomassedaten |
| | Prozessieren der UAV Daten |
| | Schreiben des Manuskriptes |
| | Erstellung von Abbildungen und Tabellen |
| | Review/Korrekturlesen des Manuskriptes |

An dieser Publikation habe ich maßgeblich von Feldmessungen und Datenverarbeitung bis hin zur Datenanalyse und Konzeption und Ausarbeitung der Publikation mitgewirkt. Der Eigenanteil an dieser Publikation ist oben im Detail aufgeführt.

## Appendix D: Eigenanteil zu Kapitel 6

| | |
|---|---|
| Titel | Combining UAV-based Crop Surface Models, Visible and Near Infrared Vegetation Indices for Biomass Monitoring in Barley |
| Autoren | **Juliane Bendig (60%)**, Kang Yu (10%), Helge Aasen (5%) Andreas Bolten (5%), Simon Bennertz (5%), Janis Broscheit (5%), Martin L. Gnyp (5%) und Georg Bareth (5%) (Erstautorenschaft) |
| Status | in Begutachtung |
| Verlag | International Journal of Earth Observation and Geoinformation |
| Publikationsjahr | |
| Band und Seitenangabe | |
| DOI | |

| | |
|---|---|
| Eigenanteil | Planung, Organisation und Durchführung der Flugkampagnen in Klein-Altendorf südlich von Bonn (April-Juli 2013) |
| | Datenerhebung im Gelände: Befliegungen mit einem Mini UAV (Unmanned Aerial Vehicle), Vermessung von Ground Control Points (GCPs) mit GPS, Mitarbeit bei Messungen der Pflanzenhöhe im Feld |
| | Aufarbeitung der gemessenen Pflanzenhöhen, GPS Daten, Biomasse- und Hyperspektraldaten |
| | Prozessieren der UAV Daten, Berechnung der Vegetationsindizes |
| | Schreiben des Manuskriptes |
| | Erstellung von Abbildungen und Tabellen |
| | Review/Korrekturlesen des Manuskriptes |

An dieser Publikation habe ich maßgeblich von Feldmessungen und Datenverarbeitung bis hin zur Datenanalyse und Konzeption und Ausarbeitung der Publikation mitgewirkt. Der Eigenanteil an dieser Publikation ist oben im Detail aufgeführt.

## Appendix E: Eigenanteil zu Kapitel 7

| | |
|---|---|
| Titel | Low-weight and UAV-based hyperspectral full-frame cameras for monitoring crops: spectral comparison with portable spectroradiometer measurements |
| Autoren | Georg Bareth (35%), Helge Aasen (30%), Köln, **Juliane Bendig (15%)**, Martin Leon Gnyp (5%), Andreas Bolten (5%), András Jung (4%), René Michels (3%), Ulm und Jussi Soukkamäki (3%) (Drittautorenschaft) |
| Status | im Druck |
| Verlag | PFG (Photogrammetrie Fernerkundung Geoinformation) |
| Publikationsjahr | 2015 |
| Band und Seitenangabe | 1 |
| DOI | |

| | |
|---|---|
| Eigenanteil | Planung, Organisation und Durchführung der Flugkampagnen in Klein-Altendorf südlich von Bonn (April-Juli 2013) |
| | Datenerhebung im Gelände: Befliegungen mit einem Mini UAV (Unmanned Aerial Vehicle), Vermessung von Ground Control Points (GCPs) mit GPS, Mitarbeit bei Messungen der Pflanzenhöhe |
| | Mitarbeit an Abbildungen |
| | Review/Korrekturlesen des Manuskriptes |

Diese Publikation stellt maßgeblich die wissenschaftliche Arbeit von Herrn Prof. Dr. Georg Bareth und Herrn Helge Aasen dar.
An dieser wissenschaftlichen Arbeit habe ich in einigen wesentlichen Punkten. Der Eigenanteil an dieser Publikation ist oben im Detail aufgeführt.

## Appendix F: Erklärung

Ich versichere, dass ich die von mir vorgelegte Dissertation selbständig angefertigt, die benutzten Quellen und Hilfsmittel vollständig angegeben und die Stellen der Arbeit – einschließlich Tabellen, Karten, und Abbildungen - , die anderen Werken im Wortlaut oder dem Sinn nach entnommen sind, in jedem Einzelfall als Entlehnung kenntlich gemacht habe; dass diese Dissertation noch keiner anderen Fakultät oder Universität zur Prüfung vorgelegen hat; dass sie - abgesehen von unten angegebenen Teilpublikationen - noch nicht veröffentlicht worden ist sowie, dass ich eine solche Veröffentlichung vor Abschluss des Promotionsverfahrens nicht vornehmen werde.

Die Bestimmungen der Promotionsordnung sind mir bekannt. Die von mir vorgelegte Dissertation ist von Prof. Dr. Georg Bareth betreut worden.

Köln, den

**Folgende Teilpublikationen liegen vor:**

BARETH, G., BENDIG, J., AASEN, H., GNYP, M.L., BOLTEN, A., JUNG, A., MICHELS, R., SOUKKAMÄKI, J., **2015**. Low-weight and UAV-based hyperspectral full-frame cameras for monitoring crops: spectral comparison with portable spectroradiometer measurements. Photogrammetrie - Fernerkundung - Geoinformation accepted.

BENDIG, J., BOLTEN, A., BARETH, G., **2013**. UAV-based Imaging for Multi-Temporal, very high Resolution Crop Surface Models to monitor Crop Growth Variability. Photogrammetrie - Fernerkundung - Geoinformation 6, 551–562. doi:10.1127/1432-8364/2013/0200

BENDIG, J., BOLTEN, A., BENNERTZ, S., BROSCHEIT, J., EICHFUSS, S., BARETH, G., **2014a**. Estimating Biomass of Barley Using Crop Surface Models (CSMs) Derived from UAV-Based RGB Imaging. Remote Sensing 6, 10395–10412. doi:10.3390/rs61110395

BENDIG, J., WILLKOMM, M., TILLY, N., GNYP, M.L., BENNERTZ, S., LENZ-WIEDEMANN, I.S., BARETH, G., MIAO, Y., **2014b**. Hochauflösende Crop Surface Models (CSM) auf der Basis von Stereobildern aus UAV-Befliegungen zur Überwachung von Reiswachstum in Nordostchina. gis.Science 01, 1–9.

BENDIG, J., YU, K., AASEN, H., BOLTEN, A., BENNERTZ, S., BROSCHEIT, J., GNYP, M.L., BARETH, G., **submitted**. Combining UAV-based Crop Surface Models, Visible and Near Infrared Vegetation Indices for Biomass Monitoring in Barley. International Journal of Applied Earth Observation and Geoinformation.

# Appendix G: Curriculum vitae

**Appendix F Publication list**                                    * = part of dissertation

*BARETH, G., BENDIG, J., AASEN, H., GNYP, M.L., BOLTEN, A., JUNG, A., MICHELS, R., SOUKKAMÄKI, J., 2015. **Low-weight and UAV-based hyperspectral full-frame cameras for monitoring crops: spectral comparison with portable spectroradiometer measurements. Photogrammetrie - Fernerkundung - Geoinformation accepted.**

BARETH, G., BOLTEN, A., BENDIG, J., **2011**. Potentials for low-cost Mini-UAVs, in: Lenz-Wiedemann, V., Bareth, G. (Eds.), Kölner Geographische Arbeiten 92. Presented at the Workshop on Remote Sensing Methods for Change Detection and Process Modelling, Geographisches Institut der Universität zu Köln, Cologne, Germany, pp. 1–8. doi:10.5880/TR32DB.KGA92.2.

BENDIG, J., BARETH, G., **2014**. Preface, in: Bendig, J., Bareth, G. (Eds.), Kölner Geographische Arbeiten 94. Presented at the Workshop on UAV-based Remote Sensing Methods for Monitoring Vegetation, Cologne, Germany, pp. 1–2. doi:10.5880/TR32DB.KGA94.1

BENDIG, J., BOLTEN, A., BARETH, G., **2012**. Introducing a low-cost mini-UAV for thermal-and multispectral-imaging. International Archives of the Photogrammetry, Remote Sensing and Spatial Information Sciences 39, 345–349.

*BENDIG, J., BOLTEN, A., BARETH, G., 2013. **UAV-based Imaging for Multi-Temporal, very high Resolution Crop Surface Models to monitor Crop Growth Variability. Photogrammetrie - Fernerkundung - Geoinformation 6, 551–562. doi:10.1127/1432-8364/2013/0200**

*BENDIG, J., BOLTEN, A., BENNERTZ, S., BROSCHEIT, J., EICHFUSS, S., BARETH, G., 2014a. **Estimating Biomass of Barley Using Crop Surface Models (CSMs) Derived from UAV-Based RGB Imaging. Remote Sensing 6, 10395–10412. doi:10.3390/rs61110395**

*BENDIG, J., WILLKOMM, M., TILLY, N., GNYP, M.L., BENNERTZ, S., LENZ-WIEDEMANN, I.S., BARETH, G., MIAO, Y., 2014b. **Hochauflösende Crop Surface Models (CSM) auf der Basis von Stereobildern aus UAV-Befliegungen zur Überwachung von Reiswachstum in Nordostchina. gis.Science 01, 1–9.**

*BENDIG, J., YU, K., AASEN, H., BOLTEN, A., BENNERTZ, S., BROSCHEIT, J., GNYP, M.L., BARETH, G., submitted. **Combining UAV-based Crop Surface Models, Visible and Near Infrared Vegetation Indices for Biomass Monitoring in Barley. International Journal of Applied Earth Observation and Geoinformation.**

HOFFMEISTER, D., BENDIG, J., WALDHOFF, G., **2011a**. Evaluating airborne laser scanning data for generation of digital evelation models and land cover mapping, in: Lenz-Wiedemann, V., Bareth, G. (Eds.), Kölner Geographische Arbeiten 92. Presented at the Workshop on Remote Sensing Methods for Change Detection and Process Modelling, Kölner, Cologne, Germany, pp. 31–38. doi:10.5880/TR32DB.KGA92.5

HOFFMEISTER, D., CURDT, C., TILLY, N., BENDIG, J., **2011b**. 3D terrestrial laser scanning for field crop modelling, in: Lenz-Wiedemann, V., Bareth, G. (Eds.), Kölner Geographische Arbeiten 92. Presented at the Workshop on Remote Sensing Methods for Change Detection and Process Modelling, Cologne, Germany, pp. 25–30. doi:10.5880/TR32DB.KGA92.4

HOFFMEISTER, D., CURDT, C., TILLY, N., BENDIG, J., BARETH, G., **2011c**. 3D change detection of different sugar-beet types by multi-temporal terrestrial laser scanning, in: Proceeding of: Int. Symposium on Remote Sensing and GIS Methods for Change Detection and Spatio-Temporal Modelling (CDSM). Presented at the Int. Symposium on remote sensing and GIS methods for change detection and spatio-temporal modelling (CDSM), Hong Kong, China, p. 5.

HOFFMEISTER, D., WALDHOFF, G., CURDT, C., TILLY, N., BENDIG, J., BARETH, G., **2013**. Spatial variability detection of crop height in a single field by terrestrial laser scanning, in: Stafford, J.V. (Ed.), Precision Agriculture '13. Presented at the 9th European Conference on Precision Agriculture, Wageningen Academic Publishers, Lleida, Spain, pp. 267–274.